Rational Design and Performance Study of Solid-State Lithium-Oxygen Batteries

Thesis submitted to University of Nottingham for the degree of Doctor of Philosophy, May 2023.

Zhi Gu

20199224

Supervised by

Yong Sun

Xiayin Yao

Jun He

George Chen

Signature：

Date：

Abstract

Lithium-oxygen (Li-O_2) batteries have received significant attentions and research interests since the beginning of the twenty-first century due to their extremely high theoretical energy density. These batteries employ oxygen as the positive active substance, which can be obtained from air, resulting in a lighter and more affordable battery. Despite these advantages, lithium-oxygen batteries face several challenges, primarily due to the use of organic liquid electrolyte, which poses risks of volatilization, leakage, combustion, and explosive hazards. Additionally, the use of lithium metal anode generates lithium dendrites that can puncture the electrolyte layer, leading to short-circuit accidents. The cathode of lithium-oxygen batteries has an open-hole structure designed to absorb active material oxygen, which allows the seepage of carbon dioxide and water into the electrolyte, adversely impacting battery performance. To address these challenges, a viable approach is to replace the organic liquid electrolyte with an inorganic solid electrolyte.

However, all-solid-state lithium-oxygen batteries are still in the early phases of development, and several key scientific and technical hurdles need to be tackled. One of the significant challenges is the lack of solid electrolytes that exhibit excellent performance. Additionally, the problem of interface contact between the solid electrolyte and the lithium anode must be resolved. The electrolyte and cathode also experience high interfacial impedance, resulting in poor capacity retention and short cycle life.

This thesis has dedicated considerable efforts and endeavors to address the aforementioned challenges. The highlights of this study are presented below.

1. Study of solid-state lithium-oxygen batteries based on oxide solid-state electrolytes $Li_{1.5+x}Al_{0.5}Ge_{1.5s}Si_xP_{3-x}O_{12}$ and $Li_{6.4}La_3Zr_{1.4}Ta_{0.6}O_{12}$.

Firstly, the synthesis and investigation of two different systems of solid-state electrolytes-$Li_{1.5+x}Al_{0.5}Ge_{1.5s}Si_xP_{3-x}O_{12}$ and $Li_{6.4}La_3Zr_{1.4}Ta_{0.6}O_{12}$ electrolytes are performed. These electrolytes were assembled with lithium metal anodes and carbon cathodes to construct solid-state (quasi-solid-state) lithium-oxygen cells. The Si-doped LAGP-Si glass-ceramic materials with high grain conductivity were prepared using inexpensive raw materials, and the effect of Si doping on the electrolyte properties of LAGP glass-ceramic solids was investigated. The solid-state and semi-solid-state lithium-oxygen batteries assembled with LAGP-Si demonstrated a certain cyclable capability at low current densities. High-performance garnet-type solid electrolyte LLZTO was successfully synthesized, and the solid-state lithium-oxygen battery assembled with it also showed a certain cycling capability. However, the polarization voltage was large, and the interfacial impedance between it and the electrode was high. Further research is needed to develop cost-effective cathode catalysts, prepare high-performance solid-state electrolytes, and enhance the interface between solid-state electrolytes and electrode materials. This work sets the groundwork for the subsequent investigations along this topic.

2. Study of bilayer NASICON/polymer hybrid electrolyte for stable solid-state lithium-oxygen batteries.

The usage of lithium-oxygen batteries in practical applications is still hampered various factors i.e., the growth of lithium dendrites, the deployment of flammable and unstable organic liquid electrolytes, which could lead to safety hazards and poor cycling stability. To overcome these issues, a bilayer organic/inorganic hybrid solid-state electrolyte is proposed. The Si-doped NASICON-type electrolyte $Li_{1.51}Al_{0.5}Ge_{1.5}Si_{0.01}P_{2.99}O_{12}$ acts as an inorganic rigid backbone, ensuring high ionic conductivity and creating a barrier between active oxygen and lithium anode. The polymer buffer layer Poly(ethylene glycol) methyl ether methacrylate (PEGMEM) is used due to its compatibility with lithium. The hybrid electrolyte, obtained from the synergistic effect between LAGP-Si and PEGMEM, displays high ionic conductivity and stability against the lithium anode.

As a result, the polarization of the Li symmetric cell is significantly decreased by substituting pure LAGP-Si with a bilayer hybrid electrolyte. The solid-state lithium-oxygen batteries using PEGMEM@LAGP-Si electrolyte have an enhanced initial discharge-charge capacity of 7.3 mA h cm^{-2} and improved cyclic performance for 39 cycles, with a limited capacity of 0.4 mA h cm^{-2}.

3. Study of garnet-based integrated architecture for high-performance all-solid-state lithium-oxygen batteries.

In this part, an integrated architecture consisting of a garnet electrolyte ($Li_{6.4}La_3Zr_{1.4}Ta_{0.6}O_{12}$, LLZTO) and a porous composite cathode is proposed to develop high-performance all-solid-state lithium-oxygen batteries. The exceptional internal structure of the battery effectively diminishes the interfacial impedance, offers a substantial number of active sites at the triple-phase boundaries, and enhances the electrochemical stability. Consequently, the resulting batteries display an excellent cyclic performance (86 cycles) and a superior full discharge capacity of 13.04 mA h cm^{-2}. In addition, X-ray photoelectron spectroscopy (XPS), differential electrochemical mass spectrometry (DEMS), and theoretical calculations of density functional theory (DFT) authenticate the effectiveness of this design in improving the interfacial performance, electrochemical performance, and stability of the battery. These findings are anticipated to facilitate the practical implementation of all-solid-state lithium-oxygen batteries and even other metal-oxygen (air) battery systems. Although the last work solved the contact problem between lithium anode and electrolyte, the present solid-state lithium-oxygen batteries still encounter a significant challenge due to the high impedance at the cathode/electrolyte interface. Moreover, the deficiency of triple-phase boundaries comprising Li^+, e^-, and O_2 substantially limits the active sites for the electrochemical reaction in the battery cathode.

The findings presented herein make a significant contribution to the ongoing development of all-solid-state lithium-oxygen batteries. The current investigation

demonstrates the potential of utilizing all-solid-state lithium-oxygen (air) batteries as a highly promising energy storage solution for the future. Further research endeavors are warranted to concentrate on the refinement of the design and fabrication of the solid-state battery, as well as to enhance the efficacy of interfacial modifications within this system.

Keywords: lithium-oxygen batteries, solid-state electrolytes, NASICON, garnet, polymer buffer layer, integrated cathode

Acknowledgements

In fact, I really do not know where to start. My PhD career is like a roller coaster ride of ups and downs. As a student in the joint training program, I have so many people and institutions to thank. Too many people have guided, helped, comforted, and inspired me when I was frustrated. For over three years, I completed my labs at NIMTE and stayed on UNNC campus to complete courses related to academic skills and academic ethics. This was a great boost to my initial exploration in the field of research. Although I may not necessarily continue my research career at a relevant research institute or work in a university in the future, I still see these gains as an important foundation for my future personal development.

First, I would like to express my sincere gratitude to all my supervisors, Dr. Yong Sun, Prof. Xiayin Yao, Prof. Jun He and Prof. George Chen. The scientific work and research results of this thesis could not have been achieved without the careful guidance of all the supervisors. Dr. Yong Sun, as my first supervisor, gave me a very good platform for PhD education, and together with the university, provided me with extraordinary academic resources. Whenever my research was not going well or I encountered setbacks in my campus life, Dr. Sun always gave me encouragement and counseling. Prof. Xiayin Yao, probably the most frequent supervisor I had contact with during these three years, was in charge of all my research activities and life matters in NIMTE. Prof. Yao's serious, meticulous and rigorous attitude towards his work is admirable. From the proposal of my research, to the publication of my articles, Prof. Yao's help is everywhere, which really benefited me a lot. When the experiment encountered difficulties, my heart tended to resist and give up. Thanks to Prof. Yao's motivation and encouragement, I was able to go further instead of quitting easily. Although Prof. He and Prof. George Chen are not my primary mentors, they still taught me enough in life and academics, for which I am very grateful. I also want to express my special thanks to Dr. Jinghua Wu and Dr. Xing Xin, who support my research experiments and

academic writing.

Second, I would like to show my gratitude to all the students in my research group. Without their presence, I may not have been able to overcome my inner vulnerability and overcome the challenges I encountered in the lab. Beyond my mentors, they are also the ones who share knowledge and exchange experiences with me to improve each other's research. We ate together, sang, played sports, and shared delicious food from our respective hometowns. We also discussed literature and talked about current affairs together, which made my journey to the university full and interesting.

Finally, I am deeply grateful to my parents, friends and girlfriend who have been working hard behind the scenes to support me. They have made my life complete and sustained me through these difficult times.

Contents

List of Tables

List of Figures

Abbreviations

AC	Alternating current
BET	Brunauer-Emmett-Teller
CV	Cyclic voltammetry
DEMS	Differential electrochemical mass spectroscopy
DFT	Density functional theory
DCP	Direct current-induced polarization
DMSO	Dimethyl sulfoxide
EIS	Electrochemical impedance spectroscopy
FT-IR	Fourier transform-infrared
HRTEM	High-resolution transmission electron microscopy
L_2O_2	Lithium peroxide
LAGP	$Li_{1.5}Al_{0.5}Ge_{1.5}P_3O_{12}$
LAGP-Si	$Li_{1.5+x}Al_{0.5}Ge_{1.5s}Si_xP_{3-x}O_{12}$
Li-air	Lithium-air
LIB	Lithium-ion battery
Li-O_2	Lithium-oxygen
Li-S	Lithium-sulfur
LLZO	$Li_7La_3Zr_2O_{12}$
LLZTO	$Li_{6.4}La_3Zr_{1.4}Ta_{0.6}O_{12}$
LSV	Linear sweep voltammetry
OER	Oxygen evolution reaction
ORR	Oxygen reduction reaction
PEGMEM	Poly(ethylene glycol) methyl ether methacrylate
PEO	Poly(ethylene oxide)
PMMA	Poly(methyl methacrylate)
PTFE	Poly(tetrafluoroethylene)
R_b	Bulk resistance
R_{gb}	Grain boundary resistance
SAED	Selected area electron diffraction
SEM	Scanning electron microscopy
TEGDME	Tetraethylene glycol dimethyl ether
TEM	Transmission electron microscopy
XPS	X-ray Photoelectron Spectroscopy
XRD	X-ray Diffraction

Chapter 1 Introduction

Abstract

This chapter provides an in-depth exploration of the development history and international research progress in the field of lithium batteries, specifically focusing on solid-state lithium batteries and lithium-air batteries. Additionally, it emphasizes the immense potential of solid-state lithium-air batteries as a next-generation energy storage system, highlighting the need for extensive research in this area. A significant aspect of solid-state lithium-air battery development lies in the advancement of solid-state electrolytes. Therefore, this chapter systematically introduces different types of electrolytes, which serve as the core component for the development of solid-state lithium-air batteries. Furthermore, a comprehensive overview of the lithium-air battery system is presented, categorized according to the type of electrolyte employed. This overview encompasses the reaction mechanism, composition structure, and prevailing challenges associated with each type. Drawing upon these discussions, the chapter concludes by providing research directions and summarizing the main findings of this thesis. These findings serve as a guide for subsequent chapters and contribute to the overall understanding of solid-state lithium batteries and lithium-air batteries.

1.1 Research Background

The invention of the internal combustion engine (ICE), laid the foundation of gasoline-chugging economy. However, the use of mineral energy sources (coals, crude oil, and natural gas) has led to issues of resource depletion and environmental pollution. Oil alone accounts for 34% of the world's primary energy structure and contributes to 40% of carbon dioxide (CO_2) emissions, making it one of the main causes of global climate change [1]. The current global energy crisis and environmental problems are becoming increasingly critical. Hence, it is imperative to vigorously develop novel, environmentally friendly, and efficient energy utilization and storage systems [2]. As an essential aspect of the new energy field, energy storage devices with large capacity, high performance, long life, low cost, and environmentally friendly characteristics, can effectively address the regional, temporal, and other objective challenges of renewable energy. For a long time, the electrochemical energy storage strategy based on secondary batteries has provided significant convenience for the use of portable electronic power equipment. Secondary batteries have broad application prospects and have been widely recognized and supported by the international community as an energy storage and conversion scheme [3, 4].

The storage of energy in batteries is achieved through the redox reactions of chemical substances. To meet the requirements of energy storage, a range of solutions are required, including the use of lithium-ion batteries. In 1991, SONY successfully commercialized lithium-ion batteries, which, due to their high energy density, have led the evolution of portable

electronics over the past two decades, surpassing other energy storage systems at the time. Lithium-ion batteries are now being used in electric vehicles (EVs) and have become a hot research topic in this field. However, for EVs to be widely accepted by consumers, it is necessary to exceed the current energy storage limits of lithium-ion batteries and adopt an energy storage system with a higher energy density, which is a consensus among researchers at this stage. Therefore, it is crucial to explore rechargeable battery systems with higher energy density than Li-ion batteries. The available options such as zinc-air batteries, lithium-sulfur (Li-S) battery systems, are limited. Among them, the combination of a lithium metal negative electrode and an oxygen positive electrode has the highest theoretical energy density, resulting in the lithium-air (Li-air) or lithium-oxygen (Li-O_2) battery. Figure 1-1 shows the recent development trend of energy storage systems, indicating that the Li-air battery system could be the ultimate objective for researchers in this field.

The concept of using oxygen as a positive active substance in batteries is not entirely new. For instance, primary zinc-air batteries have been in use for decades. The exploration of Li-air batteries began in the 1970s, with Abraham's pioneering work in 1996 being a particular focus [5]. Today, the need for improved energy sources has sparked an increased interest in rechargeable Li-air batteries among researchers. However, any technology with great potential needs to overcome significant hurdles during the transition phase to practical use. For instance, during the early stages of development of the lithium-ion battery, many researchers were skeptical about its commercialization. Similarly, the study of early prototypes of the secondary

Li-air battery showed that the actual reaction process occurring in the battery was not the mechanism originally proposed by the researchers. The clear conclusion that can be drawn from this is that a fundamental understanding of the chemical and electrochemical processes that occur during battery operation is essential. This knowledge plays a crucial role in the commercialization of Li-air batteries.

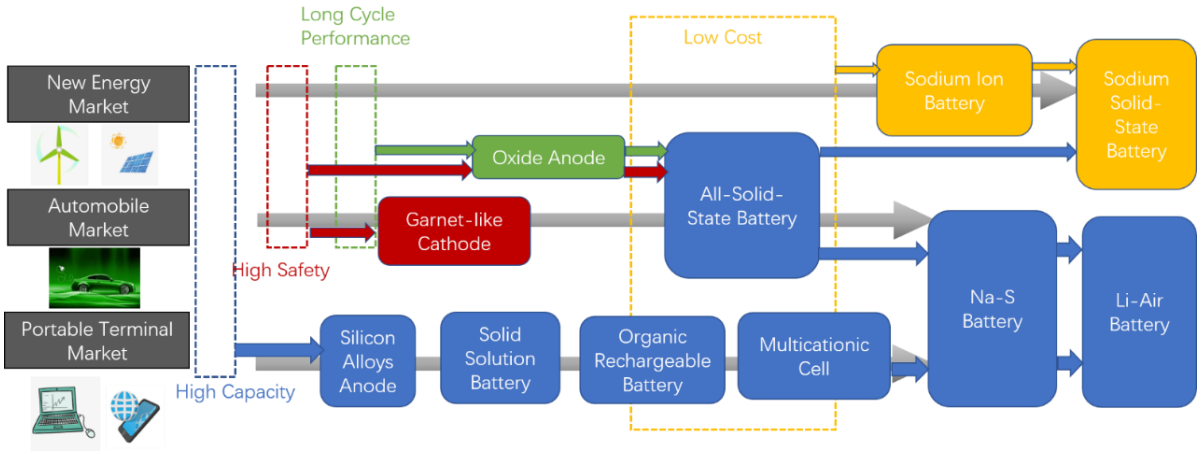

Figure 1-1 Development trend of energy storage system technology.

The electrolyte plays a crucial role in Li-air batteries. Traditional lithium batteries use organic liquid electrolytes, which have several drawbacks such as the need for extensive packaging during industrial production, as well as posing potential safety hazards i.e., leakage, flammability, and explosion. Additionally, they fail to operate normally under extreme temperatures (less than 20 °C or greater than 100 °C) [6, 7]. To address these issues, researchers have suggested to construct a solid electrolyte instead of an organic electrolyte, as it offers greater research and practical value [8-10].

1.2 Overview of Solid-State Batteries

Solid-state batteries have a construction structure and operating principle similar to that of commercial lithium-ion batteries. As shown in Figure 1-2, a lithium-ion battery consists of positive electrode (PE), negative electrode (NE), separator, liquid electrolyte, and current collector [11]. During charging, lithium ions are removed from the positive electrode and migrate through the electrolyte and separator to the negative electrode, then electrons reach the negative electrode from the positive electrode through an external circuit. During discharging, the lithium ions embedded in the carbon negative electrode deintercalate and return to the positive electrode, and the electrons move in the opposite direction at the state of charging, driving the electronic devices through the external circuit. Replacing the separator and liquid electrolyte in a conventional lithium-ion battery with a solid electrolyte, including inorganic electrolytes, polymer electrolytes and inorganic-polymer composites (IPCs), is the way to fabricate solid-state batteries, as shown in Figure 1-3a and Figure 1-3b [12], respectively. The solid electrolyte with high stability can better match the use of high-capacity lithium metal anode, so the solid-state batteries mentioned later in this thesis are all using lithium metal as the negative electrode.

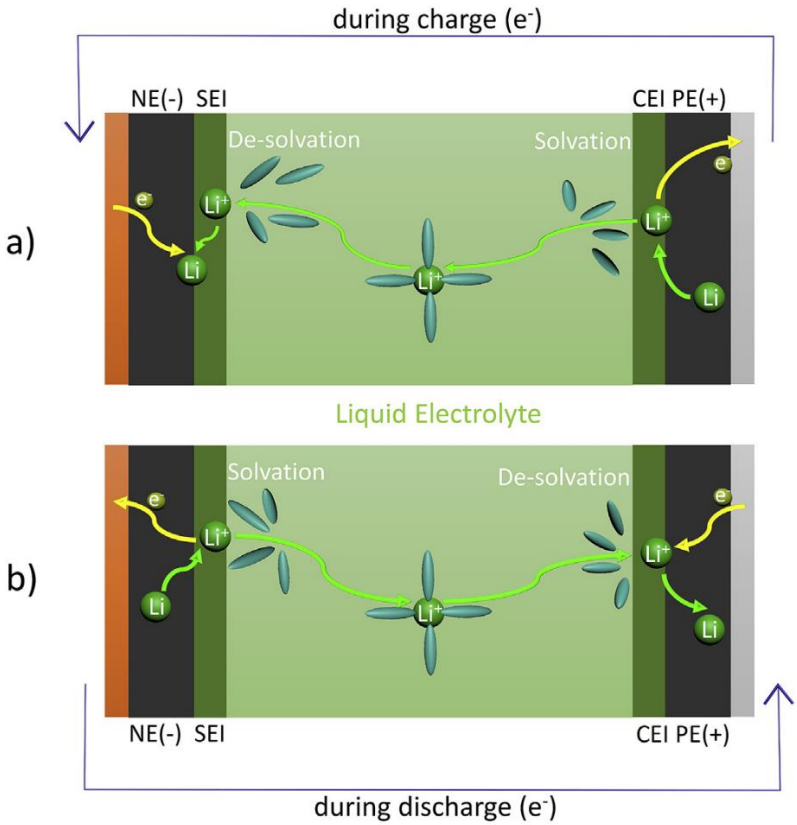

Figure 1-2 Schematic diagram of conventional lithium-ion batteries.[11]

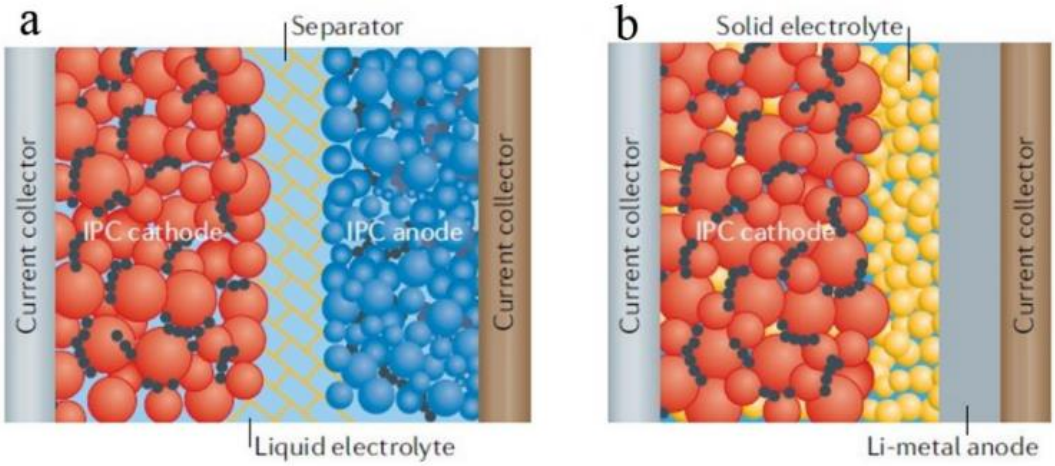

Figure 1-3 Structure of (a) a Li-ion battery cell and (b) a solid-state lithium metal battery cell.[12]

Solid-state batteries have the following technical advantages over conventional lithium-ion batteries

Higher degree of safety. Conventional lithium-ion batteries use organic liquid electrolytes, which generally use flammable and volatile carbonates solvents (i.e., propylene carbonate PC, ethylene carbonate EC, methyl ethyl carbonate EMC, and dimethyl carbonate DMC) to dissolve the salt. The addition of these highly flammable chemicals in the conventional Li-battery will become disaster if thermal runway occurs, which leads to violent combustion. Replacing liquid electrolytes by solid electrolytes offers bigger safe advantage that could greatly cushion flammability and volatility of the battery [13].

Higher potential energy density. In conventional lithium-ion batteries, the practical application of lithium metal electrode with lower potential and higher capacity is hindered by the high reactivity of the electrolyte. Thanks to the higher stability and mechanical strength of solid electrolyte, it is expected to realize the application of metal negative electrode in solid-state battery. Taking lithium-ion batteries as an example, keeping other components unchanged, replacing the separator and electrolyte with solid electrolyte together with replacing graphite with lithium metal negative electrode, the volumetric energy density of solid-state lithium batteries can be increased by 70%, and the mass density can be improved by 40% [14].

A wider range of electrode material options. Owing to the wider electrochemical window of

solid electrolytes and the use of lithium metal electrode, solid-state batteries are expected to be paired with a range of high-voltage oxide positive electrode as well as lithium-free, high-capacity transition metal sulfides to further increase energy density [15-17].

More simplified battery structure design. Solid-state batteries do not use organic electrolyte and separator, which can simplify the packaging procedures and reduce the percentage of inactive materials deployed. It also allows for internal series connection of cells to obtain higher output voltage as a single cell [13].

Wider operating temperature range. Conventional liquid batteries typically operate at temperatures above 60 ℃, causing severe decomposition of the electrolyte. If the temperature continues to increase, reaching 100 ℃ or higher, the PE/PP separator within the closed cell will also decompose, which substantially limits the high-temperature performance of the battery. In contrast, solid-state batteries are capable of operating at temperatures up to 300 ℃ or higher, making them suitable for use in extreme environments [18].

However, it should be noted that the solid electrolyte, as the key material for solid-state batteries, still faces challenges such as improvement of ionic conductivity of the electrolyte itself, and the prominent issues on the solid electrolyte/electrode interface.

1.3 Solid-State Electrolytes

As can be seen from the status of research on solid-state lithium batteries, the nature of the solid electrolyte directly determines the basic properties of solid-state lithium battery's safety, energy density, cycling stability, operating conditions, cost, and the core of all-solid-state lithium battery. The practicalization of all-solid-state lithium batteries could be achieved with the development of solid electrolyte materials with excellent comprehensive performance.

1.3.1 Development of Solid-State Electrolytes

The development history of solid electrolytes, also known as super-ionic conductors or fast ionic conductors, is summarized in Table 1-1. It can be traced back to as early as 1833, when Faraday firstly discovered the phenomenon of ion transport in Ag_2S system [19]. Later in the 20th century, with the successive discovery of lithium ion conductor Li_3N [20] and sodium ion conductor β-Al_2O_3 (Na_2O-11Al_2O_3) [21], scholars attempted to use solid electrolytes for the development of secondary batteries. In 1973, Fenton et al [22] reported the conduction phenomenon of alkali metal ions in poly(ethylene oxide) (PEO), since then, the study of solid electrolytes is no longer limited to inorganic materials. As solid electrolytes such as sodium fast ion conductor (NASICON) electrolytes [23, 24], lithium fast ion conductor (LISICON) electrolytes [25], sulfide electrolytes [26], NASICON-type lithium ion electrolytes [27], perovskite electrolytes [28], thiolithium fast ion conductor (thio-LISICON)-type electrolytes [29], and garnet-type electrolytes [30] have been reported, the preparation of solid electrolytes to obtain high ionic conductivity has become an optimal goal for researchers. Until 2011, Kanno

et al. [31] discovered a sulfide electrolyte $Li_{10}GeP_2S_{12}$ with ionic conductivity up to 12 mS cm^{-1}, which even surpassed the conventional liquid electrolyte and brought research of solid electrolytes to whole new level. While pursue higher ionic conductivity continuingly [32], researchers have gradually started to focus on the solid electrolytes in solid-state battery applications, and this triggers the efforts of giving full play to the application value of solid electrolytes.

Table 1-1 Brief development history of solid-state electrolytes.

Year of Report	Compositions	Features	Ref.
1833	Ag_2S	Ion transport in solids	[19]
1935	Li_3N	Lithium-ion conductor	[20]
1967	β-Al_2O_3	Sodium-ion conductor	[21]
1973	PEO-Alkali metal salts	Ion transport in polymer	[22]
1976	$Na_{1+x}Zr_2Si_xP_{3-x}O_{12}$	NASICON	[23, 24]
1978	$Li_{14}Zn(GeO_4)_4$	LISICON	[25]
1984	Li_3PS_4	Sulfides	[26]
1989	$Li_{1.3}Al_{0.3}Ti_{1.7}(PO_4)_3$	NASICON-type lithium-ion conductor	[27]
1993	$Li_{0.34}La_{0.51}TiO_{2.94}$	Perovskite	[28]
2001	$Li_{3.25}P_{0.75}Ge_{0.25}S_4$	*thio*-LISICON	[29]
2003	$Li_5La_3M_2O_{12}$	Garnet	[30]
2011	$Li_{10}GeP_2S_{12}$	Ultrahigh ion conductivity	[31]
2016	$Li_{9.54}Si_{1.74}P_{1.44}S_{11.7}Cl_{0.3}$	Highest lithiu-ion conductivity at room temperature	[32]

After a long period of research and practice on all-solid-state lithium batteries, it is worthwhile to summarize the main performance indicators of solid electrolytes as follows.

First, the ionic conductivity of the solid electrolyte directly determines the internal resistance of the solid-state lithium battery, which affects the cycling performance and capacity retention

of the battery. It is the most important performance index of solid electrolyte. To optimize the charge and discharge performance of solid-state lithium batteries, the ionic conductivity of solid electrolyte should reach 10^{-4} S cm^{-1} or even 10^{-3} S cm^{-1} or higher at room temperature.

Second, the solid electrolyte needs to contain high chemical stability to ensure stable utilization of the lithium metal anode and to avoid the occurrence of side reactions in the cycle of all-solid-state lithium batteries. Let alone the higher chemical stability also guarantees the safety of all-solid-state lithium batteries.

Moreover, solid state electrolytes require a wide electrochemical window for use with high voltage positive electrode materials, thereby increasing the energy density of all-solid-state lithium batteries. Further, the solid electrolyte needs to have a high ion migration number, that is, a low electronic conductance, to prevent self-discharge and internal short circuit, and improve the system stability of the battery. Finally, solid electrolytes need to have high mechanical strength to inhibit the growth of lithium dendrites while ensuring the structural integrity of all-solid-state lithium batteries.

Understanding the ion transport mechanism of solid electrolytes is essential for designing solid electrolytes with high ionic conductivity. The ion transport behavior of solid electrolytes is generally based on the classical diffusion phenomena, where a single ion leaps directly from one lattice position to an adjacent position, as shown in Figure 1-4a, and can be divided into

vacancy conduction, interstitial conduction, and knock-off conduction, respectively. Among them, the ionic conductivity (σ) is closely related to the crystal structure of the solid electrolyte, the carrier concentration (n), the activation energy (E_a), and the carrier migration rate (μ), respectively. The interrelationship is shown in Equation (1-1) [33].

$$\sigma = nq\mu \qquad (1-1)$$

where q is the charge carried by the carrier (C), μ is proportional to $\exp(E_a/kBT)$, kB is the Boltzmann constant (m^2 kg s^{-2} K^{-1}), and T is the ambient temperature (K). Lower activation energies and higher carrier concentrations (migratable ions or the presence of vacancies) are favorable to obtain high ionic conductivity. However, according to the classical single ion diffusion model, solid electrolytes with the same crystal structure should have similar migration potential barriers, which cannot explain some doped obtained solid electrolytes that exhibit significantly lower activation energies and substantially higher ionic conductivity after doping (e.g. doped LLZO and NASICON) [34]. Therefore, apart from the classical single ion leap model, another transport mechanism model has been proposed.

Shi et al. [35] used density functional theory (DFT) calculations to show that Li^+ in Li_2CO_3 tends to undergo multi-ion concerted transport rather than direct leap through a single ion. And in β-Li_3PS_4 electrolytes, they also found that Li^+ synergistic transport along the [010] crystal plane has the lowest migration potential barrier [36]. Subsequently, Mo et al. [34] investigated the ion transport behavior of a series of solid electrolytes (including $Li_7P_3S_{11}$, β-Li_3PS_4, LISICON, and LLTO) *via* computational chemistry. As shown in Figure 1-4b, there is a

synergistic transport process when ions occupying high energy sites migrate to low energy sites, and strong Coulomb interactions between ions can facilitate the migration of ions from low energy sites to high energy sites, thus greatly reducing the migration potential barrier. Zhang et al. [37] also demonstrated this synergistic transport mechanism in NASICON structured sodium ion solid electrolytes. The synergistic transport mechanism suggests that if as many mobile ions as possible are introduced to the high energy sites inside the solid electrolyte, higher ionic conductivity can be obtained by greatly reducing the ion migration potential barrier.

The ion transport mechanism in polymeric solid electrolytes is different. It generally relies on the motion of polymer chain segments in the amorphous region, which requires polymer chain segments to contain some polar groups such as -O-, =O, -S-, -N-, -P-, C=O, C≡N, etc. Their generally high dielectric constants can facilitate the dissociation of inorganic salts in the polymer matrix, which leads to effective free mobile ions [38]. As shown in Figure 1-4c, the coordination of freely moving alkali metal ions or ion clusters with polar groups generates new coordination sites through the local chain segment motion of the polymer, which leads to ion conduction within and between chains [39]. This transport mechanism suggests that polymeric solid electrolytes can only operate above the glass transition temperature T_g to achieve chain segment motion in the amorphous region, therefore, to obtain polymeric solid electrolytes with higher ionic conductivity, the glass transition temperature and crystallinity of polymeric solid electrolytes are preferably reduced.

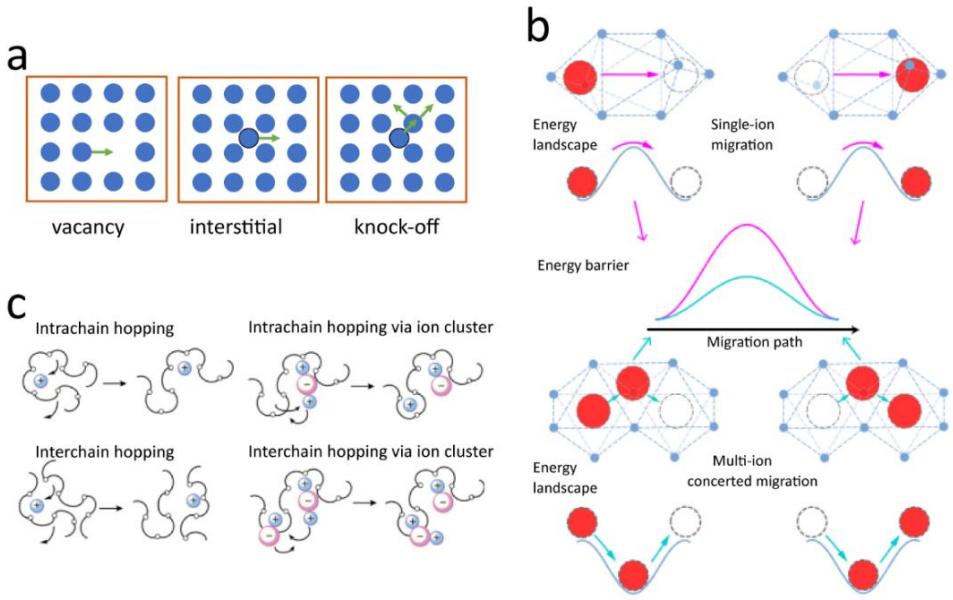

Figure 1-4 Schematic illustration of (a) Single-ion direct hop mechanism, (b) Multi-ion concerted migration mechanism, (c) segment motion mechanism.[39]

1.3.2 Classification of Solid-State Electrolytes

Depending on the material composition and ion transport mechanism, solid electrolytes can be divided into two categories: polymeric solid electrolytes and inorganic solid electrolytes. According to the chemical composition, the main categories of inorganic solid electrolytes include oxide solid electrolytes, sulfide solid electrolytes, etc.

1.3.2.1 Polymer solid electrolytes

Polymer electrolytes are usually low modulus of elasticity and are therefore well suited for flexible batteries. The good safety performance, low mass density, and high shear modulus make it an important candidate in its application in lithium metal batteries. However, its low

room temperature ionic conductivity, low lithium-ion mobility number, poor oxidation resistance, and poor thermal stability need to be further investigated. The polymer solid electrolyte is composed of a polymer matrix with polar groups and an alkali metal salt complexed, which has good flexibility and film-forming processability. In 1973, Fenton et al. [22] firstly discovered that the complexation of polyethylene oxide (PEO) with alkali metal sodium salts could form a solid electrolyte with ionic conductivity. Then in 1978, Armand et al. [40] formally proposed that PEO solid electrolytes with ion-conducting properties are expected to be used in solid-state batteries, which opened the prelude to the research of polymer solid electrolytes. PEO solid electrolytes (Figure 1-5) have received extensive attention as the most representative polymer solid electrolyte system. However, PEO is a semi-crystalline polymer at room temperature, so its ionic conductivity at room temperature can only reach 10^{-8}~10^{-6} S cm^{-1}, which is far below the required value during practical applications. When it exceeds the crystalline melting temperature (~60 °C), the amorphous region increases greatly, and the conductivity can reach 10^{-4} S cm^{-1}. Therefore, PEO-based polymer electrolytes tend to work only at temperatures above 60 °C [41, 42]. In addition to PEO-based polymer electrolytes, various types of polymer solid electrolytes are also being developed in great numbers, such as polyacrylonitrile (PAN) [43], polycarbonate (PC) [44], poly(vinylidene fluoride-co-hexafluoropropylene) (PVDF-HFP) [45], polymethyl methacrylate (PMMA) [46], etc. At the same time, people have also begun to try to compound the polymer matrix with liquid components containing alkali metal salts to develop gel polymer solid electrolytes [47]. This type of polymer solid electrolytes often has superior ion transport property.

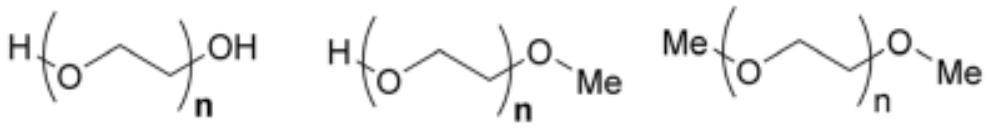

Figure 1-5 Different types of linear PEO.

Polymer solid electrolytes have been developed and researched and have made significant breakthroughs in performance recently. The prototypes of electric cars and buses boarded with solid-state batteries based on PEO polymer electrolytes were successful launched by Bolloré (France) in 2011 [48]. However, the intrinsic poor conductivity at low temperature of those on-board batteries renders the system to be functional over 80 °C. In addition, the poor mechanical strength of the polymer solid electrolyte and the high voltage instability pose great challenges for high safety standard and high energy density of solid-state batteries. In general, the advantages of polymer electrolytes such as good interfacial compatibility, good flexibility, easy processing, and low cost, tandem with its disadvantages i.e., low lithium-ion conductivity at room temperature, easy hydrolysis of lithium salts in presence of water, and narrow electrochemical window.

1.3.2.2 Inorganic solid electrolytes

Albeit the employment of polymer electrolytes reduces the chance of ignition, it does not guarantee zero chance for combustion. In contrast, the inorganic solid electrolyte is a single ionic conductor that mitigates the concentration polarization effect. The noncombustible

property due to mainly contain oxide and sulfide compounds in system effectively avoid safety issues such as spontaneous ignition [49]. Figure 1-6 illustrates the ionic conductivity of some common Li-ion inorganic solid electrolytes based on metal oxides, nitrides, sulfides, phosphates, and halides, respectively.

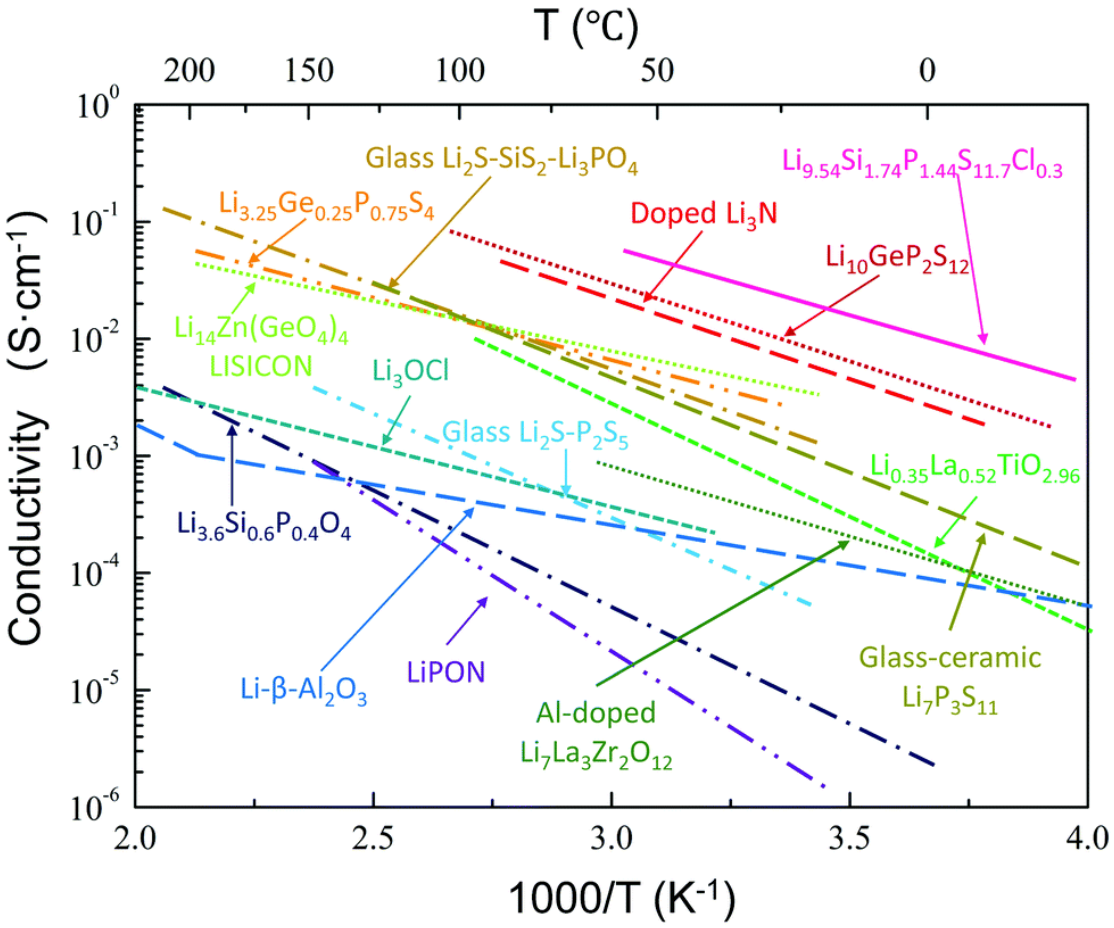

Figure 1-6 Ion conductivity of several well-known inorganic solid-state electrolyte.[50]

Oxide solid electrolytes. Oxide solid electrolytes usually synthesize precursor powder by primary calcination of raw materials, and then the precursor powder is synthesized by high temperature sintering to obtain a stiff and brittle electrolyte. It has better air stability, as the

synthesis process is generally carried out in presence of air, which is conducive to simplifying the material preparation process, battery manufacturing process, reducing the difficulty of encapsulation, and improving battery safety [51]. In addition, the high thermal stability of these electrolytes allows the battery to maintain safe operation and performance stability over a range of temperatures, reducing the need for accessory modules such as thermal management and power electronics in the battery module, thereby significantly reducing the quality, cost, and complexity of the battery pack. The crystal configuration of oxide solid electrolytes consists of a primary and a secondary atomic structure [52]. The primary atomic structure consists of a three-dimensional network of oxidized polyhedra. The secondary atomic structure is located within the pores of the three-dimensional network and consists of a permeable grid of occupied/ unoccupied sites. To move from one site to another, the cation needs to leap over the "bottleneck" of the oxidation polyhedra with an activation energy varying from 0.2 to 0.5 eV. Three of the most common oxide solid electrolytes are briefly described below, including perovskite, NASICON-type, and garnet-type electrolytes, respectively.

The general chemical formula of a perovskite solid electrolyte is ABO_3 (A = Ca, Sr, La; B = Al, Ti, etc.,), which belongs to the cubic unit cell and the Pm/3m space group. A-type atoms are generally at the apex angle of the cubic unit cell, B-type atoms are in the center, and the remaining oxygen atoms are in the face-centered position. In this way, the type A atoms are at the 12-coordination center, and the type B atoms are at the 6-coordination center. Lithium ions are introduced by hetero-valent doping. The introduction of lithium ions not only increases the

lithium content of the compound, but also increases the vacancy concentration. Such doping leads to the ordering of lithium ions and vacancies at c-axis, which greatly increases the lithium-ion conductivity in this direction. At room temperature, lithium ions can jump through the octahedral bottleneck formed by oxygen atoms in the AB plane and transition through adjacent vacancies. The octahedral bottleneck can be widened by using large-diameter rare earth elements and alkaline earth elements, thereby further improving lithium-ion conductivity. At present, among the discovered perovskite solid electrolytes, the highest lithium ion conductivity is $Li_{0.34}La_{0.56}TiO_3$, whose body ion conductivity is about 10^{-3} S cm^{-1} with overall lithium ion conductivity of 7 x 10^{-5} S cm^{-1} [53]. The most significant problem with perovskite solid electrolytes is that tetravalent titanium reacts with lithium resulting in reduction. In addition, the long-term storage stability of perovskite solid electrolytes also needs to be improved. Zhao et al. [54-57] reported a novel Li-rich anti-perovskite with a general formula of Li_3OX (X = Cl, Br). In this structure, lithium ions occupy the top corner of the octahedron and connect with the oxygen ions (B-site) at the center of the octahedron, while the halogen element (A-site) is in the center of the dodecahedron. The benefits of anti-perovskite solid electrolytes are lithium-rich elements and light weight. More noticeably, the lithium-ion conductivity at room temperature of Li_3OCl and $Li_3OCl_{0.5}Br_{0.5}$ are as high as 0.85 x 10^{-3} S cm^{-1} and 1.94 x 10^{-3} S cm^{-1}, respectively. Further research found that Li_2OHX with an inverse perovskite structure can also be used as a solid electrolyte, and it is also stable with lithium metal. Substituting fluoride anions for hydroxide ions results in compounds with the chemical formula $Li_2(OH)_{0.9}F_{0.1}Cl$. The electrochemical window of this solid electrolyte is as high as 9 V. However, the first-

principles calculations indicate that Li_3OX may decompose, so the stability of anti-perovskite solid electrolytes and the improvement of ionic conductivity require further study.

NASICON-type solid electrolyte was first proposed in 1976 by Goodenough and Hong et al. It is based on $NaZr_2(PO_4)_3$ solid solution with partial replacement of P^{5+} by Si^{4+} to form a three-dimensional (3D) sodium fast ionic conductor with the general formula $Na_{1+x}Zr_2Si_xP_{3-x}O_{12}$ ($0 \leq x \leq 3$), where $Na_3Zr_2Si_2PO_{12}$ exhibits a high ionic conductivity of 6.7×10^{-4} S cm^{-1} at room temperature and 0.2 S cm^{-1} at 300 °C when x = 2 [23, 24]. The NASICON solid electrolyte has a covalent skeleton structure consisting of interconnected polyhedra, where the ZrO_6 octahedra and PO_4/SiO_4 tetrahedra are connected at common vertices to form a 3D skeleton. Na^+ ions and vacancies are located at the skeleton gap sites and conduct along the three-dimensional channels formed by these gaps. As shown in Figure 1-7, NASICON electrolytes exist in both hexagonal phase (space group R-3c) and monoclinic phase (space group C2/c) structures [58]. It is commonly believed that $Na_{1+x}Zr_2Si_xP_{3-x}O_{12}$ exhibits a monoclinic phase when $1.8 \leq x \leq 2.2$, and the remaining components exhibit a hexagonal phase structure [23, 59, 60]. Also, the change in temperature causes a transition in the phase structure, and when the temperature is heated to 420-450 K, the monoclinic phase transforms into the hexagonal phase [61, 62].

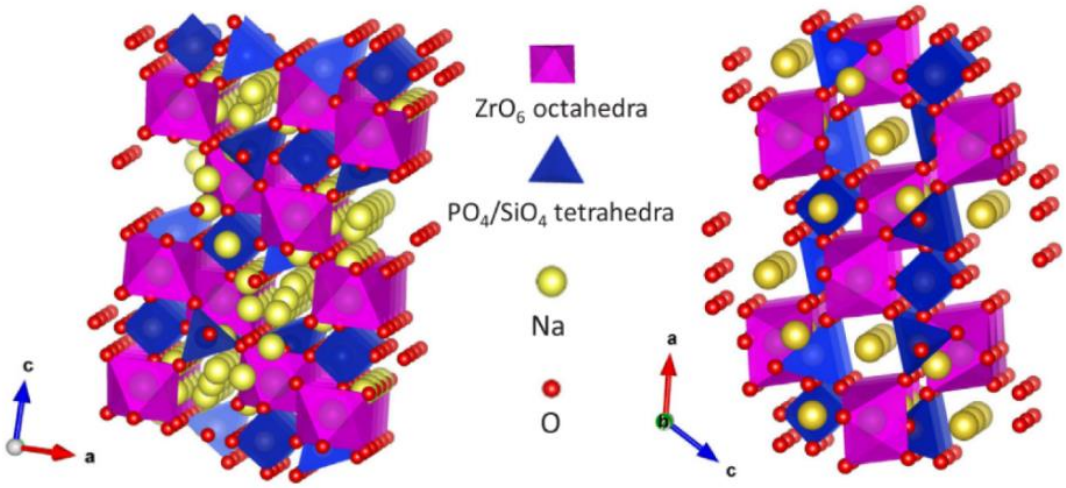

Figure 1-7 Crystal structure of NASICON-type electrolyte.[58]

Zhang et al. [37] investigated the Na^+ distribution in hexagonal and monoclinic phases based on molecular dynamics simulations and the maximum entropy method. As shown in Figure 1-8, Na1 (6b), Na2 (18e) and Na3 (36f) sites exist in the hexagonal phase, where Na^+ ions mainly occupy two sites, Na1 (6b) and Na2 (18e), and less occupies the Na3 (36f) site. Based on the hexagonal phase, a slight distortion deformation is performed to obtain the monoclinic phase structure, at which time the Na2 (18e) site splits into Na2 (4e) site and Na3 (8f) site, and Na3 (36f) splits into Na4 (8f) and Na5 (8f) site, respectively. Due to the presence of the high-energy site Na5, its migration to the low-energy Na site can offset part of the potential barrier of the migration from the low-energy Na site to the high-energy Na site based on the synergistic transport mechanism, thus reducing the ion transport activation energy. Therefore, the monoclinic phase tends to have higher ionic conductivity, and most of the current studies have been carried out based on the monoclinic phase of $Na_3Zr_2Si_2PO_{12}$ electrolyte. Because of the

appealing features of NASICON electrolytes, such as being insusceptible to the reaction of CO_2 and H_2O in presence of air, higher air stability, wide electrochemical window, higher sodium ion mobility number, and excellent stability to sodium, it makes them a very promising solid electrolyte material [63].

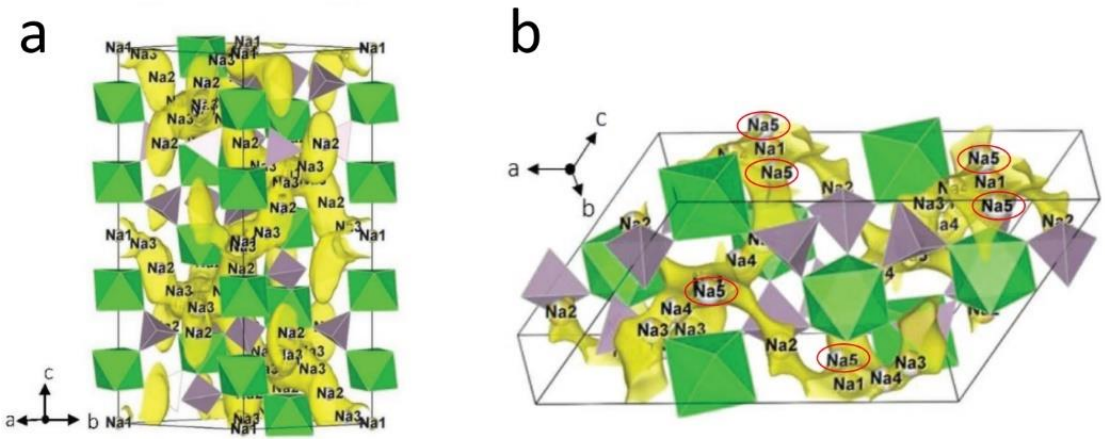

Figure 1-8 Na-ion probability density iso-surfaces (yellow) of (a) rhombohedra NASICON and (b) monoclinic NASICON from ab initio molecular dynamics (AIMD) simulations and maximum entropy method (MEM). Green region, light purple region and red circle represent ZrO_6 octahedra, $Si(P)O_4$ tetrahedra and high energy site (Na5 site), respectively.[37]

Na^+ in $Na_3Zr_2Si_2PO_{12}$ can be replaced by Li^+ ions to obtain NASICON type lithium-ion solid electrolyte. However, since the Li^+ radius (0.68 Å) is smaller than that of Na^+ radius (0.97 Å), the direct introduction of Li^+ into the high coordination position of Na^+ will easily lead to the collapse of the framework structure, which is not conducive to Li transport. Therefore, the ionic conductivity of $Li_3Zr_2Si_2PO_{12}$ obtained directly by solid-phase ion exchange using high-

temperature molten salt is three orders of magnitude lower than that of $Na_3Zr_2Si_2PO_{12}$. In this case, suitable ions can be used to replace the skeletal ions to construct a proper Li coordination environment and stabilize the framework structure of the precursor to improve the ionic conductivity [49]. In 1989, Aono et al. [27] prepared a NASICON-type lithium-ion solid electrolyte $Li_{1.3}Al_{0.3}Ti_{1.7}(PO_4)_3$ (also known as LATP) with a high ionic conductivity of 7×10^{-4} S cm^{-1} at room temperature and 0.09 S cm^{-1} at 300 °C by replacing Zr^{4+} with Ti^{4+} and doping it with an appropriate amount of Al^{3+}. Subsequently in 1992, Aono et al. [64] used Ge^{4+} instead of Zr^{4+}, also doped with an appropriate amount of Al^{3+}, to obtain a NASICON-type lithium-ion solid electrolyte $Li_{1.5}Al_{0.5}Ge_{1.5}(PO_4)_3$ (also known as LAGP) with a room temperature ionic conductivity of 2.4×10^{-4} S cm^{-1}. NASICON-type lithium-ion solid electrolytes therefore include two main types, LATP and LAGP. However, the tendency for Ti^{4+} and Ge^{4+} to be reduced at low potentials has led to NASICON-type lithium-ion solid electrolytes being unstable to lithium metal, thus limits the application of these electrolytes. It has been reported that the use of solid electrolytes containing tetravalent germanium (Ge) is more stable, but there are still reports that tetravalent Ge will also react with lithium and be reduced to elemental and bivalent Ge.

Since Thangadurai et al. [30] firstly reported the garnet-type solid electrolyte $Li_5La_3M_2O_{12}$ (M = Ta, Nb), it has received much attention due to its chemical stability for lithium metal electrode and its wide electrochemical window. In 2007, Murugan et al. [65] replaced M with Zr and increased the Li concentration to achieve a garnet-type electrolyte $Li_7La_3Zr_2O_{12}$ (also known as

LLZO) with a higher ionic conductivity of 3×10^{-4} S cm^{-1} at room temperature. As shown in Figure 1-9, LLZO electrolytes can be divided into two structures: the tetragonal phase (space group $I4_1/acd$) and the cubic phase (space group Ia-3d). Lithium exists in three different sites in the tetrahedral phase, with Li1 occupying position 8a in the tetrahedral gap, Li2 occupying position 16f in the ortho-octahedral gap and Li3 occupying position 32g in the partial-octahedral gap, showing an ordered distribution of lithium ions [66]. In contrast, there are two different sites for lithium in the cubic phase, with Li1 occupying the 24d position in the tetrahedral gap and Li2 occupying the 96h position in the eccentric octahedral gap, where the lithium ions show a disordered distribution, making ion migration easier and thus exhibiting higher ionic conductivity [67]. Stabilization of the cubic phase at room temperature is therefore the key to the synthesis of LLZO-based electrolytes with high ionic conductivity. It is worth noting that garnet-type electrolytes tend to react with CO_2 and H_2O in the air and a layer of Li_2CO_3 impurities is generated on the surface, leading to a decrease in their affinity for the electrode [68].

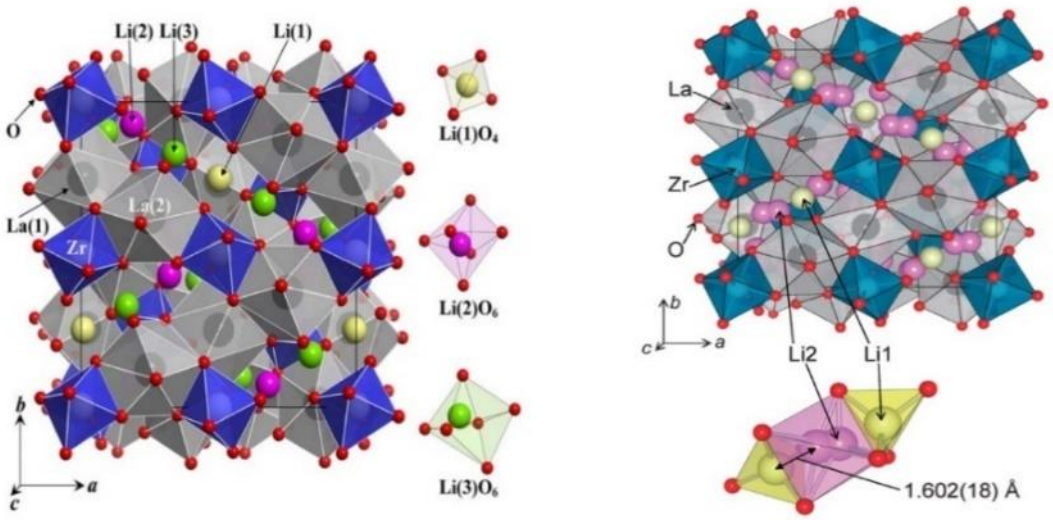

Figure 1-9 Crystallite structure of LLZO.[66, 67]

Sulfide solid electrolytes. Sulfide solid electrolytes are derived from oxide solid electrolytes by replacing the oxygen ions in the oxide with sulfur ions of larger ionic radius, which can form a wider ion conducting pathway. In addition, the strong polarization of sulfur ions and the weaker binding ability of lithium ions give lithium ions a higher mobility, so sulfide solid electrolytes tend to exhibit higher ionic conductivity compared to oxide solid electrolytes [32, 33]. Meanwhile, sulfide solid electrolytes have better mechanical ductility than oxide electrolytes. Dense interfaces can be easily achieved by cold pressing [69, 70], and thus are receiving increasing attention today. Sulfide solid electrolytes can be divided into two main types, binary sulfide and ternary sulfide, according to the type of synthetic raw materials [15]. Binary sulfides are mainly synthesized by M_2S (M = Li, Na) and P_2S_5 as raw materials, and ternary sulfides are mainly synthesized by M_2S (M = Li, Na), P_2S_5 and MS_2 (M = Si, Ge, Sn) or MX (M = Li, Na; X = Cl, Br, I). Since sulfide electrolytes tend to contain P-S bonds with

weak bonding energy, the vast majority of sulfide solid electrolytes exhibits poor air stability and reactivity with H_2O to form H_2S gas [71]. The sulfide raw materials used are also less stable to humid air, so the sulfide solid electrolytes are generally synthesized and stored under dry atmosphere. Nowadays, in order to improve the air stability of sulfide solid electrolytes, P is partially or even completely replaced by other elements, and the air stability of the electrolytes obtained is greatly enhanced, such as $Li_{3.06}P_{0.98}Zn_{0.02}S_{3.98}O_{0.02}$ [72] and Na_3SbS_4 [73].

In 2011, Kanno et al. [31] synthesized the ternary sulfide solid electrolyte $Li_{10}GeP_2S_{12}$ using Li_2S, GeS_2, and P_2S_5 under argon atmosphere, and its crystal structure is shown in Figure 1-10. The $(Ge_{0.5}P_{0.5})S_4/PS_4$ tetrahedra, LiS_4 tetrahedra and LiS_6 octahedra form a 3D skeleton structure, and the LiS_4 tetrahedra at positions 16h and 8f are connected co-sideways along the c-axis to form a one-dimensional zigzag lithium ion conduction path. Due to the isotropic transport of lithium ions, $Li_{10}GeP_2S_{12}$ demonstrates an ultra-high room temperature ionic conductivity of 12 mS cm^{-1}, which is the first time that the ionic conductivity of a solid electrolyte has surpassed that of a conventional liquid electrolyte, indicating a milestone. However, the introduction of Ge^{4+} leads to the instability of $Li_{10}GeP_2S_{12}$ to lithium metal electrode. The first $Li_{10}GeP_2S_{12}$-based battery assembled by Kanno et al., also used indium metal electrode with higher potential. Therefore, the improvement of the interfacial stability of $Li_{10}GeP_2S_{12}$/Li is the key to realize $Li_{10}GeP_2S_{12}$-based solid-state batteries.

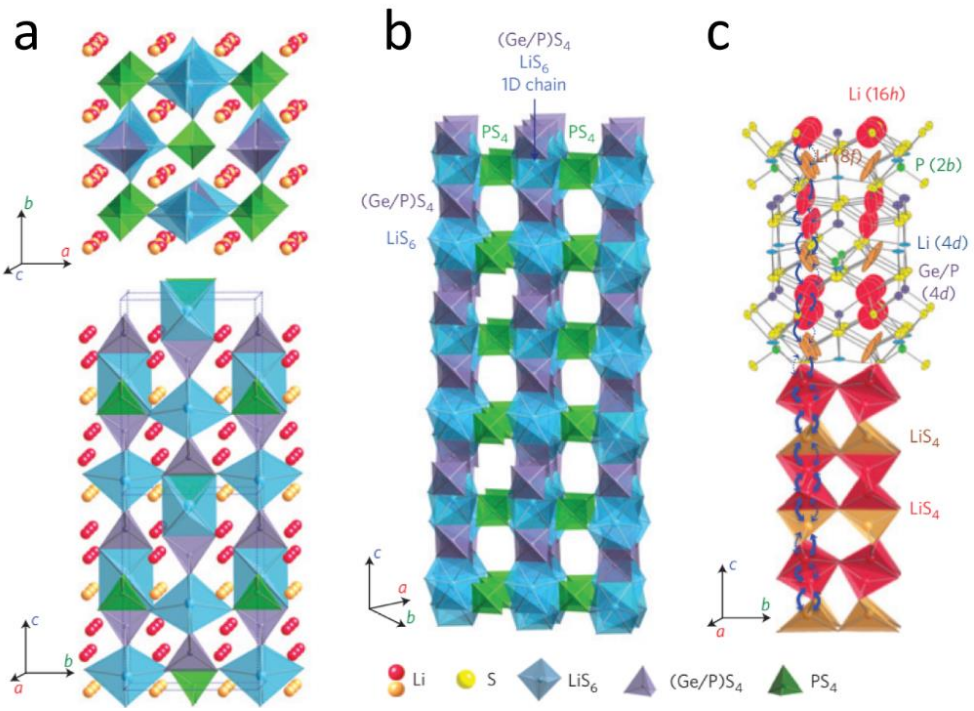

Figure 1-10 Crystal structure of typical $Li_{10}GeP_2S_{12}$.[31]

1.3.2.3 Organic-inorganic hybrid electrolytes

Inorganic solid electrolytes exhibit satisfactory ionic conductivity and mechanical properties, but their applications are impeded by large interfacial impedance and poor machinability. In contrast, polymer electrolytes have the advantage of flexible shape and low cost, but they have insufficient ionic conductivity at room temperature and poor mechanical strength. Therefore, the inorganic and polymeric electrolytes synergistically integrated to construct inorganic-organic composite electrolytes to compromise ionic conductivity, mechanical strength, and interfacial stability, is a prosperous promising technological strategy for the overall enhancement of electrolyte performance [74]. On the one hand, polymers are used to improve mechanical flexibility and processability, contributing to a good physical contact between electrolyte and electrode, thus reducing the interfacial impedance. Alternatively, inorganic

materials can act as solid plasticizers to reduce polymer crystallinity and promote lithium salt dissociation, enhancing the conductivity of the polymer. Currently, inorganic-organic composite electrolytes are mostly mechanical blends of polymers (e.g., PEO, PVDF-HFP, PPC, etc.) and inorganic ion-conducting inert/active materials (e.g., SiO_2, $Li_7La_3Zr_2O_{12}$, $Li_{10}GeP_2S_{12}$, etc.). Hybrid electrolytes can be further subdivided into 'ceramic in polymer' and 'polymer in ceramic', depending on the ratio of their contents. They differ slightly in the mechanism of lithium-ion conduction. The former ion conduction path is mainly in the polymer bulk phase, and inorganic particles are used for polymer modification, the latter ion conduction path is mainly in the inorganic solid electrolyte bulk phase and organic/inorganic interfacial percolation, and the polymer is used for electrolyte molding [75, 76].

1.4 Lithium-Air (Oxygen) Batteries

1.4.1 Development of Lithium-Air Batteries

The concept of Li-air batteries was first introduced in the 1970s by Littauer and Tsai et al., [77] using an aqueous electrolyte. These batteries are primary batteries based on a lithium negative electrode/aqueous electrolyte/oxygen positive electrode structure. Electrochemical tests have shown that the discharge product of this battery is lithium superoxide and has an open circuit voltage of 2.9-3.0 V, exhibiting a very high theoretical energy density. However, as lithium metal is very active, the reaction in the aqueous electrolyte is relatively violent and accompanied by more side reactions, resulting in irreversible consumption and continuous corrosion of lithium metal resulting in a poor reversibility of the battery. Therefore, Li-air

batteries did not receive much attention from the scientific community at that time. In 1996, Abraham et al. [5] first designed a stable secondary rechargeable Li-air battery using a gel polymer electrolyte. The structure of this cell is lithium negative electrode/gel polymer electrolyte/carbon positive electrode. In this case, the PAN-based gel polymer electrolyte replaces the liquid electrolyte and separator and can be used both as a medium to isolate the positive and negative electrodes and as a medium for lithium-ion conduction. Through further studies, they detected the presence of lithium peroxide (Li_2O_2) during discharge using *in situ* Raman techniques and concluded that this is the final reaction product of the Li-air cell. When the surface current density was 0.1 mA cm^{-2}, the specific capacity of the cell was 1400 mA h g^{-1}, but the cycle reversibility was not improved. In the following decade, despite some reports on Li-air batteries, a breakthrough in cycle stability and energy density was never achieved, and the research on Li-air batteries fell into a period of atrophy.

In 2006, Bruce and his co-workers [78] reported a Li-air cell assembled using a carbon cathode loaded with a manganese dioxide catalyst, $LiPF_6$ liquid electrolyte, glass fibers, and lithium metal (Figure 1-11). Using *in situ* mass spectrometry analysis, they found the presence of lithium peroxide inside the cell and showed that the formation and decomposition of lithium peroxide is reversible. At the same time, they confirmed that the capacity of these batteries was still retained after 50 charge/discharge cycles, breaking the bottleneck that previous Li-air batteries could not be cycled, and achieving a new breakthrough in cycling stability. Since then, the research on Li-air batteries enters into the phase of booming.

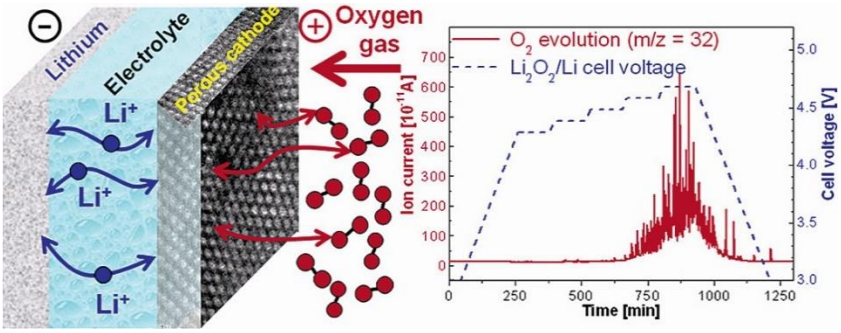

Figure 1-11 Schematic diagram of a typical Li-O_2 batteries with gas evolution profile.[78]

In recent years, research teams (Peter.G.Bruce's group and Yuhui Chen's group at the University of St. Andrews, UK; S.Gowda's team at IBM's Almaden Research Center, Nikolay Goncharenko's team at PolyPlus Batteries, and B.Kumar's team at the Energy Technologies and Materials Division of the University of Dayton Research Institute, USA. Fuminori Mitchell's team at Toyota Motor Battery Research, Osamu Yamamoto's team and Nobuyuki Imanishi's team at Mie University Department of Chemistry in Japan; Haoshen Zhou's group at Nanjing University, China; Xinbo Zhang's group at Changchun Institute of Applied Chemistry, Chinese Academy of Sciences, and Qiang Zhang's group at Tsinghua University, China.) around the world have also been working on high energy density Li-air battery development technologies. For example, With the continuous research work, researchers identified the electrolyte as one of the key factors affecting the performance of Li-air batteries. Scrosati et al., [79] reported that the electrolyte of TEGDME-$LiCF_3SO_3$ has not decayed in discharge capacity after 100 cycles at a capacity limit of 1 A h g^{-1}.Kuboki et al., [80] reported that the hydrophobic ionic liquid 1-methyl-3-octylimidazolium bis(trifluoromethylsulfonyl)imide can discharge a specific capacity

of 5360 mA h g^{-1}. Hassoun et al., [81] reported that polyethylene-based polymer electrolytes for Li-air batteries can be charged at lower voltages. The development of new electrolytes has led to a significant development of lithium-oxygen batteries, which has greatly improved the cycle life and multiplicative performance of the batteries. Simultaneously, the advantages of Li-air batteries are becoming increasingly evident as one of the most promising secondary batteries.

1.4.2 Classification of Lithium-Air Batteries and Their Research Development

According to the different electrolytes used, Li-air batteries can be divided into four main types: aprotic (non-aqueous liquid) Li-air battery, aqueous Li-air battery, hybrid Li-air battery and solid-state Li-air batteries, as shown in Figure 1-12 [82]. The reaction paths of different types of Li-air batteries are different. Since the research hotspots of Li-air batteries, or strictly speaking Li-O_2 batteries, are focused on aprotic electrolyte systems, this chapter will analyze the current development status of Li-air batteries with organic electrolytes as an introduction, further extend to aqueous electrolyte and hybrid electrolyte systems, and finally elaborate on solid-state Li-air batteries, which are the key focus of this thesis.

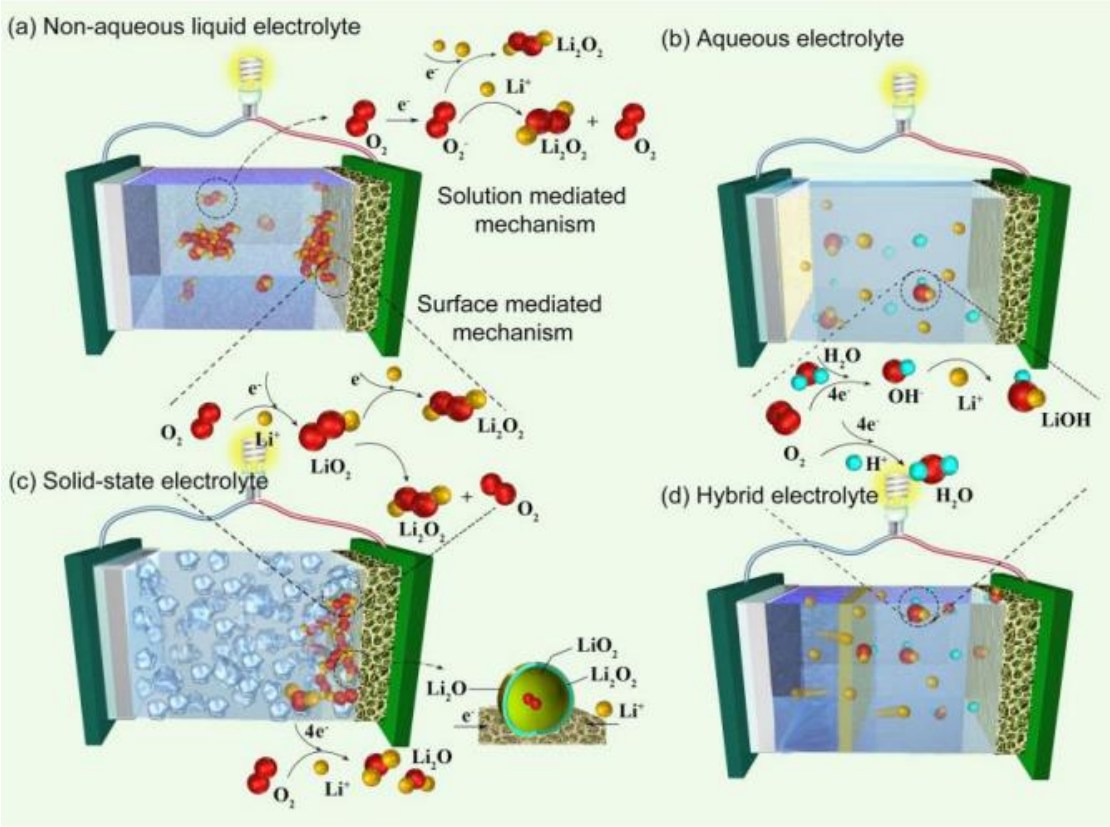

Figure 1-12 Mechanisms of Li–air battery with different types of electrolytes.[82]

1.4.2.1 Aprotic Lithium-Air Batteries

The structure of lithium-air battery is similar to that of conventional lithium-ion battery, which consists of positive electrode, negative electrode, electrolyte and separator. Among them, lithium metal is used as the negative electrode, which has a relatively high electrochemical capacity. The positive electrode usually consists of a porous carbon material, a mixture of binder and catalyst coated on the collector fluid. The separator is immersed in an organic electrolyte that is located between negative and positive electrodes. The electrolyte is usually an organic electrolyte such as carbonate, ether, dimethyl sulfoxide, etc. Throughout the reaction of the

aprotic Li-air cell (as shown in Equations 1-2 to1-8), a reversible redox reaction occurs between oxygen and lithium metal. Oxygen reduction reaction (ORR) occurs during the discharge process. In this process, the lithium in the negative electrode loses electrons and becomes lithium ions which are released into the electrolyte. O_2 enters the porous positive electrode and dissolves into the electrolyte for reduction to form dissolved oxygen, which reacts with Li^+ ions in the electrolyte to form LiO_2, and the final product is formed as Li_2O_2 after further transformation. The charging process corresponds to the oxygen evolution reaction (OER). In this process, Li_2O_2 is used as the starting material for the inverse reaction of the above reaction, resulting in the formation of Li and O_2. From the above reaction mechanism, it is clear that, on the one hand, Li-air batteries store electrical energy through chemical energy by undergoing a multi-step complex reactions *via* a gas-liquid-solid phase transition [83-85]. On the other hand, the positive electrode material does not participate in the electrochemical reaction and is only a reserve site for the formation and decomposition of lithium peroxide, which is a similar to the mechanism of fuel cells [86, 87]. Figure 1-13 shows the schematic diagram of the working principle of Li-air batteries and the electron and ion migration during charging and discharging process.

$$e^- + O_2 \rightarrow O_2^- \qquad 1\text{-}2$$

$$Li^+ + O_2^- \rightarrow LiO_2 \qquad 1\text{-}3$$

$$Li + e^- + LiO_2 \rightarrow Li_2O_2 \qquad 1\text{-}4$$

$$LiO_2 + LiO_2 \rightarrow Li_2O_2 + O_2 \qquad 1\text{-}5$$

$$Li_2O_2 \rightarrow O_2 + 2e^- + 2Li^+ \qquad 1\text{-}6$$

$$Li_2O_2 \rightarrow LiO_2 + e^- + Li^+ \qquad 1\text{-}7$$

$$2LiO_2 \rightarrow Li_2O_2 + O_2 \qquad 1\text{-}8$$

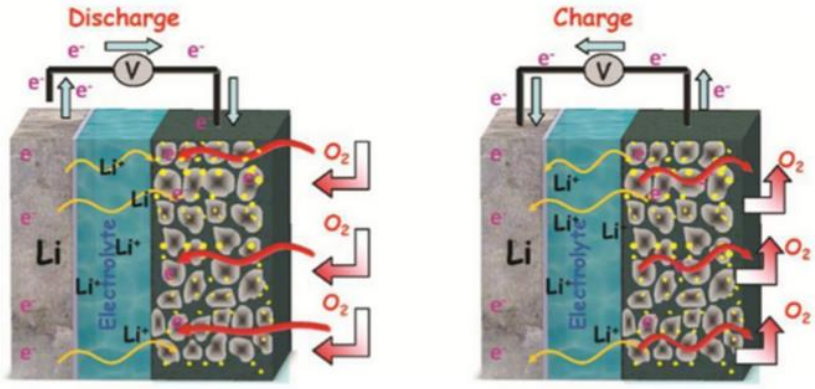

Figure 1-13 Schematic diagram of the working principle of Li-air batteries.

Organic electrolyte has better lithium salt solubility, stronger ionic conductivity, and its reaction with lithium metal forms a solid electrolyte interphase (SEI) at the electrode/electrolyte interface, which mitigates the corrosion of lithium metal to a certain extent. However, there are still some problems that cannot be ignored. For example, the electrolyte has poor chemical/electrochemical stability during cycling and is prone to side reactions, producing solid by-products that hinder oxygen transport and lithium-ion diffusion. Secondly, the electrolyte has limited oxygen-carrying capacity and has difficulty in dissolving the discharged product (lithium peroxide), which continuously accumulates on the porous air electrode, causing blockage of the positive electrode oxygen channel and reduction of the diffusivity rate, resulting in an increase in the overcharge potential and a decrease in the cycling performance of the

battery. In addition, the OER process generates very reactive lithium superoxide and oxygen radicals, which have strong oxidation ability. It will attack the liquid electrolyte to decompose and generate lithium carbonate, lithium carboxylate and other by-products, leading to rapid failure of lithium-oxygen batteries within a short cycle time [88]. Figure 1-14 illustrates the reaction principle of a typical aprotic Li-air battery during charging and discharging.

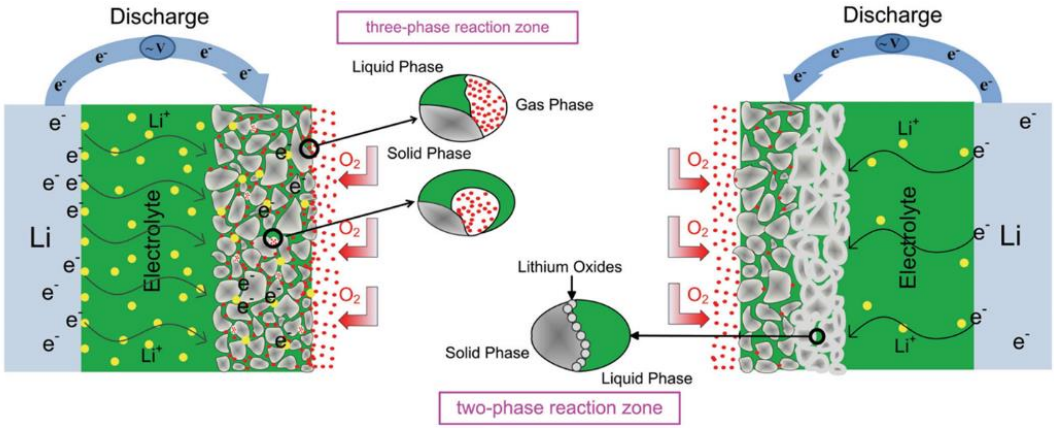

Figure 1-14 A REDOX partition model for aprotic Li-air batteries.[88]

1.4.2.2 Aqueous Lithium-Air Batteries

The structure of aqueous Li-air battery consists of three major parts: lithium metal negative electrode, separator and aqueous electrolyte, and positive electrode. As from Equations 1-9 and 1-10, during discharge, the lithium in the negative electrode loses electrons to become Li^+ ions and then migrate to the positive electrode to form lithium hydroxide. The oxygen at the positive electrode undergoes reduction to form hydroxide ions. During the charging process, lithium hydroxide occurs as the starting material in the reverse direction of the above reactions [89, 90].

$$Li \rightarrow Li^+ + e^- \qquad 1\text{-}9$$

$$O_2 + 2\ H_2O + 4\ e^- \rightarrow 4\ OH^- \qquad 1\text{-}10$$

The discharge product of aqueous Li-air battery, lithium hydroxide, is soluble in aqueous electrolyte, which enables reversible formation/decomposition throughout the battery process, circumventing the risk of blocking the porous channel of the positive electrode and providing the possibility of Li-air battery cycling. However, due to the reactive nature of the lithium metal, it is highly susceptible to react with the electrolyte. Therefore, the battery cycling process is accompanied by self-discharge of lithium metal or even serious corrosion reaction ($Li + H_2O \rightarrow LiOH + 1/2\ H_2$), resulting in low coulombic efficiency of the battery, which affects the practical application of Li-air batteries. In order to solve the above problems, an improved approach is to introduce a protective film that allows the passage of oxygen and inhibits the contact of gases such as CO_2, nitrogen (N_2), and water vapor with the lithium metal, but this approach is not ideal due to the limitations of materials and technology [77].

1.4.2.3 Hybrid Li-Air Batteries

The hybrid Li-air battery uses organic electrolyte, inorganic solid electrolyte and aqueous electrolyte combination as the electrolyte layer, as shown in Figure 1-15 [91]. The organic electrolyte layer is in contact with the lithium sheet, which can form a SEI layer to protect the lithium negative electrode. The aqueous electrolyte can be in direct contact with air. Compared to organic electrolyte lithium-air batteries, hybrid Li-air batteries have a couple advantages. First, the use of inorganic solid electrolyte separating aprotic electrolyte and aqueous electrolyte can effectively avoid the erosion of lithium negative electrode by water vapor and CO_2 in the

air, so that this type of Li-air battery can be charged and discharged directly in the atmosphere. Second, since the reaction product is lithium hydroxide (LiOH) soluble in aqueous electrolyte, the discharge product of the battery will not block the electrode, making the discharge of the battery sustainable. These advantages make the combined Li-air battery one of the promising future energy storage devices. The reaction mechanism of this type of cell is similar to that of a fuel cell. In the discharge phase, the negative electrode of lithium metal loses oxygen to lithium ions into the organic electrolyte, and the positive active material oxygen is reduced to hydroxide ions by gaining electrons in the aqueous electrolyte.

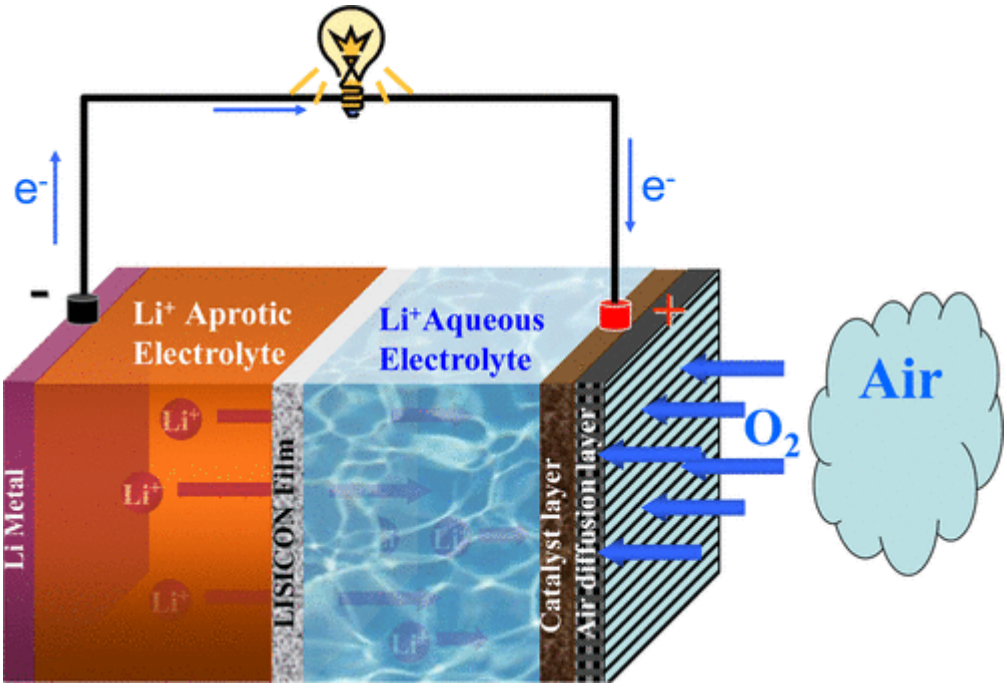

Figure 1-15 Schematic illustration of hybrid electrolyte Li-air batteries.[91]

On this basis, Zhou et al. [91-94] proposed and designed a liquid-flow Li-O_2 battery, the structure is shown in Figure 1-16. Like the hybrid electrolyte system Li-air battery, this type of

Li-O_2 battery also consists of a liquid organic electrolyte in contact with the lithium anode. The organic electrolyte is separated from the aqueous electrolyte by an inorganic electrolyte. The difference is that its aqueous cathode solution contains redox pairs and is pumped to make it flow.

In summary, this hybrid Li-air battery can effectively protect the lithium negative electrode and avoid the discharge products from blocking the air to positive electrode. The most significant problem at present is that the inorganic solid electrolyte needs to be stable in an aqueous electrolyte, otherwise the by-products generated by its decomposition will deplete the lifespan of the battery. On the other hand, the lithium-ion conductivity of inorganic solid-state electrolytes is limited, and sulfur-based electrolytes with high lithium-ion conductivity are highly adsorptive, which cannot be used in hybrid Li-air batteries. Further development of solid-state electrolytes with high ionic conductivity and high stability plays a key role in improving the performance of this type of Li-air batteries.

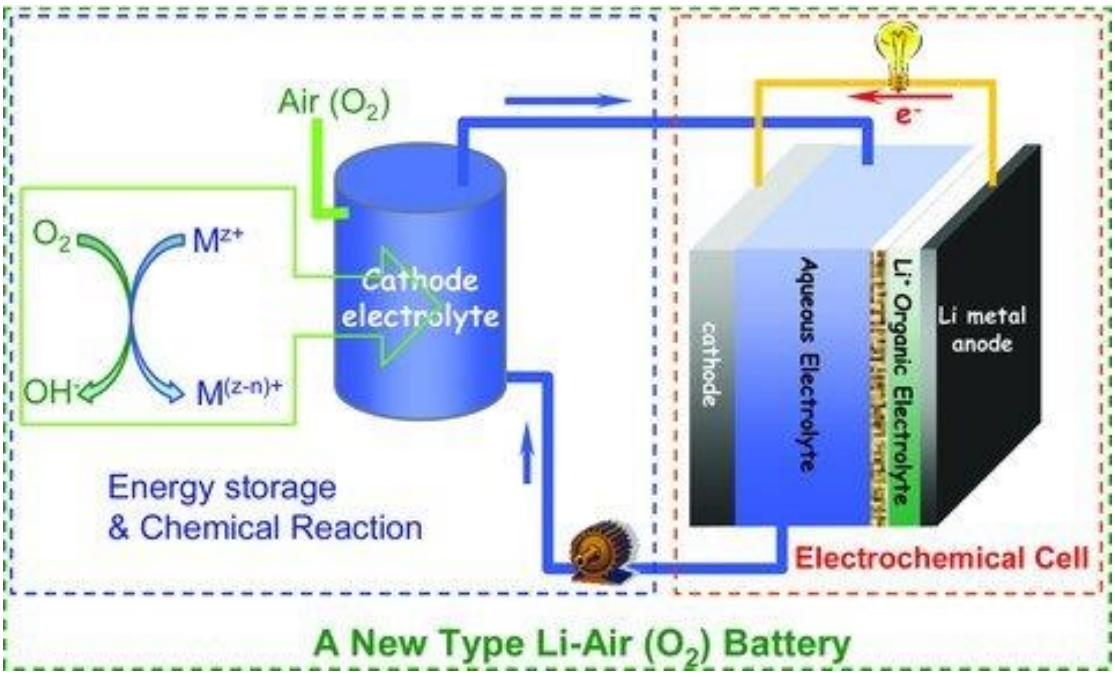

Figure 1-16 Schematic illustration of a new type Li-redox Li-air (O_2) battery.[93]

1.4.2.4 Solid-State Li-Air Batteries

Solid-state Li-air batteries can address the safety issues of leakage, volatilization, and flammability caused by aprotic Li-air battery and hybrid Li-air battery with organic liquid electrolytes. As shown in Figure 1-17, the solid-state Li-air battery is a new type of battery that replaces liquid electrolyte and separator with a safe and stable solid electrolyte, and its electrical and chemical energy is converted through cation deem bedding and charge exchange between positive and negative electrodes. Compared with organic liquid electrolyte, the solid electrolyte usually has better mechanical strength and higher stability, which can inhibit the growth of lithium dendrites, reduce the risk of oxygen shuttling to the lithium anode, and achieve higher power density and recyclability. Furthermore, solid-state Li-air batteries can operate at high

temperatures and have good thermal stability, which improves the applicability of the batteries.

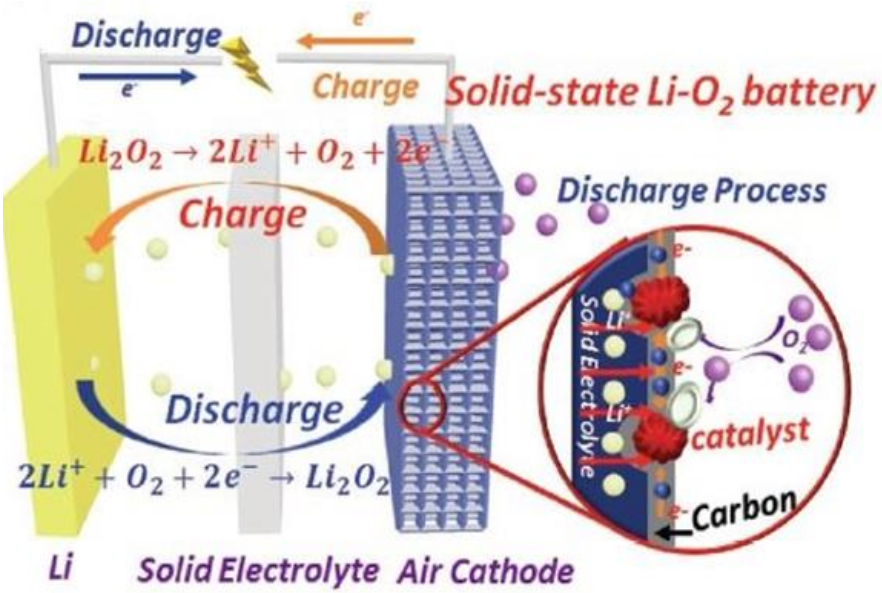

Figure 1-17 Schematic illustrations of a solid-state Li–O_2 battery.[95]

The world's research on solid-state lithium-air batteries started late. The first all-solid-state lithium-oxygen battery was prepared by Kumar et al. in 2010 [96]. As illustrated in Figure 1-18, they formed a solid-state separator with PEO/LiBETI polymer film and LAGP glass film, and prepared the positive electrode with carbon black, PTFE and LAGP powder, both of which were assembled with lithium metal sheets in a sandwich structure to form an all-solid-state Li-air battery. The battery can be discharged/charged at 0.1 and 0.0625 mA cm^{-2} at 75°C, respectively. The discharge and charge capacities are up to 4.87 mA h as well as 5.00 mA h, respectively. In addition, the battery can operate in cycles between 30-105°C with a discharge voltage of 2 V or more and maintain some reversibility. Based on this, S. Rodrigues et al., improved the air anode by using nitrogen-doped carbon powder as an anode catalyst to increase the discharge

voltage to 2.5 V [97].

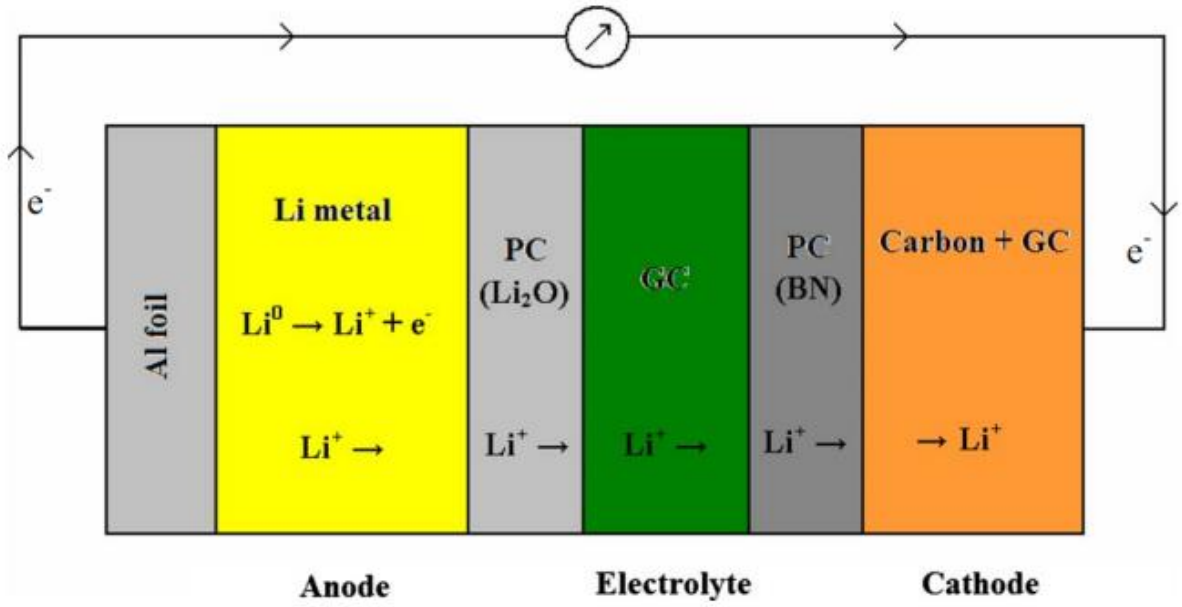

Figure 1-18 Schematic illustration of the Li-O_2 cell reported by Kumar et al.[96]

In 2021, Yu et al., [98] reported a highly stable flexible solid-state lithium-air battery in Nature (Figure 1-19), in which an ultrathin, high-ion conductivity lithium-ion exchange zeolite X (LiX) membrane (LiXZM) is used as the solid-state electrolyte. LiXZM has high ionic conductivity, low electronic conductivity, and excellent stability to air and lithium anodes. Meanwhile, carbon nanotubes (CNT) are used as the cathode in the integrated structure of the solid-state Li-air battery, which facilitates the reduction of interfacial impedance. The inherent chemical stability of zeolites effectively suppresses the degradation of cell performance caused by lithium or air action of the electrolyte. In addition, the integrated SSLAB exhibits superior performance in ambient air compared to the conventional Li-air cells containing organic electrolytes.

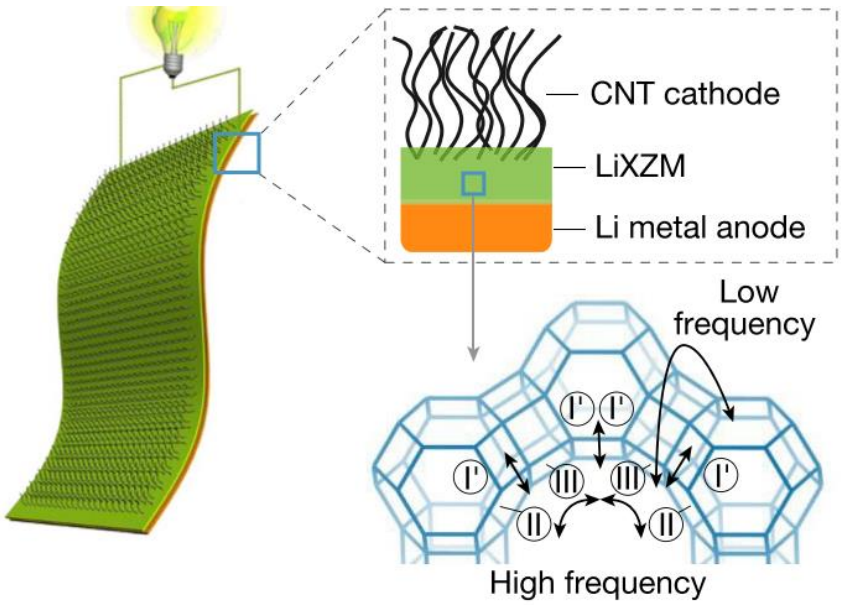

Figure 1-19 Schematic of the integrated SSLAB with C-LiXZM and the conduction mechanism of Li ions in LiX.[98]

However, further experimental results show that the solid/solid interfacial contact between the solid electrolyte and the electrode leads to a large interfacial impedance and low electrical conductivity. In addition, the internal structure of solid-state Li-air batteries are more complicated, and the mechanism is still unclear, which needs to be further investigated [99-101].

1.4.3 Positive Electrode for Lithium-Air Batteries

Based on the reaction principle of Li-air batteries, the air electrode material does not participate in the electrochemical reaction but is only a reserve site for the discharge product. The air positive electrode of a Li-air battery has four main functions. First, it can provide oxygen

diffusive channels so that oxygen can reach the electrode/electrolyte interface smoothly. Second, the air positive electrode provides the site for the discharge reaction of the battery and holds the resulting discharge product, usually lithium peroxide. Third, it can play a catalytic role in the charging/discharging process of Li-air batteries, providing the active sites of the reaction. Finally, the use of different air electrodes can influence the morphology of the reaction products.

The type and structure of the air electrode have an important impact on the specific capacity, energy density and cycling life of Li-air batteries, so its selection must consider various factors. Li-air battery positive electrode materials need to meet some basic properties as follows: 1) Good electronic conductivity and ionic conductivity. 2) With suitable porosity. It can ensure rapid oxygen diffusion. The experiments indicate that the pore size of 2-50 nm is beneficial to the performance of Li-air batteries. 3) With large specific surface area (SSA) and porosity, it can accommodate products from solid reaction. 4) The electrochemical and chemical properties are stable enough not to react with the reaction gas or electrolyte and not to participate in side reactions. 5) With a low manufacturing cost.[102-104]

Carbon materials are widely used as catalyst carriers, conductors and electrode materials in fuel cells, lithium-ion batteries and electrochemical supercapacitors because of their excellent electrical conductivity and large SSA [105]. Recently, porous carbon materials have been widely studied as air electrode materials because they have the merits of high electrical conductivity, large specific surface area, low density and suitable porosity as required above.

And they can catalyze oxygen reduction during the discharge of lithium-air batteries due to the presence of defective sites. The current research on porous electrodes is mainly made of carbon materials synthesized in the laboratory. For example, carbon materials such as CNTs, graphene, Super P, Ketjen Black, Vulcan XC-72, Denka Black CNT, hollow carbon fiber and graphene have been widely used and investigated [106-111]. Among them, the hollow carbon fibers are grown directly on the porous ceramic substrate without binder, which facilitates the observation of the morphology of the recruitment surface products. Straight-walled carbon nanotubes have a highly ordered structure, which can be easily used to observe the morphology of the discharge products and to observe the growth and decomposition processes of the discharge products *in situ*. Graphene-based materials have a particularly large SSA, a special pore structure, high electrical conductivity and certain catalytic activity, which can greatly improve the specific capacity of Li-air batteries [112]. Mizuno et al. [113] prepared stacked carbon nanotubes (CSCNT) with different surface properties for organic electrolyte lithium-air battery cathodes and observed how the discharge products were deposited on the cathode at high magnification. It is concluded that the active edge of the carbon surface was essential to control the morphology of the cathode deposits and improve the battery performance. In a nutshell, the study of the above new materials shows that the capacity, rate performance, cycling performance and discharge product morphology of Li-air batteries are closely related to the type and structure of the air electrode active materials.

Yet, a study using isotope tracing combined with differential electrochemical mass

spectrometry has shown that carbon materials are unstable at high potentials (>3.5 V vs. Li/Li^+) [114] and are subject to oxidative decomposition to CO_2. It is also shown that carbon materials rich in defects are more susceptible to nucleophilic attack by the discharge intermediate superoxide groups than carbon materials with fewer defects, which can cause corrosion of carbon-based air electrode materials [115]. Moreover, the presence of by-product CO_2 further generates the Li_2CO_3, which is difficult to decompose [114]. This will significantly reduce the discharge capacity and increase the cell polarization. During the battery cycling, with the continuous accumulation of Li_2O_2, the active sites on the air electrode surface are occupied or even completely blocked, and their storage or reaction area is greatly reduced, leading to the early failure of battery discharge and capacity decay. Therefore, stable non-carbon materials such as porous gold [116], TiC [117], TiO_2, Co_3O_4 [118] etc. were used as air electrode materials for Li-air batteries, which also exhibited good cycling stability. To solve the above problems, carbon materials are usually modified using doping and introduction of functional groups to enhance the catalytic ability of cathode materials. For example, Liu et al. [101] proposed a solid-state Li-air battery with single-walled carbon nanotubes, ruthenium oxide (RuO_2) nanoparticles and NASICON-type LAGP particles as the negative electrode. The results showed that RuO_2 has high catalytic activity during OER and ORR process, and the Li-air battery with RuO_2 as catalyst has very small charge/discharge overvoltage and long-term cycling stability.

In addition to the study of improving the corrosion resistance of carbon-based air electrode

materials, the accumulation of discharge products Li_2O_2 between the pores of air cathodes [119] is also an important and critical topic for the study of air electrodes. The discharge product Li_2O_2 is deposited on the air electrode skeleton. The poor deposition morphology of Li_2O_2 and the accumulation of Li_2O_2 caused by the low decomposition during the charging process can cause the blockage of pores in the air electrode. Moreover, due to the insulating property of Li_2O_2, the electrons involved in the redox reaction cannot be transferred smoothly, leading to the termination of the redox reaction, and eventually causing the battery failure, as shown in Figure 1-20.

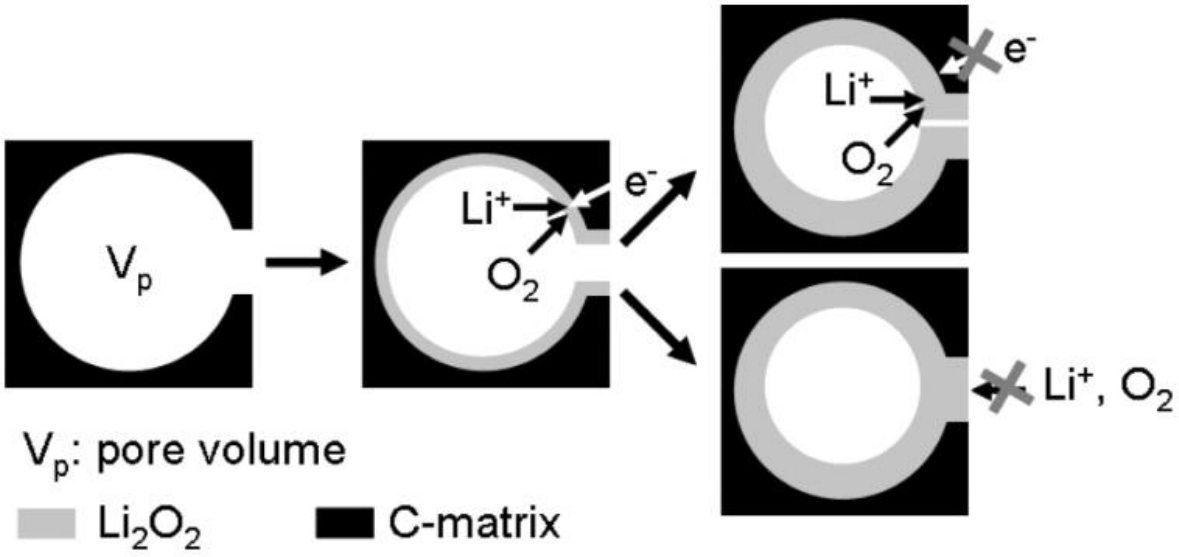

Figure 1-20 Schematic illustration of the mechanism in Li-air batteries failed caused by Li_2O_2 accumulate in air-electrode pores.[120]

From the reaction kinetics point of view, the kinetic of generation and decomposition of the discharge product Li_2O_2 on the air electrode is slow [121], and the enhancement of battery rate

performance is greatly constrained. For example, it cannot meet the demand for fast charging of electric vehicles (EVs). Therefore, suitable catalysts are generally loaded on the air electrode or catalytic units are added to the liquid electrolyte to promote the kinetics of the process.

1.4.4 Catalyst for Lithium-Air Batteries

As mentioned earlier, the Li-air cell discharge process is an oxygen reduction reaction (ORR) of O_2 on the air electrode, i.e., the reduction of O_2 to the discharge product Li_2O_2. The charging process, on the other hand, is in Oxygen Evolution Reaction (OER) on the air electrode, i.e., the discharge product Li_2O_2 is oxidized and hence releasing O_2. In the absence of catalyst, the kinetic of discharge/charge reactions is slow and the reaction potential is high. At the same time, the insulating Li_2O_2 also leads to blocked electron transport and increased cell polarization, which affects the rate performance of the cell, accelerates the decomposition of electrolyte and air electrode material, and eventually leads to cell failure. Therefore, Li-air batteries need catalysts to promote ORR and OER to facilitate the reaction kinetics on the one hand. On the other hand, it can improve the discharge platform, lower the charging platform, and reduce the battery polarization. At present, researchers have borrowed the catalysts widely used in fuel cell and Zn-air batteries and applied them to Li-air batteries. The ORR and OER kinetics of Li-air cells have been improved by using such catalysts. Currently, the catalysts used in Li-air batteries can be generally classified into two types according to the form in which they are present: solid-phase catalysts and liquid-phase catalysts, respectively. These two types of catalysts are described below.

Solid-phase catalysts. The solid-phase catalyst is loaded in solid form on the air electrode of Li-air batteries. Currently, the widely studied solid-phase catalysts include noble metals such as Pt, Pd, Au and Ru, as well as several alloys and oxides of these noble metals. Transition metal oxides such as MnO_x, and Co_3O_4 are also among the choices of solid-phase catalysts for Li-air cells [107, 116, 118, 122-125]. Noble metal catalysts are the first type of catalysts studied in Li-air batteries. Li-air batteries using these catalysts not only have better electrochemical performance, but also increase the specific capacity of discharge. In addition, precious metal catalysts have a modulating effect on the morphology of the discharge products. In the Li-air cell with Pd, Au and Ru as catalysts, the growth pattern of Li_2O_2 on the electrode surface is different from the growth pattern on the electrode surface with Pt as catalyst or without catalyst. With Pd, Au and Ru as catalysts, Li_2O_2 is grown vertically on the electrode surface in the form of nanosheet arrays, while Li_2O_2 generated with Pt catalyst and without catalyst is covered on the electrode surface in the form of thin film-like epitaxy. The advantage of the former growth method is that the Li_2O_2 grown in vertical arrays can provide more contact area and increase the contact opportunities with the electrolyte, thus shortening the transport paths of Li^+ and O_2 and improving the pore utilization on the electrode surface. On the contrary, the latter form of film growth not only fail to improve the transport of Li^+ and O^{2-}, but also the electron transport involved in redox reaction would be restricted when the Li_2O_2 deposition exceeds a certain amount due to the insulating nature of Li_2O_2. In addition, it has also been shown that using AuPt alloy as a catalyst has the good ORR catalytic performance of Au catalyst and the strong OER

performance of Pt catalyst. This means that the use of AuPt alloy catalysts can simultaneously increase the discharge plateau, decrease the charging plateau, and reduce the cell overpotential. However, since the high cost of noble metal catalysts, the transitional metal oxide catalysts with good catalytic performance are also used in Li-air batteries. The most typical transitional metal oxide catalyst is the Mn oxide catalyst. A study comparing the catalytic performance of MnO_x with different morphologies shows that α-MnO_2 nanowires have the best catalytic performance. Scott et al., [126] assembled Li-air cells with a discharge capacity of 4750 mA h g^{-1} using Super P as the carrier and MnO_2 as the catalyst. In addition, Co_3O_4 has also become a hot research topic because it has been shown to have both ORR and OER catalytic functions. Liu et al. [127] obtained a high specific capacity and cycle-stable Li-air cell by in situ loading of Co_3O_4 on foam Ni using evaporative ammonia-induced method. The maximum discharge potential of the cell was 2.95 V and the minimum charge point was 3.45 V, which is a perfect example of the combination of ORR and OER catalytic functions of Co_3O_4 compared with the conventional carbon-based cathode material. During long-term studies, researchers have also found that sulfides, nitrides, carbides, and nitrogen oxides of transition metals also have better catalytic properties in Li-air cells [128, 129]. In addition, heteroatom (N, O, S) [130, 131] doped carbon materials have higher ORR catalytic activity and relatively lower cost compared to undoped carbon materials, especially nitrogen hetero-carbon materials have also become a class of choice for catalysts. At the same time, the use of nitrogen-doped carbon materials could also mitigate the corrosion of carbon-based electrode materials. Non-noble metals such as CuFe alloys have also been studied due to their price advantage, and studies have shown that CuFe

alloys [132] can lower the battery discharge plateau and increase the battery energy density, especially in the case of high-rate discharge. However, both the ORR and OER processes require the participation of electrons, regardless of the discharge process or the charging process. And the above solid-phase catalysts are non-homogeneous catalysts with severe charge transfer resistance. As shown in Figure 1-21, the Li_2O_2/catalyst interface is a solid-solid contact interface with high contact impedance. Coupled with the slow kinetic process and the inherent insulating property of Li_2O_2, there is also a voltage hysteresis problem. In particular, with the use of noble metal catalysts, the resistance to electron transfer is increased by the vertical growth of Li_2O_2 flakes. Therefore, alleviating the electron transfer hindrance is a goal for the development of new catalysts. In addition, the extent of the role of non-homogeneous catalysts in the whole catalytic process and the deeper mechanism need to be further investigated.

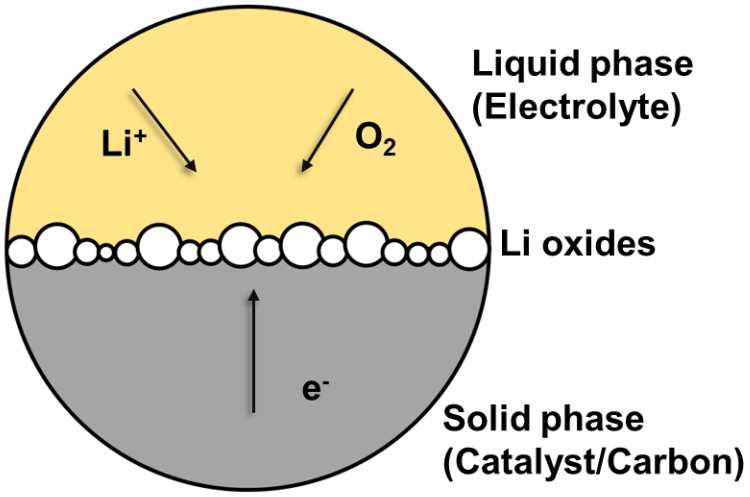

Figure 1-21 Schematic illustration of the reactive site in solid-solid-gas triple-phase boundaries.

Liquid-phase catalysts. Liquid-phase catalyst is a homogeneous catalyst, which can solve the problem of charge transport obstruction in solid-phase catalyst to a certain extent. In fact, the research on Li-air battery catalysts started from liquid-phase catalysts. Inspired by the fields of dye-sensitized solar cells (DSSC) and bioenzyme catalysis, researchers have introduced soluble redox mediators (RMs) in the electrolyte of Li-air cells or on the air electrode [133-135]. The introduction of RMs in Li-air cells, during the discharge process, the RMs with redox ability can catalyze both the adsorbed O_2 on the electrode surface and the dissolved O_2 in the electrolyte, enhancing the transport of Li^+, O_2 and electrons, relieving the accumulation of discharge products on the electrode surface, promoting the depth of discharge, and finally increasing the discharge capacity of the battery. During the charging process, RMs transfer electrons to eliminate the increase in polarization caused by the high solid-solid contact impedance (as shown in Figure 1-22) [136], allowing the charging potential to be maintained, avoiding decomposition of the electrolyte and the cathode material, and improving the charging performance.

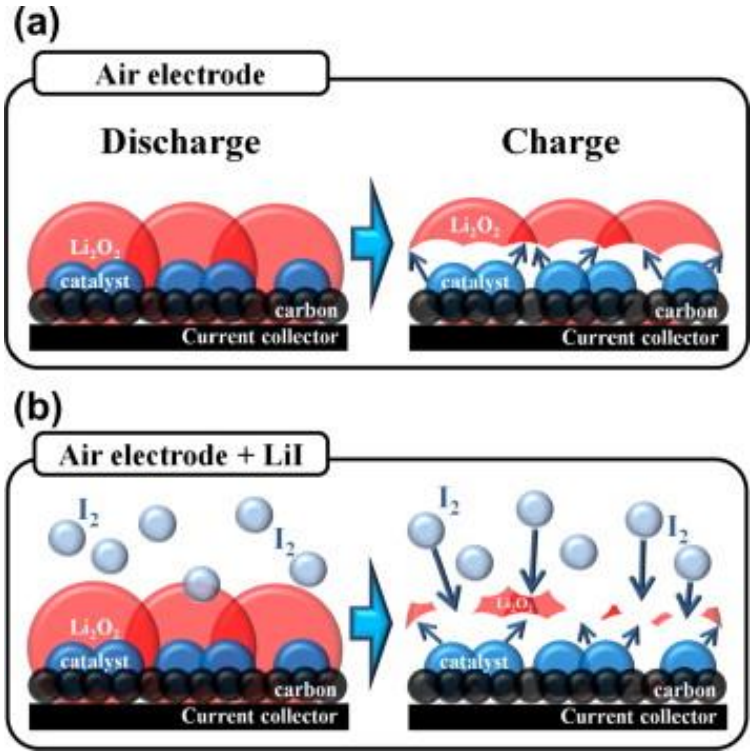

Figure 1-22 Charging decomposition on Li_2O_2 (a) only using Co_3O_4 (b) using Co_3O_4 and LiI.[136]

The basic catalytic principles that facilitate the OER process are shown in reaction Equations (1-11) and (1-12):

$$RMs^R - e^- \rightarrow RMs^O \qquad (1-11)$$

$$RMs^O + Li_2O_2 \rightarrow RMs^R + Li^+ + O_2 \qquad (1-12)$$

The basic catalytic principles that facilitate the ORR process are shown in reaction equations (1-13) and (1-14):

$$RMs^O + e^- \rightarrow RMs^R \qquad (1-13)$$

$$RMs^R + O_2 \rightarrow RMs^o + {O_2}^- \qquad (1-14)$$

Although RMs have significant effects in promoting ORR and OER processes, reducing cell polarization, and inhibiting the occurrence of side reactions, the liquid-phase catalysts reported so far for use in Li-air cells suffer from electrophoretic losses, which become a barrier to the practical use of liquid-phase catalysts.

1.5 Challenges for Lithium-Air (Oxygen) Batteries

1.5.1 Challenges of Conventional Liquid Li-Air Batteries

Despite the relatively high voltage and ultra-high theoretical energy density of Li-air batteries, there are still many challenges and problems, such as low Coulombic efficiency, poor rate performance, low cycle life and poor safety characteristics limiting their practical applications [137]. The challenges for conventional liquid Li-air batteries are mainly caused by the following aspects:

(1) Lithium metal electrode. Li-air batteries use lithium metal as the negative electrode, but they have safety issues and instability, making it difficult to meet the reversibility and long-term cyclability required by the battery. This is due to the fact that the lithium metal negative electrode reacts easily with organic electrolyte components (solvents, anions, additives, etc.) and generates a solid-solid phase or solid-liquid phase interface (SEI). Ideally, the desired SEI is an electrically insulating and ion-conductive passivation layer that effectively separates the lithium metal electrode from the electrolyte solution and prevents further decomposition of the

electrolyte [138]. In fact, however, the SEI formed on lithium metal is far from ideal. The lithium metal electrode of an organic electrolyte lithium-air cell is irreversible, but constantly reacts with the electrolyte and consumes the cell's liquid electrolyte. During the continuous cycle of charging and discharging, large volume changes will occur, resulting in repeated rupture and generation of SEI, forming irregular lithium dendrites. SEI or lithium dendrite can even pierce the battery separator and cause the positive and negative electrodes to be connected, resulting in a short circuit and endangering the safety of the battery [139]. In addition, Li-air batteries are a relatively open system, although the current research testing conditions are in high purity oxygen or oxygen-nitrogen gas mixture. However, in order to truly move towards the path of practicality, it is inevitable that using real air in Li-air batteries. It is necessary to consider the gases such as H_2O and CO_2 in the air react with the lithium metal anode and affect the battery cycle performance [140].

(2) Stability of liquid electrolyte. The ideal electrolyte for organic electrolyte Li-air batteries should have a high chemical and electrochemical stability, low or no volatility, high oxygen solubility, and inertness to superoxide radicals, to ensure the long-term operation of the battery. The viscosity and conductivity of the liquid electrolyte also have an important influence on the electrochemical performance of the battery [141]. However, existing electrolytes are not yet able to fully meet these requirements. On the one hand, intermediates such as superoxide radicals are generated when the battery is discharged, and these intermediates have ultra-high activity and strong nucleophilic ability, which constantly attack the electrolyte, electrolyte

solvent and lithium salt, promoting electrolyte decomposition and serious battery side reactions [95]. On the other hand, due to the high voltage during charging, the positive electrode material or the loaded catalyst has a certain catalytic activity and reacts with the electrolyte, which also promotes the electrolyte decomposition. In addition, the low oxygen solubility of the organic electrolyte and the low solubility of the by-products generated, such as discharge products and electrolyte decomposition by-products, lead to the constant deposition of these products on the electrode surface, clogging the air electrode and causing passivation [142]. Meanwhile, the currently commonly used liquid electrolytes are volatile and will volatilize and deplete with cycling, limiting the stability and long cycling of the battery. Therefore, finding or developing a stable electrolyte system is the most pressing scientific challenge for current Li-air battery [143].

(3) Air positive electrode passivation. The air porous positive electrode of Li-air batteries can provide reactive active sites for the growth and storage of discharge products during the charging and discharging process [143]. However, due to the relatively low solubility of the solid insulating discharge product Li_2O_2 in organic electrolyte and its poor conductivity and reversibility, it will continuously deposit in the pores of the air positive electrode, thus blocking the electrode. Hence, the air positive electrode cannot effectively transfer lithium ions and electrons, leading to electrode passivation, discharge termination, reduction of Coulombic efficiency as well as capacity, and decay of cycling performance, which seriously affects the electrochemical performance of the battery [144]. On the other hand, the existing air positive

electrode materials are not chemically stable enough. During the charging process, the intermediate products, discharge products, and electrolyte components will react with the air electrode at high potentials and decompose the air electrode material to form a series of byproducts, which affects the battery cycle performance [145].

1.5.2 Challenges for Solid-State Li-Air Batteries

In the past ten years, research on solid-state lithium-air batteries has made significant progresses, but there are still considerable gaps between all-solid-state lithium-air batteries and practical application standards. Various factors, such as lithium-ion conductivity, energy efficiency, cycle life, and interfacial stability need rigorous investigation, which pose several fundamental scientific questions to be answered.

First, the mechanism of ion transport and leapfrogging in the inorganic solid electrolyte bulk phase, which is the key factor of the solid-state lithium-air battery, is not clear. The low lithium-ion conductivity leads to a high overall impedance of all-solid-state Li-O_2 batteries. The impedance of a solid electrolyte is generally an order of magnitude greater than that of an organic electrolyte lithium-air cell of the same size, resulting in low energy utilization of the cell. Therefore, the design and preparation of solid electrolytes with high ionic conductivity and performance tuning are needed to understand the synthesis and preparation of solid electrolytes suitable for lithium-air batteries. One method is to improve existing solid-state electrolytes by element doping, and the other is to prepare organic-inorganic composite solid-state electrolytes.

In addition, a systematic study of the lithium-ion migration mechanism in solid electrolytes is needed to lay the foundation for understanding the mechanism of electrochemical reactions in the air electrode of solid-state lithium-air batteries. Finding solid-state electrolytes that combine high ionic conductivity, negligible electronic conductivity, stability to lithium in air, and a wide electrochemical window is the key to address this issue.

Second, like aprotic lithium-air batteries, the voltage difference between charging and discharging process of solid-state lithium-air batteries is too large and the energy utilization is low. In the absence of an effective catalyst, the discharge potential of solid-state lithium-air batteries is around 2.6 V and the charging potential is up to 4.5 V or more, resulting in low energy efficiency of the batteries for practical use. Taking a cue from aprotic lithium-air batteries, efficient catalysts can generally be sought to reduce the decomposition potential of lithium peroxide. And the use of soluble oxidation-reduction catalysts to prepare quasi-solid-state lithium-air batteries is also a good approach.

Furthermore, the mechanism of charge transfer and substance migration at the multiphase interface of active substance/electrolyte in solid-state lithium batteries is still unknown. The current generally accepted working mechanism of Li-O_2 batteries is as follows. During the discharge process, the lithium metal at the negative electrode oxidizes to lithium ions through the solid electrolyte, while oxygen undergoes a reduction reaction at the air-positive interface to chemically combine with lithium ions to produce lithium peroxide. These understandings are

deduced from the liquid electrolyte lithium-air battery, which seems rough and not detailed enough. The introduction of solid electrolyte eliminates the interference of electrolyte decomposition side reactions and organic solvent volatilization, and has excellent thermal stability, which can better establish and simplify the electrochemical reaction model. It is conducive to the development of catalytic and electrochemical theoretical research related to lithium-oxygen reaction. In particular, there is a lack of systematic researches on the charge transfer and lithium-ion migration mechanism during the electrochemical reaction at the gas/solid interface, the principle of redox reaction during the oxygen electrocatalysis at the air cathode surface, the lithium ion transport mechanism, and oxygen adsorption mechanism in the composite air electrode.

Moreover, there are still many problems with the negative electrode of solid-state lithium-air batteries. Compared with conventional aprotic lithium-air batteries, the introduction of solid electrolytes in solid-state lithium-air batteries inhibits the growth of lithium dendrites and short-circuiting of the battery. In addition, the use of solid electrolyte separator fundamentally avoids the issues of electrochemical decomposition of liquid electrolyte and better protects the lithium metal electrode from corrosion by N_2, O_2 and moisture in the air. However, the problems of low utilization of lithium metal electrode and low Coulombic efficiency still exist. One of the solutions is to use alloy negative electrodes to alleviate these two problems, but the adverse volume expansion from alloy negative electrode needs to be further mitigated.

Finally, there is a lack of in-depth study on the solid/solid interface in terms of lithium-ion migration impedance. The internal resistance of the battery affects its output energy, power, and storage efficiency. However, the ionic conductivity of the solid electrolyte at room temperature is approximately an order of magnitude lower than that of the organic liquid electrolyte. This inherent disadvantage makes it challenging to increase the operating current of an all-solid-state lithium-air battery. Moreover, the fluidity of the organic electrolyte enables it to effectively wet the positive and negative electrodes, while the solid/solid interface between the solid electrolyte and the electrodes has a high impedance. To improve the contact between the solid electrolyte and the electrodes, a polymer electrolyte buffer layer is generally introduced between them. Alternatively, the electrolyte surface can be processed by making it porous or coating it with a thin film. Furthermore, designing and preparing ultra-thin solid-state lithium-air batteries can significantly reduce the internal resistance of the battery, and thus improve its performance.

1.6 Thesis Scope

Solid-state lithium-oxygen battery has attracted wide attention due to its ultrahigh theoretical specific energy density, but the actual energy density and cycling stability of lithium-oxygen batteries are not yet up to the theoretical value, or even far from it. This is mainly due to the slow and unsustainable ORR and OER reactions of Li-O_2 batteries [146, 147]. After decades of unremitting efforts, a series of solid electrolytes with various structures have been developed to enhance the stability of lithium-oxygen batteries and their electrochemical performance, in terms of charge and discharge capacity, power efficiency and energy density, and battery cycle

life. However, the technological development of Li-O_2 or Li-air batteries is still in the exploration stage, and there are a series of challenges that need to be solved [148-150]. For example, the mechanism of ion transport and jumping in the inorganic solid electrolyte are not clear. Second, the voltage difference between the charging and discharging processes of solid-state Li-O_2 batteries is too large. The energy utilization of the cell is low, and its cycle life is poor. In addition, the coulomb efficiency of the lithium metal anode and the utilization rate are low. Third, the migration impedance of lithium ions at the solid/solid interface is large and not well studied. The first problem is rooted in the electrolyte itself, and this thesis will investigate from the current popular solid-state electrolyte to propose a solid-state electrolyte suitable for lithium-oxygen batteries. The second issue is mainly due to the high decomposition point of lithium-oxygen batteries during the re-charging process of discharge products, which requires the design of efficient catalysts or adjustment of the battery structure to reduce the charging potential and improve the battery energy utilization and service life. The last issue concerns with the electrolyte-electrode interfacial contact and the ion transport capacity at the interface. which requires interfacial modification and structural engineering.

This thesis aims to create stable, high-conductivity electrolytes for solid or quasi-solid lithium-oxygen batteries. The electrolytes' electrochemical properties will be improved *via* synthesis method variation, elemental doping, and organic-inorganic composites. Additionally, the thesis will investigate electrode structural modification and electrolyte/electrode interfacial engineering. **Chapter 2** outlines the experimental chemistries, instruments, material and

electrochemical characterization methods, and test principles. Subsequent chapters will depict the specific material synthesis and methodology of cell structure design. This thesis will cover the following topics:

(1) **Chapter 3** explores two types of solid electrolytes, LAGP and LLZTO, for use in lithium-oxygen batteries. The electrolytes were made in the lab using different methods and their properties were studied. The performance of electrolytes from the same class can differ depending on how they were made. The electrolytes were then used to make semi-solid or all-solid batteries, and their performance was tested under mild conditions. However, the presented battery performance was not sufficient for practical use. Although the electrodes made of commercial lithium metal and carbon material were systematically investigated, the areas such as modification the electrolyte, engineering the battery interface and cathode materials optimization still require additional efforts.

(2) **Chapter 4** builds on the findings from **Chapter 3** by selecting the Si-doped LAGP oxide and applying poly(ethylene glycol) methyl ether methacrylate (PEGMEM) electrolyte, to make quasi-solid-state lithium-oxygen batteries. A bilayer organic/inorganic hybrid solid-state electrolyte, called PEGMEM@LAGP-Si, is developed to improve safety and enhance battery performance. The LAGP-Si serves as an inorganic backbone to ensure high ionic conductivity and provide a barrier between oxygen and the lithium anode. PEGMEM acts as a buffer layer between the anode and electrolyte, reducing side reactions. The hybrid electrolyte shows high

ionic conductivity and stability against the anode, with better performance than pure LAGP-Si. This work provides a promising double-layered hybrid solid electrolyte for high-performance solid-state lithium-oxygen batteries.

(3) **Chapter 4** results showed a quasi-solid-state battery, but it falls short of being truly safe and reliable. While the previous work solved the contact issue between the lithium metal anode and electrolyte, poor contact between the cathode and electrolyte still causes high interfacial impedance. Additionally, the battery cathode's electrochemical reactive sites are limited due to the deficiency of triple-phase boundaries for Li^+, e^-, and O_2. In **Chapter 5**, an integrated architecture using a garnet electrolyte $Li_{6.4}La_3Zr_{1.4}Ta_{0.6}O_{12}$ and a composite cathode is proposed for high-performance all-solid-state Li-O_2 batteries. The garnet electrolyte's chemical and electrochemical stability, combined with the unique integrated structure's reduced interfacial resistance, allows for exceptional electrochemical performance. This battery boasts a superior large first discharge capacity, long cycling capability, and good interfacial contact. This study's outstanding results could pave the way for practical applications in all-solid-state Li-O_2 batteries and other metal-oxygen energy storage systems with large capacity and long cycle life.

In summary, this thesis starts with the design and preparation of solid-state electrolytes which are applicable to lithium-oxygen batteries, and then proceeds to modify their electrochemical properties. Following this, the interfacial engineering inside the cell, the synergistic effect of multiple electrolytes and the structural properties of the battery cathode are investigated

successively. The experimental results demonstrate that the solid-state lithium-oxygen battery is a very promising energy storage system for practical applications, which contribute to hedge global energy transition on broader perspective.

Chapter 2 Methodology and Techniques

Abstract

This chapter provides a comprehensive description of the chemicals, experimental apparatus, and research methods utilized throughout this thesis. The research methods can be categorized into two primary classifications: material characterization and electrochemical testing. These methodological divisions serve as the foundation for the subsequent chapters, as they form the basis for the research approaches employed in this study.

2.1 Experimental Reagents and Apparatus

The chemical reagents and materials used in this thesis are shown below.

Table 2-1 Main experimental chemical reagents and raw materials

Chemicals	Molecular formula/abbreviation	Specification	Manufacturers
Lithium carbonate	Li_2CO_3	99.9%	Aladdin
Zirconia	ZrO_2	99.99%	Aladdin
Magnesium oxide	MgO	99.9%	Aladdin
Silicon dioxide	SiO_2	99.99%	Aladdin
Ammonium dihydrogen phosphate	$NH_4H_2PO_4$	99%	Aladdin
Anhydrous ethanol	C_2H_6O	≥99.5%	Aladdin
N-methyl-2-pyrrolidone	NMP	AR	Aladdin
Aluminum hydroxide	$Al(OH)_3$	99.9%	Aladdin
Phosphoric acid	H_3PO_4	99.99%	Aladdin
Tantalum oxide	Ta_2O_5	99.99%	Aladdin
Oleic acid	\	99.9%	Aladdin
Isopropyl alcohol	C_3H_8O	99.99%	Aladdin
Lithium metal	Li	\	China Energy

			Lithium Co., Ltd.
Germanium dioxide	Ge_2O_2	99.999%	Sinopharm Chemical Reagent Co., Ltd

Table 2-2 Experimental apparatus

Apparatus	Model	Manufacturers
Electronic balance	ME204E	METTLER TOLEDO
Vacuum drying oven	DZF-6050	Shanghai Huitai Equipment Manufacturing Co., Ltd.
Blast drying oven	DHG-9070A	Shanghai Huitai Equipment Manufacturing Co., Ltd.
Planetary ball mill	QM-3SP04	Nanda Instruments
High and low temperature test chamber	SU-641	ESPEC
Inert gas system - glove box	MBC200	MBRAUN
Multi-channel electrochemical workstation	1470E+1260	Solartron
Pellet presses	769YP-15A	RIKEN
Isostatic presses	WUP-21M	RIKEN

LAND Battery Test System	CT2001A	Wuhan Lanbo
Muffle furnace	KSL-1700X+KSL-1100X	HF-Kejing
Oxygen gas circuit system	N/A	Wuxi Xhlt Technology Co., Ltd.
Small ion sputterer	JS-1600	Beijing Hetong
Tube furnace	OTF-1500	HF-Kejing
Differential electrochemical Mass spectrometer	Probe Type	Shanghai Linglu

2.2 Materials Characterization Methods

X-ray diffraction analysis (XRD)

In this research, the XRD pattern is analyzed to confirm the phase composition and crystal structure of the prepared solid electrolytes and other related materials. When the atomic spacing (d) and the wavelength of the incident X-rays (λ) satisfy the Bragg equation ($2d\sin\theta = n\lambda$), X-rays are diffracted in certain directions (diffraction angle θ.) By determining the orientation and intensity of the diffraction lines in space, it is possible to analyze the material phase, determine the crystallinity and measure the cell parameters. In 1912, German physicist M. von Laue made an important scientific foresight: crystals can be used as space diffraction gratings for X-rays, i.e., when a beam of X-rays passes through a crystal, diffraction will occur, and the superposition of diffraction waves results in the intensity of the rays strengthening in some directions and weakening in others, thus opening up the boulevard of X-ray diffraction science. X-rays are essentially the same electromagnetic wave as visible light, with a wavelength of 0.01-100Å, between ultraviolet and γ-rays, also known as Röntgen rays. They are highly penetrating and can ionize irradiated materials, as well as fluorescence, heat, and interference, reflection, and refraction. Scientists have used these principles of X-rays to develop a wide variety of inspection equipment for use in various industries in the medical and industrial fields, and particularly in the fields of materials science and failure analysis.

When X-rays interact with a substance, they are generally divided into three parts in terms of energy conversion: one part is scattered, one part is absorbed, and one part continues to

propagate in the original direction through the substance. Diffraction occurs when the scattered X-rays are of the same wavelength as the incident X-rays, i.e., when the difference in optical range produced by the crystal plane spacing is equal to an integer multiple of the wavelength. By comparing the diffraction pattern specific to each crystal substance with the standard diffraction pattern and using the principle of three strong peaks, the phase present in the sample can be identified. X-rays are produced by an accelerated electron stream of 30-60 kV in an X-ray tube (at a vacuum of 10^{-4} Pa), which impinges on a metal (e.g., pure Cu or Mo) target surface. The commonly used rays are Cu-Kα rays, including both Kα1 and Kα2 rays (intensity ratio of 2:1), with a wavelength of 71.073 pm.

Diffraction must occur to satisfy the Bragg equation: $2d\sin\theta = n\lambda$ (Where d is crystal plane spacing; θ is Bragg angle; λ is wavelength of X-rays; n is number of reflection levels). When X-rays irradiate the sample, the scattered X-rays from each atom in the crystal interfere and will produce strong X-rays diffraction lines in a specific direction. When X-rays irradiate the sample from different angles, diffraction will occur at different crystal faces, and the detector will accept the number of diffracted photons reflected from that crystal face, thus obtaining a spectrogram of the angle-intensity relationship. The Bragg equation reflects the relationship between the direction of diffraction lines and the crystal structure. For a particular crystal, only the angle of the incident rays satisfying the Bragg equation can produce interference enhancement and exhibit diffraction fringes. This is the fundamental meaning of XRD spectra. In this thesis, the material was characterized using a Bruker D8 Advance X-ray diffractometer

with a Cu-Kα radiation source, a wavelength of 0.15418 nm, an operating voltage of 40 kV and a current of 40 mA. Considering that the discharge product volume of solid-state Li-O_2 batteries is small, and the product form is different from that generated in the organic electrolyte system, the solid-state battery discharge products in this thesis cannot be detected by XRD.

Scanning electron microscope (SEM)

Scanning Electron Microscope (SEM) is an electron microscope developed after transmission electron microscope (TEM). 1952, British engineer Charles Oatley built the first scanning electron microscope (SEM). The imaging principle of SEM is different from that of optical microscope and transmission electron microscope. It uses electron beam as the illumination source and shines the finely focused electron beam onto the specimen in a raster-like scanning manner, and then collects and processes the electrons through the secondary electrons and backscattered electrons generated by the interaction between the electrons and the specimen to obtain a microscopic morphological magnification. SEM plays an essential role in fracture failure analysis, material microstructure morphology observation and composition analysis.

In this thesis, material sample was characterized by a field emission scanning electron microscopy (FESEM, Hitachi S4800) to observe the grain size and morphology in the microstructure, and to study the distribution of elements in the structure. The sample composition was analyzed by energy dispersive spectrometer (EDS). This electron microscope also provides qualitative and quantitative analysis of the composition of the sample surface

micro-regions, as well as information on the distribution and content of elements (element mapping).

Transmission electron microscope (TEM)

The microstructure of the sample was analyzed by high resolution transmission electron microscope (HRTEM). The accelerated and focused electron beam is projected onto a very thin sample, and the electrons collide with the atoms in the sample and change direction, resulting in stereo angular scattering and high magnification, high resolution, and different light and dark images. The size of the scattering angle is related to the density and thickness of the sample in the test area, so it can show the structural information inside the sample. In the HRTEM test, the crystal plane spacing of the crystal sample can be derived from the bright and dark stripes in the high-resolution transmission image, and by measuring the spacing of the stripes, the crystal plane corresponding to the stripes can be determined, and the comparison with the standard crystal plane spacing can further obtain information about the internal structure composition of the crystal. Therefore, the HRTEM test can be used to analyze the orientation and composition of the crystalline material of the sample. The HRTEM instrument used in the study to observe the microstructure of the sample was a Tecnai F20 transmission electron microscope from FEI company, U.S.

X-ray photoelectron spectroscopy (XPS)

Multifuncrtional X-ray Photoelectron Spectroscope (XPS) is an electron spectrometer for

chemical analysis based on the photoelectric effect. XPS is one of the most important techniques for surface analysis, not only for detecting the chemical composition of the sample surface, but also for determining the chemical state of individual elements. X-rays excite valence electrons or inner electrons from atoms and molecules on the surface of the sample, which possess different binding energies through different orbital energy levels of the electrons and combine with the photoelectron emission formula to obtain the photoelectron spectrum. The instrument used in this thesis is AXIS ULTRA DLD multifunctional X-ray photoelectron spectrometer from Shimadzu, Japan. XPS photoelectron spectroscopy allows us to analyze the composition and chemical state of the products on the electrode surface in the discharged or charged state, and to analyze the elemental composition qualitatively, semi-quantitatively, and in the valence state.

Brunauer-Emmett-Teller area method (BET)

The BET method measures the adsorption of a sample at different partial pressures of nitrogen in multiple layers. The results are plotted by the BET equation and linearly fitted to obtain the slope and intercept of the line to calculate the true specific surface area (SSA) of the sample. In this thesis, nitrogen adsorption using BET area method (Micromeritics ASAP 2010, USA) was used to obtain information on the specific surface area, pore volume, and pore size distribution of the material.

Thermogravimetric analysis (TGA)

Thermogravimetric Analysis (TG or TGA) is a thermal analysis technique that measures the mass of a sample to be measured versus temperature at a programmed controlled temperature to study the thermal stability and components of a material. TGA is a more commonly used assay in both R&D and quality control. Thermogravimetric analysis is often used in conjunction with other analytical methods in practical materials analysis to perform comprehensive thermal analysis and to analyze materials comprehensively and accurately. In this thesis, the instrument of STA 449F3 from NETZSCH Germany was used to conduct TGA.

2.3 Electrochemical Measurements and Analysis

Discharge-charge testing of battery

The charge and discharge performance of the battery is the most important manifestation of the functionality of the entire battery system. The work on electrode materials, electrolyte materials, interface modification, etc. should be assembled into a battery for charge/discharge cycles in order to make an objective evaluation of the research results. In this thesis, constant current (CC) is used to characterize the capacity, rate performance, and cyclic performance of all-solid-state batteries.

Electrochemical impedance spectroscopy (EIS)

EIS test was used to study the grain impedance, grain boundary impedance, Warburg impedance and different frequency capacitance of the solid electrolyte prepared at different temperatures, and to analyze the lithium ion conductivity and Arrhenius of the solid electrolyte Curves and

other information; study the change of the AC impedance spectrum of the solid electrolyte before and after the coating before and after the cycle, in order to analyze the change of the coating composition on the surface stability of the solid electrolyte and other information; Information of different stages in the chemical reaction process, this judgment infers the reversible generation and decomposition of discharge products.

The principle of electrochemical impedance testing is to apply a small amplitude sinusoidal AC disturbance signal to the system under test. After the system is stabilized, the impedance/conductance of the system is measured to calculate it, and finally the electrode state information such as impedance and electrode process kinetic parameters can be output. AC impedance testing requires that the system under test must be stable before and after the perturbation (stability); the response signal must correspond one-to-one with the perturbation signal (causality); and the perturbation voltage is approximately linear with the response current (linearity). In this study, the total impedance, solid electrolyte conductivity, and electrolyte/electrode interfacial stability of solid-state cells were determined using EIS with a test perturbation voltage of 10 mV and a frequency range of 1 MHz - 0.01 Hz.

For quasi-reversible electrode systems where ohmic polarization, electrochemical polarization, and concentration differential polarization are all present, different curves appear at the high, middle, and low frequencies of the impedance spectrum complex plane diagram (Nyquist plot), owing to the differences in the intra-phase and interfacial bilayer charge transfer relaxation

processes in the electrolyte and the speed of the semi-infinite diffusion relaxation process in the electrode. When multiple interfaces are present (e.g., positive and negative SEI films), multiple interface capacitive arcs or their superimposed arcs are generated.

For an all-solid-state cell similar to Li/LiPON/$LiCoO_2$, the impedance spectrum is roughly shown in Figure 2-1a. R_Ω is the ohmic impedance brought about by wiring problems and poor contact. R and Q are impedance and capacitive resistance, respectively, caused by the solid electrolyte LiPON bulk, $LiCoO_2$/LiPON interface, Li/LiPON interface, and electron transfer of electrochemical reaction. Z_w is the semi-infinite diffusion Warburg impedance of Li^+ in the electrode. Combined with the Bode mode diagram (Figure 2-1b), the region corresponding to the Nyquist plot at different frequencies can be determined [151]. The high frequency region (I) is mainly controlled by the Li^+ movement in LiPON, which reacts with the ionic conductivity of the solid electrolyte; the medium frequency region (II) is mainly controlled by the Li^+ transportation in LiPON, the cathode interface phase, and the charge transfer caused by the cathode reaction; the low frequency region (III) is dominated by the diffusion of Li^+ in the electrode. However, since Li^+ does not diffuse in the lithium metal anode without concentration gradient, therefore, the low frequency region responds to the diffusion of Li^+ in the positive and negative SEI and $LiCoO_2$ electrode phases.

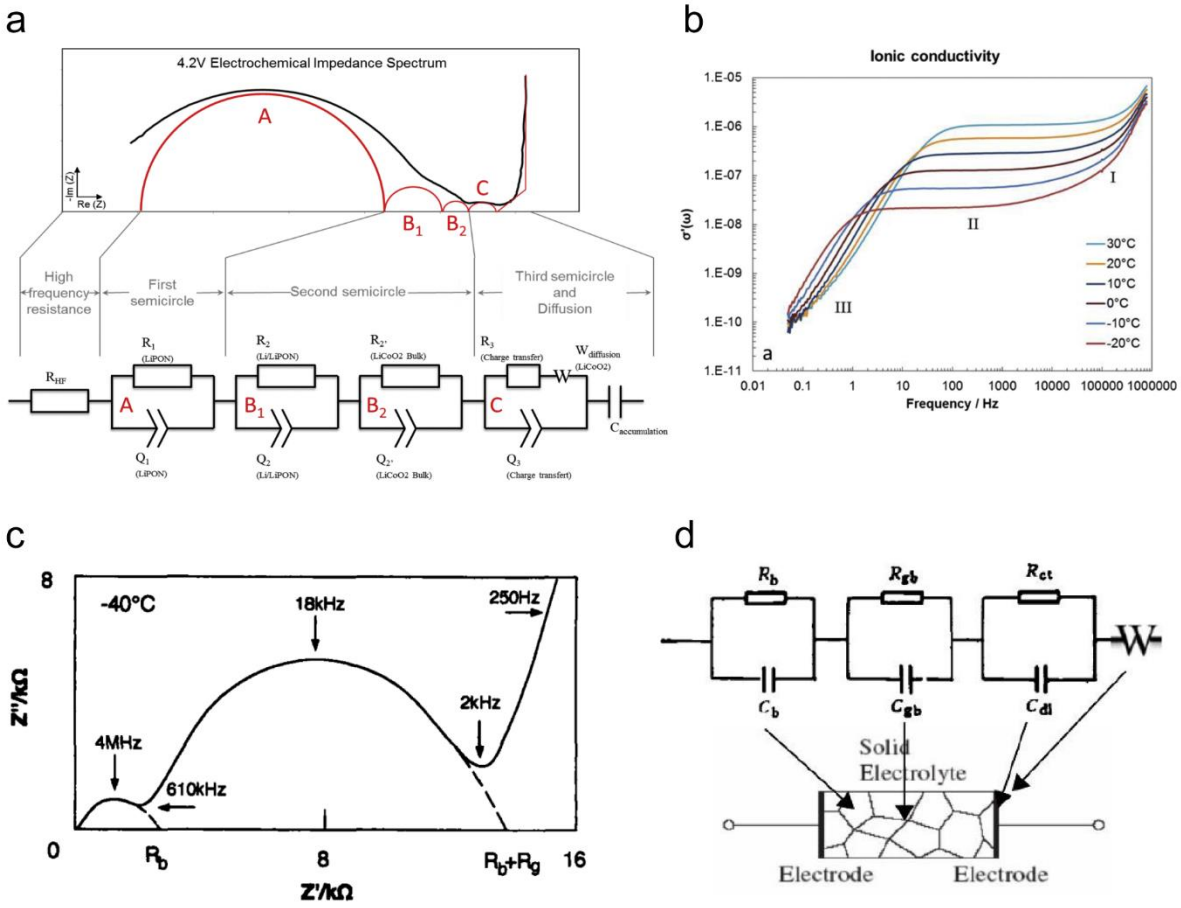

Figure 2-1 (a) Nyquist plots, equivalent circuit, and (b) Bode plots of Li/LiPON/$LiCoO_2$ ASSLiB at 4.2 V. (c) Nyquist plots and (d) equivalent circuit of Au/LAGP/Au.[151, 152]

For a two-blocking electrode system like Au/LAGP/Au, the impedance spectrum is approximately as shown in Figure 2-1c. Where R_b is the grain impedance (bulk), R_{gb} is the grain boundary impedance, R_b+R_{gb} is the total impedance (R_{total}), and R_{ct} is the leap impedance at the interface between the electrode and the sample (which occurs when the interface contact is poor). C is their capacitance, and Z_w is the semi-infinite diffusion Warburg impedance of Li^+ in the electrode. At room temperature, only R_{gb} arcs and Z_w ramps are usually measured at room temperature because the Li^+ within the LAGP grains moves too fast, requiring ultra-high

frequency AC (e.g., above 10 MHz) to measure the capacitive arcs of the complete R_b. The conductivity (σ) of the electrolyte can be calculated by Equation 2.1:

$$\sigma = \frac{L}{RS} \qquad (2-1)$$

Where L is the electrolyte thickness (cm), R is the impedance (Ω), and S is the electrode area (cm^2). The conductivity of the inorganic solid electrolyte or polymer electrolyte at different temperatures is measured and substituted into the Arrhenius Equation (2.2) to find the activation energy E_a used to determine the ion transport capacity of the solid electrolyte.

$$\sigma_t = \frac{A}{T}\exp\left(-\frac{E_a}{RT}\right) \qquad (2-2)$$

where E_a is the migration activation energy of the ion (kJ mol^{-1}), A is preexponential factor (-), T is the test temperature (K), and R is the molar gas constant (8.314 J K^{-1} mol^{-1}).

Cyclic voltammetry (CV)

Cyclic voltammetry is a test method that monitors the relationship between the response current and the potential by controlling the working electrode potential in a certain direction and at a certain rate, linearly reciprocating over time within a certain potential range. It is not fundamentally different from linear sweep voltammetry (LSV), except that the latter no longer reciprocates potential changes. A scan in the CV in the negative direction of the potential results in a reduction peak, corresponding to the reduction reaction. Scanning in the positive direction of the potential results in an oxidation peak, corresponding to the oxidation reaction (i.e., LSV). In this thesis, a two-electrode system is assembled with the blocking electrode as the working

electrode and the lithium metal as the counter electrode to measure the electrochemical window of the solid electrolyte using CV or LSV. In addition, for batteries, the redox peaks of CV curves can be used to infer the location of their electrode charging and discharging plateaus, or calculate the battery cycle reversibility, the diffusion rate of lithium ions in the working electrode. The blocking electrode of the LAGP and LLZO electrolyte is thin gold obtained by sputtering, and the blocking electrode of the polymer electrolyte is polished stainless steel; the LSV scan range is 2.5-6 V, and the CV scan range is -0.5-2.5 V with a scan rate of 5 mV s^{-1}.

Differential electrochemical mass spectrometry (DEMS)

For lithium batteries, since the electrode materials and the electrolyte would undergo side reactions during the continuous electrochemical cycle, and the side reactions are often accompanied by gas generation, the qualitative and quantitative analysis of the gas reduction/evolution during the battery operation is significant for deep understanding electrolysis reaction mechanism. The active substance directly involved in the reaction within Li-O_2 batteries is oxygen, so the corresponding side reactions that may occur must also pass a gas detection system. Differential electrochemical mass spectrometry (DEMS) is an electrochemical field research technology that can qualitatively and quantitatively analyze the gas generated / consumed during the operation of the battery. By combining the electrochemical reaction device with the mass spectrometer, the volatile products of the electrochemical interface reaction enter the mass spectrometer through the membrane interface, and the mass signal detects the changes of the signals of various mass ions with time, thereby performing

qualitative or quantitative analysis. It is of great significance for studying battery reaction mechanism, SEI film formation, irreversible capacity, cycle life, overpotential, electrolyte and electrode stability, and the safety of the battery system. The new DEMS system needs to be equipped with a dual-channel carrier gas system and equipped with a low-temperature cooling system, which is used for long-term battery multiple-cycle testing of solid-state lithium batteries and for the detection of battery oxygen consumption during lithium-oxygen battery discharge. Thus, the molar amount of oxygen consumed is quantitatively calculated, the number of electron transfers is calculated, and the reaction mechanism is speculated.

Direct current-induced polarization (DCP)

In this thesis, a DC polarization test was used to determine the ion mobility number of solid electrolyte samples. The conductivity measured by EIS testing is strictly a mixed conductivity, the sum of ionic and electronic conductivities. To accurately measure ionic conductivity, the ionic mobility number needs to be measured to assess the ionic conductivity as a percentage of the total conductivity. The ion transportation number t_i is calculated as follows:

$$t_i = \frac{\sigma_i}{\sigma_i + \sigma_e} \quad (2.3)$$

Where σ_i is ion conductivity (S cm^{-1}), σ_e is electronic conductivity (S cm^{-1}), and the sum of the two is the total conductivity measured by the EIS. When the ion transportation number is close to 1, it indicates that the material under test is a pure ionic conductor [153].

Density functional theories (DFT)

Density Functional Theory (DFT) is a quantum mechanical theory that provides a practical framework for understanding and predicting the properties of atoms, molecules, and condensed matter systems. Unlike traditional quantum mechanical methods that rely on wavefunctions, DFT focuses on the electron density as the central quantity to describe the system. It treats the interacting many-body problem of electrons within an approximation, where the total energy of the system is expressed as a functional of the electron density. By solving the Kohn-Sham equations derived from this energy functional, DFT allows for the determination of various properties, including electronic structure, energies, forces, and response properties. DFT has become a powerful tool in materials science, chemistry, and solid-state physics due to its ability to handle large systems and complex interactions. However, it's important to note that the accuracy of DFT results depends on the choice of exchange-correlation functional, and additional approximations may be necessary for certain systems or phenomena. Overall, DFT has revolutionized computational materials science and has significantly contributed to our understanding of diverse physical and chemical phenomena at the atomic and molecular level. DFT can be regarded as an approximate method within the framework of first-principles, aiming to improve computational efficiency by simplifying the treatment of many-body problems and introducing density functionals. However, this approximation may result in a loss of accuracy. Therefore, it is important to choose appropriate methods for calculations and analysis based on research requirements and system complexity.

In this thesis, DFT was employed to rigorously compute the Gibbs free energy and adsorption

energy. To calculate the Gibbs free energy, DFT is used to determine the total energy of various system configurations, utilizing appropriate functionals and basis sets. The contribution of entropy is estimated by computing the vibrational frequencies and considering the force constant matrix obtained from DFT calculations. By combining the energy and entropy contributions according to statistical mechanics, the Gibbs free energy for each configuration is evaluated. The comparison of Gibbs free energies allows for the identification of the most stable system configuration. In the case of adsorption energy, DFT is used to calculate the total energy of the adsorbate molecule on the surface without adsorption. Subsequently, the total energy of the adsorbed state is computed, taking into account both the adsorbate-surface interaction energy and the adsorbate's internal energy. The adsorption energy is obtained by subtracting the total energy of the non-adsorbed state from the total energy of the adsorbed state. It is crucial to select appropriate functionals and basis sets for accurate energy calculations and to consider the contribution of zero-point vibrational energy. Additionally, the periodicity of the surface and the use of periodic boundary conditions should be considered in adsorption energy calculations. While DFT provides valuable insights, it is advisable to incorporate experimental data and employ complementary computational methods to validate and refine the obtained results.

Chapter 3 Preparation and Characterization of NASICON-type and Garnet-type Electrolytes and Their Applications in Li-O_2 Batteries

Abstract

The selection, synthesis and modification of solid-state electrolytes are key to the study of solid-state lithium-air batteries. To begin with, the synthesis and analysis of two distinct systems of solid-state electrolytes: $Li_{1.5+x}Al_{0.5}Ge_{1.5}Si_{0.5}P_{3-x}O_{12}$ and $Li_{6.4}La_3Zr_{1.4}Ta_{0.6}O_{12}$ electrolytes were conducted. These electrolytes were utilized in the construction of solid-state (or quasi-solid-state) lithium-oxygen cells, alongside lithium metal anodes and carbon cathodes. Si-doped LAGP-Si glass-ceramic materials with excellent grain conductivity were prepared, using low-cost raw materials, and impact of Si doping on the electrolyte properties of LAGP glass-ceramic solids was then investigated. The solid-state and semi-solid-state lithium-oxygen batteries assembled with LAGP-Si exhibited certain cycling capabilities when operated at low current densities. Furthermore, a high-performance garnet-type solid electrolyte called LLZTO was successfully synthesized, and the solid-state lithium-oxygen battery assembled with LLZTO also demonstrated a certain cycling capability. However, it exhibited a large polarization voltage and high interfacial impedance between the electrolyte and the electrode. Further research is necessary to develop cost-effective cathode catalysts, prepare high-performance solid-state electrolytes, and enhance the interface between solid-state electrolytes and electrode materials. This study lays the foundation for subsequent investigations in this field.

3.1 Introduction

As discussed in **Chapter 1**, in recent years, the trajectory of transition from traditional fossil energy to clean renewable energy is gradually slowing down due to the lack of efficient and reliable energy storage systems. Lithium-oxygen (air) batteries are a promising new energy storage system with the highest theoretical specific energy density available [5, 149, 154]. The battery's negative electrode uses lithium metal, which has the advantage of being the lightest in weight, high specific capacity, and lowest potential. On the other hand, the positive electrode of the battery contains oxygen as the active material, which can be obtained from air and not consume the volume and mass of the battery itself. Exactly this, lithium-oxygen batteries have a specific energy density comparable to that provided by petroleum internal combustion engines and are expected to serve as energy storage systems for electric vehicles (EVs) in the foreseeable future. With abovementioned benefits, the territory of lithium-oxygen batteries has expanded dramatically during the last decades or so. Nevertheless, road of the practical application of lithium-oxygen batteries is not smooth, intrinsic drawbacks of using liquid organic electrolytes makes the bumpy journey towards its complete replacement. The protonic inert organic electrolytes commonly used in lithium-oxygen batteries have many safety hazards, including volatility, leakage, flammability, low oxygen solubility and migration rate, poor electrochemical stability, and many other problems [155]. These problems can be solved by using inorganic solid electrolytes instead of organic electrolytes, like lithium-ion batteries. In addition, the inorganic solid electrolyte can prevent the negative electrode of lithium metal from being eroded by H_2O, O_2, N_2, CO_2 and other components in the air, which greatly improves the

long-term cycle stability of lithium-oxygen batteries. Meanwhile, the inorganic solid electrolyte has excellent mechanical strength, which can effectively block lithium dendrites and prevent lithium dendrites from puncturing the electrolyte separator and causing short circuit accidents. However, the research on solid-state lithium-oxygen batteries, or all-solid-state lithium-oxygen batteries, is still in a preliminary stage.

The structure and components of a solid-state lithium-oxygen battery are shown in Figure 3-1. The choice of materials for each part of the battery depends on the desired operating temperature range, energy density and cycle life of the battery. In an electrochemical cell, the positive and negative electrodes are separated by an electrolyte membrane. When discharged, the negative electrode of the lithium-containing metal in a lithium-oxygen cell undergoes an oxidation reaction, in which the lithium loses electrons and is converted into lithium ions. The lithium ions generated by the reaction are transported inside the cell through the membrane to the positive electrode. Electrons then travel through the external circuit to the positive electrode, where they participate in the oxygen reduction reaction. Subsequently, the oxygen in the reduced state reacts with lithium ions to obtain the discharge product. Therefore, the cathode must have the ability to transport lithium ions and electrons, catalyze the redox reaction, and provide storage space for the discharge products to grow nucleated. Therefore, to develop solid-state lithium-oxygen batteries, the problems and challenges posed by anodes, electrolytes and cathodes in materials science and engineering need to be successfully addressed.

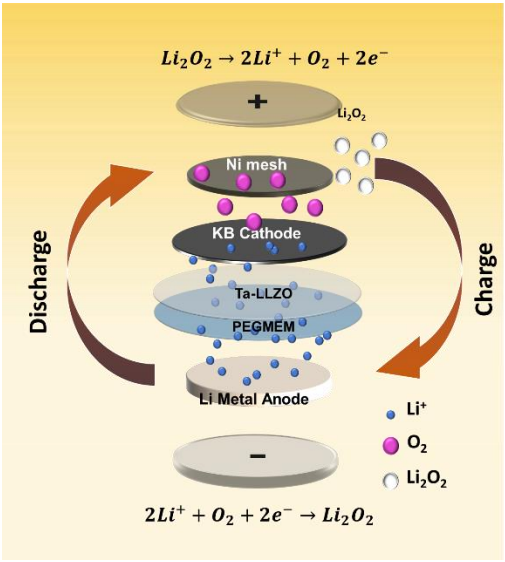

Figure 3-1 Schematic illustration of the structure of a typical solid-state lithium-oxygen battery.

First, for the negative electrode of lithium-oxygen batteries, materials such as lithium metal, lithium alloy (Al-Li, Cu-Li), embedded lithium graphite (Li_xC_6), tin alloy (Sn-Li) and alloy germanium (Ge-Li) are usually used. For the anode design, the key properties required are an efficient electrode reaction (oxidation reaction), high conductivity (ionic and electronic conductivity), and a large potential difference compared to the positive electrode. Lithium metal has the highest specific capacity, but it is unable to maintain chemical and morphological stability in most liquid electrolytes. Moreover, the current understanding of the stability of lithium metal protected by solid electrolytes is still very limited. How to solve the stability of lithium metal has become the primary concern of the lithium battery community. Reversible energy storage requires reversible dissolution (discharge) and deposition (charge) of lithium on the anode surface with high Coulomb efficiency. It is believed that the introduction of solid-

state electrolytes can significantly suppress both chemical and morphological instability of lithium metal anodes. In addition, the specific capacity and energy density of alloy and lithium-embedded graphite materials are slightly lower, which can be compensated by the optimization of oxygen cathode and battery structure design. Therefore, when studying solid-state lithium-oxygen batteries, the capacities of the positive and negative electrodes should also be matched during design optimization. In this chapter, efforts will be devoted to solid-state lithium-oxygen batteries using lithium metal as the anode.

Second, the solid electrolyte is also one of the critical aspects of solid-state lithium-oxygen battery design. In a battery, the electrolyte is the only medium for positive and negative electrodes with ionic conduction and electronic insulation, and varieties such as polymers, glass, ceramics, and composite materials could be candidates. Compared with solid inorganic electrolyte materials, polymers have the advantages of low density, superior flexibility, good interfacial contact, manufacturability, and adaptability to volume deformation [156, 157]. However, their ionic conductivity is relatively low, and they demonstrate high electron conductivity. Soft polymer chains facilitate close interfacial contact between electrolytes and electrodes, making them beneficial for manufacturing processes [158, 159]. In recent years, a series of polymer electrolytes such as poly(ethylene oxide), poly(vinylidene difluoride), and poly(acrylonitrile) have been widely and systematically studied in battery energy storage systems [160-162]. Compared to lithium-ion batteries, Li-air batteries have distinct differences due to their use of an open-air system and the formation of unique discharge/charge products,

such as Li_2O_2, LiO_2, LiOH, Li_2CO_3, and O_2. These differences make it challenging to use polymer electrolytes in Li-air batteries, and overcoming these challenges requires extensive research efforts that primarily focus on enhancing the stability, ionic conductivity, interfacial chemistry, and functionalization of polymer electrolytes [163]. In addition, polymer-ceramic composite electrolytes have some additional advantages, such as exhibiting some mechanical strength and high electrical conductivity, and thus have received considerable attention during the last decade [164]. The doping of ceramic components with ion-conducting polymers results in the formation of a bilayer space charge. The thermal energy of ions and electrons increases with the temperature and the bilayer spreads. At lower temperatures, especially in the operating temperature range of conventional batteries, the space charge will affect the ionic transport properties. Its mediating effect on ionic transport may increase the ionic conductivity. Considering the stability, the difficulty of preparation, and the nature of the reactive material such as oxygen in air, this chapter will focus on inorganic solid electrolytes and establish the foundation for the subsequent chapters.

The commonly used inorganic solid electrolytes are divided into two main categories: those containing oxygen and those are not. Most of the oxygen-free solid electrolytes, such as sulfur-based thio-LISICON, LiN, LiI, etc., tend to absorb moisture or react with air. In contrast, inorganic oxide solid electrolytes are more stable in air and mainly include perovskite-type, anti-perovskite-type, garnet-type, LISICON-type, and NASICON-type. Among them, garnet-like electrolytes and NASICON electrolytes stand out considering their ionic conductivity.

Garnet-type solid electrolytes were firstly discovered in 2003 by Weppner et al. [30]. Their research showed that $Li_5LaM_2O_{12}$ (M = Nb, Ta) possessed a room temperature ionic conductivity of ~10^{-6} S cm^{-1}. By replacing some of the M atoms with Ca, Sr, Ba, and other elements, the Li^+ ion conductivity could be increased by almost ten folds [165]. In 2007, the $Li_7La_3Zr_2O_{12}$ (LLZO) was discovered, with a room temperature ionic conductivity of up to $7.74x10^{-3}$ S cm^{-1} and an activation energy of 0.32 eV [65]. Garnet-based solid-state electrolytes have a significant advantage as they are stable to lithium metal. However, these electrolytes face two major challenges: first, they have poor contact with the lithium metal anode, resulting in high interfacial impedance [166]. Second, they are less stable in air and readily react with H_2O and CO_2, leading to the formation of an inert film on the electrolyte surface [167].

In contrast, LATP has the highest room temperature lithium ion conductivity, up to $3x10^{-3}$ S cm^{-1}, among the NASICON-type solid-state electrolytes studied so far [168]. Furthermore, NASICON-type electrolytes are highly stable in air, and their electrochemical window is wide. However, NASICON-type solid-state electrolytes containing tetravalent titanium are easily reduced by lithium, while electrolytes containing tetravalent germanium elements, such as LAGP, are more stable to lithium.

This chapter aimed to synthesize and evaluate the electrochemical properties and characterization of two oxide solid electrolytes, namely LAGP-Si (NASICON), and LLZTO (garnet). These electrolytes were subjected to modifications such as elemental doping, and

synthesis conditions alteration. The characterization methods used to verify the morphological and electrochemical properties of these electrolytes include XRD, SEM, CV, EIS, DC, and other techniques. To assess the feasibility and electrochemical performance of the electrolytes in the lithium-oxygen battery system, all electrolyte pellets were sandwiched between the lithium metal anode and carbon cathode, resulting in the assembly of a solid-state lithium-oxygen battery. A small quantity of liquid electrolyte was introduced at the cathode to explore the difference in impedance between the solid-solid and solid-liquid interfaces within the battery. Given that the primary purpose of this chapter is to investigate the potential of certain solid electrolytes in lithium-oxygen batteries, all cells were evaluated for charging and discharging in a pure oxygen environment to minimize the influence of air, carbon dioxide, and water. The experimental results indicated that all three electrolytes show some promises in lithium-oxygen batteries, albeit the battery's performance was still a kind of far from practical application. The following work on this thesis will focus on optimizing the electrolytes, battery structures, and electrodes to develop high-performance all-solid-state lithium-oxygen batteries.

3.2 Experimental Methods

3.2.1 Preparation of NASICON-type Electrolytes

The NASICON type glass-ceramic solid electrolyte materials (LAGP and LAGP-Si) prepared in this study were fabricated by melt quenching and controlled crystallization method. The preparation process is shown in Figure 3-2. Firstly, the required raw materials are accurately weighed according to the chemical formula ratio, well mixed by ball milling and dried. The

resulting mixture was heat treated at 700 ℃ for 2 h to remove volatile gases. After ball milling and crushing, the glass melt was placed in a platinum crucible and melted with 1400 ℃ to obtain a glass melt and quenched and cooled to shape. After the resulting glass is crushed uniformly again, the glass powder was pressed into shape with a mold and crystallized by heating at 800 to 1000 ℃ according to the experimental requirements to obtain the final NASICON type structural glass-ceramic solid electrolyte sample.

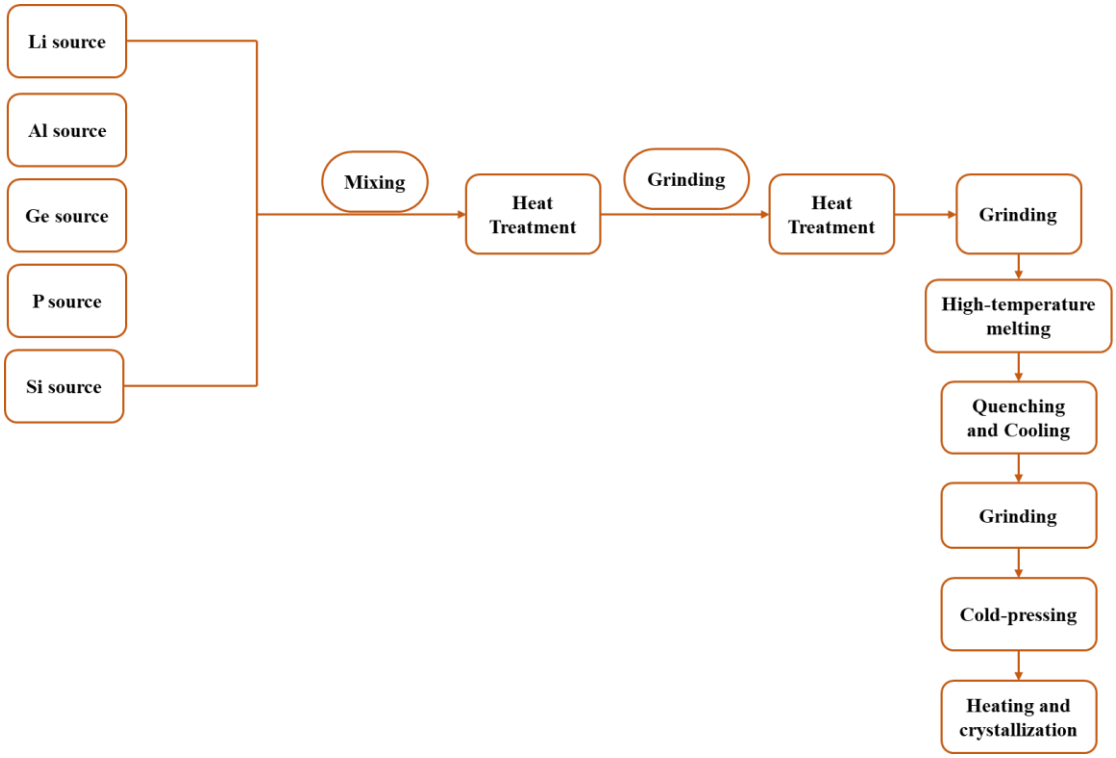

Figure 3-2 The synthesis process of NASICON type structure glass-ceramics solid electrolyte.

3.2.2 Preparation of Garnet-type Electrolytes

Firstly, the precursor buried powder of garnet-type solid electrolytes was synthesized by the conventional solid-phase method. The raw materials Li_2CO_3, La_2O_3, ZrO_2, and Ta_2O_5 were

mixed by ball milling at 400 rpm for 6 h using isopropanol as solvent by stoichiometric ratio. Of which Li_2CO_3 was in excess of 15% (molar basis) to compensate for the loss of lithium elements during the heat treatment. The obtained slurry was dried in a blast oven at 70 ℃, passed through a forty-mesh sieve, and then placed in a Al_2O_3 or MgO crucible and sintered at 900 ℃ for 12 h. The buried powder was then collected, ground and passed through a forty-mesh sieve and stored in a desiccator until use. $Li_{6.4}La_3Zr_{1.4}Ta_{0.6}O_{12}$ (LLZTO) was chosen as a representative material for LLZTO with cubic phase in this chapter because of its high Li ion conductivity and feasibility of preparation.

The preparation of LLZTO powder was similar to the buried powder described above, except that the excess Li was controlled at 5%. After calcination at 900℃ for 12 h, the powder was passed through a forty-mesh sieve and stored in a desiccator for future use. 40 g of LLZTO powder was placed in an agate ball mill jar with an inner diameter of 10 cm and a height of 14 cm. Isopropyl alcohol was used as the solvent and 120 g zirconia balls were used as ball mill media. The ball mill was operated at 400 rpm for 4 h to further reduce the particle size and improve the powder activity. The resulting slurry was dried at 70 ℃ and passed through a 200-mesh sieve. The obtained powder was then pressed into thin pellets and compacted by cold isostatic pressing at 200 MPa. The pellets were sintered at 700 ℃ in an oxygen atmosphere to remove any adhesive. After that, the pellets were coated with the same mother powder to prevent possible lithium loss and heated in the crucible from room temperature to 1100 ℃, 1150 ℃, and 1200 ℃, respectively, and held at this temperature for 15 h.

3.2.3 Preparation of Oxygen Cathode

In this chapter, porous oxygen cathodes were prepared by mixing commercial carbon black Ketjen Black (KB, 80 wt%) with polyvinylidene fluoride binder (PVDF, 20 wt%). The mixture was coated and pressed onto Toray carbon paper, blast dried at 80 °C for 10 h, and then transferred to a vacuum oven for drying at 110 °C for 12 h before being cut to the appropriate size. The PVDF solution was obtained from PVDF powder and NMP in the ratio of 5:95 by mass, and then stirred magnetically for 12 h.

3.2.4 Assembly of Lithium-Oxygen Batteries

The stainless-steel plate, Li anode, solid-state electrolyte, carbon cathode, and nickel foam are sequentially encapsulated in the cell mold in Figure 3-3 and Figure 3-4. Notably, a trace amount of liquid organic electrolyte (1 M LiTFSI in TEGDME) was added dropwise to wet the cathode sheet in this work. The assembled lithium-oxygen battery was tested on the LAND system for electrochemical performance.

Figure 3-3 Photographic view of the experimental setup of battery mold.

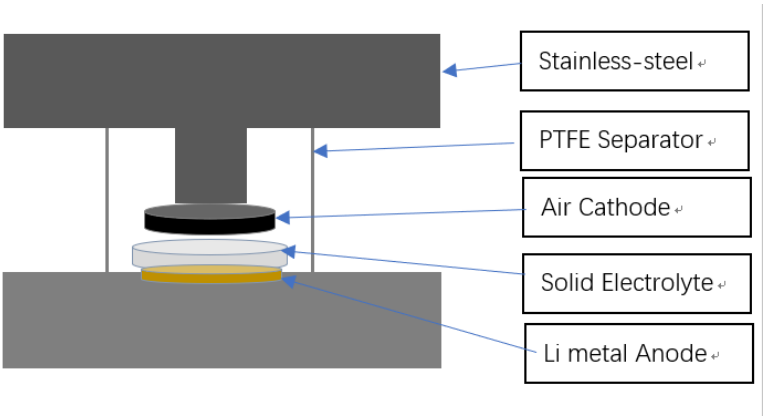

Figure 3-4 Schematic drawing of the internal structure of the lithium-oxygen battery mold.

3.2.5 Characterization and Electrochemical Analysis

The material characterization methods and electrochemical test methods used in this chapter are in accordance with those mentioned in **Chapter 2.2**.

3.3 Results and Discussion

3.3.1 Characterization of Solid Electrolytes

NASICION-type electrolyte LAGP-Si

In the NASICON-type structured solid electrolyte materials, it is known that the substitution of P^{5+} by heterovalent ions can lead to higher ionic conductivity at room temperature. In this chapter, the ionic conductivity of solid electrolytes of the LAGP system is improved by replacing some of the P^{5+} with Si^{4+}, which has a lower valence and larger diameter, using a heterovalent ion substitution method. $NH_4H_2PO_4$ was chosen for the experiments because of its low cost, easy handling and production, and ease of scale-up. The LAGP glass-ceramic materials were prepared according to the preparation procedure in **Chapter 3.2.1**, based on which $Li_{1.5+x}Al_{0.5}Ge_{1.5}Si_xP_{3-x}O_{12}$ (LAGP-Si) samples with different Si doping levels were prepared by replacing part of P^{5+} with Si^{4+}, where x = 0.005, 0.01, 0.02, 0.05 and 0.1. The corresponding samples were labeled as Si0.005, Si0.01, Si0.02, Si0.05, and Si0.1, respectively.

First of all, it is necessary to examine the solid before and after Si doping grains and grain boundaries of electrolyte samples before and after Si doping. The effect of Si on the phase composition of the sample grains was firstly analyzed in the experiments. The samples of Si0.005, Si0.01, Si0.02, Si0.05 and Si0.1 were heated uniformly at 850 °C for 6 h. The phase composition of the samples was investigated by XRD. The XRD patterns of each sample are shown in Figure 3-5. It can be seen that the main crystallite phase of all samples corresponds to the NASICON-type structure, and the diffraction peaks of the samples with different Si doping amounts are in the same position, indicating that Si doping does not affect the main

crystalline phase of the samples. The XRD patterns of Si-doped samples show that at low Si doping levels, the XRD patterns do not exhibit diffraction spurious peaks, which is consistent with the patterns of LAGP samples (PDF#41-0034). However, when the Si doping amount was increased, the XRD pattern showed the presence of SiO_2 diffraction peaks, indicating that higher Si doping amounts lead to the generation of heterogeneous phases. When the doping amount is too high, Si^{4+} will not be completely retained in the cell of the main crystalline phase of NASICON-type structure, and the excess part will exist as SiO_2 heterophase. In addition, XRD results showed that Si^{4+} could enter the main crystalline phase lattice and elemental substitution occurred in the crystalline phase.

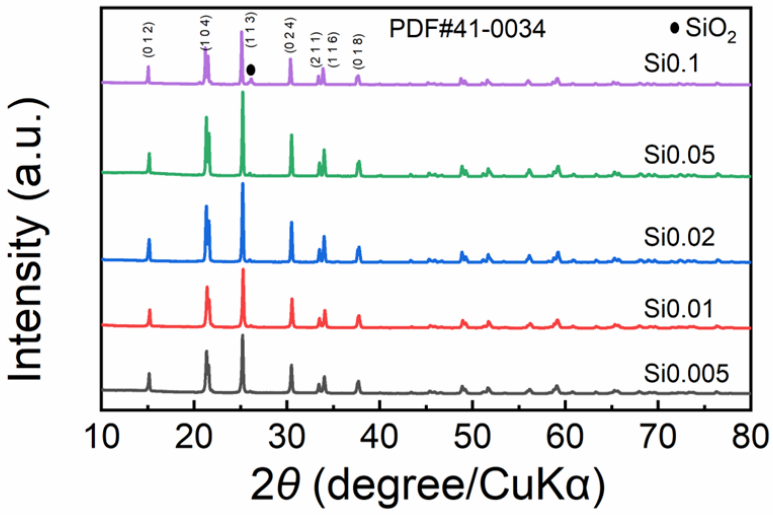

Figure 3-5 XRD patterns of glass-ceramics samples with different silica contents.

HRTEM tests were performed on the sample Si0.01 to investigate the grain microstructure composition by lattice striations. The result is shown in Figure 3-6. The crystal structure can be

clearly observed as the coexistence of crystalline and amorphous phases. The measurement of the crystal plane spacing in the crystal phase region in the figure is 0.421 nm, which corresponds to the (104) plane in $LiGe_2(PO_4)_3$ (JCPDS No. 01-080-1924), indicating the existence of the key crystal phase in NASICON type structure, which agrees with the XRD results. Since the crystalline spacing on the (104) face of the main crystalline phase of the Si0.01 sample is 0.421 nm, while the crystalline spacing on the (104) face of the standard card of $LiGe_2(PO_4)_3$ is 0.417 nm, which leads to the spacing discrepancy. The ionic substitution in the sample is presumed to occur in conjunction with the chemical composition of the sample. From the literature and the ionic radius data, it can be seen that Al^{3+} ion can be substituted by some of the Ge^{4+} in the main crystalline phase of the sample. However, the radii of Ge^{4+} and Al^{3+} at the center of the oxygen octahedron are 0.053 nm and 0.054 nm, respectively, which are not significantly different from each other and do not affect the crystal plane spacing. The radii of P^{5+} and Si^{4+} at the center of the oxygen tetrahedra are 0.017 nm and 0.026 nm, respectively, and the difference between the two values is large. By HRTEM, it was proved that the substitution of Si^{4+} for P^{5+} occurred in the main lattice phase of the sample grains after Si doping, and the expected Si doping was achieved.

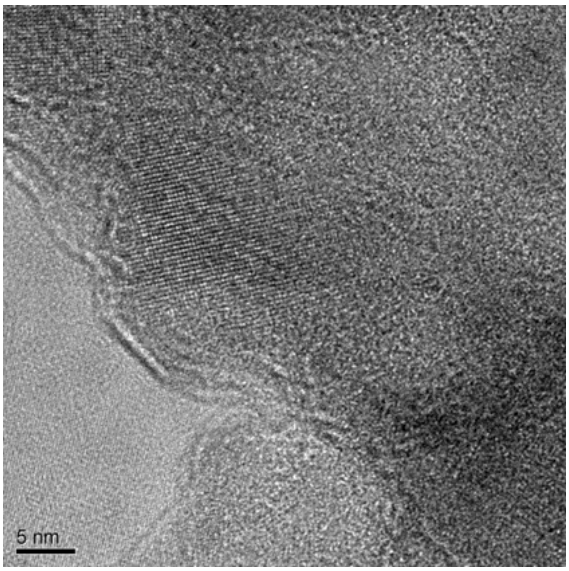

Figure 3-6 HRTEM image of Si0.01 glass-ceramics sample.

To investigate the influence of Si doping on the microscopic morphology of the samples, SEM tests were conducted on cross-sections of Si-doped electrolyte pellet samples that were heat treated at 850 °C for 6 h. The results are presented in Figure 3-7, which clearly demonstrates the relationship between the microscopic morphology of the glass-ceramics and Si doping. Compared to the LAGP samples shown in Figure 3-7a, the grain contour of the Si-doped samples is more distinct, and the grain size is more uniform, indicating a higher degree of crystallization after Si doping. As the Si doping amount increases to x = 0.02, the grain size becomes more uniform and tends to increase, while the inter-grain holes gradually decrease, suggesting that an appropriate amount of Si doping can improve the grain boundaries of the sample.

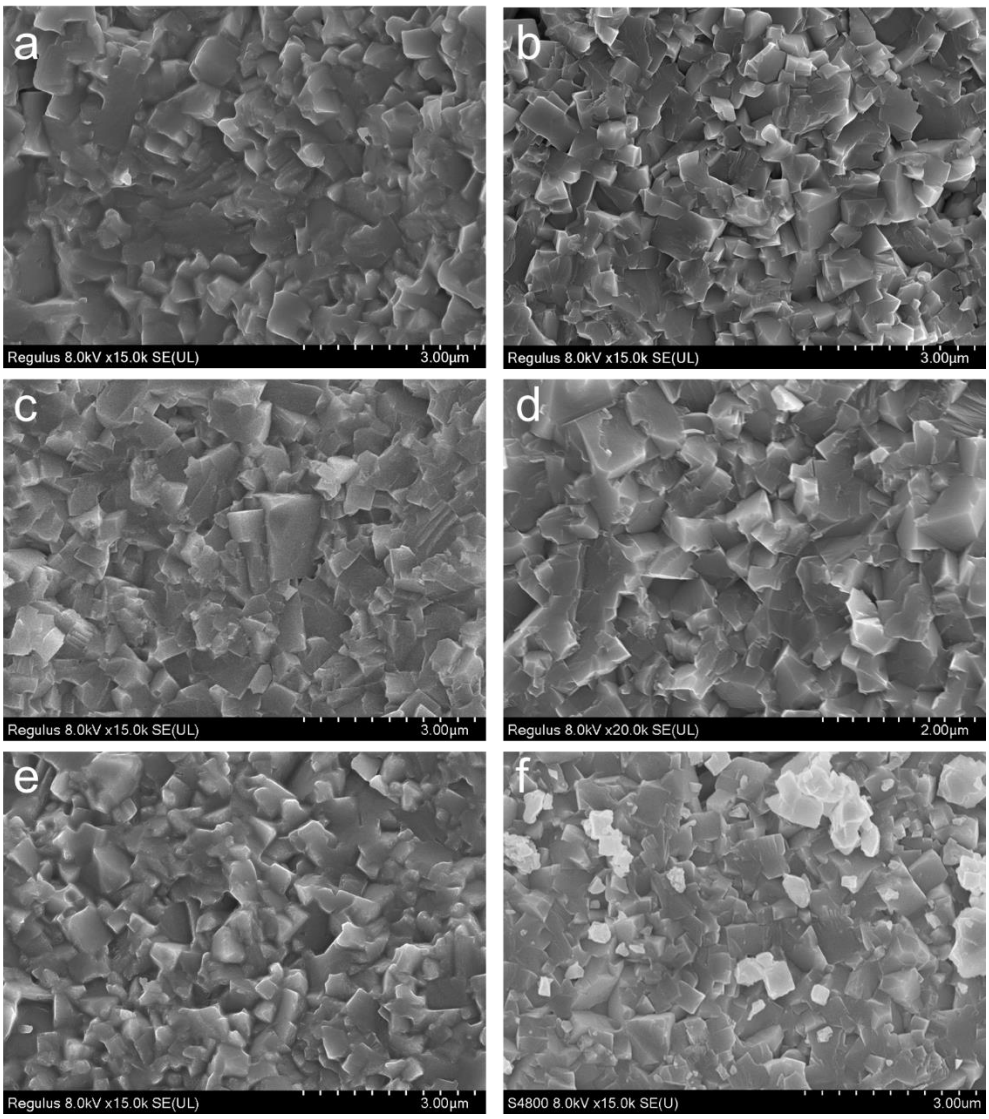

Figure 3-7 Cross-sectional SEM images of glass-ceramics samples with different silica contents: (a) LAGP; (b) Si0.005; (c) Si0.01; (d) Si0.02; (e) Si0.05; (f) Si0.1.

As seen in Figure 3-7e and f, the Si0.05 and Si0.1 samples exhibit an increase in the number of grains but a significant decrease in size and an increase in the number of intergranular pores compared to the other samples. According to literatures, a high Si content in glass increases the fluidity of glass, hinders the growth of grains, leads to the generation of inter-grain pores, and decreases densities [169]. Therefore, the surplus Si doping results in more holes at the grain

boundaries of the samples.

Among all the samples, the Si0.01 sample tends to be well developed with a regular shape and uniform size, and no obvious pores were observed at the grain boundaries. Moreover, the presence of amorphous phases in the Si0.01 samples is also beneficial for reducing holes at grain boundaries, as shown in Figure 3-6 [170]. The reduction of pores at the grain boundaries is crucial for the application of solid-state lithium batteries, as it can effectively prevent the growth of lithium dendrites and avoid short circuits and other safety problems.

Garnet-type electrolyte LLZTO

The solid-phase reaction method is a traditional sintering technique for ceramic powders, which offers the advantages of simple experiments and high-volume production. However, it also suffers from material inhomogeneity caused by uneven diffusion during high-temperature sintering. In this chapter, the solid-phase sintering method is used to prepare Ta-doped cubic-phase LLZTO solid electrolyte materials with high electrical conductivity. To avoid material inhomogeneity and ensure the stability of LLZTO material properties, segmented solid-phase sintering is employed in this section. The XRD patterns of the prepared LLZTO powders and the ceramics sintered at different temperatures are shown in Figure 3-8. The tetragonal and cubic LLZO standard peaks were calculated from the cell parameters given in Refs. [66, 67] using Jade software.

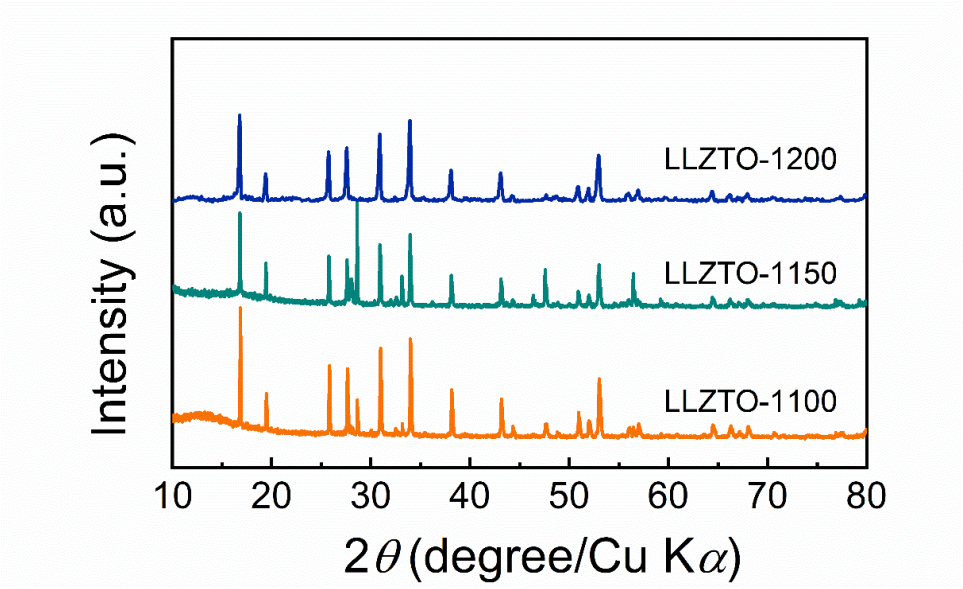

Figure 3-8 XRD patterns of LLZTO ceramic pellets sintered at different temperatures.

The morphology of the material was characterized using SEM. Figure 3-9a shows the SEM image of LLZTO particles sintered at 1200 °C without high-energy ball milling. The size of LLZTO particles sintered by the solid-phase method varies from a few hundred nanometers to a few microns. Figure 3-9b exhibits the SEM of LLZTO particles after high-energy ball milling. The size of LLZTO particles becomes homogeneous, ranging from 800 nm to 1 μm. Figure 3-9c shows the selected diffraction pattern of LLZTO particles, indicating that the material after ball milling is LLZTO polycrystalline. In addition, Figure 3-9d presents the TEM scan of LLZO nanoparticles, which agrees with the XRD and SEM results, further verifying that LLZTO particles can be obtained by high-energy ball milling.

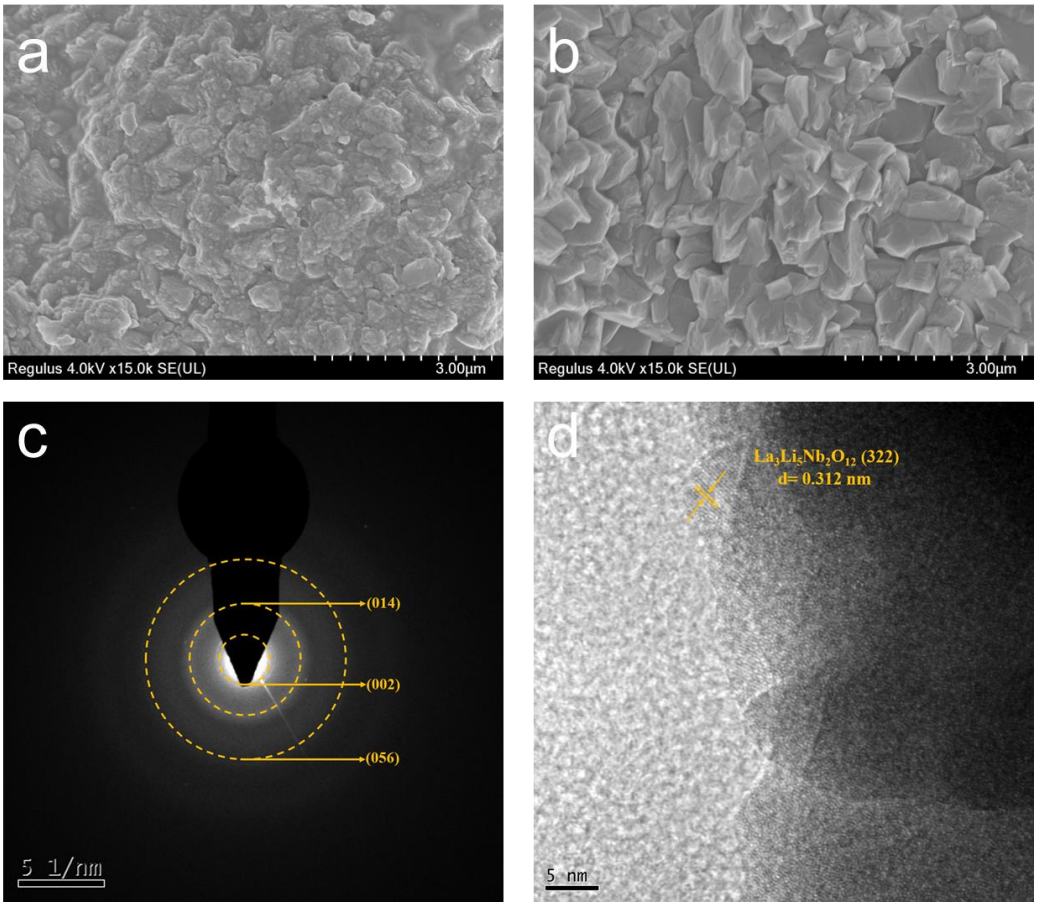

Figure 3-9 (a) SEM image of the LLZTO prepared by solid state method. (b) SEM image of the LLZTO after ball-milling. (c) SAED pattern of LLZTO. (d) TEM image of the LLZTO.

3.3.2 Electrochemical Properties of Solid Electrolytes

NASICION-type electrolyte LAGP-Si

From the previous analysis, the Si doping produces changes in the grain and grain boundary related properties of LAGP solid electrolyte samples, which will also influence the electrical properties of LAGP solid electrolyte samples. The results of the EIS spectra of the samples at room temperature are shown in Figure 3-10, and the variation pattern of the sample conductivity with temperature is shown in Figure 3-11. In EIS spectra, the semicircles and straight lines

correspond to different electrochemical processes and resistance components. Semicircles typically represent the charge transfer processes at the electrochemical interface. The radius and shape of the semicircle provide information about the rate of charge transfer reactions and the charge transfer impedance at the interface. A larger semicircle diameter indicates a slower charge transfer process, while a smaller semicircle represents a faster charge transfer rate. Straight lines generally indicate diffusion-controlled electrochemical processes or the influence of electrolyte conductivity. The slope and intercept of the straight line can provide information about the diffusion process, such as the diffusion coefficient of species in the solution or the conductivity of the electrolyte. A steeper slope indicates a higher diffusion rate or conductivity. It is important to note that the characteristics and interpretations of semicircles and straight lines in EIS spectra may vary depending on the specific experimental system and conditions. Therefore, accurate interpretation and analysis of EIS results for a particular research subject require consideration of other experimental data and theoretical models. In EIS mapping, the grain boundary impedance usually corresponds to a semicircle. The grain boundary impedance (R_{gb}) is caused by charge transfer and ion diffusion at the grain boundary surface. The grain boundary impedance often appears as a semicircle, and the radius and shape of the semicircle provide information about the rate of charge transfer reactions and the charge transfer impedance at the grain boundary. The size and shape of the semicircle can be used to evaluate the electrochemical properties and impedance characteristics of the grain boundary. The straight-line segment typically corresponds to the impedance of electrolyte conductivity or diffusion-controlled electrochemical processes (R_b). The slope and intercept of the straight-line

segment provide information about the electrolyte conductivity or diffusion processes. A steeper slope indicates higher diffusion rate or conductivity, while a smaller slope indicates lower diffusion rate or conductivity. The position and trend of the straight-line segment can be analyzed to understand the influence and contribution of the electrolyte in electrochemical processes. As can be seen from Figure 3-10, the R_b and R_{gb} values tend to decrease and then increase with the increase of Si doping. Among all the samples, the R_b values of the samples with different Si doping amounts differed greatly, and the R_b value of the Si0.01 sample was significantly lower than that of the other samples. It shows that Si doping can affect the ion transport properties within the grains of the sample, and the change in the size of the lithium-ion transport channel produced by the appropriate amount of Si doping is beneficial to the lithium-ion transport. This is consistent with the results of HRTEM analysis. Therefore, among all samples, Si0.01 sample is more suitable for lithium-ion transport within the grains. Compared to the other samples, Si0.005, Si0.01 and Si0.02 samples have smaller R_{gb} values, indicating that the sample grain boundaries are suitable for lithium-ion transport in this Si doping interval. The analysis of the SEM results shows that the Si0.005, Si0.01 and Si0.02 samples have a dense structure and fewer holes at the grain boundaries, so the R_{gb} values are low. As shown in Figure 3-11, the log(σt T) *vs*. 1000/T relationship curve is linear in the test temperature range and agrees well with the *Arrhenius* equation.

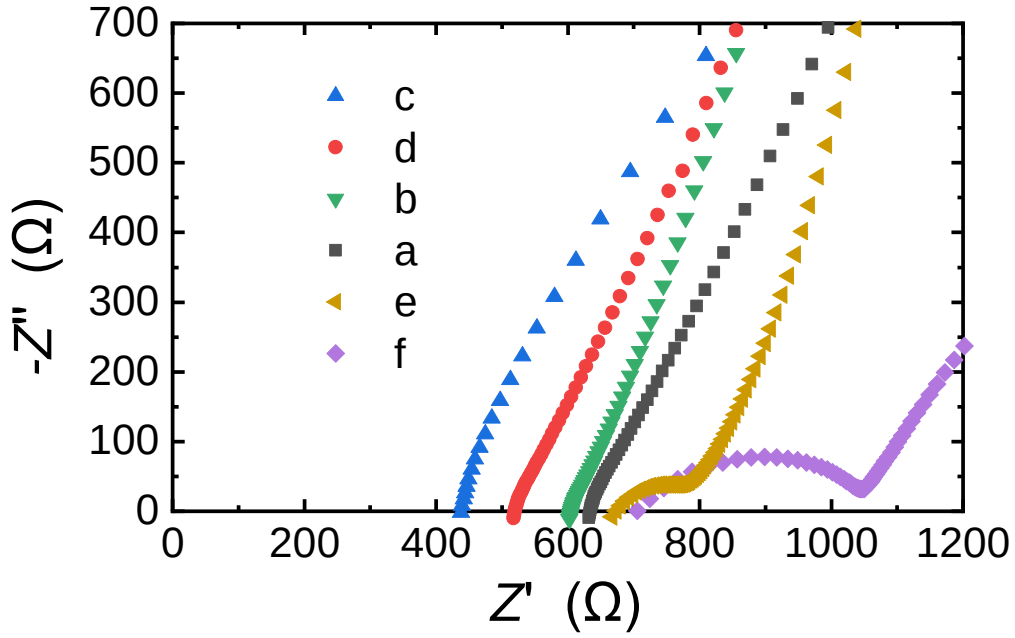

Figure 3-10 Room temperature complex impedance plots of glass-ceramics samples with different silica contents: (a) LAGP; (b) Si0.005; (c) Si0.01; (d) Si0.02; (e) Si0.05; (f) Si0.1.

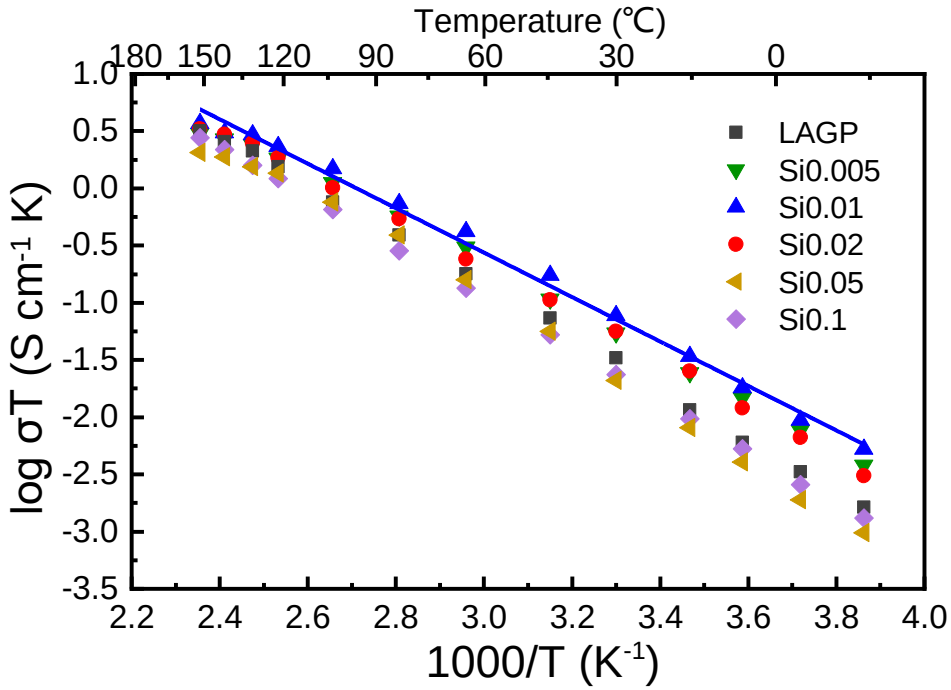

Figure 3-11 Arrhenius plots of glass-ceramics samples with different silica contents.

The results of the room temperature conductivity, activation energy, and relative density of the samples are shown in Table 3-1. From the table, it can be seen that the grain conductivity, grain boundary conductivity, and total conductivity of the samples show a trend of increasing and then decreasing with increasing Si doping. Among all the samples, the Si0.01 sample has the highest grain conductivity and boundary conductivity, resulting in the highest total conductivity of 3.7×10^{-4} S cm^{-1}. These conductivity results indicate that the optimal Si doping is x = 0.01. The relative density values show a positive correlation with conductivity, tending to increase and then decrease with increasing Si doping. The Si0.01 sample has the highest relative density of 97.9%. The activation energy results indicate that the activation energy of the sample decreases and then increases with an increase of Si doping, corresponding to the change in conductivity and verifying the calculation of conductivity. The Si0.01 sample has the lowest activation energy of 0.34 eV.

Table 3-1 Bulk conductivities, grain-boundary conductivities, total conductivities, activation energies and relative densities of glass-ceramics samples with different silica contents.

Sample	R_b (S cm^{-1})	R_{gb} (S cm^{-1})	R_t (S cm^{-1})	Activation Energy (eV)	Relatively Density (%)
LAGP	2.23×10^{-4}	1.38×10^{-3}	1.98×10^{-4}	0.38	90.8
Si0.005	3.47×10^{-4}	1.65×10^{-3}	2.87×10^{-4}	0.36	96.6

Si0.01	4.54×10^{-4}	2.23×10^{-3}	3.74×10^{-4}	0.34	97.9
Si0.02	3.98×10^{-4}	1.62×10^{-3}	3.32×10^{-4}	0.35	97.6
Si0.05	2.04×10^{-4}	1.15×10^{-3}	1.78×10^{-4}	0.37	95.5
Si0.1	1.88×10^{-4}	4.89×10^{-3}	1.25×10^{-4}	0.37	93.2

After EIS testing, it was demonstrated that the ionic conductivity of the solid electrolyte could be improved with the appropriate amount of Si doping. Among all the samples, the Si0.01 sample had the highest room temperature ionic conductivity. However, the application of solid electrolytes in solid-state lithium batteries requires not only high room temperature ionic conductivity but also good electrochemical stability to avoid side reactions during the charging /discharging process. Since the Si0.01 sample exhibited good ion transport capability, its electrical properties were investigated in-depth to explore its feasibility for application in solid-state lithium batteries.

Cyclic voltammetry was used to test the electrochemical window of the samples to study their electrochemical stability. The DC polarization method was used to test the ion migration number of the samples and to study the proportion of migrating carriers accounted for by lithium ions. Cyclic voltammetry was performed on the Si0.01 sample with a scan rate of 0.5 mV/S and a scan range of -0.5 V to 6 V. The cyclic voltammetry results are shown in Figure 3-12. Two redox peaks were observed at -0.5 V and 0.5 V for the Si0.01 sample, and no other

redox peaks were observed in the test voltage range, indicating that the Si0.01 solid electrolyte material can maintain electrochemical stability within the testing voltage range and has an electrochemical window above 6 V.

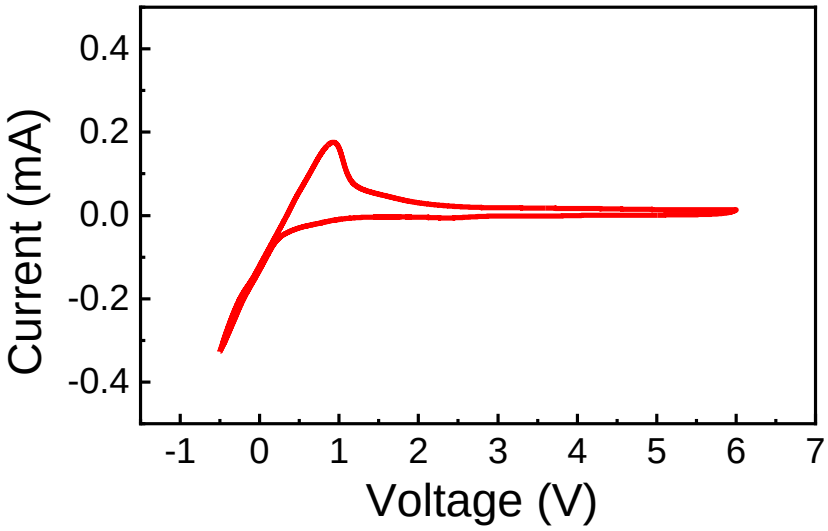

Figure 3-12 The CV curve of Si-0.01 glass-ceramics sample.

In lithium-ion batteries, the solid electrolyte functions as the lithium-ion conductor and must act as an electron insulator to prevent short circuits caused by electron currents at both poles of the battery. To determine the total conductivity of the electrolyte, which is the sum of the electronic and ionic conductivities, EIS impedance testing is performed. The electronic conductivity of the Si0.01 sample was evaluated using DC polarization, and the results of this evaluation are presented in Figure 3-13. In the DC polarization curve of the Si0.01 sample, the ionic current gradually decays until it disappears, and then the current gradually flattens out, leaving only the electron current. The calculation shows that the ionic mobility number is close

to 1, indicating that the fabricated Si0.01 sample is a pure ionic conductor. These tests demonstrate that LAGP-Si glass-ceramic materials, including the Si0.01 sample, have promising prospects to be used in high-energy density solid-state lithium batteries.

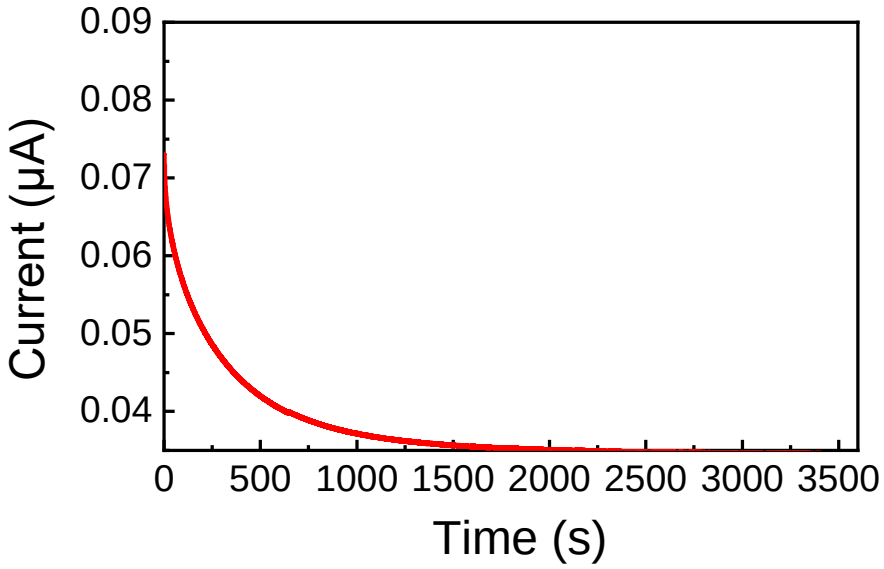

Figure 3-13 The DC polarization curve of Si0.01 glass-ceramics sample.

Garnet-type electrolyte LLZTO

The ionic conductivity test of LLZTO is similar to the process of LAGP-Si. The LLZTO precursor powder was poured into a cold pressing mold after ball milling, and the pressure was set at 4 MPa. After holding the pressure, the mold was demolded to obtain LLZTO billets. The LLZTO billet was then placed into a magnesium oxide crucible, and the upper and lower surfaces as well as the surrounding area were covered using the LLZTO mother powder. The crucible was then placed into a chamber muffle furnace and sintered for 12 hours at temperatures of 1100, 1150, and 1200 °C, respectively. The relative densities of the LLZTO

electrolyte pellets were tested under different conditions. After sintering at 1150 ℃, the relatively density of the LLZTO pellet is 89.2%, and after sintering at 1200 ℃, the relatively density was 92.7%. The ionic conductivity of the electrolyte was tested after grinding, polishing, and gold spraying.

The ionic conductivity of the LLZTO solid electrolyte sheets obtained by sintering at different temperature conditions was tested separately on an electrochemical workstation. The EIS test results are shown in Figure 3-14. Using the ionic conductivity calculation equation, the ionic conductivity of LLZTO electrolytes sintered at different temperatures was derived and the results are shown in Table 3-2. Comparing the results, it was found that the sintering temperature affects the density and ionic conductivity of the electrolyte material. In addition, the prepared LLZTO powder and the formed electrolyte sheets were kept in a sealed environment because LLZTO tends to produce Li_2CO_3 material with low ionic conductivity in air.

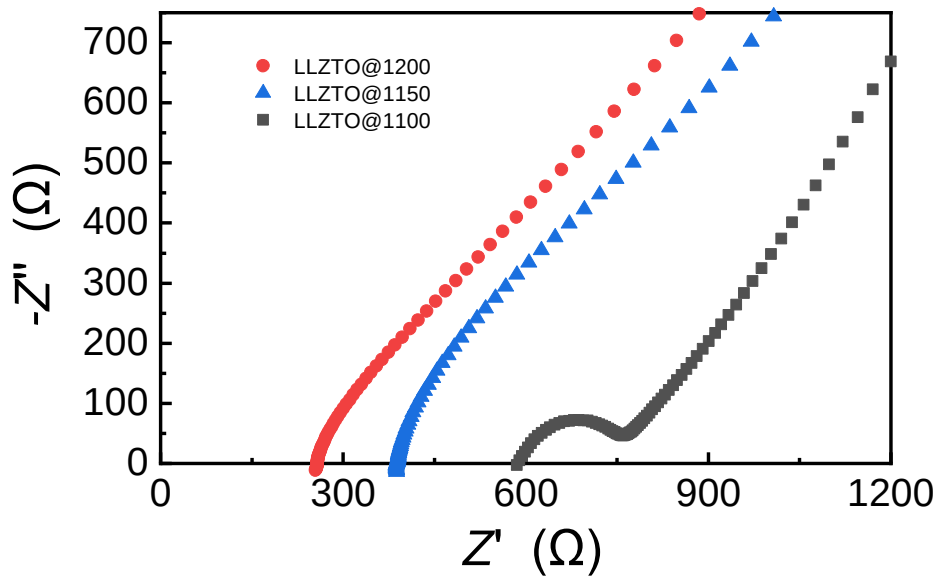

Figure 3-14 Room temperature EIS test of bulk LLZTO sintered at different temperatures.

Table 3-2 The bulk ionic conductivity of LLZTO sintered at various temperatures.

Sintering Temperature (℃)	1100	1150	1200
Room temperature bulk conductivity (S cm^{-1})	2.10×10^{-4}	2.72×10^{-4}	3.32×10^{-4}

The LLZTO's electrochemical window and electronic conductivity underwent the same testing method as LAGP-Si. The cyclic voltammetry results of LLZTO, displayed in Figure 3-15, show two redox peaks at -0.5 V and 0.3 V. Within the test voltage range, no other redox peaks were observed, implying that the solid electrolyte material LLZTO maintains electrochemical stability and possesses an electrochemical window greater than 6 V.

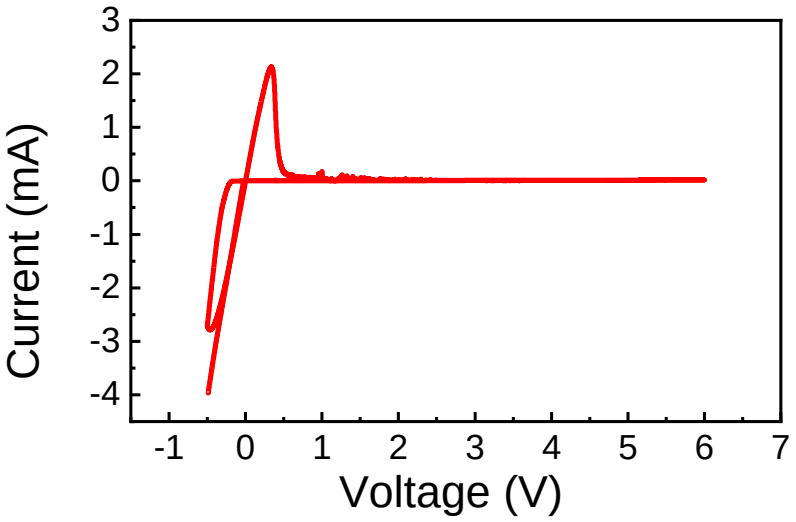

Figure 3-15 The CV curve of LLZTO (1200 ℃) electrolyte sample.

Using DC polarization, the electronic conductivity of the LLZTO sample was evaluated, and Figure 3-16 shows the outcomes. The calculation of the ion mobility number demonstrated that LLZTO is a pure ionic conductor, similar to LAGP-Si studied above.

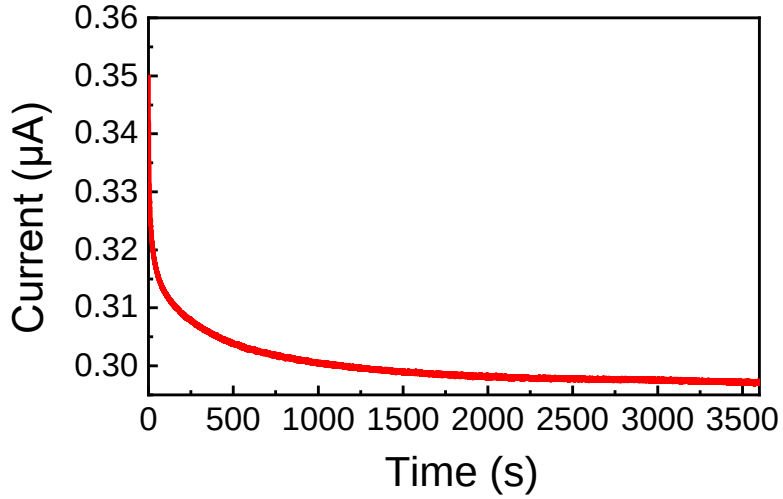

Figure 3-16 The DC polarization curve of LLZTO (1200 ℃) electrolyte sample.

3.3.3 Electrochemical Performance Testing of Lithium-Oxygen Batteries

NASICION-type electrolyte LAGP-Si

To verify the performance of Si-doped LAGP electrolyte in batteries, this chapter compares the first-cycle discharge-charge performance of pure LAGP-assembled and LAGP-Si-assembled solid-state lithium-oxygen batteries. The sample with a Si doping of 0.01 was selected to assemble the LAGP-Si-based cell because it has the highest lithium-ion conductivity. All the batteries were tested at room temperature in pure oxygen atmosphere. As shown in Figure 3-17, at the current density of 0.1 mA cm^{-2}, the initial discharge capacity of the battery with LAGP-Si is about 6.09 mA h cm^{-2}, while that of the LAGP-based battery is 3.52 mA h cm^{-2}. Additionally, Si doping effectively reduces the charging potential and overvoltage, and the battery charging plateau is below 4 V. This indicates that the Si-doped LAGP electrolyte has better ion transport capability. Therefore, the following tests in this chapter primarily focus on the solid-state lithium-oxygen battery containing a LAGP-Si electrolyte, lithium metal anode, and a KB carbon-oxygen cathode.

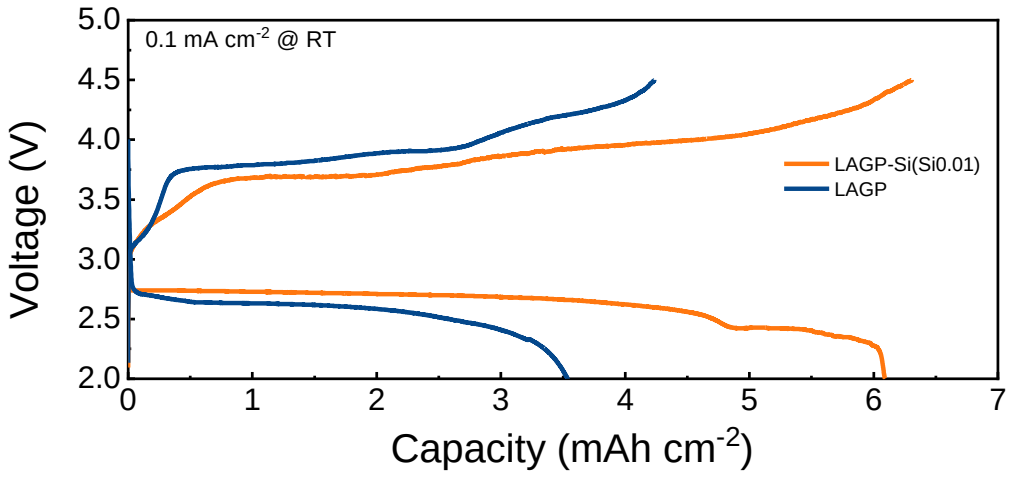

Figure 3-17 The first discharge-charge curves of solid-state lithium-oxygen batteries with LAGP and LAGP-Si electrolytes. The cutoff voltage range is between 2 V and 4.5 V.

Figure 3-18 shows the room temperature discharge-charge curves of a solid-state lithium-oxygen battery at different currents. The battery was discharged/charged at currents of 0.05, 0.1, and 0.2 mA cm^{-2}, with capacities of up to 7.11/7.59, 6.08/6.14, and 2.50/2.62 mA h cm^{-2}. The corresponding discharge plateaus are 2.60, 2.57, and 2.45 V. As the current increases, the discharge plateau decreases and the charging and discharging time of the battery decreases, thus the generation of side reactions can be avoided. The similarity in charging platforms of batteries can be attributed to the fact that the charging process in all the batteries requires the breakdown of side reaction products. When the capacity is limited to 0.25 mA h cm^{-2}, the battery can cycle steadily for more than 23 cycles, demonstrating good cycling performance (Figure 3-19). However, the cells assembled in this section are wetted with organic liquid electrolyte on the positive side to reduce the interfacial impedance, so they cannot be called all-solid-state lithium-

oxygen batteries.

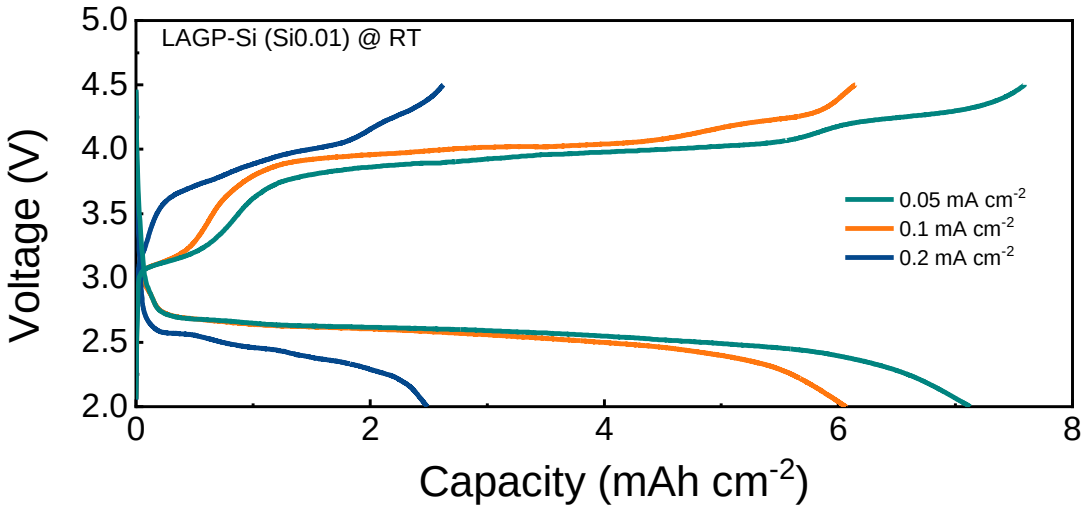

Figure 3-18 Initial discharge-charge curves of the solid-state lithium-oxygen batteries under a current of 0.05, 0.1 and 0.2 mA cm^{-2}, respectively.

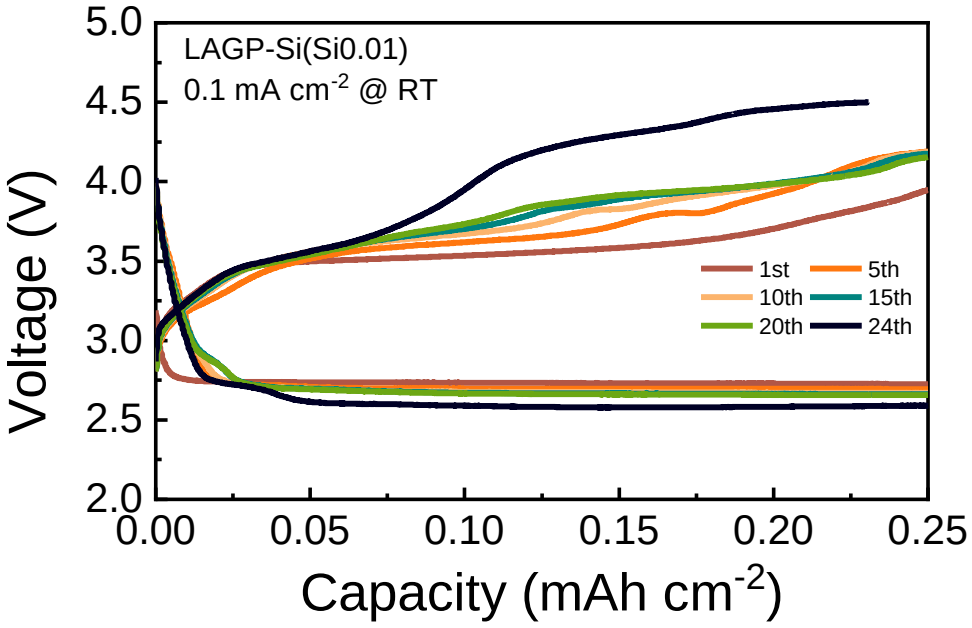

Figure 3-19 Cycling performance of the batteries using LAGP-Si (Si0.01) at 0.1 mA cm^{-2} and limited capacity of 0.25 mA h cm^{-2}.

Garnet-type electrolyte LLZTO

Similar to the LAGP-Si-based solid-state lithium-oxygen battery, a solid-state battery was prepared using LLZTO, a lithium metal anode, and a KB carbon-containing cathode for charge and discharge testing under pure oxygen. This chapter focuses on the assembly of lithium-oxygen cells using LLZTO obtained by sintering at 1200 °C, as the electrolyte exhibits the highest ionic conductivity at this temperature.

The initial charge/discharge curves of the solid-state lithium-oxygen battery with LLZTO at different current densities are shown in Figure 3-20. These batteries have a discharge plateau around 2.65 V, while the charging process has an insignificant two-step plateau. The first of the two plateaus correspond to the decomposition of lithium peroxide, while the second can be attributed to the decomposition of the by-product Li_2CO_3. Li_2CO_3 will accumulate on the surface of the positive electrode, and the charging process can only partially decompose it. The residual Li_2CO_3 leads to a decrease in conductivity within the positive electrode, which in turn causes a reduction in subsequent cycling capacity. Compared with the capacity of the LAGP-Si-based cell in Figure 3-18, the first-discharge-charge capacity of LLZTO is not comparable to that of LAGP-Si, so it needs further modification work before it can be applied into practical application.

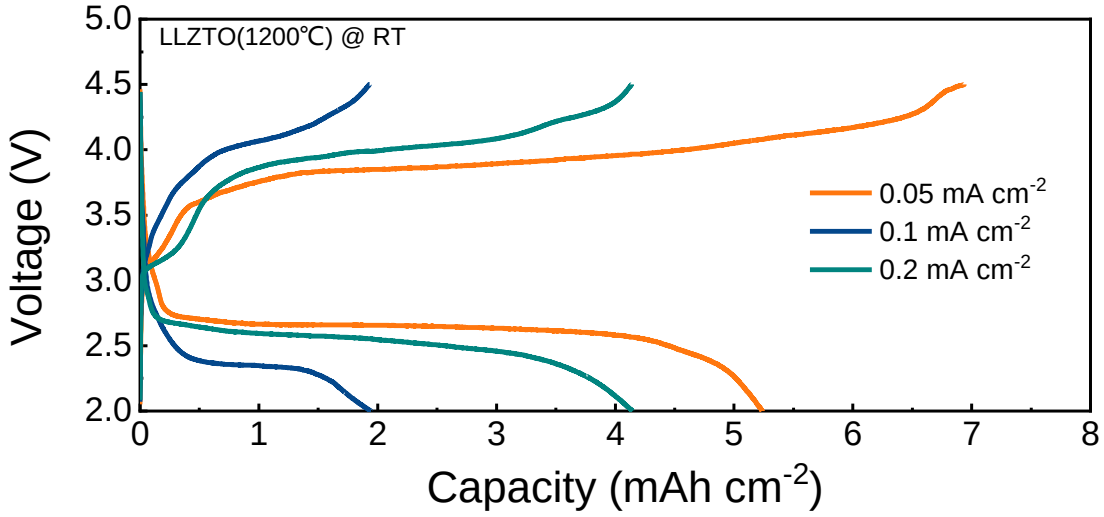

Figure 3-20 Initial discharge-charge curves of the solid-state lithium-oxygen batteries under a current of 0.05, 0.1 and 0.2 mA cm^{-2}, respectively.

The cycling performance of the LLZTO-based solid-state lithium-oxygen battery was tested at room temperature in pure oxygen, and the results are shown in Figure 3-21. The capacity-limited cycling approach mitigates severe degradation of battery performance under full charge and discharge, which is a measure of battery cycling performance. Under the limited capacity of 0.25 mA cm^{-2} at 0.1 mA cm^{-2} capacity, the LLZTO-based solid-state lithium-oxygen battery can be stably cycled for 12 times without any depletion in its capacity. However, as the cycle number increases, the charging overpotential also increases, indicating the accumulations of the main product-Li_2O_2 and the difficult-to-decompose by-product-Li_2CO_3 on the positive electrode. Therefore, finding effective catalysts that can promote the decomposition of Li_2CO_3 is one of the ways to improve the battery's performance.

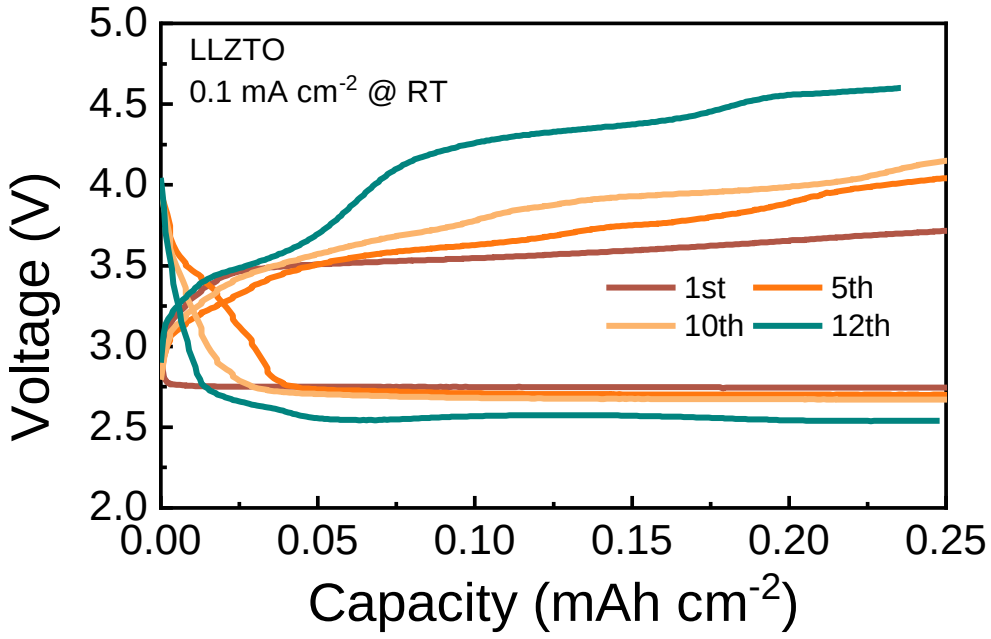

Figure 3-21 Cycling performance of the batteries using LLZTO at 0.1 mA cm^{-2} and limited capacity of 0.25 mA h cm^{-2}.

3.4 Conclusion

In this work, two different systems of solid-state electrolytes, including LAGP-based electrolytes and LLZTO-based electrolytes, are synthesized, and their morphological and electrochemical properties are investigated. These electrolytes are then assembled with lithium metal anodes and carbon cathodes to assemble solid-state (quasi-solid-state) lithium-oxygen cells, and the electrochemical performance of these cells is systematically investigated. The main results are as follows.

(1) The Si-doped LAGP-Si glass-ceramic materials with high grain conductivity were

successfully prepared by the melt-quenching-controlled crystallization method using inexpensive raw materials, and the effect of Si doping on the electrolyte properties of LAGP glass-ceramic solids, and the mechanism were systematically investigated. The solid-state and semi-solid-state lithium-oxygen batteries assembled with LAGP-Si have a certain cycling capability at low current densities, demonstrating their application potential.

(2) High-performance garnet-type solid electrolyte LLZTO was successfully synthesized by solid-phase synthesis method. The experimental results demonstrate that both sintering temperature and crucible type influence the physical properties and electrochemical performance of LLZTO. The solid-state lithium-oxygen battery assembled with it has a certain cycling capability, but the polarization voltage is large and the interfacial impedance between it and the electrode are high.

In summary, a series of oxide solid-state electrolytes were successfully prepared in this chapter, which were utilized to construct solid-state (or quasi-solid-state) lithium-oxygen cells. The electrochemical performance of these cells was assessed, and the feasibility and potential of solid-state lithium-oxygen batteries were demonstrated. Nonetheless, the advancement of all-solid-state lithium-oxygen batteries necessitate further research on developing cost-effective cathode catalysts, preparing high-performance solid-state electrolytes, and enhancing the interface between solid-state electrolytes and electrode materials. This chapter sets the tunes for the subsequent investigations presented in **Chapter 4** and **Chapter 5**.

Chapter 4 Bilayer NASICON/Polymer Hybrid Electrolyte for Stable Solid-State Li-O_2 Batteries

Adapted and rewritten from the published article:

Z. Gu, X. Xin, J. Yang, D.C. Guo, S.J. Yang, J.H. Wu, Y. Sun and X.Y. Yao, *Bilayer NASICON/Polymer Hybrid Electrolyte for Stable Solid-State Li-O_2 Batteries.* ACS Applied Energy Materials, 2022. **5**(7): p. 9149-9157.

Abstract

The practical application of lithium-oxygen (Li-O_2) batteries is limited by the formation of lithium dendrites and the use of flammable and unstable organic liquid electrolytes, which would cause safety issues and poor cycling stability. Herein, we present a bilayer organic/inorganic hybrid solid-state electrolyte to improve the safety and enhance the electrochemical performance of Li-O_2 batteries. Si-doped NASICON-type electrolyte $Li_{1.51}Al_{0.5}Ge_{1.5}Si_{0.01}P_{2.99}O_{12}$ (LAGP-Si) serves as an inorganic rigid backbone to guarantee high ionic conductivity and provide a barrier between active oxygen and lithium anode. Poly(ethylene glycol) methyl ether methacrylate (PEGMEM) is chosen as a polymer buffer layer due to its compatibility with lithium. Benefiting from the synergistic effect between LAGP-Si and PEGMEM, the obtained hybrid electrolyte exhibits high ionic conductivity and good stability against lithium anode. Consequently, the polarization of the Li symmetric cell is dramatically reduced by replacing pure LAGP-Si with a bilayer hybrid electrolyte. The solid-state Li-O_2 batteries employing PEGMEM@LAGP-Si electrolyte deliver a greater initial discharge-charge capacity of 7.3 mAh cm^{-2} and enhanced cyclic performance for 39 cycles with a restricted capacity of 0.4 mAh cm^{-2}. The present work delivers a promising category of hybrid solid electrolytes for high-performance solid-state Li-O_2 batteries.

4.1 Introduction

With the increasing global demand for electrical energy storage devices, lithium-oxygen (Li-O_2) batteries have garnered considerable interest due to their extraordinarily high theoretical energy density (3600 Wh kg^{-1}) and high specific capacity density (1675 mA h g^{-1}) [1, 5, 95, 171, 172]. However, the development of Li-O_2 batteries is largely hindered by the poor cycling stability and safety issues, which are caused by the growth of lithium dendrite and the use of flammable organic liquid electrolytes (LEs) [173-176]. Organic liquid electrolytes are volatile, flammable, explosive, and unstable at high voltage, which may greatly decrease the safety and cyclic performance in the actual application of the battery. Moreover, the undesired growth of lithium dendrite would pierce the separator and cause a short circuit, ultimately leading to battery overheating and explosion. Besides, the Li-O_2 battery is a semi-open system where the liquid solvent may leak during battery operation, resulting in further battery deterioration and combustion. Substituting solid electrolytes for organic liquid electrolytes is considered a realistic and promising approach in resolving the aforementioned concerns. Solid electrolytes could eliminate evaporation and leakage of volatile liquid electrolytes, mitigate side reactions or decomposition processes in batteries and shield lithium from oxygen and moisture, hence extending the cycling life. On the other hand, the solid electrolytes may serve as a physical barrier, preventing short circuits induced by lithium dendrites and assuring safe operation.

Generally, solid-state electrolytes for Li-O_2 batteries can be divided into solid polymer electrolytes and solid inorganic electrolytes [82]. Although solid polymer electrolytes provide

machinability and flexibility benefits for portable electronics, their poor ionic conductivity at ambient temperature necessitates operation at raised temperatures [177-180], which would exacerbate the side reactions between the polymer and the Li-O_2 battery's discharge products [181-183]. Diverse solid inorganic electrolytes have been extensively investigated for solid-state Li-O_2 batteries, such as perovskite-type, anti-perovskite-type, garnet-type, sodium superionic conductor (NASICON-type) and so on [168, 184-186]. These solid electrolytes are desirable due to their high shear modulus, good thermal/chemical stability, and high lithium-ion transference number, which enable them to inhibit Li dendrites, avoid short circuits and enhance discharge-charge performance [181, 187-191]. Among these solid inorganic electrolytes, NASICON-type electrolyte $Li_{1.5}Al_{0.5}Ge_{1.5}(PO_4)_3$ (LAGP) is considered as the most promising candidate for Li-O_2 batteries owing to its high ionic conductivity, wide electrochemical window, good mechanical strength, and especially the excellent chemical stability towards oxygen radicals in Li-O_2 cells [24, 95, 192-196]. However, the large interfacial resistance caused by insufficient solid-solid phase contact between electrolytes and electrodes is a tough issue for solid inorganic electrolytes - based Li-O_2 batteries [197-199]. The solid electrolyte and the electrode material could not be wettable, which makes them exhibit rigid contact and high interface resistance, inevitably leading to slow electrochemical dynamics and unexpected battery polarization [200-204]. Furthermore, the great challenge of LAGP solid electrolytes is that Ge^{4+} could be reduced when in direct contact with Li metal, probably leading to the formation of mixed ion-conducting interface and the deterioration of solid electrolytes [194, 195, 205, 206]. Thus, it is critical to attain both high ionic conductivity and excellent

interfacial contact between electrodes and electrolytes while employing NASICON-type solid inorganic electrolytes in Li-O_2 batteries [207, 208]. Inserting a Li^+ conductive interlayer made of a solid polymer electrolyte between the Li anode and LAGP could be a feasible solution to the aforementioned issues in Li-O_2 batteries [209-214]. Solid polymer electrolyte poly(ethylene glycol) methyl ether methacrylate (PEGMEM) can be synthesized by a simple solvent-free UV-cured method [215]. This polymer electrolyte exhibits a wide electrochemical window, excellent compatibility with metallic lithium, and good thermal stability. It is anticipated that PEGMEM polymer could be chosen as a buffer layer coating on the surface of LAGP to reduce the interfacial resistance and side reactions between the Li electrode and electrolyte.

In this work, a bilayer hybrid solid electrolyte consisting of an oxide solid inorganic electrolytes backbone and an organic SPE buffer layer is developed for high-performance Li-O_2 batteries. Poly(ethylene glycol) methyl ether methacrylate (PEGMEM) precursor was *in situ* UV-cured on the surface of solid inorganic electrolytes $Li_{1.5+x}Al_{0.5}Ge_{1.5}Si_xP_{3-x}O_{12}$ (LAGP-Si) pellet under UV light to produce an SPE interlayer, forming a bilayer hybrid electrolyte (PEGMEM@LAGP-Si). Herein, Si^{4+} with lower valence and larger diameter was used to replace part of P^{5+} in the pristine LAGP glass-ceramics to improve the lithium ionic conductivity. The introduction of PEGMEM was aimed to provide the improved interfacial contact and eliminate the side reactions between LAGP-Si and the Li anode. This hybrid electrolyte enables the enhanced the Li symmetric cell cycling stability, exhibiting narrower polarization voltage after near 1000 hours than pure LAGP-Si. Furthermore, solid-state Li-O_2 batteries employing

PEGMEM@LAGP-Si electrolytes deliver a high discharge-charge capacity of 7.3 mA h cm^{-2} and advanced cycling stability of 39 cycles with a limited capacity of 0.4 mA h cm^{-2} at a current density of 0.1 mA cm^{-2}. Given the advantages of a bilayer oxide-polymer structure, this strategy might pave the way for the development of solid-state Li-O_2 batteries with improved cycle life and stability.

4.2 Experimental

4.2.1 Preparation of LAGP-Si Glass-Ceramics

The NASICON-type solid electrolytes LAGP-Si were prepared by a melt-quench method in ambient air. Based on the stoichiometric amounts of $Li_{1.51}Al_{0.5}Ge_{1.5}Si_{0.01}P_{2.99}O_{12}$, a mixture of Li carbonate Li_2CO_3 (99.99%, Aladdin), aluminum hydroxide $Al(OH)_3$ (99.9%, Aladdin), germanium oxide GeO_2 (99.999%, Aladdin), ammonium dihydrogen phosphate $NH_4H_2PO_4$ (99%, Aladdin) and silicon dioxide (SiO_2) (99.9%, Aladdin) were first ball-milled for 4h at 400 rpm and then annealed at 700 ℃ for 2h to remove volatile gases. After that, the calcination products were ground again and heated up to 1400 ℃ to achieve homogeneous glass melt, which was subsequently quenched to obtain LAGP-Si glass. The obtained LAGP-Si glass powders were pressed in a mold with a diameter of 13 mm and further isostatic pressed at 200 MPa. These densified pellets were then annealed at 850 ℃ for 6 hours to achieve LAGP glass-ceramic samples.

4.2.2 Preparation of PEGMEM@LAGP-Si Electrolytes

To prepare the solid polymer buffer layer, poly(ethylene glycol) methyl ether methacrylate (M_w ~ 950, sigma-Aldrich) and lithium bistrifluoromethanesulfonimide salt (LiTFSI, sigma-Aldrich, 99.95%) were initially mixed based on the molar ratio of EO/Li^+=18:1 at ambient temperature in Ar glove box. After physical stirring, the Li salt would dissolve in a creamy mixture and a homogenous transparent solution was obtained. Then 0.1 wt.% of the 2, 2-dimethoxy-2-phenylacetophenone (DMPA, Sigma-Aldrich, 99%) was added to the solution as a photoinitiator and stirred for 12 hours until DMPA was completely dissolved. The polymer precursor solution was then laid flat on one side of the LAGP-Si pellet and exposed to the UV beam for 2 hours to conduct polymerization, achieving bilayer oxide-polymer electrolyte.

4.2.3 Sample Characterization

The surface and cross-sectional morphology and element distribution of the sample were characterized using a field emission scanning electron microscope (FESEM, Hitachi, S4800) together with an energy-dispersion spectrometer (EDS). The detailed crystallography of the sample was analyzed by transmission electron microscopy (TEM, FEI Tecnai G2 F20) and high-resolution transmission electron microscopy (HRTEM). The crystal structure of the synthesized electrolytes was studied by X-ray diffraction (XRD, D8 Advance Davinci, Bruker) using Cu K_α radiation of λ=1.5418 Å in a 2θ range of 10°-80°. Thermogravimetric studies (TGA) were carried out in an N_2 environment (Pyris Diamond). Fourier transform infrared spectroscopy (FT-IR, Nicolet 6700 spectrometer) was used to identify the chemical bonds in

the region of 2000-500 cm^{-1} at ambient temperature. The electrochemical impedance spectroscopy (EIS), direct current polarization (DC), and cyclic voltammetry (CV) were tested by Solartron 1470E multichannel potentiostat electrochemical workstation. The ionic conductivity was tested by EIS in the frequency ranging from 1 MHz to 0.1 Hz. The polished pellet samples were sputtered with gold on both sides as blocking electrodes for EIS test. The ionic conductivity (σ_t) is determined by the following equation: $\sigma_t = L/(R \cdot S)$, where L (cm), R (Ω) and S (cm^2) represent the thickness of the electrolyte, the total resistance value of the electrolyte, and the effective contacting area of blocking electrodes, respectively. The ionic conductivities of LAGP-Si pellet samples were measured from -20 to 120 ℃ and the activation energy was calculated according to the equation: $\sigma = A/T \exp(-E_a/RT)$, where A is the pre-exponential factor (-); T is the test temperature (K); R is the molar gas constant (8.314 J K^{-1} mol^{-1}); and E_a is the activation energy (kJ mol^{-1}) for Li^+ ion migration. The electrochemical window of the electrolyte was determined by CV of Li/electrolyte/Au at a scan rate of 0.5 mV s^{-1} at room temperature from -0.5 to 6 V (vs. Li/Li^+). Electronic conductivity (σ_e) was measured by DC polarization experiment. The sample of PEGMEM@LAGP-Si was inserted into two Au electrodes, and then apply a DC voltage. Then the lithium-ion transference number (t_{Li^+}) was calculated based on the equation: $t_{Li^+} = (\sigma_t - \sigma_e)/\sigma_t$.

4.2.4 Assembly and Testing of Solid-State Li-O_2 Cells

To prepare the porous oxygen cathode, Ketjen Black (KB, EC600JD, Lion) carbon powder (90 wt %) was mixed with polyvinylidene fluoride (PVDF) (10 wt %) binder in 1-methyl-2

pyrrolidone (NMP) solvent to make a paste. The slurry was then cast onto carbon paper, which was dried in a vacuum at 110 °C for 12 hours before the test cell was assembled, and the areal loading of KB materials was about 0.6 mg cm^{-2}. All Li-O_2 batteries were assembled in a glovebox in an argon atmosphere with water and oxygen contents of less than 0.1 ppm. The Li-O_2 battery was fabricated by inserting a PEGMEM@LAGP electrolyte between a KB cathode and a Li metal anode, and 20 μL of nonaqueous liquid electrolyte composed of 1 M LiTFSI and 0.05 M redox mediator (RM) Li bromide (LiBr) in tetraethylene glycol dimethyl ether (TEGDME) was added to infiltrate the cathode. Thus, a Li/PEGMEM@LAGP-Si/KB cell was obtained. After the solid-state Li-O_2 battery is installed in the cell, it was sealed up for 1 h and then pass a continuous flow of high purity O_2 through the cell for about 2 h.

The electrochemical performance of Li-O_2 cells was tested under a continuous oxygen supply system. Specific capacities and current densities were calculated according to the area of the cathode. Discharge and charge profiles of the assembled KB/PEGMEM@LAGP-Si/Li and KB/LAGP-Si/Li cells were tested under the voltage ranging from 2 to 4.5 V on a LAND-CT2001A testing system (Wuhan Jinnuo Elec-tronics, Ltd.) at room temperature. The differential electrochemical mass spectrometry (DEMS, QMG250M1, Pfeiffer) was employed to detect the volatile products in battery charging. The electrochemical flow cell was specially manufactured using the same components (anode, electrolyte, and cathode) mentioned above. Gas evolution during charging was continuously measured in flowing argon gas at a constant rate of 3 ml min^{-1}.

4.3 Results and Discussion

The schematic illustration for the synthesis of PEGMEM@LAGP-Si is illustrated in Figure 4-1a. Firstly, $Li_{1.5}Al_{0.5}Ge_{1.5}P_3O_{12}$ and $Li_{1.51}Al_{0.5}Ge_{1.5}Si_{0.01}P_{2.99}O_{12}$ glass-ceramic pellets were synthesized by a conventional melt-quench method in ambient air. As the pristine LAGP-based electrolytes would react with Li anode through direct contact, a polymer precursor poly(ethylene glycol) methyl ether methacrylate (PEGMEM) was subsequently coated on the one side of a LAGP-Si pellet and then UV-cured to generate a solid polymer electrolyte buffer layer. Such a buffer layer could alleviate Li dendrite and mitigate the reactivity between electrolyte and electrode, as shown in Figure 4-1b.

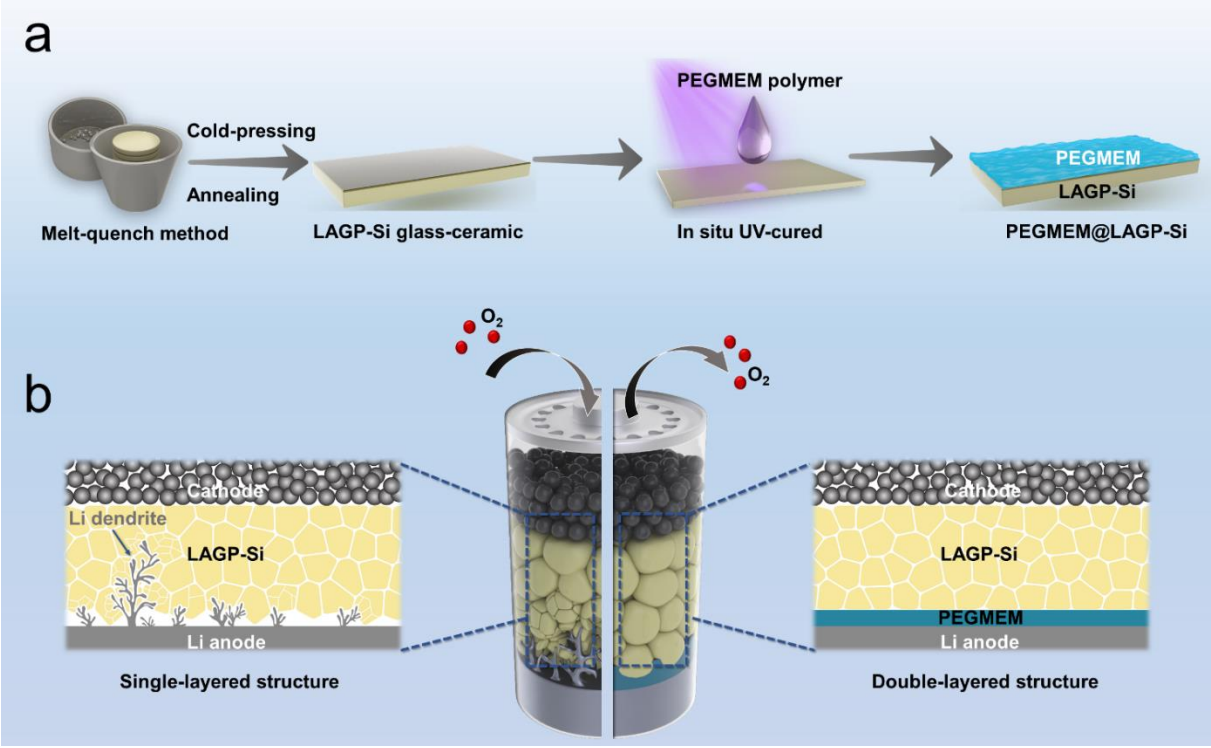

Figure 4-1 (a) Schematic illustration of preparing LAGP-Si electrolytes with a PEGMEM buffer layer. (b) Detailed schematic illustration of the Li-O_2 batteries before and after the modification with PEGMEM.

The structure and morphology of the as-prepared LAGP/LAGP-Si and PEGMEM@LAGP-Si were characterized by SEM and XRD. As shown in Figure 4-2a, both LAGP and LAGP-Si exhibit typical NASICON-type phase structure (PDF#41–0034), and no impurity phase were detected, which indicates that the Si doping would not affect the crystal structure of LAGP. Here, the $Li_{1.51}Al_{0.5}Ge_{1.5}Si_{0.01}P_{2.99}O_{12}$ (LAGP-Si) refers to the one with the optimal doping content. To further verify the Si doping effect, the cross-sectional morphologies of the LAGP and LAGP-Si pellets were investigated as shown in Figure 4-2b-d. The SEM-EDS mapping of LAGP-Si (Figure 4-2c) verified that all elements are uniformly distributed throughout the LAGP electrolyte, indicating the Si^{4+} has been successfully incorporated into the LAGP. In addition, LAGP-Si particles (Figure 4-2b) show more uniform size, clearer grain boundary and fewer cracks between different grains, resulting in better contact between grains and enhanced densification when compared to pure LAGP (Figure 4-2d). The size distribution of LAGP-Si sample (Figure 4-3) is corresponding to its SEM morphology. The compact structure within LAGP-Si can not only facilitate lithium-ion transport, but also inhibit the growth of lithium dendrites along the grain boundary. Moreover, as a consequence of the presence of higher lithium concentrations in solid phase, doping of Si could benefit the movement of lithium ions among lattice sites in NASICON structure, thereby increasing the ionic conductivity [216]. To check the crystalline state of LAGP-Si, the LAGP-Si electrolyte pellet was pulverized and investigated through TEM as shown in Figure 4-4, showing distinct lattice fringes and amorphous phases coexist. Interplanar spacing of the main phase in LAGP-Si is 0.417 nm, corresponding to the interplanar spacing of crystal plane (104) in standard $LiGe_2(PO_4)_3$. Figure

4-4c and d show diffused diffraction rings of LAGP-Si sample, verifying the existence of amorphous phases in LAGP-Si. Figure 4-2**e** shows the top-view SEM image of the PEGMEM@LAGP-Si. It can be seen that after coating on the LAGP-Si surface, a homogeneous organic buffer layer is formed on the LAGP-Si surface and shows similar morphology with that of the pure PEGMEM (Figure 4-5). In addition, the smooth and elastic character (the optical photograph of the pure PEGMEM is shown in Figure 4-6) are favorable for adequate contact with the electrode, thus ensuring lower interfacial impedance. The FT-IR spectra of solid polymer PEGMEM and PEGMEM precursors are shown in Figure 4-7. The C=C double bond peaks at roughly 1600-1650 cm^{-1} in monomer vanished, indicating that the PEGMEM monomer had completely cured into a solid polymer buffer layer [217]. Besides, thermogravimetric analysis (TGA) is performed to determine the thermal stability of the solid polymer PEGMEM in a nitrogen environment at temperatures ranging from 15 to 600 °C. As demonstrated in Figure 4-8, the PEGMEM is rather stable below 341 °C, while the decomposition of polymer or Li salts occurs at higher temperatures, suggesting its good thermal stability [218, 219]. Finally, the cross-sectional image (Figure 4-2f) of the PEGMEM@LAGP-Si indicates the thickness of the PEGMEM layer is about 25 μm, and it bonds tightly on the LAGP-Si, which can facilitate the lithium ions transport across the interface.

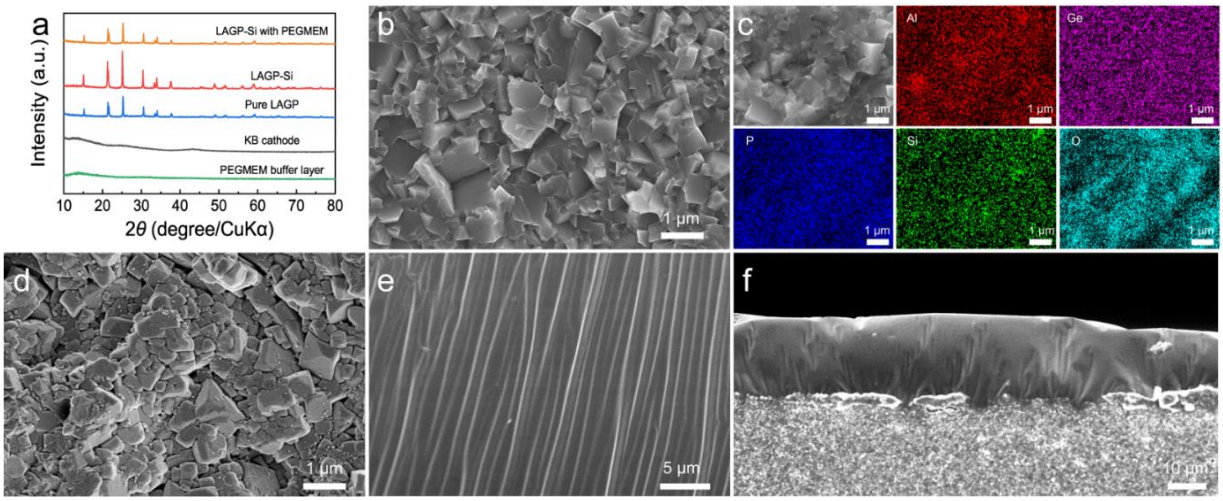

Figure 4-2 (a) XRD patterns of pure LAGP, LAGP-Si, PEGMEM@LAGP-Si, PEGMEM, and KB cathode. (b) Cross-sectional SEM image of LAGP-Si glass-ceramic pellet. (c) SEM and EDX images of LAGP-Si glass-ceramic pellet (d) Cross-sectional SEM image of pure LAGP. (e) Top-view SEM image of PEGMEM@LAGP-Si. (f) Cross sectional SEM image of the PEGMEM@LAGP-Si electrolyte.

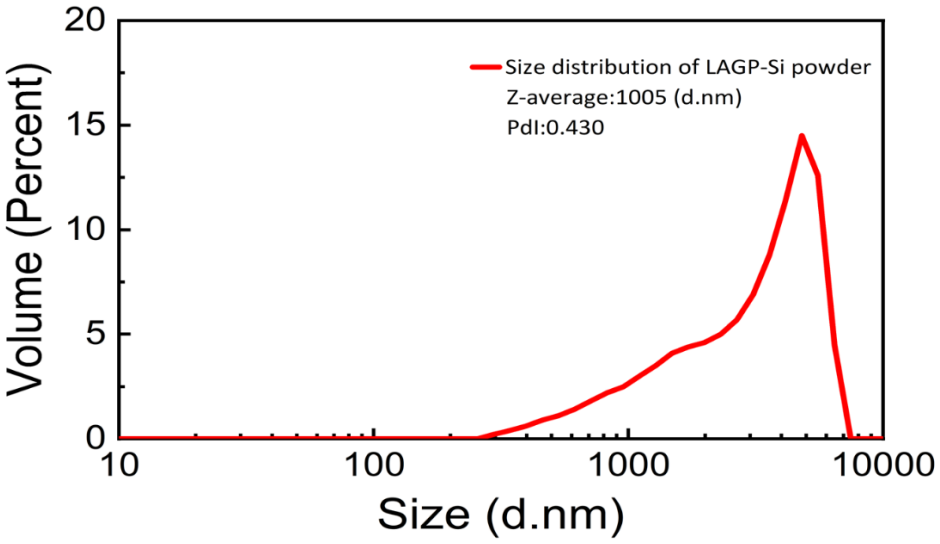

Figure 4-3 The size distribution of LAGP-Si sample.

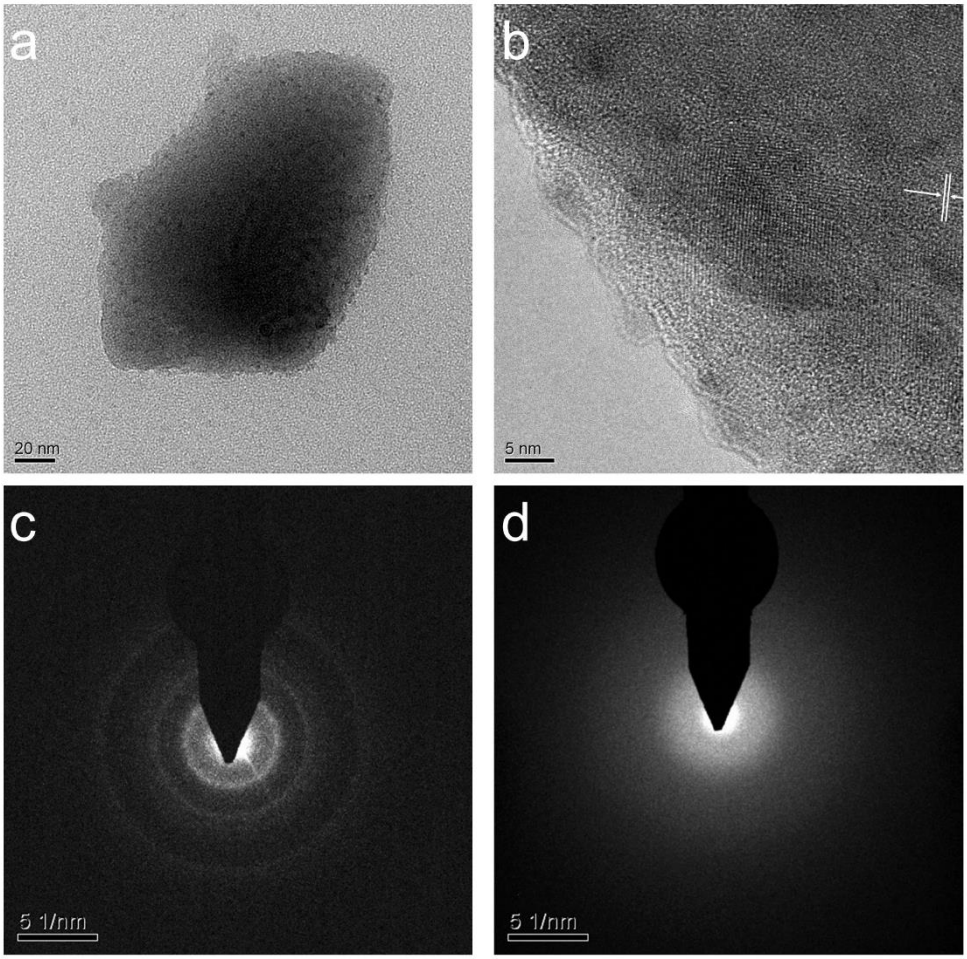

Figure 4-4 (a) TEM image of LAGP-Si glass-ceramic sample. (b) HRTEM image of LAGP-Si glass-ceramic sample. (c) and (d) corresponding SAED patterns of LAGP-Si glass-ceramic sample.

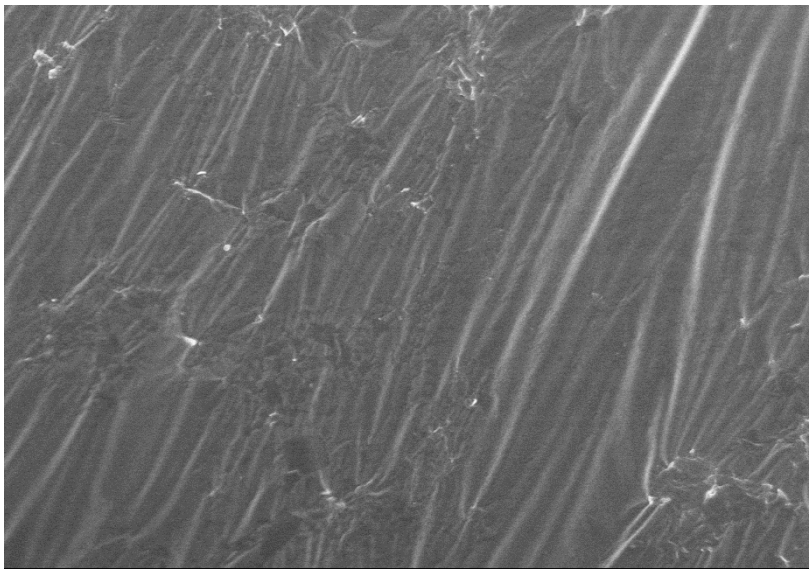

Figure 4-5 Top-view SEM image of pure PEGMEM layer.

Figure 4-6 The optical picture of pure PEGMEM polymer electrolyte.

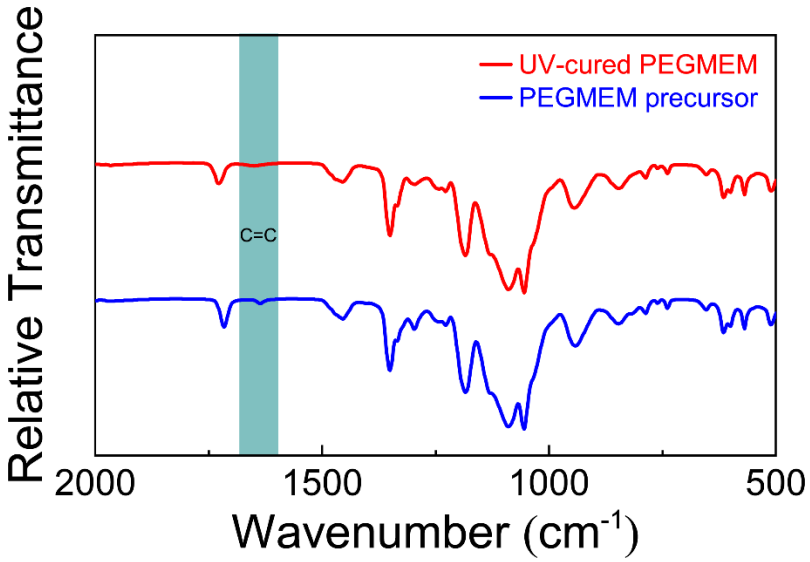

Figure 4-7 The FT-IR spectra of PEGMEM precursor and UV-cured PEGMEM.

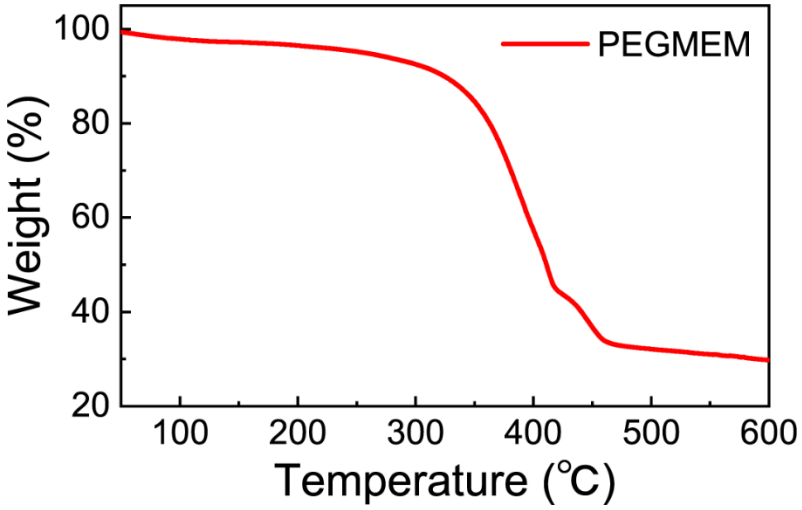

Figure 4-8 TGA curve of solid polymer PEGMEM.

The Nyquist plots of LAGP-Si and PEGMEM@LAGP-Si are measured as shown in Figure 4-11a, and the calculated ionic conductivities are 3.7×10^{-4} S cm^{-1} and 3.0×10^{-4} S cm^{-1} at room temperature, respectively. The experimental data collected in **Chapter 3** (Table 3-1) shows that

x = 0.01 for $Li_{1.5+x}Al_{0.5}Ge_{1.5}Si_xP_{3-x}O_{12}$ is the most appropriate Si-doping amount for the optimum conductivity in this work. After being coated with a polymer buffer layer, the bulk conductivity of the PEGMEM@LAGP-Si electrolyte at room temperature was 3.0×10^{-4} S cm^{-1}, which is comparable to that of the pure LAGP-Si. The temperature dependences of ionic conductivity for LAGP-Si and PEGMEM@LAGP-Si were measured every 20 ℃ from -20 to 100 ℃ as illustrated in Figure 4-11b. Both samples show good linear fitting results, obeying the Arrhenius relationship. The corresponding activation energy (E_a) is 0.371eV and o.374eV for LAGP-Si and PEGMEM@LAGP-Si, respectively. These results suggest that the introduction of PEGMEM would not substantially increase bulk resistance and activation energy of the LAGP-Si electrolyte. Nyquist plots of PEGMEM@LAGP-Si (Figure 4-9) and pure LAGP-Si electrolytes (Figure 4-10) at different temperatures are provided in supporting information.

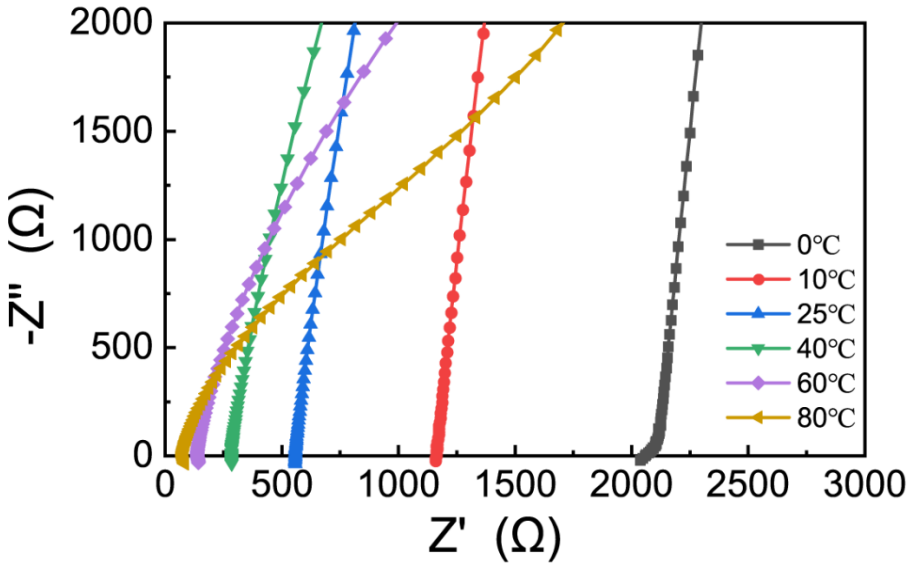

Figure 4-9 The Nyquist plots of LAGP-Si at different temperatures.

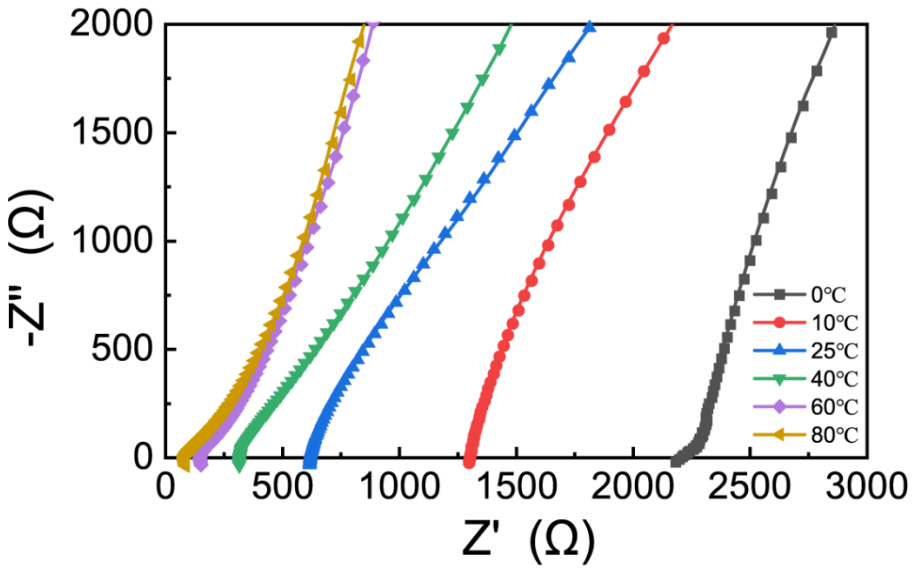

Figure 4-10 The Nyquist plots of PEGMEM@LAGP-Si at different temperatures.

Cyclic voltammetry (CV) was used to assess the electrochemical window of PEGMEM@LAGP-Si utilizing a Li/PEGMEM@LAGP-Si/Au battery in the voltage range of -0.5 V to 6 V at a scan rate of 0.5 mV s^{-1}. As shown in Figure 4-11c, there are two reversible peaks at around -0.5 V and 0.5 V, which are attributable to reversible Li plating and stripping. Up to 6 V, no obvious oxidation peak is found, showing that PEGMEM@LAGP-Si has exceptional electrochemical stability. The electronic conductivities of the PEGMEM@LAGP-Si are probed through direct current (DC) polarization measurement as shown in Figure 4-11d. The electronic conductivity is calculated to be 1.6 $\times$ 10^{-8} S cm^{-1} at ambient temperature, and the calculated Li ion transference number t_{Li^+} of PEGMEM@LAGP-Si is 0.99, which is close to 1 and higher than that of pure PEGMEM (0.252) [215]. This result reveals that the bilayer

PEGMEM@LAGP-Si could be regarded as a pure ionic conductor like conventional NASICON-type electrolytes by inhibiting the mobility of anions in polymer PEGMEM and only Li^+ ions participate in charge transfer.

The long-term compatibility and stability with lithium metal were investigated by constructing Li//Li symmetric battery. Figure 4-11e shows the voltage profiles cycling at a current density of 0.1 mA cm^{-2} and areal capacity of 0.05 mA h cm^{-2}. The Li/LAGP-Si/Li symmetric battery exhibited a large initial polarization voltage, and then the polarization voltage gradually increased in the following cycles, suggesting the continuously increased internal resistance during the stripping/plating process. In contrast, the Li/PEGMEM/LAGP-Si/PEGMEM/Li symmetric battery demonstrated lower polarization voltage and stable cyclic performance. The polarization voltage exhibits almost no change during 1000 hours cycling, indicating that the interfacial reaction between the LAGP-Si and lithium metal was greatly inhibited. In addition, EIS of the Li//Li symmetric cell with PEGMEM@LAGP-Si shows lower interfacial and total resistances than the cell with pure LAGP-Si after 100 hours of cycling, as shown in Figure 4-12. The PEGMEM@LAGP-Si solid electrolyte clearly outperforms the LAGP-Si electrolyte in terms of interfacial stability against Li anode. Clearly, PEGMEM@LAGP-Si can be regarded as an excellent choice for solid-state Li-O_2 batteries because of its strong ionic conductivity, wide electrochemical window, low electronic conductivity, and high Li-ion transference number.

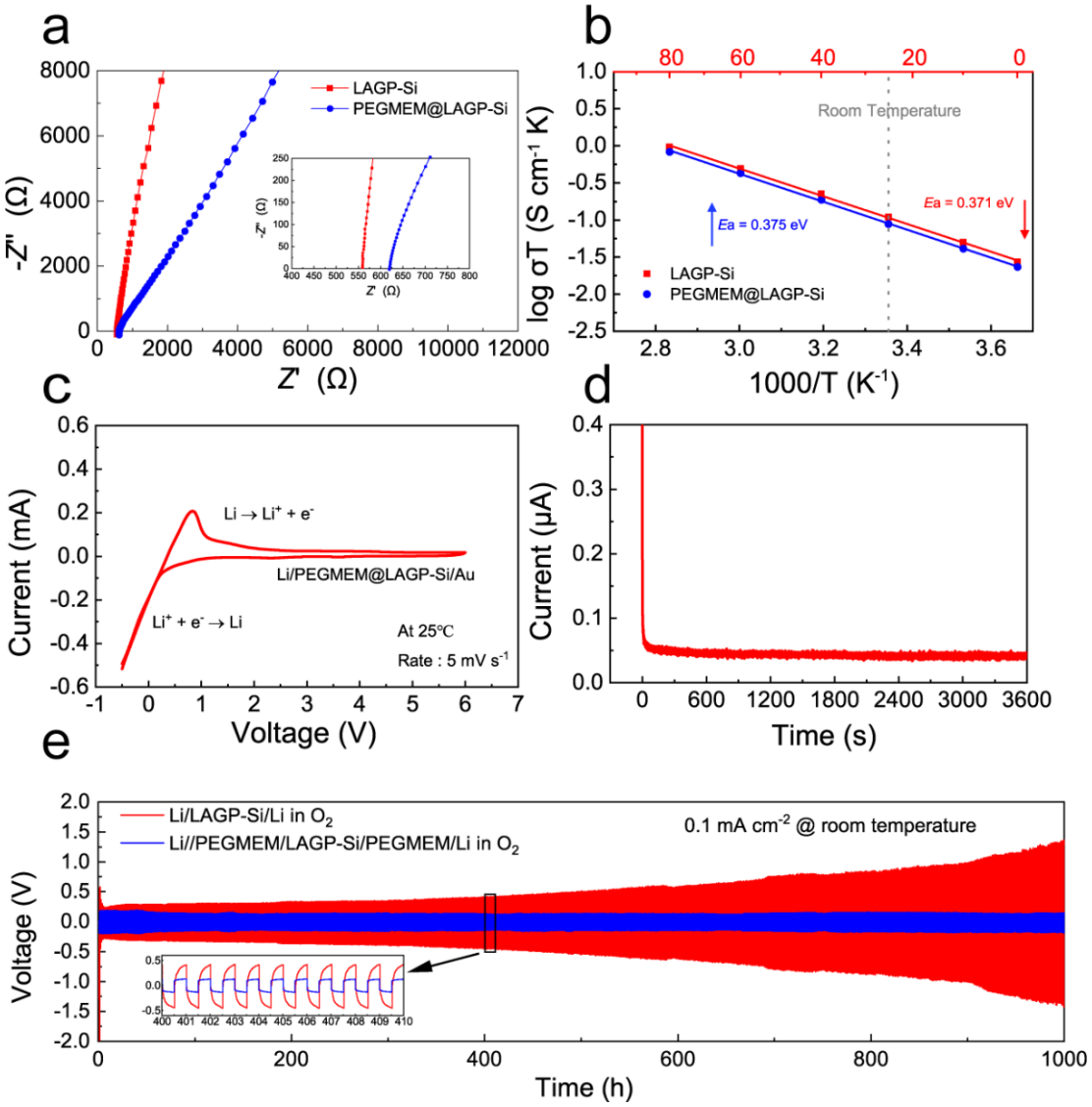

Figure 4-11 (a) The Nyquist plots of LAGP-Si and PEGMEM@LAGP-Si at room temperature. (b) Arrhenius plots of LAGP-Si and PEGMEM@LAGP-Si. (c) CV curve and (d) DC polarization curve of PEGMEM@LAGP-Si electrolyte. (e) Galvanostatic cycling of Li/LAGP-Si/Li and Li/PEGMEM/LAGP-Si/PEGMEM/Li symmetric batteries at a current density of 0.1 mA cm^{-2} at room temperature in the oxygen atmosphere.

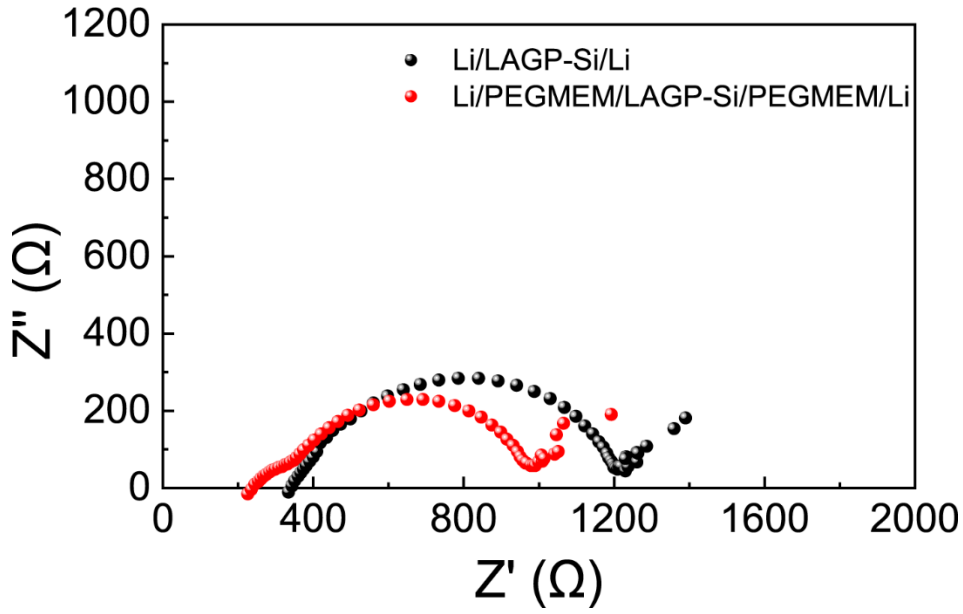

Figure 4-12 The impedance spectra of the Li symmetric battery with PEGMEM@LAGP-Si and pure LAGP-Si after 100 hours of cycling.

The electrochemical performances of the solid-sate Li-O_2 batteries employing LAGP-Si and PEGMEM@LAGP-Si electrolytes were investigated with a KB cathode and a Li anode. The schematic of the battery structure and the discharge/charge mechanism are illustrated in Figure 4-13a. The PEGMEM@LAGP-Si electrolyte was sandwiched between KB carbon cathode and Li anode. Here, nickel foam is adopted as a cathode host to accommodate the discharge products and prevent carbon paper from being crushed by the spring. Figure 4-13b presents the first galvanostatic discharge/charge profiles of solid-state batteries of Li-O_2 with LAGP-Si and PEGMEM@LAGP-Si at a current density of 0.05 mA cm^{-2} between 2.0 V and 4.5 V. The solid-state Li-O_2 battery with PEGMEM@LAGP-Si delivers a higher discharge specific capacity of 7.3 mA h cm^{-2} than the battery with pure LAGP-Si (3.3 mA h cm^{-2}). In addition, the morphology

of the discharge product is investigated by SEM as shown in Figure 4-14, which shows a typical toroidal shape, indicating the generation of Li_2O_2.

To further analyze the cyclic performance of the solid-state Li-O_2 batteries, the cells were discharged and charged ranging from 2.0 to 4.5 V under a current density of 0.1 mA cm^{-2}, with a limited capacity of 0.4 mA h cm^{-2}, and the corresponding gravimetric capacity is 666 mA h g^{-1}. Figure 4-13c demonstrates that the discharge curve of the PEGMEM@LAGP-Si assembled cell has a plateau of around 2.7 V. The charge curve climbed from 3.0 to 3.9 V and then gradually increased to around 4.3 V. This cell also exhibits a stable cyclic performance of 39 cycles, which outperforms the LAGP-Si assembled cell with only 12 stable cycles (Figure 4-13d) and pure PEGMEM-based cell with 10 stable cycles (Figure 4-15). Besides, the discharge plateau of Li-O_2 batteries using pure PEGMEM polymer is below the theoretical value of 2.7V and the voltage curve is fluctuating. Visually, Figure 4-13e shows the relationship between the charging capacity and the number of cycles for both batteries under the limiting capacity and the restricted voltage range conditions. Moreover, Figure 4-13f exhibits the median voltage of charging and discharging varies with the cycling number for both batteries. It could be clearly seen that the cell equipped with PEGMEM@LAGP-Si has a smaller overcharge potential and a more stable voltage variation during discharge-charge cycles, corresponding to the previous results of discharge-charge curves. The surface morphology of lithium anode after electrochemical cycling are also investigated by SEM imagines (Figure 4-16). After 10 cycles, the lithium surface with bilayer PEGMEM@LAGP electrolyte exhibits a relative flat surface

though some cracks were observed, (Figure 4-16b), while the lithium with LAGP-Si electrolyte exhibits a pulverization and rough surface (Figure 4-16c). Figure 4-17 shows that PEGMEM@LAGP-Si could stably cycle at a higher current density of 0.2 mA cm^{-2} with a restricted capacity of 0.4 mA h cm^{-2} for 10 cycles, which demonstrates the potential of Li-O_2 batteries assembled with this electrolyte also at high current densities. In the nutshell, PEGMEM@LAGP-Si has excellent interfacial contact, strong ionic conductivity, and superior electrochemical stability, which makes it an ideal electrolyte for solid-state Li-O_2 batteries.

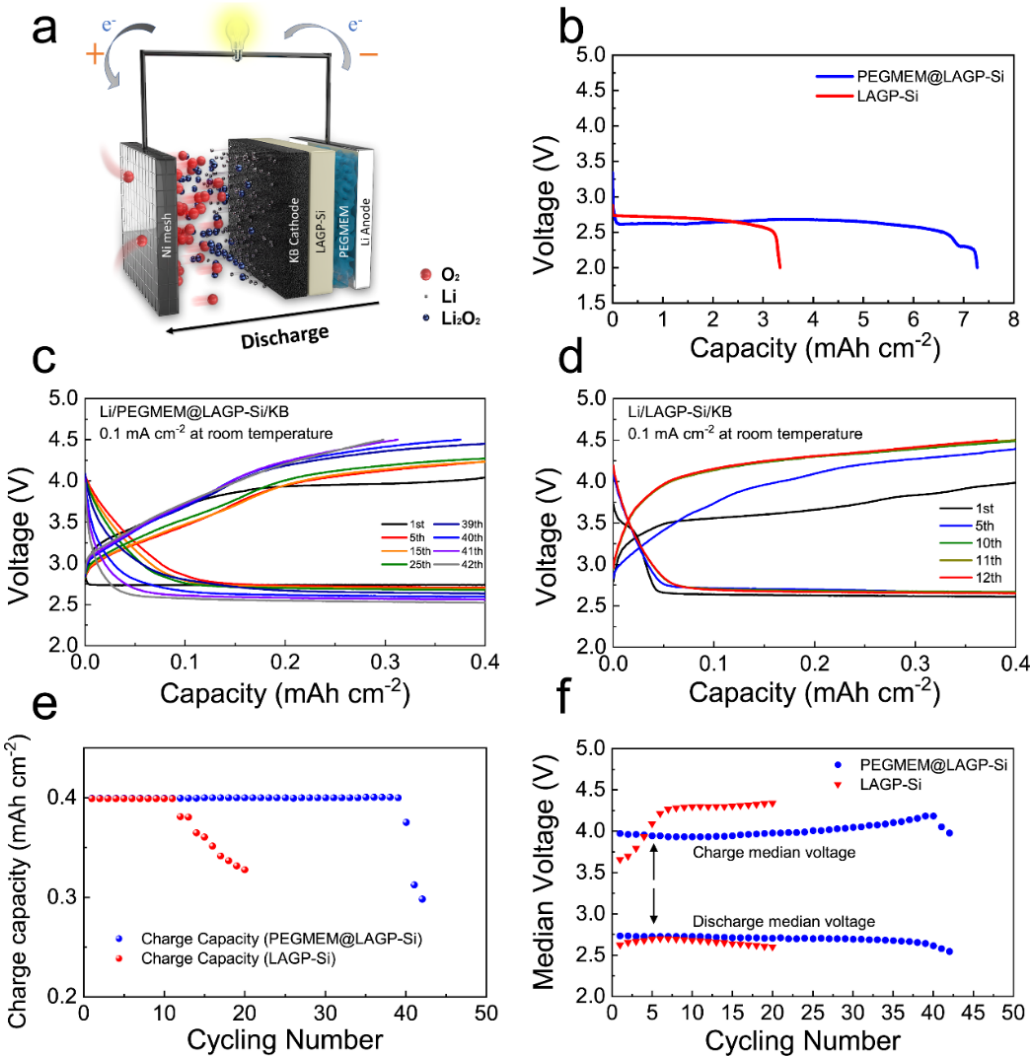

Figure 4-13 Battery performances of the solid-state Li-O_2 batteries. (a) Schematic diagram of

the solid-state Li-O_2 cell. (b) The first discharge profile of the Li−O_2 cell with LAGP-Si and PEGMEM@LAGP-Si measured within 2.0 to 4.5 V. Discharge-charge curves of the (c)PEGMEM@LAGP-Si-based battery and (d) LAGP-Si based battery under a capacity limitation of 0.4 mA h cm^{-2} at a current density of 0.1 mA cm^{-2}. (e) Charge capacity variation against cycling number. (f) Median voltages of the discharge-charge curves against cycling number.

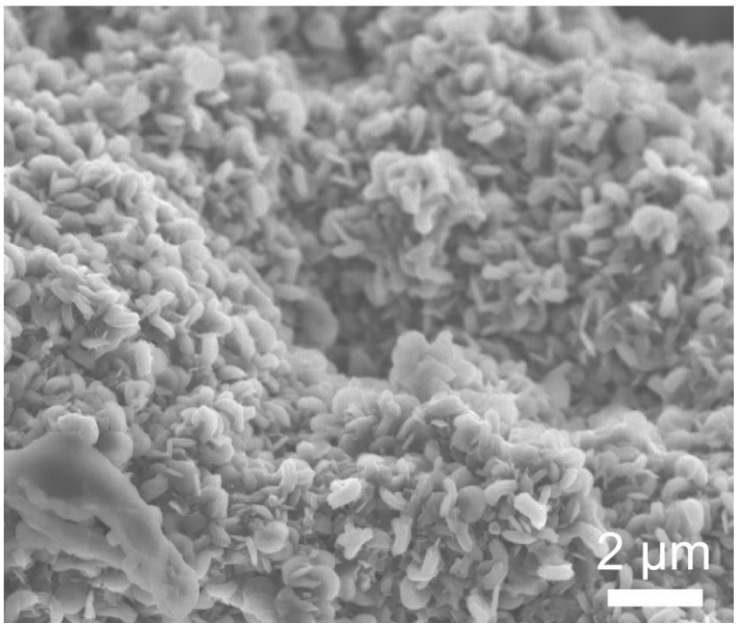

Figure 4-14 SEM image of the KB cathode after discharging.

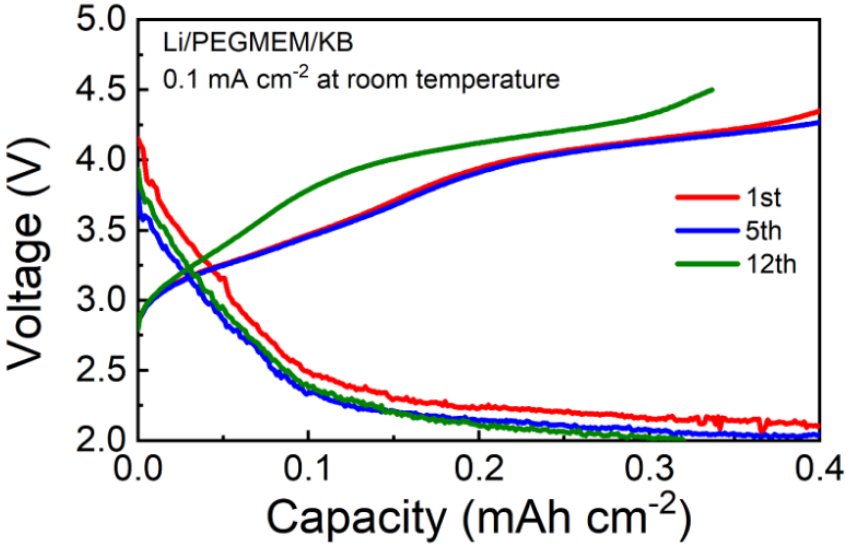

Figure 4-15 Discharge-charge curves of the pure PEGMEM-based battery under a capacity limitation of 0.4 mA h cm^{-2} at a current density of 0.1 mA cm^{-2}.

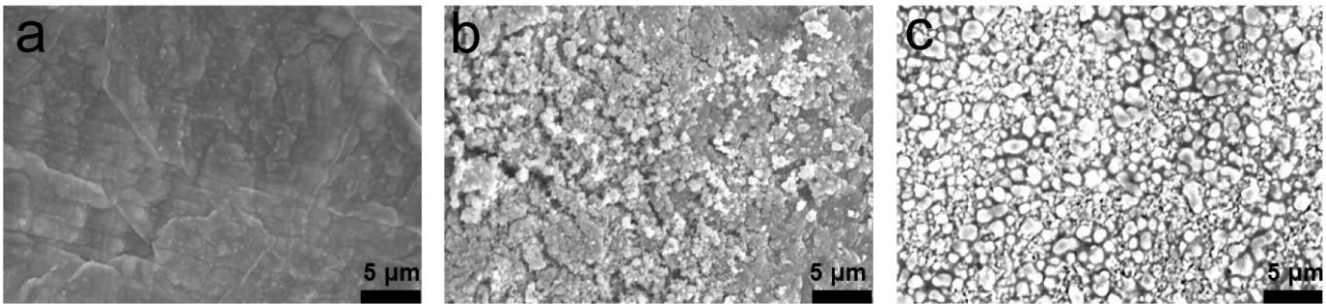

Figure 4-16 The SEM images of (a) pristine Li foil, (b) Li foil applied in PEGMEM@LAGP-Si-based Li-O_2 battery after 10 cycles and (c) Li foil applied in LAGP-Si-based Li-O_2 battery after 10 cycles.

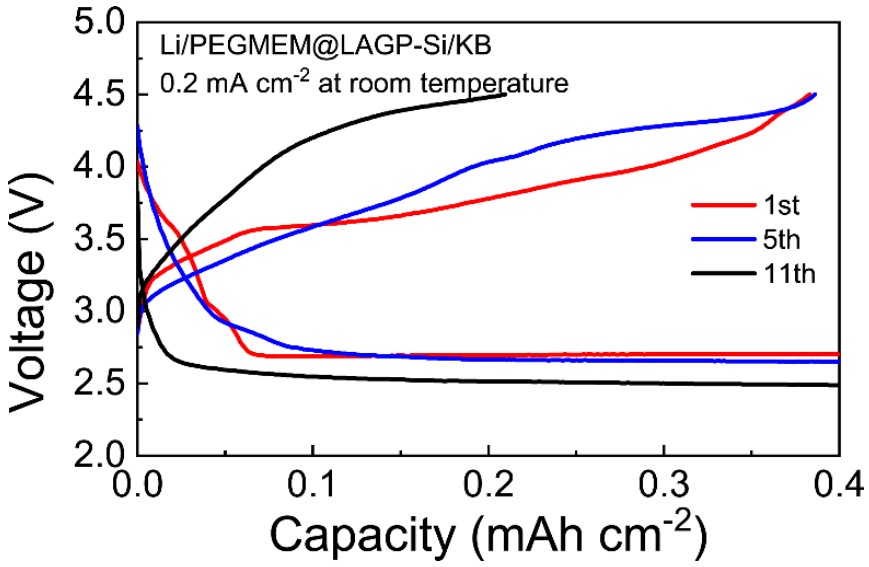

Figure 4-17 Discharge-charge curves of the PEGMEM@LAGP-Si-based battery under a capacity limitation of 0.4 mA h cm^{-2} at a current density of 0.2 mA cm^{-2}.

To further analyze the electrochemical reaction mechanism occurring on the cathode, *in situ* differential electrochemical mass spectrometry (DEMS) was conducted to evaluate the gas evolution during the charging process. The gas evolution by DEMS analysis in Figure 4-18b corresponds well to the three-stage charging process depicted in Figure 4-18a. During the initial stage of charging with very low overpotential, the Li_2O_2 on the surface undergoes spontaneous delithiation to $Li_{2-x}O_2$. In the second stage, Li_2O_2 decomposes to produce oxygen with increasing voltage.-During the final stage, the voltage continues to rise with the production of CO_2, which may be related to the decomposition of Li_2CO_3 [123, 220]. Significantly, more O_2 was created after 0.05 mA h cm^{-2} than the initial stage, which might be attributed to the partially degradation of Li_2O_2 to LiO_2-like species during the early stage of the charging process [221, 222]. Compared to the DEMS results of conventional liquid Li-O_2 batteries, this solid-state Li-

O_2 batteries present less side products such as CO_2, CO, and organic gases during the charge process, which means less side reactions occurring by the use of this solid bilayer electrolyte [123]. At roughly 4.6 V, the O_2 evolution rapidly decreased, indicating that the Li_2O_2 had been dissolved completely and the battery was fully recharged. The integral calculation of the curve in Figure 4-18b gives the amount of gas generated during the charging process. Also, the number of electrons transferred during the charging process can be calculated from the charging capacity. Consequently, the conversion ratio of e^-/O_2 is calculated to be 2.14, which is a little higher than 2, indicating that the Li_2O_2/O_2 conversion is inferred to be the predominant reaction during the charging. These results demonstrate that the reaction mechanism during charging of solid-state Li-O_2 batteries using PEGMEM@LAGP-Si electrolyte could be considered basically consistent to the theoretical reaction: $Li_2O_2 \rightarrow 2Li^+ + O_2 + 2e^-$.

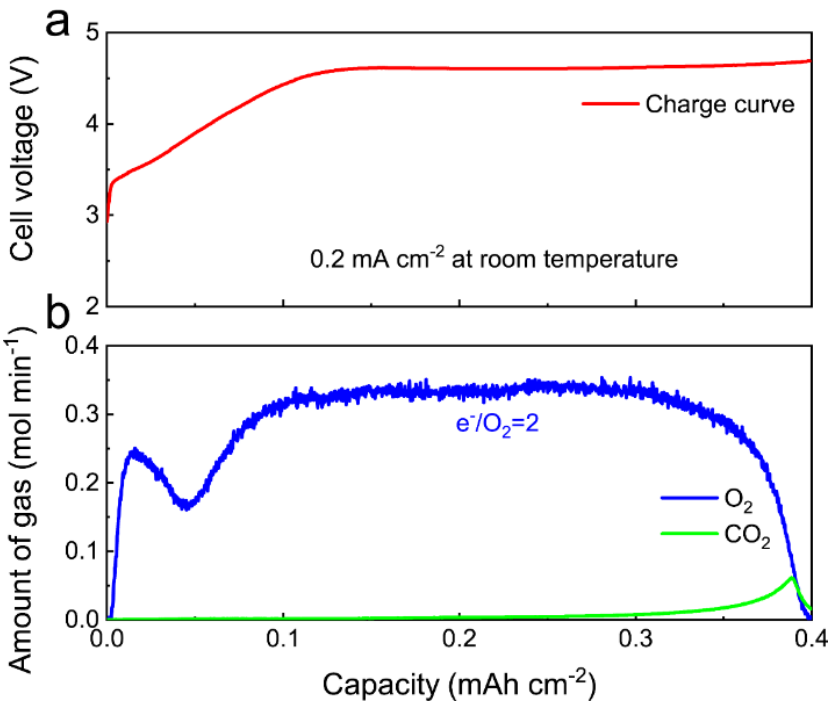

Figure 4-18 (a) The charge curve of the Li/PEGMEM@LAGP-Si/KB battery at a current

density of 0.2 mA cm^{-2} with a limited capacity of 0.4 mA h cm^{-2} at room temperature. (b) Gas evolution measured by DEMS upon charging process in the Li/PEGMEM@LAGP-Si/KB battery.

4.4 Conclusion

In this chapter, a bilayer hybrid solid electrolyte by combining Si doped LAGP with PEGMEM buffer layer is fabricated for high-performance solid-state Li-O_2 batteries. The solid inorganic electrolyte LAGP-Si was synthesized by a melt-quench method and the solid polymer buffer layer PEGMEM was *in situ* UV-cured on the one side of the LAGP-Si pellet towards the Li anode. The doping of Si^{4+} in glass-ceramic LAGP effectively improved the lithium-ion conductivity of NASICON-type electrolytes. The introduction of polymer PEGMEM buffer layer successfully enhanced the interfacial contact and reduced the side reactions between electrolyte and Li metal, leading to improved cycling stability of the Li//Li symmetric battery for 1000 h. The solid-state Li-O_2 battery employing PEGMEM@LAGP-Si delivered a larger capacity of 7.3 mA h cm^{-2} for the initial discharging process. Moreover, this battery exhibited a longer cycling performance of 39 cycles with a limited capacity of 0.4 mA h cm^{-2}, while the Li-O_2 battery employing pure LAGP-Si only shows 12 cycles. In addition, the mechanism of electrochemical reactions in the charging process of batteries was confirmed by DEMS, corresponding to the reaction $Li_2O_2 \rightleftarrows 2Li^+ + O_2 + 2e^-$. This work reveals that the application of a high-performance oxide solid inorganic electrolyte with a suitable solid polymer for interfacial modification is an efficient approach for next-generation stable solid-state Li-O_2 batteries.

Chapter 5 Garnet-Based Integrated Architecture for High-Performance All-Solid-State Lithium-Oxygen Batteries

Adapted and rewritten from the published article:

Z. Gu, X. Xin, Z. Xu, J. He, J. Wu, Y. Sun and X. Yao, *Garnet Electrolyte-Based Integrated Architecture for High-Performance All-Solid-State Lithium-Oxygen Batteries.* Advanced Functional Materials, 2023. DOI: 10.1002/adfm.202301583.

Abstract

All-solid-state lithium-oxygen (Li-O_2) battery is considered to be a promising next-generation energy storage system to address the issues related to low specific capacity, unsafety and unstable electrochemistry that exist in conventional liquid Li-O_2 batteries. However, current solid-state Li-O_2 batteries still encounter the challenge of high impedance at the electrode/electrolyte interface. In addition, the deficiency of triple-phase boundaries (Li^+, e^- and O_2) limits the active sites for electrochemical reaction in the battery cathode. Herein, we develop an integrated architecture based on garnet electrolyte $Li_{6.4}La_3Zr_{1.4}Ta_{0.6}O_{12}$ (LLZTO) and porous composite cathode for high-performance all-solid-state Li-O_2 batteries. The unique internal structure effectively reduces the interfacial impedance of the battery, provides a large number of active sites at triple-phase boundaries and increases the electrochemical stability. As a result, the obtained batteries can deliver a superior high full discharge capacity of 13.04 mA h cm^{-2} and an excellent cyclic performance (86 cycles). In addition, X-ray photoelectron spectroscopy, differential electrochemical mass spectrometry and theoretical calculations further demonstrate the effectiveness of this design in enhancing the interfacial performance, electrochemical performance, and stability of the battery. This work is thus expected to facilitate practical applications for truly all-solid-state Li-O_2 batteries, and even for other systems of metal-oxygen (air) batteries.

5.1 Introduction

In the work of **Chapter 4**, a polymer and NASICON based bilayer electrolyte was successfully prepared for use in a quasi-solid-state lithium-oxygen battery. However, the use of conventional organic liquid electrolytes in aprotic Li-O_2 batteries and quasi-solid-state batteries greatly restricts the safety and electrochemical stability. First, one of the key challenges is the high overpotential during the charging process will induce side reactions and ultimately lead to low round-trip efficiency and poor cycling stability. Furthermore, the intermediate products such as O_2^- and LiO_2 formed during the discharge would attack the organic electrolyte, leading to the further deterioration of the electrochemical performance [223-225]. Second, the generated byproducts including insoluble and insulating carbonates would cover the surface of the main discharging product Li_2O_2, resulting in reduced electron conduction and elevated overpotential. Third, lithium dendrites would grow and potentially puncture the electrolyte separator during the battery cycling process, leading to short-circuiting, and thereby causing combustion or explosion [173-176, 226]. To alleviate the above problems, researchers proposed the completely substitution of the liquid organic electrolytes by the solid electrolytes [149, 227]. Solid electrolytes are nonflammable, thermally stable, and chemically stable, which could avoid the loss and decomposition of liquid electrolytes in an open system [95]. Simultaneously, they are capable of preventing the lithium electrode from corrosion by blocking moisture or O_2 in the open systems and their high mechanical strength could mitigate short-circuit accidents aroused by lithium dendrites [82, 228].

The common solid electrolytes are mainly categorized into polymers, sulfides, and oxides [9]. Among all solid electrolyte types, oxide electrolytes are regarded as the most suitable electrolytes for Li-O_2 batteries, attributed to their high chemical and electrochemical stability in an oxygen atmosphere [30, 95, 99, 152, 165, 168, 183, 194, 229, 230]. Especially, garnet electrolytes contain both comparably high ionic conductivity and stability to the lithium, thereby receiving the most attention. $Li_7La_3Zr_2O_{12}$ (LLZO) ceramic is a widely investigated high-performance garnet-type electrolyte that applies to solid-state Li-O_2 batteries [231-233]. However, the rigid LLZO electrolyte has poor interfacial contact with both the cathode and anode, leading to a large interfacial impedance in Li-O_2 batteries [234-237]. For the electrolyte/anode interface, an interlayer prepared from lithiophilic materials is usually inserted to mitigate the interfacial resistance [238, 239]. In last chapter, a polymer buffer layer consisting of lithiophilic poly(ethylene glycol) methyl ether methacrylate (PEGMEM) was sandwiched at the electrolyte-anode interface, which effectively enhance the anode interface stability and interfacial compact [240]. However, for the cathode, the situation is more complicated. Due to the large size of the solid electrolyte particles, it is difficult to guarantee adequate contact between the solid electrolyte and the conductive agent. The insufficient solid-solid contact between the electrolyte and conductive agent in the cathode restricts ion transport and electronic conduction. Different from other solid-state battery systems, Li-O_2 batteries cannot utilize the method of applying internal stack pressure in the battery to promote the electrolyte/electrode interface contact due to the requirement for the diffusion of active gaseous substances [241, 242]. Therefore, in many studies, a small amount of liquid organic electrolyte was usually added

to the cathode to facilitate interfacial contact and promote ion transport, but this cannot completely avoid the aforementioned negative effects induced by the liquid electrolyte [243-245]. As a result, continuous efforts are needed to design more advanced air electrodes and battery structures to improve the electrochemical performance of Li-O_2 batteries.

In solid-state Li-O_2 batteries, multiple factors determine battery performance. First, the cathode layer and electrolyte layer must be in close contact to ensure low interfacial impedance. Second, inside the cathode, the electrolyte and the conductive agent require sufficient contact to ensure rapid ion and electron transport. Third, the flowing air and electronic/ionic conductors must be interfaced (sufficient porosity is required) to supply oxygen diffusion and accommodate more discharge products [187, 242, 246-248]. Therefore, a large number of triple-phase boundaries (accommodating O_2, Li^+ and electrons) are expected to be constructed to serve as active sites for electrochemical reactions in Li-O_2 batteries [241]. There have also been numerous attempts to achieve a truly all-solid-state Li-O_2 battery. Yu et al. reported an integrated zeolite-based solid-state Li-air battery by chemical vapor deposition (CVD) and seed-assisted growth method. The ingenious design ensures rapid transport of electrons/ions, as well as oxygen supply [98]. More importantly, the integrated structure reduced the interfacial resistance greatly compared with that of the non-integrated batteries. However, the preparation method of composite cathode with integrated electrolyte/cathode structure still needs to be simplified for large-scale practical applications.

In this work, a facile and scalable strategy to prepare an integrated cathode for an all-solid-state Li-O_2 battery is presented. The schematic illustration of the integrated all-solid-state Li-O_2 battery is shown in Figure 5-1. To promote the rapid migration of the lithium ions, electrons and oxygen, LLZTO electrolyte and single-walled carbon nanotubes were mixed homogeneously by high-energy ball milling. Then the composite cathode was deposited on the electrolyte pellet by liquid phase method combined with low-temperature annealing. After low-temperature annealing, an integrated cathode/electrolyte interface is successfully obtained, resulting in low interfacial impedance. In addition, the interior of the composite cathode is rich in porous structure, which can provide enough space for the growth of discharge products and the diffusion of flowing oxygen. To improve the anode interface stability and contact, the lithiophilic poly(ethylene glycol) methyl ether methacrylate (PEGMEM) was sandwiched as the buffer layer. Thanks to the unique structure, the integrated all-solid-state Li-O_2 battery exhibit enhanced electrochemical properties. It delivers excellent first discharge capacity and outstanding cyclic performance. In addition, compared with Li-O_2 batteries containing a non-integrated cathode and LLZTO-free cathode, the all-solid-state batteries exhibit reduced interfacial resistance and more stable electrochemical reactions. XPS analysis, DEMS testing and DFT calculations are further exploited to verify the effectiveness of this structural engineering strategy.

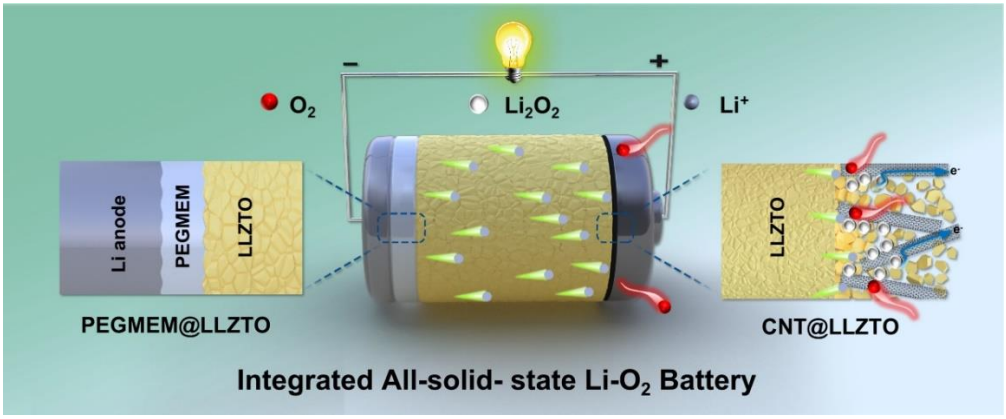

Figure 5-1 Schematic illustration of the integrated all-solid-state Li-O_2 batteries.

5.2 Experimental

5.2.1 Synthesis of LLZTO Ceramic Electrolytes

LLZTO with nominal compositions of $Li_{6.4}La_3Zr_{1.4}Ta_{0.6}O_{12}$ were prepared by the conventional solid-phase method. The stoichiometric amount of precursor, including Li_2CO_3 (99.9%, Aladdin, 15 wt.% excess was added to compensate for the loss of lithium during sintering at high temperature), La_2O_3 (99.99%, Aladdin, pre-sintered at 900 ℃ for 12 h), ZrO_2 (99.99%, Aladdin) and Ta_2O_5 (Aladdin 99.99%) was mixed and ball-milled at 400 rpm utilizing Zirconia balls in isopropanol for 6 h. After the evaporation of solvents, the powders were annealed at 900℃ for 12 h in the tube furnace under a pure oxygen environment and then cooled down to room temperature. The one-third of obtained powders were collected and stored as mother powder. The rest of the powders was ball-milled again for another 6 h using zirconia balls in isopropanol. After drying in an air blower oven, the powders were ground with adhesive and cold-pressed into pellets under isostatic pressure of 200 MPa). Then the pellets were sintered at

700 ℃ in the atmosphere of pure oxygen to remove the adhesive. The as-obtained pellets were covered with the mother powder prepared before to reduce possible lithium loss and annealed in a magnesium oxide crucible at 1200 ℃ for 15 h, respectively.

5.2.2 Preparation of Cathode and Buffer Layer

To prepare the composite oxygen cathode CNT@LLZTO, 20 wt% of single-walled carbon nanotubes (SWCNTs, Aladdin) was firstly mixed with 80 wt% of LLZTO mother powder particles described above and then ball-milled under 400 rpm for 2 h. The obtained mixed particles were dispersed into the binder containing 3 wt% of polyvinylidene fluoride (PVDF) in 1-methyl-2 pyrrolidone (NMP) solvent to make a slurry. The slurry was homogeneously cast onto one side of the polished LLZTO pellet and then was dried in a vacuum oven at 110 °C for 12 h. After that, the LLZTO pellet with CNT@LLZTO cathode was low temperature annealed at 400 ℃ for 15 min. The areal loading of cathode material was approximately 0.6 mg cm^{-2}. For comparison, the non-integrated carbon paper-based cathode (CP-CNT@LLZTO) was prepared by coating the CNT@LLZTO cathode on a carbon paper and infiltrated in a liquid electrolyte composed of 1 M LiTFSI in tetraethylene glycol dimethyl ether (TEGDME). In addition, the LLZTO-free SWCNT cathode was also *in situ* coated on the LLZTO electrolyte pellet as a comparison sample.

The poly(ethylene glycol) methyl ether methacrylate (M_w ~ 480, Sigma-Aldrich) and lithium bistrifluoromethanesulfonimide salt (LiTFSI, sigma-Aldrich, 99.95%) were initially mixed

based on the molar ratio of EO/Li^+=18:1 at ambient temperature in an argon glovebox to prepare the solid polymer precursor. After physical stirring, the Li salt would dissolve in the polymer precursor and a homogenous transparent solution was obtained. Then 0.1 wt.% of the dibenzoyl peroxide (BPO, Aladdin, 99%) was added to the solution as an initiator and stirred for 6 h until BPO was completely dissolved. The polymer precursor solution was then laid flat on the other side of the LLZTO pellet and placed in an oven under 70 ℃ for 12 h to realize *in situ* polymerization by heat curing, eventually achieving bilayer garnet-polymer electrolyte with an integrated cathode.

5.2.3 Material Characterization

The as-prepared LLZTO-based electrolytes were characterized by X-ray diffraction (XRD, D8 Advance DaVinci, Bruker) with Cu $K\alpha$ radiation of λ = 1.5418 Å at room temperature in 2θ range from 10 to 80° with a step of 0.025° to confirm the phase formation. The morphology and elemental distribution of the sintered electrolyte pellets were characterized by scanning electron microscope (SEM, FEI Quanta FEG 250). The detailed crystallography and morphology of samples were analyzed by transmission electron microscopy (TEM, FEI Tecnai G2 F20) and high-resolution transmission electron microscopy (HRTEM). The differential electrochemical mass spectrometry (DEMS, QMG250M1, Pfeiffer) was employed to detect the gas evolution rate in battery charging. The amount of gas generated and the number of charges transferred during the charging process can be calculated by the computational fit. X-ray photoelectron spectroscopy (XPS, Axis UltraDLD, Kratos) was performed to investigate the

elemental composition of discharge products on the cathode.

5.2.4 Electrochemical Measurement

The electrochemical performance of electrolytes was tested on Solartron 1470E multichannel potentiostat electrochemical workstation. The ionic conductivity was tested by electrochemical impedance spectroscopy (EIS) in a frequency ranging from 1 MHz to 10 Hz. The polished LLZTO pellet with PEGMEM layer was sputtered with gold on both sides as blocking electrodes for the EIS test from -10 to 80 ℃. The ionic conductivity (σ_t) is determined by the following equation of $\sigma_t = L/(R \cdot S)$, where L (cm), R (Ω) and S (cm^2) represent the thickness of the electrolyte, the total resistance value of the electrolyte, and the effective contacting area of blocking electrodes, respectively. the activation energy was calculated according to the equation of $\sigma = A/T \exp(-E_a/RT)$, where A is the pre-exponential factor (-); T is the test temperature (K); R is the molar gas constant (8.314 J K^{-1} mol^{-1}); and E_a is the activation energy for Li-ion migration (kJ mol^{-1}). The electrochemical window of the electrolyte was determined by the CV of Li/electrolyte/Au at a scan rate of 5 mV s^{-1} from -0.5 to 6 V (vs. Li/Li^+). Electronic conductivity (σ_e) was measured by a direct current (DC) polarization experiment. The lithium-ion transference number (t_{Li^+}) was then calculated based on the equation of $t_{Li^+} = (\sigma_t - \sigma_e)/\sigma_t$.

All batteries were assembled in a glovebox in an argon atmosphere with water and oxygen contents of less than 0.1 ppm. The all-solid-state Li-O_2 battery was fabricated by inserting an

integrated electrolyte pellet coated with a CNT@LLZTO cathode and PEMEM buffer layer between a nickel foam current collector and a lithium metal anode. After the battery was assembled in a cell mold, it was sealed up for 1 hour and then pass a continuous flow of high-purity O_2 through the cell for 2 h. The electrochemical performance of all Li-O_2 cells was tested under a continuous oxygen supply system. Specific capacities and current densities were calculated according to the area of the cathode. Discharge and charge profiles of all the assembled LLZTO-based Li-O_2 batteries were tested in the voltage range of 2-4.5 V under room temperature in a pure oxygen atmosphere on a LAND-CT2001A testing system (Wuhan Jinnuo Electronics, Ltd.).

5.2.5 Computational Details

Density functional theory (DFT) calculations were conducted using the projector augmented wave method implemented in the Vienna Ab-initio Simulation Package (VASP) [249]to investigate the variation in free energy during the Li-O2 reaction on the surfaces of LLZTO and SWCNT. The Perdew-Burke-Ernzerhof (PBE) parameterized generalized gradient approximation (GGA) functional [250] was employed to describe the exchange-correlation potential. PBE is a popular exchange-correlation functional widely used in DFT calculations. It was developed by Perdew, Burke, and Ernzerhof to improve the accuracy of earlier functionals by incorporating a more refined description of the electronic density gradient. This functional has been extensively applied in various research fields, including materials science, chemistry, and physics, due to its ability to provide reasonably accurate results while maintaining

computational efficiency. However, it's important to note that the choice of exchange-correlation functional should be carefully considered depending on the specific system and phenomena of interest, as no single functional is universally accurate for all cases. The geometry structures were fully relaxed until the energy and Hellmann-Feynman force on each atom converged to values below 10^{-5} eV $atom^{-1}$ and 0.01 eV $Å^{-1}$, respectively. An energy cutoff of 600 eV was applied. For the LLZTO and SWCNT surfaces, a 3 x 3 and 5 x 5 supercell, respectively, were employed, and an 18 Å vacuum region along the z-direction was included to eliminate interactions between periodic cells. To account for the long-range interactions, the density functional theory with dispersion correction version 3 (DFT-D3) method was employed to supplement the description provided by the PBE generalized function [251]. DFT-D3 is a method that incorporates dispersion interactions into DFT calculations. It improves the accuracy of predictions for non-covalent interactions by accounting for van der Waals forces. DFT-D3 is widely used in chemistry, materials science, and biology to study systems with significant dispersion interactions. It helps provide more reliable results for large molecular systems and weakly bonded molecules.

5.3 Results and Discussion

Figure 5-2 schematically illustrates the fabrication process of the integrated all-solid-state Li-O_2 battery. Firstly, LLZTO electrolyte powders were synthesized by a conventional solid-state method under an oxygen atmosphere, and the corresponding ceramic pellet was obtained by cold pressing and subsequent annealing. To realize the intimate contact between the LLZTO

and SWCNT, LLZTO powder is pre-grinded and then mixed with SWCNT by high-energy ball milling to obtain the homogeneous CNT@LLZTO composite cathode. Afterward, the cathode was cast on one side of the electrolyte pellet by a liquid method using NMP as solvent. After solvent removal and low-temperature annealing, an integrated electrolyte-cathode architecture was successfully achieved. Finally, a solid PEGMEM polymer buffer layer was *in situ* polymerized on the other side of the LLZTO pellet to improve anode interface contact.

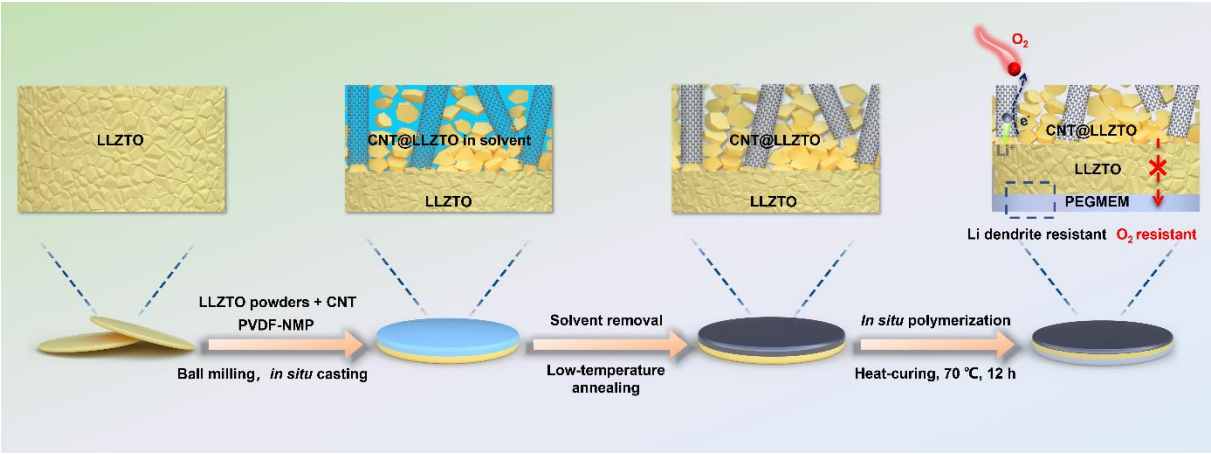

Figure 5-2 Schematic illustration of preparing integrated structure composed of LLZTO electrolyte with CNT@LLZTO cathode and PEGMEM buffer layer.

The surface and interior structure of the integrated Li-O_2 battery was investigated by SEM and TEM. Figure 5-3a and b illustrate the surface and cross-sectional image of the LLZTO pellet. It can be seen in Figure 5-3a that the surface of the LLZTO pellet is flat and smooth, which is beneficial to construct a tight electrolyte/electrode interface. The cross-sectional image (Figure 5-3b) exhibits that the electrolyte particles are packed tightly in the interior of the electrolyte and almost no cracks were observed. The compact structure is not only conducive to the

transport of lithium ions but also can resist the diffusion of oxygen and water from cathode to anode. The component and crystallinity of the electrolyte were further verified by examining the pulverized pellet. As shown in Figure 5-4, the XRD pattern of the electrolyte shows a typical cubic garnet structure (PDF#80-0457) and all the peaks indexed well, no impurity was detected. Moreover, the high-resolution TEM and selected area electron diffraction (Figure 5-5) further demonstrated the LLZTO is a pure phase and well crystallized composite.

Figure 5-3c shows the top-view SEM image of the CNT@LLZTO composite cathode and the corresponding elemental mapping. LLZTO particles have uniformly adhered to the periphery of SWCNTs, and unlike the dense LLZTO pellet, the cathode shows a loose and porous morphology. In addition, the cross-sectional image of the composite cathode in Figure 5-3d further verified the loose and porous structure in the internal of the CNT@LLZTO composite cathode. This porous structure is beneficial for oxygen diffusion, which is superior to that in conventional Li-O_2 batteries because the O_2 diffusion in the liquid electrolyte is thought to be the rate-determining step. The corresponding elemental mapping of the cross-sectional images illustrated in Figure 5-3g-j further confirms the homogeneous distribution of the electrolyte and conductive carbon in two separate layers. More importantly, the composite cathode and electrolyte pellet contact closely, which should be attributed to the annealing process after solvent removal. The high-resolution SEM image of CNT@LLZTO in Figure 5-6 further verifies that loose SWCNT is dispersed in the cathode with partially affixed LLZTO particles. The homogenous mixing and sufficient contact of the solid electrolyte and conductive carbon

nanotubes in a porous cathode could facilitate the conduction of ions, transportation of electrons and diffusion of oxygen molecules which are necessary for the electrochemical reaction occurring in Li-O_2 batteries. Besides, this integrated structure of cathode and electrolyte would also facilitate the migration of lithium ions between cathode and electrolyte layer, thereby reducing interface impedance effectively. Figure 5-3e demonstrates the flat *in situ* thermally cured polymer buffer layer PEGMEM on the LLZTO. The PEGMEM layer enables sufficient coverage of the LLZTO electrolyte surface (Figure 5-3f), which can optimize the wettability between rigid solid electrolyte and lithium and hence reduce the interfacial resistance.

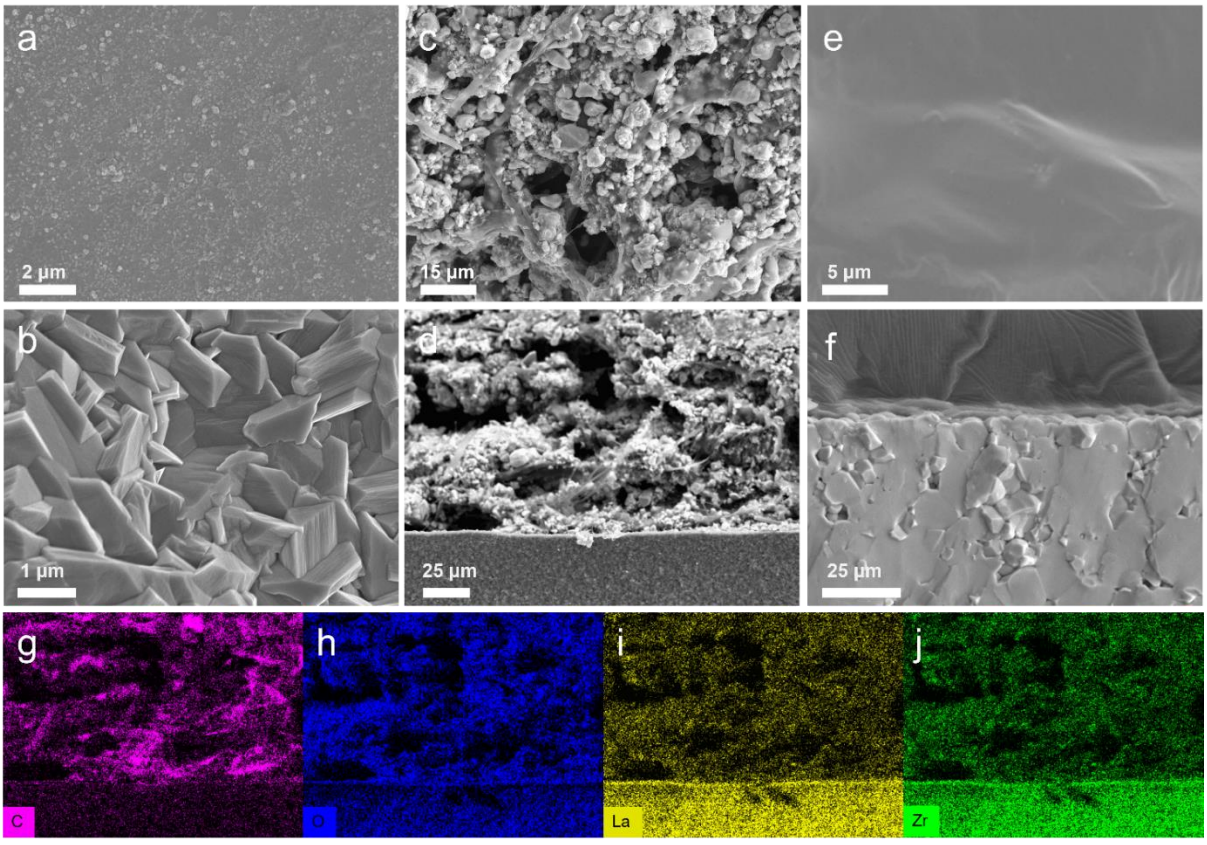

Figure 5-3 (a) Top-view and (b) cross-sectional image of LLZTO electrolyte pellet. (c) Top-view image of CNT@LLZTO cathode coated on the LLZTO pellet. (d) Cross-sectional image of the integrated structure composed of LLZTO electrolyte and CNT@LLZTO cathode, as

well as (g-j) corresponding elemental mapping images. (e) Top-view image of PEGMEM buffer layer. (f) Cross-sectional image of PEGMEM@LLZTO bilayer electrolyte.

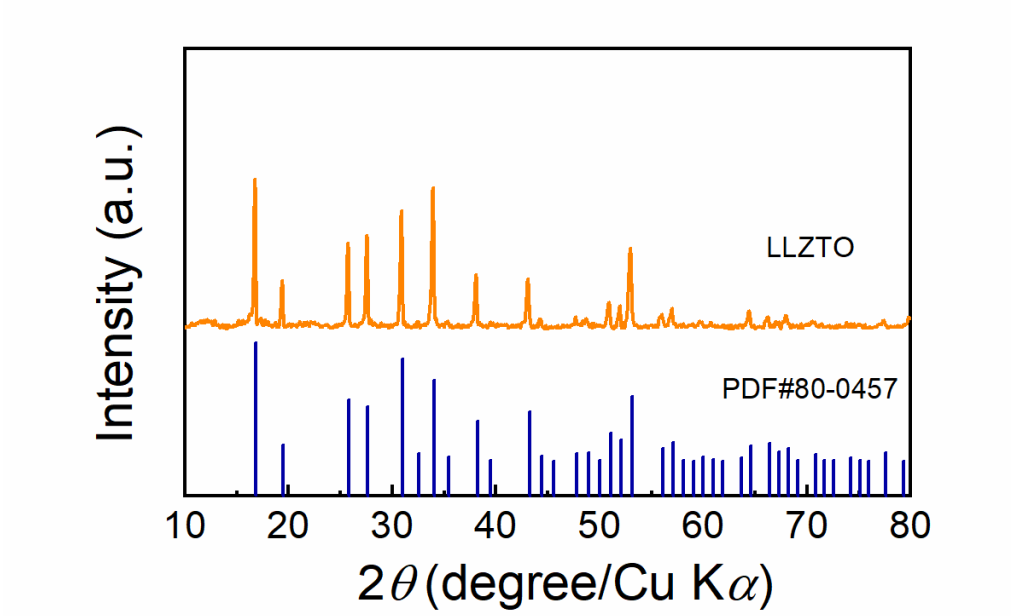

Figure 5-4 XRD pattern of LLZTO electrolyte.

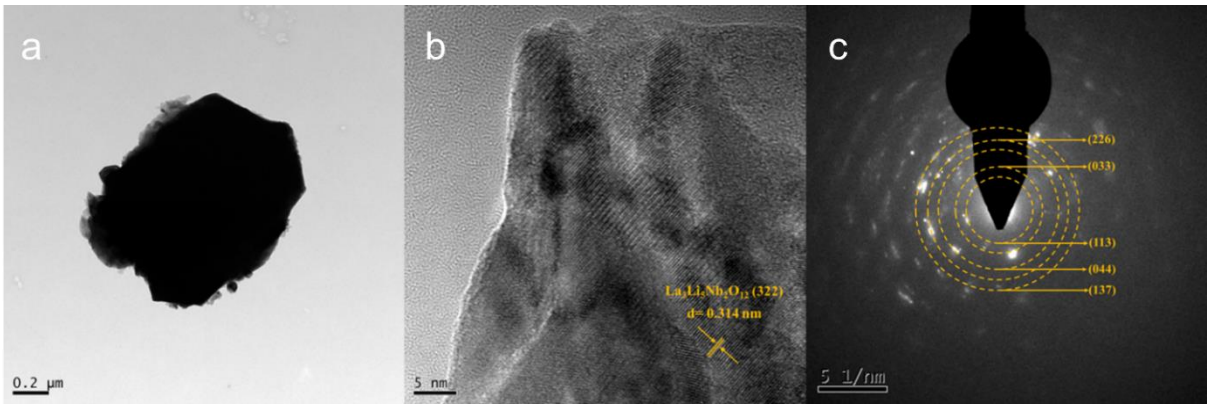

Figure 5-5 (a) TEM image, (b) HRTEM image and (c) SAED pattern of LLZTO particles.

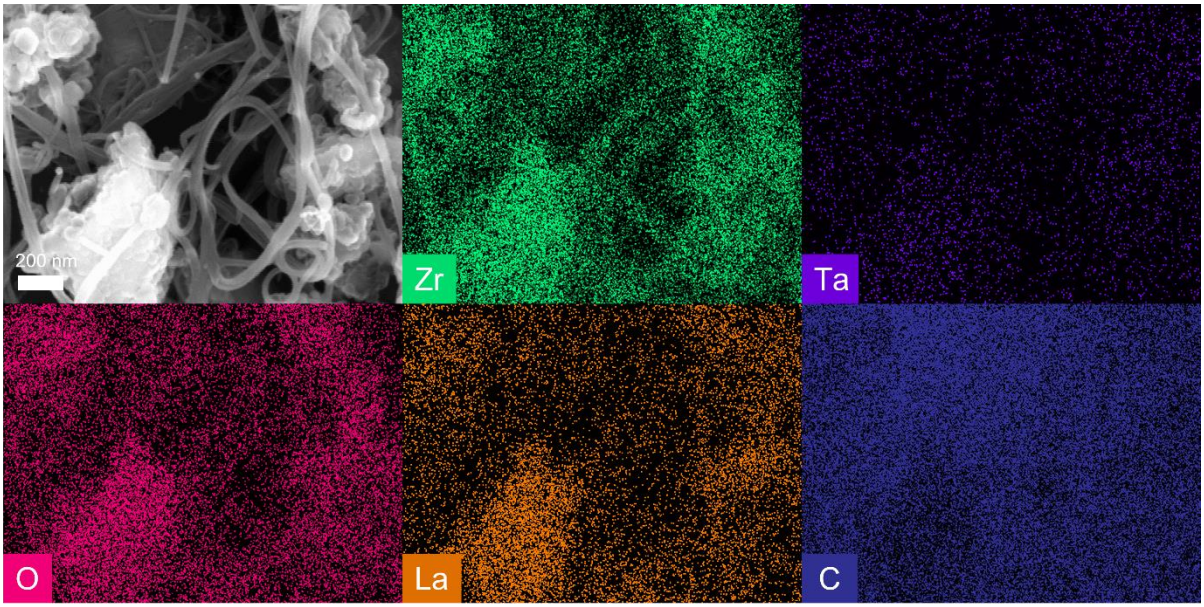

Figure 5-6 High-resolution cross-sectional SEM image of CNT@LLZTO cathode with corresponding elemental mapping results.

The ion conductivities of the PEGMEM@LLZTO bilayer electrolyte at different temperatures were obtained by electrochemical impedance spectroscopy. Figure 5-7a shows the impedance spectrum of PEGMEM@LLZTO electrolyte at room temperature with the corresponding ion conductivity of 3.16×10^{-4} S cm^{-1}. According to the Arrhenius equation and the temperature dependences of ionic conductivity from -10 to 80 ℃ (Figure 5-8) the activation energy of PEGMEM@LLZTO electrolytes is calculated to be 0.382 eV, demonstrating good linear fit results as shown in Figure 5-7b. The electrochemical window of PEGMEM@LLZTO was investigated by the cyclic voltammetry method over a voltage of -0.5 to 6 V as shown in Figure 5-7c. Two reversible peaks appear at around -0.5 and 0.5 V, corresponding to the reversible lithium plating and stripping. Besides, no obvious oxidation peak was observed until the

scanning reaches 6 V, indicating the excellent electrochemical stability of PEGMEM@LLZTO. Figure 5-7d exhibits the direct current polarization curve of the PEGMEM@LLZTO electrolyte. The calculated electronic conductivity is as low as 2.5×10^{-8} S cm^{-1} and its corresponding lithium-ion transference number is approaching 0.99. This result reveals that the bilayer PEGMEM@LLZTO could be considered a pure ionic conductor for Li^{+}. Moreover, Li symmetric cells were assembled to verify the lithium stability. As shown in Figure 5-7e, Li/PEGMEM@LLZTO/Li battery demonstrates a much smaller polarization voltage, as well as a longer cycling stability (400 h at 0.1 mA cm^{-2} under 0.05 mA h cm^{-2}) than that of the Li/LLZTO/Li battery. Furthermore, the critical current density (CCD) was also compared, which evaluates the maximum current density before the voltage drop occurs by short circuits. As shown in Figure 5-9a, the PEGMEM@LLZTO battery maintains a low polarization even at high current density, delivering a remarkably high CCD value of 0.5 mA cm^{-2}. However, even under low current density, the polarization of the pristine LLZTO-based battery is high and short circuits occur quickly, which recorded the CCD value of 0.2 mA cm^{-2} (Figure 5-9b). This result illustrates the PEGMEM buffer layer could maintain cell stability even under high current densities.

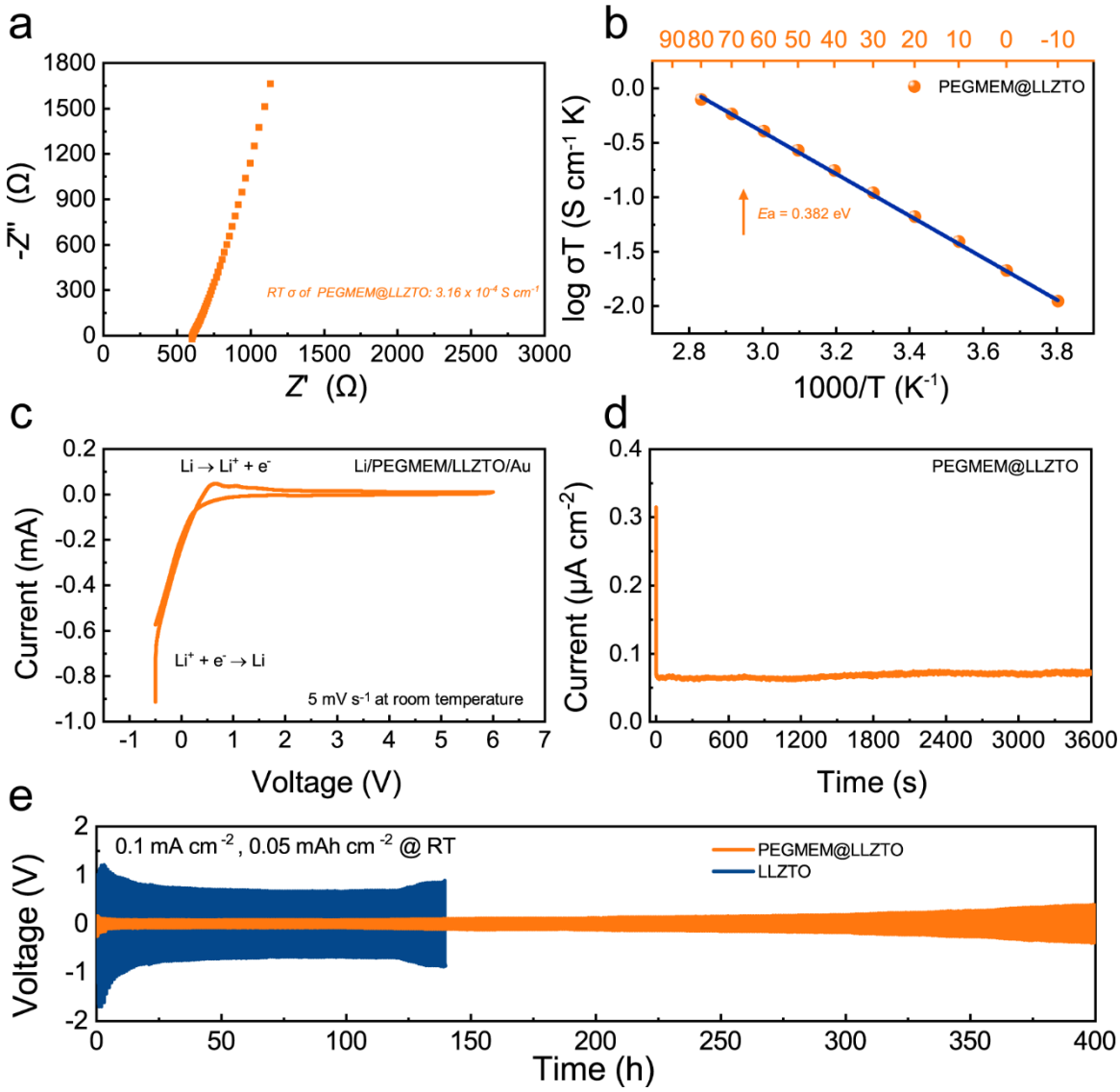

Figure 5-7 (a) Nyquist plots of PEGMEM@LLZTO bilayer electrolyte at room temperature. (b) *Arrhenius* plots of PEGMEM@LLZTO. (c) CV curve and (d) DC polarization curve of PEGMEM@LLZTO under room temperature. (e) Galvanostatic cycling of Li/LLZTO/Li and Li/ PEGMEM/LLZTO/PEGMEM/Li symmetric batteries at a current density of 0.1 mA cm^{-2} with a fixed capacity of 0.05 mA h cm^{-2} at room temperature in the oxygen atmosphere.

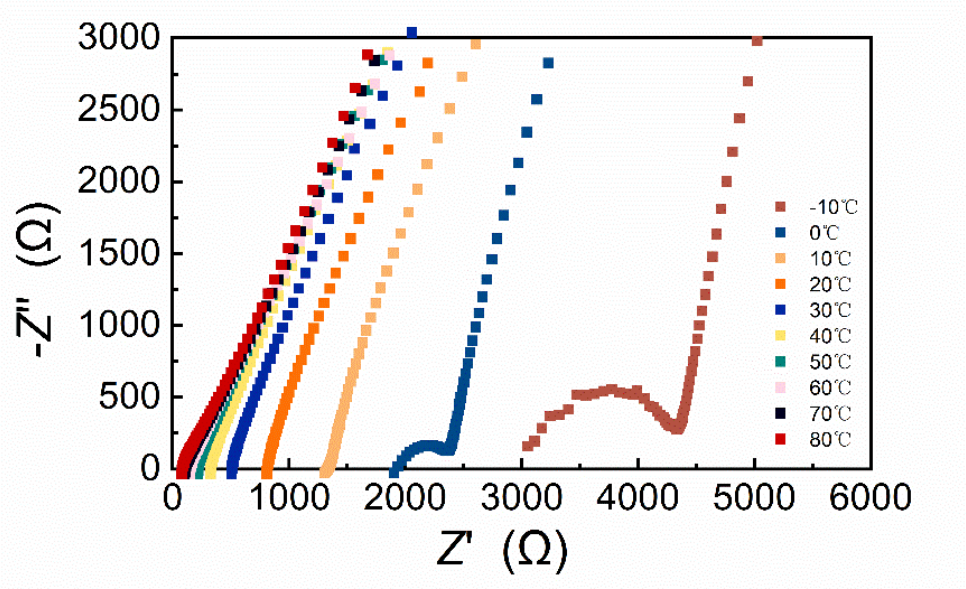

Figure 5-8 Nyquist plots of PEGMEM@LLZTO bilayer electrolyte at different temperatures.

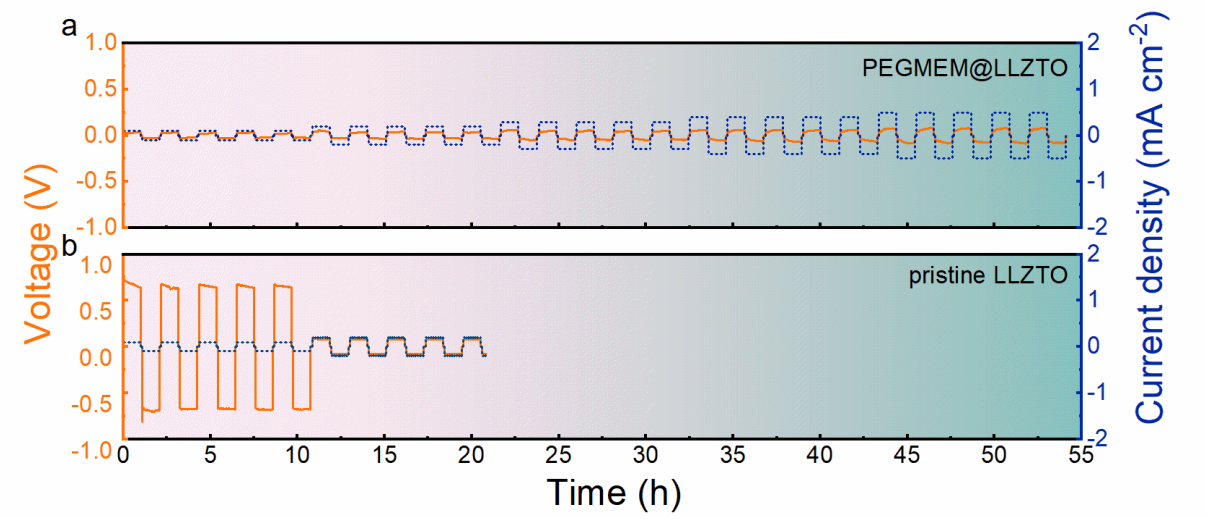

Figure 5-9 Galvanostatic cycling of Li/PEGMEM/LLZTO/PEGMEM/Li symmetric battery and Li/LLZTO/Li battery at step-increased current densities.

The electrochemical performance of corresponding all-solid-state Li-O_2 batteries was investigated comprehensively under room temperature in presence of high purity oxygen. As a

comparison, quasi-solid-state batteries assembled by coating composite cathode on the carbon paper and infiltrated by the liquid electrolyte of 1 M LiTFSI in TEGDME (denoted as CP-CNT@LLZTO), and solid-state batteries assembled by LLZTO-free cathode (denoted as integrated pure CNT) were also studied under the same test conditions. Figure 5-10a shows the initial full discharge/charge curves of solid-state Li-O_2 batteries with different cathodes. The battery employing the integrated CNT@LLZTO shows a superior initial discharging capacity of 13.04 mA h cm^{-2} at a current density of 0.1 mA cm^{-2}, which outperforms the currently reported solid-state Li-O_2 or Li-air batteries (The detailed comparison is shown in Table 5-1)[98, 99, 173, 241, 242, 246, 247, 252-256]. By contrast, solid-state batteries with integrated pure CNT cathode, and quasi-solid-state batteries with non-integrated CP-CNT@LLZTO cathode exhibit much lower initial discharge capacities of 5.6 and 4.4 mA h cm^{-2}, respectively. Batteries utilizing integrated CNT@LLZTO cathode also exhibit a more stable voltage plateau and a smaller overpotential than others. To confirm the ability of the integrated architecture in reducing the interface resistance, electrochemical impedance spectra (EIS) tests of Li-O_2 batteries with different cathodes were conducted after the initial full discharge/charge cycle. Figure 5-10b reveals that the cell with CNT@LLZTO has the lowest impedance, demonstrating the enhanced interfacial properties of the integrated electrolyte/cathode structure.

The cyclic performance of Li-O_2 batteries at different fixed capacities was also investigated carefully. Figure 5-10c-f, Figure 5-11 and Figure 5-12 exhibit the discharge/charge profiles and corresponding terminal voltages for different cathodes. It can be observed that the batteries

employing integrated CNT@LLZTO display excellent cyclic performance of 68 stable cycles at 0.1 mA cm^{-2} with a limited capacity of 0.5 mA h cm^{-2}. By contrast, batteries assembled with non-integrated CP-CNT@LLZTO (Figure 5-12) only achieve 29-cycle cycling capability under the same testing conditions. Moreover, at a reduced fixed capacity of 0.25 mA h cm^{-2} at 0.1 mA cm^{-2}, the Li-O_2 battery employing integrated CNT@LLZTO cathodes delivers an impressive cycling life of 86 cycles with stable terminated voltage, as shown in Figure 5-10e and 4f. In addition, the all-solid-state battery employing CNT@LLZTO cathode can also stably cycle for 31 cycles at a higher current rate of 0.2 mA cm^{-2} with a limited capacity of 1 mA h cm^{-2} as shown in Figure 5-13, demonstrating good reversibility and practical potentials.

The large capacity and enhanced cyclic performance of the battery are primarily attributed to the comparably high conductivity of the bilayer electrolyte and the superior cathode interface performance induced by the integrated structure. Overall, the integrated structure of the all-solid-state cell promotes ion/electron transport at the triple-phase boundaries, diffusion of oxygen, and ion transport between the positive electrode and the electrolyte, greatly reducing the interfacial impedance. In addition, the interfacial reaction between Li_2O_2 and electrolyte may be suppressed due to the absence of organic electrolyte addition.

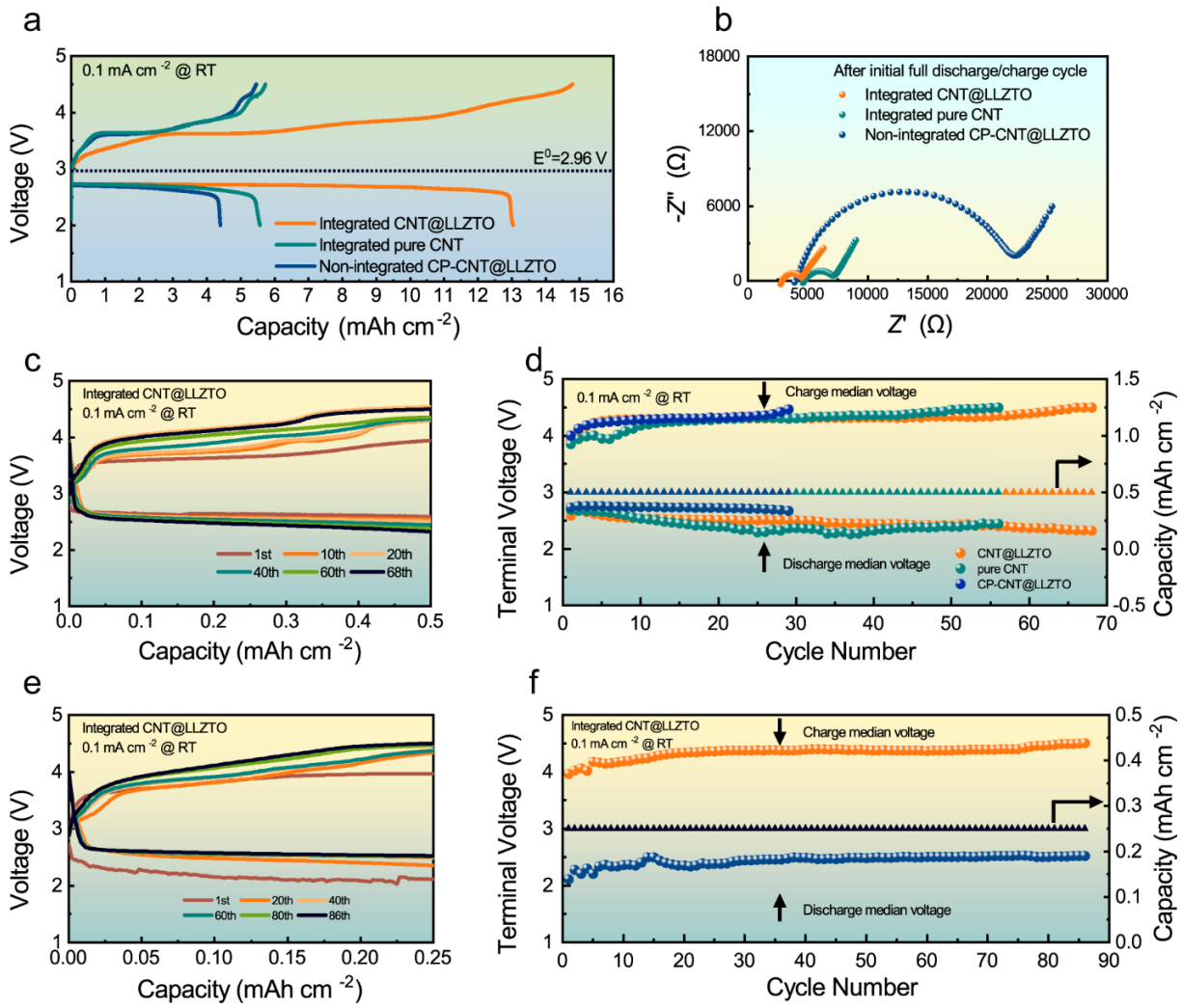

Figure 5-10 (a) Initial discharge/charge profiles of Li-O_2 batteries with different cathodes at 0.1 mA cm^{-2} under room temperature. (b) Nyquist plots of batteries with different cathodes after the initial cycle. (c) Discharge/charge curves of the battery employing CNT@LLZTO at 0.1 mA cm^{-2} with a fixed capacity of 0.5 mA h cm^{-2}. (d) Cycling performance with corresponding terminated voltages at 0.1 mA cm^{-2} and 0.5 mA h cm^{-2}. (e) Discharge/charge curves of the battery employing CNT@LLZTO at 0.1 mA cm^{-2} with a fixed capacity of 0.25 mA h cm^{-2} and (f) corresponding cycling performance with terminated voltages.

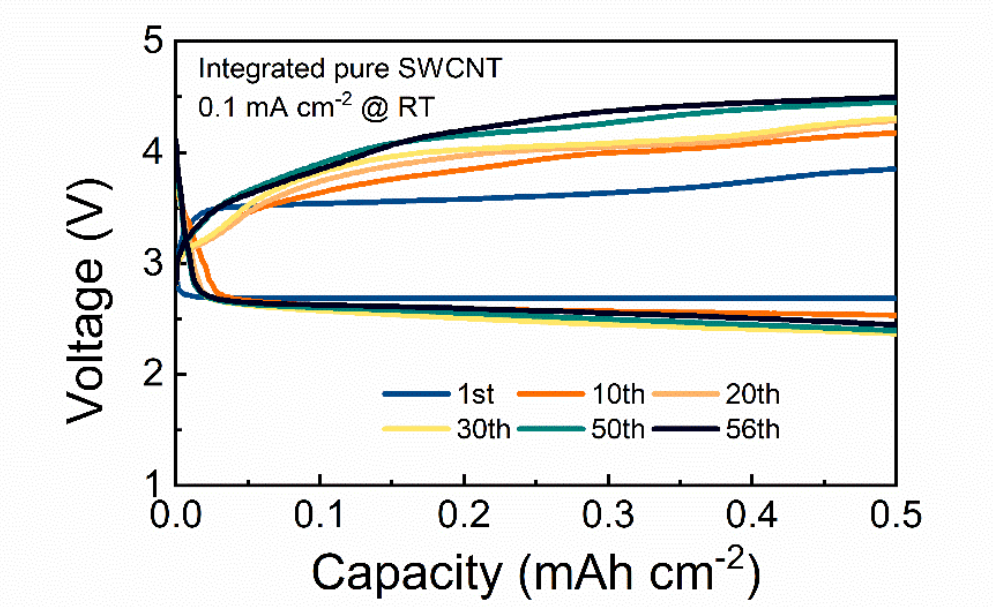

Figure 5-11 Discharge/charge curves of Li-O_2 batteries employing integrated pure CNT cathode at 0.1 mA cm^{-2}.

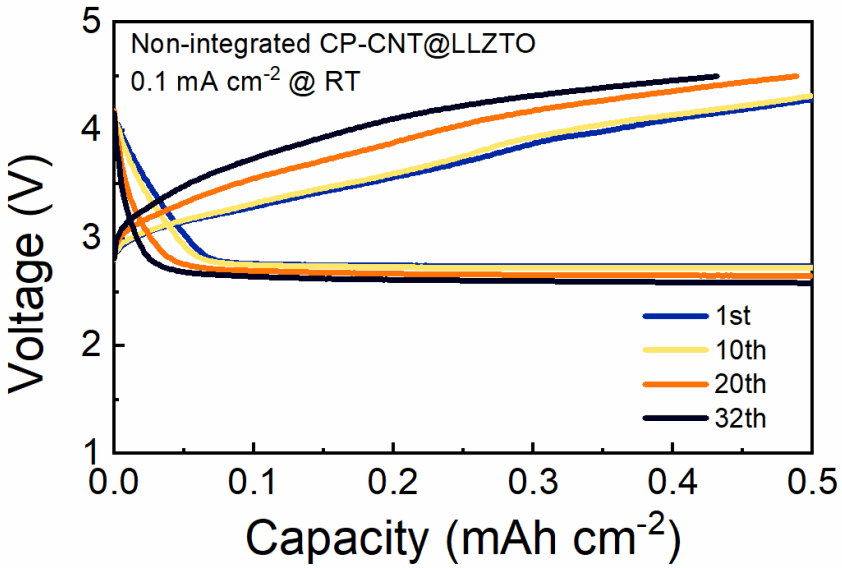

Figure 5-12 Discharge/charge curves of Li-O_2 batteries employing non-integrated CP-CNT@LLZTO cathode at 0.1 mA cm^{-2}.

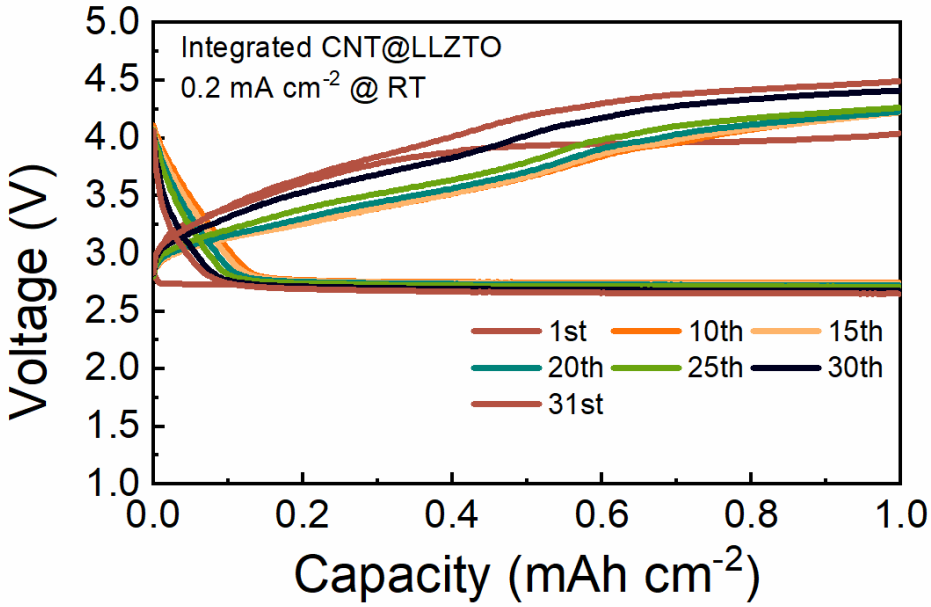

Figure 5-13 Discharge/charge curves of Li-O_2 batteries employing integrated CNT@LLZTO cathode at 0.2 mA cm^{-2}.

Table 5-1 Recent report on solid-state lithium-oxygen or lithium-air batteries.

Materials	Areal current density [mA cm^{-2}]	Areal specific capacity [mA h cm^{-2}]	Current density [mA g^{-1}]	Specific capacity [mA h g^{-1}]	Cycling performance	First discharge capacity [mA h cm^{-2}]	First discharge capacity [mA h g^{-1}]	Ref.
LAGP with CNTs	0.01	0.05	200	1000	2	7.85 @ 0.0005 mA cm^{-2}	7850 @ 10 mA g^{-1}	[173]
Ethylene glycol dimethyl ether (glyme)	0.2	–	–	220	40	–	1480 @ 0. 1 mA cm^{-2}	[252]
LAGP/SWCNT	0.07	0.175	400	1000	10	0.49 @ 0.035 mA cm^{-2}	2800 @ 200 mA g^{-1}	[99]

LLZTO with polymer cathode	0.02	0.1, @ 80°C	200	316	50	6.43 @ 0.02 mA cm^{-2}, 80°C	6430 @ 200 mA g^{-1}, 80°C	[246]
SWCNT/RuO_2	–	–	400	1000	10	–	4587 @ 200 mA g^{-1}	[253]
Germanium protected LAGP	–	–	200	1000	30	–	–	[254]
Ultrafine LAGP	0.2	0.5	400	1000	27	–	–	[247]
Carbon coated porous LAGP with dense LAGP	0.01	0.08	–	–	6	0.48 @ 0.005 mA cm^{-2}		[242]
Adjustable-porosity plastic crystal electrolyte	0.02	0.05	200	500	130	0.59 @ 0.02 mA cm^{-2}	5963 @ 200 mA g^{-1}	[241]
Ultra-dry polymer electrolytes P(VDF-HFP)	0.4	1	400	1000	60	2.8 @ 0.4 mA cm^{-2}	2800 @ 400 mA g^{-1}	[255]
Zeolite-based thin membrane	0.05	0.1	500	1000	149	1.202 @ 0.05 mA cm^{-2}	12020 @ 500 mA g^{-1}	[98]
LiIL-MOF	0.03	0.15 @ 60°C	100	500	110	0.945 @ 0.03 mA cm^{-2} 60°C	3150 @ 100 mA g^{-1}, 60°C	[256]
PEGMEM@LLZTO, CNT@LLZTO	**0.1**	**0.5**	**–**	**–**	**68**	**13.04 @ 0.1 mA cm^{-2}**	**–**	**This work**
PEGMEM@LLZTO, CNT@LLZTO	**0.1**	**0.25**	**–**	**–**	**86**	**–**	**–**	**This work**

To deeply identify discharge products in all-solid-state Li-O_2 batteries, X-ray photoelectron spectroscopy (XPS) was performed on the cathode surface after the full discharging process. The spectra of Li 1s and O 1s in integrated CNT@LLZTO cathode are shown in Figure 5-14a and b, respectively. The peak at a binding energy of around 56.3 eV in the Li 1s spectrum corresponds to $Li_{2-x}O_2$, while the peak at a binding energy of approximately 54.6 eV is attributed to the generation of Li_2O_2 [221, 257]. The larger peak area of Li_2O_2 reveals that it is the main discharge product rather than $Li_{2-x}O_2$ in this all-solid-state Li-O_2 battery. Moreover, the morphology of the discharge product of the battery employing CNT@LLZTO observed by SEM is shown in Figure 5-15, which presents a toroid-like shape, by the expected major discharge product Li_2O_2. The corresponding binding energy of Li_2O_2 in the O 1s spectrum is about 531.5 eV. As a comparison, the Li 1s spectrum of non-integrated CP-CNT@LLZTO cathode in Figure 5-14c shows an increased peak area of $Li_{2-x}O_2$ and by-product Li_2CO_3, possibly as a result of side reactions caused by the decomposition of the liquid organic electrolyte. The O 1s spectrum of the CP-CNT@LLZTO cathode can also corroborate this interpretation, as the peak of -OH or C-O is present with a decreased peak area of Li_2O_2 (Figure 5-14d).

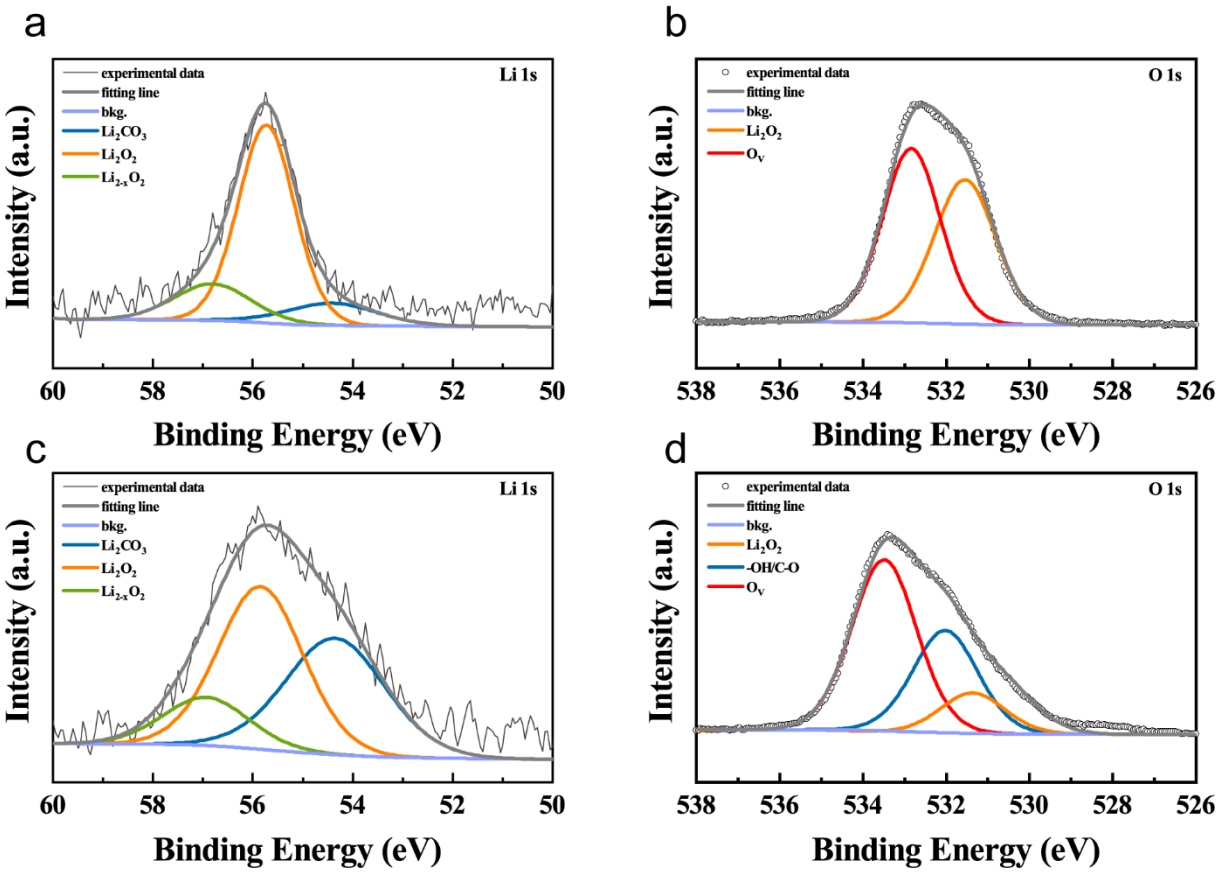

Figure 5-14 High resolution (a) Li 1s XPS spectra and (b) O1 s XPS spectra of integrated CNT@LLZTO cathode after full discharging at 0.1 mA cm^{-2}. High resolution (c) Li 1s XPS spectra and (d) O1 s XPS spectra of non-integrated CP-CNT@LLZTO cathode after full discharging at 0.1 mA cm^{-2}.

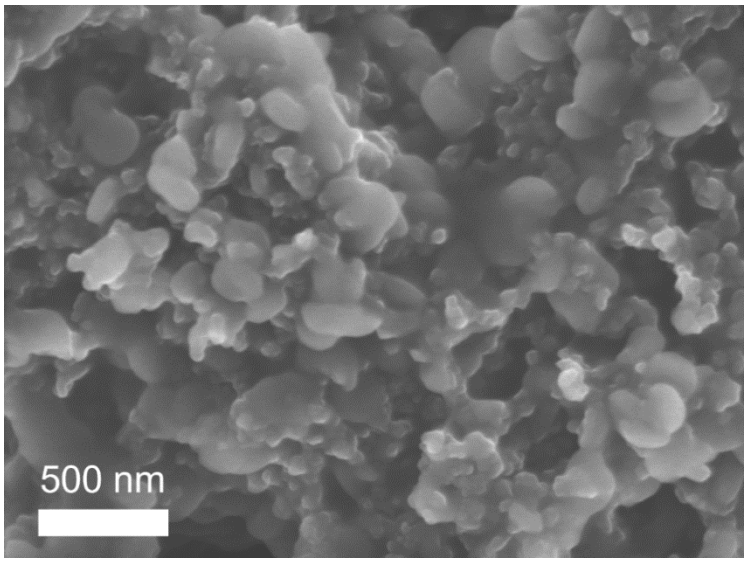

Figure 5-15 SEM image of SWCNT@LLZTO cathode in all-solid-state Li-O_2 batteries after full discharge.at 0.1 mA cm^{-2} under room temperature in dry oxygen.

To further analyze the reaction mechanism of Li-O_2 batteries, *in situ* differential electrochemical mass spectrometry (DEMS) test was undertaken to detect the gas evolution. Based on the chemical reaction of $Li_2O_2 \rightleftharpoons 2Li^+ + O_2 + 2e^-$, the theoretical molar ratio of charge transfer to oxygen should be 2:1. The gas evolution curves of O_2 and CO_2 during the galvanostatic charging process with a cut-off capacity of 0.5 mA h cm^{-2} at 0.2 mA cm^{-2} and corresponding voltage profiles of the batteries employing integrated CNT@LLZTO cathode are illustrated in Figure 5-16a. During the initial charging process, the theoretical final discharge product of Li_2O_2 on the cathode surface would experience spontaneous delithiation to $Li_{2-x}O_2$. Afterward, Li_2O_2 decomposes completely and generates more oxygen, as the voltage grows to a stable charging plateau. Electron transfer was calculated from the parameters of the charging process while the amount of oxygen evolution was obtained by integrating the gas evolution rate over

the charging period. The result reveals that the calculated molar ratio of charge to oxygen is close to 2, indicating the Li_2O_2/O_2 conversion is the predominant reaction during the charging process. As a comparison, under the same test conditions, the Li-O_2 battery based on a non-integrated CP-CNT@LLZTO cathode tested by DEMS exhibits different results in Figure 5-16b. A greater amount of CO_2 is produced during the charging process, probably due to side reactions caused by the addition of liquid organic electrolyte added on the carbon paper or the decomposition of the by-product Li_2CO_3. These results, combined with the XPS spectra and SEM images of the cathode after discharging, fully illustrate that the reaction mechanism of the CNT@LLZTO-based integrated all-solid-state Li-O_2 battery is dominated by the reversible chemical reaction of $Li_2O_2 \rightleftharpoons 2Li^+ + O_2 + 2e^-$.

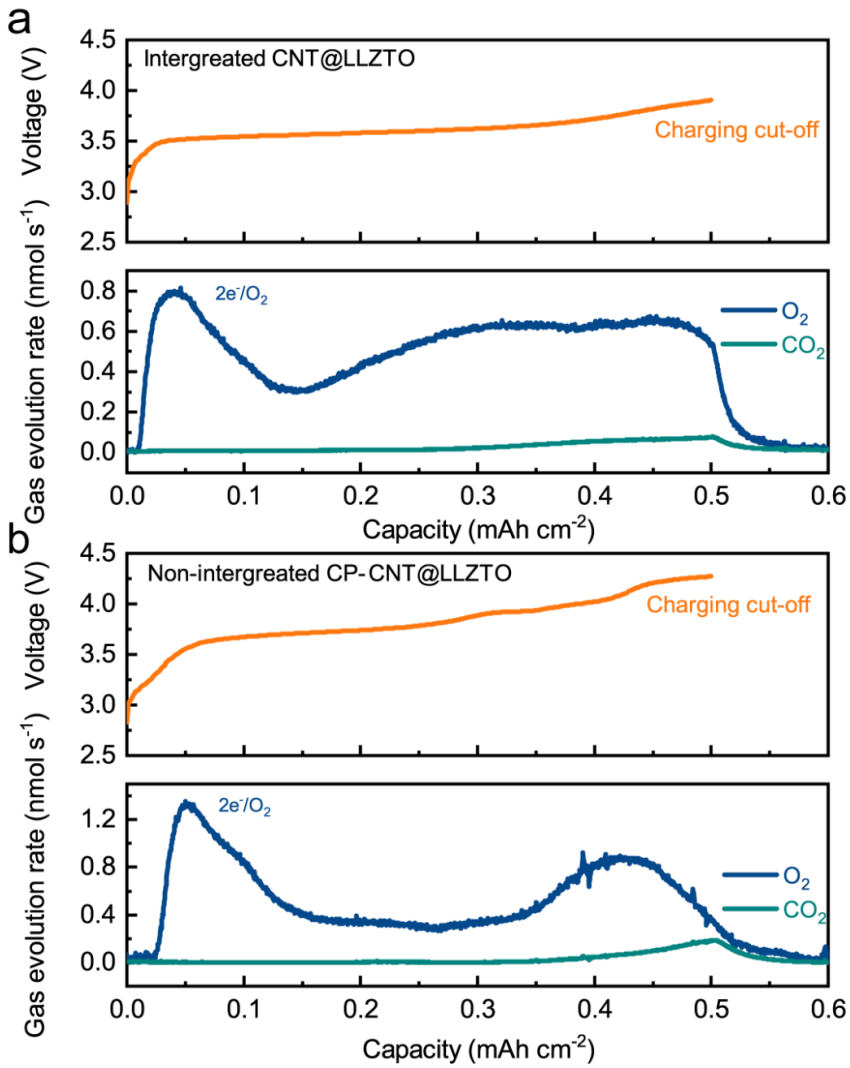

Figure 5-16 Gas evolution rate tested by *in situ* DEMS during the charging process at 0.2 mA cm^{-2} with a limited capacity of 0.5 mA h cm^{-2} in Li-O_2 batteries assembled with (a) integrated CNT@LLZTO cathode and (b) non-integrated CP-CNT@LLZTO cathode.

DFT calculations were performed to confirm the positive effects of integrated CNT@LLZTO cathode on discharge/charge processes and to understand ORR/OER mechanism during battery operation. The Gibbs free energy of each pre-assumed reaction procedure during ORR/OER processes for CNT@LLZTO cathode and pure CNT cathode are

depicted in Figure 5-17a and b, and the specific reaction paths during ORR (discharging) process are shown below, where the * represents different active species on the cathode surface[258, 259]:

$$O_2 + Li^+ + e^- \rightarrow LiO_2{}^* \quad (5-1)$$

$$LiO_2{}^* + Li^+ + e^- \rightarrow Li_2O_2{}^* \quad (5-2)$$

$$Li_2O_2 + O_2 + 2Li^+ + 2e^- \rightarrow (Li_2O_2)_2{}^* \quad (5-3)$$

In this free energy diagram, U, U_{DC}, U_{EQ} and U_C represent the free energy paths at zero potential, highest discharge potential, equilibrium voltage, and lowest charge potential, respectively. Theoretically, the overpotential of total reaction in Li-O_2 batteries could be calculated according to $U_C - U_{DC}$[260-262]. It can be obtained that the Li-O_2 battery with CNT@LLZTO composite cathode exhibits a lower calculated overpotential (1.73 V) than the battery with pure CNT cathode (6.91 V), which is compatible with the superior electrochemical activity in OER/ORR process delivered by the CNT@LLZTO composite cathode. Moreover, the optimized structure and adsorption energy (E_{ads}) of Li_2O_2 on the surface of pure CNT and LLZTO cathode is shown in Figure 5-18. The DFT calculation results show that Li_2O_2 has stronger adsorption energy of -11.8914 eV on the LLZTO cathode surface than on the pure CNT surface (-0.4965 eV), indicating that Li_2O_2 adsorbs more stably and tightly on the surface of the composite cathode containing LLZTO, which is conducive to the promotion of electrochemical performance. The exposed active sites show that the binding strength between Li_2O_2 and the composite cathode is strong enough to allow for successful discharge product deposition.

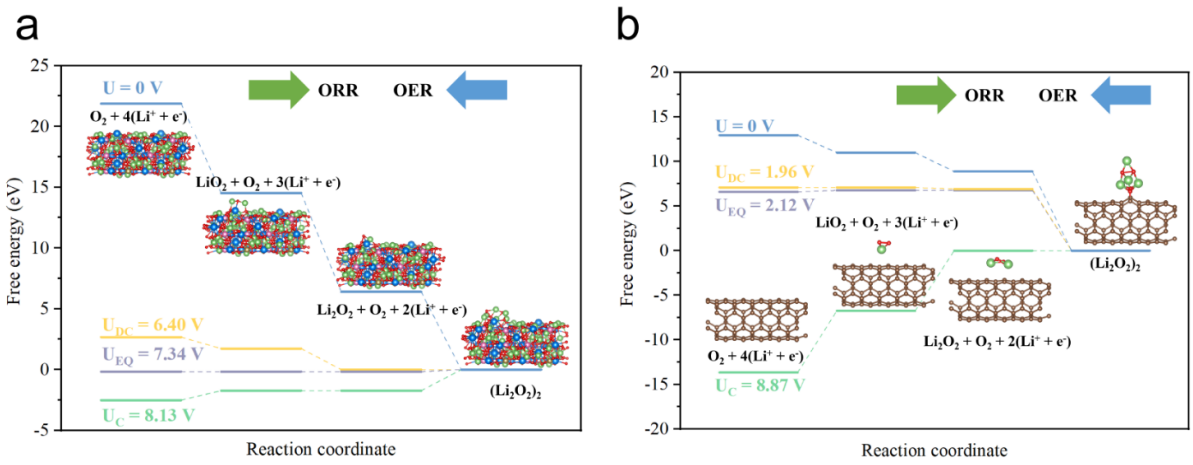

Figure 5-17 Calculated Gibbs free energy diagrams for the ORR/OER processes in Li-O_2 batteries employing (a) CNT@LLZTO cathode and (b) pure CNT cathode.

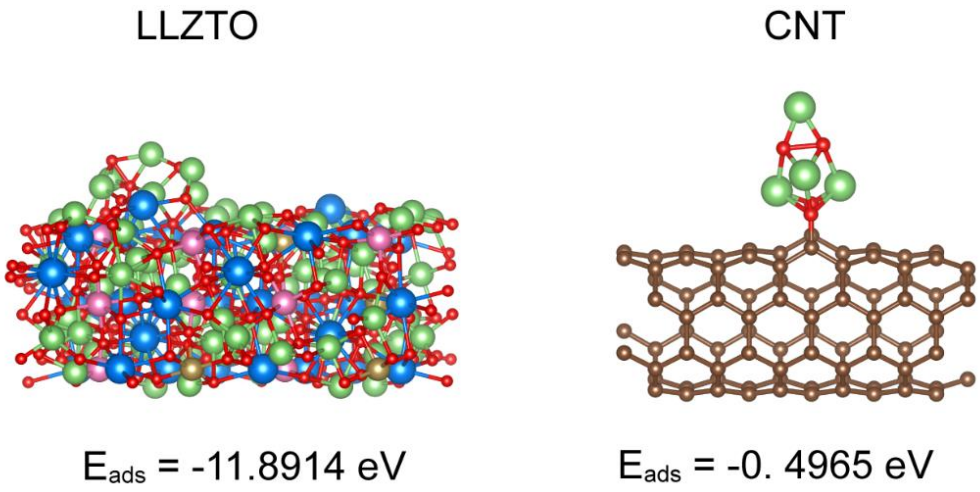

Figure 5-18 The optimized structure and adsorption energy (E_{ads}) of Li_2O_2 on the surface of pure CNT and CNT@LLZTO cathode.

5.4 Conclusion

In summary, an integrated electrolyte/cathode structure for all-solid-state Li-O_2 batteries was successfully designed and prepared. A homogeneous composite cathode was obtained with the

aid of high-energy ball milling. Thanks to the mild liquid method and subsequent low-temperature annealing, not only the integration of cathode and electrolyte were realized, but also the porous structure inside the cathode was also guaranteed. Therefore, this uniquely integrated structure provides a large number of triple-phase boundaries that can accommodate lithium ions, electrons and oxygen, as well as greatly reducing the cathode-electrolyte interfacial impedance inside the battery. More importantly, since no liquid electrolyte is deployed in wet the cathode, the side reaction at the interface is greatly suppressed, thus realizing the real sense of an all-solid-state battery. The obtained all-solid-state Li-O_2 batteries deliver a superior large first discharging capacity of 13.04 mA h cm^{-2} and long cyclic performances of 86 cycles. It is expected that the present study may provide a simple and feasible strategy for the enhancement of air electrodes and the development of next-generation all-solid-state Li-O_2 batteries.

Chapter 6 Conclusion and Perspectives

6.1 Summary of the Research

Solid-state lithium-oxygen batteries are a novel battery technology that is currently in the research and development phase. They use solid-state electrolytes instead of traditional liquid electrolytes, which can improve the safety, stability, and energy density of the battery. Additionally, lithium-oxygen batteries have a high theoretical energy density, reaching up to approximately 3600 Wh kg^{-1}, which is the highest energy density among all known battery technologies. However, the research and development of solid-state lithium-oxygen batteries still faces some challenges. For example, the conductivity and ion transport properties of solid-state electrolytes need to be further improved. Additionally, issues such as the lithium metal negative electrode during charging and discharging, positive electrode material contact issues, manufacturing processes, and costs need to be addressed.

The research findings of this thesis provide many valuable references for the design and preparation of all-solid-state lithium-oxygen batteries, which paves the way for their practical applications in the near future. The main outcomes summarized below:

(1) The practical application of lithium-oxygen batteries is limited by the formation of lithium dendrites and the use of flammable and unstable organic liquid electrolytes, which would cause safety issues and poor cycling stability. In **Chapter 3**, two types of solid-state electrolytes, LAGP-Si and LLZTO have proven to be suitable for the assembly of solid or quasi-solid lithium-oxygen batteries. The characterization and electrochemical properties of these electrolytes were systematically carried out. The performance of electrolytes obtained by

different synthesis methods varies. In general, oxide ceramic electrolytes including both LAGP and LLZTO exhibit high ionic conductivity and good stability. However, these electrolyte-assembled batteries deliver poor cycling performance and the low initial full charge/discharge capacity, which are not comparable to that of lithium-oxygen batteries assembled with conventional liquid or gel electrolytes. Therefore, in the subsequent chapters, related works targeting the modification of the electrolyte itself and the improvement of the cell structure are presented. The synergistic effect of different electrolytes in lithium-oxygen batteries is also explored.

(2) In **Chapter 4**, a bilayer organic/inorganic hybrid solid-state electrolyte is proposed to improve the safety and enhance the electrochemical performance of lithium-oxygen batteries. The Si-doped NASICON-type electrolyte $Li_{1.51}Al_{0.5}Ge_{1.5}Si_{0.01}P_{2.99}O_{12}$, which was synthesized based on the LAGP electrolyte studied in **Chapter 3**, serves as an inorganic rigid backbone to guarantee high ionic conductivity, and provide a barrier between active oxygen and lithium anode. PEGMEM was chosen as a polymer buffer layer due to its compatibility with lithium. Benefiting from the synergistic effect between LAGP-Si and PEGMEM, the obtained hybrid electrolyte exhibits high ionic conductivity and good stability against lithium anode. Consequently, the polarization of the Li symmetric cell is dramatically reduced by replacing pure LAGP-Si with a bilayer hybrid electrolyte. The solid-state lithium batteries employing PEGMEM@LAGP-Si electrolyte deliver a greater initial discharge-charge capacity of 7.3 mA h cm^{-2} and enhanced cyclic performance for 39 cycles with a restricted capacity of 0.4 mA h

cm^{-2}. This work optimizes the electrolyte-anode structure inside the lithium-oxygen battery by innovatively laminating oxide ceramics and polymer films to create a double-layer electrolyte. In addition, the effect of elemental doping on the performance of electrolytes is studied and demonstrated in this chapter. As a result, it delivers a promising property of hybrid solid electrolytes for high-performance solid-state lithium-oxygen batteries.

(3) Despite demonstrating the feasibility of several solid electrolytes, however, current solid-state lithium-oxygen batteries still encounter the challenge of high impedance at the electrode/electrolyte interface. In addition, the deficiency of triple-phase boundaries (Li^+, e^- and O_2) limits the active sites for electrochemical reaction in the battery cathode. **Chapter 5** shifts the focus to improving the cathode structure to reduce the overall impedance of the cell. In this work, an integrated architecture based on garnet electrolyte $Li_{6.4}La_3Zr_{1.4}Ta_{0.6}O_{12}$ (LLZTO) and porous composite cathode is designed for high-performance all-solid-state Li-O_2 batteries. The PEGMEM buffer layer used in **Chapter 4** was added between the lithium metal anode and LLZTO in this work, again greatly reducing the overall impedance and interfacial stability of the cell. The unique internal structure effectively reduces the interfacial impedance of the battery, provides a large number of active sites at triple-phase boundaries and increases the electrochemical stability. As a result, the obtained batteries can deliver a superior high full discharge capacity of 13.04 mA h cm^{-2} and an excellent cyclic performance (86 cycles). In addition, X-ray photoelectron spectroscopy, differential electrochemical mass spectrometry and theoretical calculations further demonstrate the effectiveness of this design in enhancing the

interfacial performance, electrochemical performance, and stability of the battery. This work is thus expected to facilitate practical applications for truly all-solid-state Li-O_2 batteries, and even offers potential alternative trials for other systems of metal-oxygen (air) batteries.

6.2 Outlook for Future Work

The results reported in this thesis revealed successful ways for enhancing the (electro)-chemical of solid electrolytes and modifying battery structure for rechargeable solid-state lithium-oxygen batteries and indicate new research directions. High-performance all-solid-state lithium-oxygen batteries have also been shown to be feasible. High conductivity and stability of inorganic oxide electrolyte can be well adapted to the energy storage system of lithium-oxygen battery. Their performances can be effectively improved by changing the synthesis conditions, elemental doping, and other means. Polymeric solid electrolytes with flexibility and good interfacial wettability can be used as a buffer layer between the lithium anode and electrolyte, not only to promote interfacial contact and reduce interfacial impedance, but also to protect the solid electrolyte surface. The electrochemical performance and stability of lithium-oxygen batteries can also be improved using composite cathodes and the unique integrated structure of cathodes and electrolytes. Given some technical thorny problems persist in this investigated topic, the following perspectives are worthwhile for the future works:

(1) The design of high-performance solid-state electrolytes is a top priority. A solid-state electrolyte with both high ionic conductivity and high stability will enable the application of

all-solid-state lithium-oxygen (air) batteries. At present, the research of solid-state electrolytes is still not sufficient, and knowledge gaps of deployment of solid-state electrolytes in lithium-oxygen battery system need to be narrowed.

(2) The design of porous integrated cathodes and efficient catalysts suitable for all-solid-state lithium-oxygen batteries is also paramount. The interconnected porous 3D network structure not only facilitates the transport of diffusive gas, but also provides a support and storage sites for the discharge point products. The development of inert non-carbonaceous electrodes is also one of the ways to enhance the stability of solid-state lithium-oxygen batteries. Efficient cathode catalysts, whether solid particles or liquid-phase redox pairs, can be applied in solid-state battery applications to reduce their cyclic overpotential and improve their energy conversion efficiency. In addition, the development of catalysts that promote Li_2CO_3, a common by-product in lithium-air batteries, is also pivotal to improve battery performance.

(3) There is still potential for the development of interface engineering between the electrolyte and electrode. Solid electrolytes can be designed with porous materials so as to increase the contact area with the electrode material. In addition, different materials can be developed as a buffer layer between electrode and electrolyte to promote contact, reduce resistance, and protect the electrolyte from air corrosion. High temperature batteries may be able to solve the problem of slower reaction kinetics at the interface.

(4) More theoretical calculations can surely facilitate the understanding of the reaction mechanism of solid-state lithium-oxygen batteries. Since the final form of solid-state lithium-oxygen battery is a solid-state lithium-air battery, its operation in atmospheric environment must consider of the effects of multiple gaseous compositions and humidity. Relevant studies can be conducted on how different atmospheric conditions affect the composition, morphology, and reaction mechanism of the reaction products in solid-state lithium-air batteries.

In summary, it is worthy of belief and attention that all-solid-state lithium-oxygen batteries and even metal-air batteries will become a rosy prosperous realm in the foreseeable future, which will facilitate mankind to further explore the efficient, safe, and green energy storage systems.

Publication List

Research on lithium-air or lithium-oxygen batteries

1. **Z. Gu**, X. Xin, Z. Xu, J. He, J. Wu, Y. Sun and X. Yao, *Garnet Electrolyte-Based Integrated Architecture for High-Performance All-Solid-State Lithium-Oxygen Batteries.* Advanced Functional Materials, 2023. DOI: 10.1002/adfm.202301583.

2. **Z. Gu**, X. Xin, J. Yang, D.C. Guo, S.J. Yang, J.H. Wu, Y. Sun and X.Y. Yao, *Bilayer NASICON/Polymer Hybrid Electrolyte for Stable Solid-State Li-O_2 Batteries.* ACS Applied Energy Materials, 2022. **5**(7): p. 9149-9157.

3. X.X. Liu, X. Xin, L. Shen, **Z. Gu**, J.H. Wu and X.Y. Yao, *Poly(methyl methacrylate)-Based Gel Polymer Electrolyte for High-Performance Solid State Li-O_2 Battery with Enhanced Cycling Stability.* ACS Applied Energy Materials, 2021. **4**(4): p. 3975-3982.

4. Z.L. Xu, Z.Q. Liu, **Z. Gu**, X.L. Zhao, D.C. Guo and X.Y. Yao, *Polyimide-Based Solid-State Gel Polymer Electrolyte for Lithium-Oxygen Batteries with a Long-Cycling Life.* ACS Applied Materials & Interfaces: p. 9.

5. Z.L. Xu, D.C. Guo, Z.Q. Liu, Z.Y. Wang, **Z. Gu**, D. Wang and X.Y. Yao, *Cellulose Acetate-Based High-Electrolyte-Uptake Gel Polymer Electrolyte for Semi-Solid-State Lithium-Oxygen Batteries with Long-Cycling Stability.* Chemistry-an Asian Journal, 2022. **17**(21): p. 9.

Research on lithium-ion and lithium-sulfur batteries

1. Y. Zhao, **Z. Gu**, W. Weng, D. Zhou, Z.Q. Liu, W.T. Fan, S.G. Deng, H. He and X.Y. Yao, *Nitrogen doped hollow carbon nanospheres as efficient polysulfide restricted layer on commercial separators for high-performance lithium-sulfur batteries.* Chinese Chemical Letters, 2023. **34**(2): p. 5. **(co-first author)**

2. S.J. Yang, Z.H. Zhang, L. Shen, P. Chen, **Z. Gu**, M.Y. Chang, Y. Zhao, H. He and X.Y. Yao, *Gravity-driven Poly(ethylene glycol)@Li1.5Al0.5Ge1.5(PO4)(3) asymmetric solid polymer electrolytes for all-solid-state lithium batteries.* Journal of Power Sources, 2022. **518**: p. 8.

3. J.F. Ma, Z.Y. Wang, J.H. Wu, **Z. Gu**, X. Xin and X.Y. Yao, *In Situ Solidified Gel Polymer Electrolytes for Stable Solid-State Lithium Batteries at High Temperatures.* Batteries-Basel, 2023. **9**(1): p. 11.

4. M. Wu, M. Li, Y. Jin, X. Chang, X. Zhao, **Z. Gu**, G. Liu and X. Yao, *In situ formed LiF-Li3N interface layer enables ultra-stable sulfide electrolyte-based all-solid-state lithium*

batteries. Journal of Energy Chemistry, 2023. **79**: p. 272-278.

5. Y. Jin, Q. He, G. Liu, **Z. Gu**, M. Wu, T. Sun, Z. Zhang, L. Huang and X. Yao, *Fluorinated Li(10) GeP(2) S(12) Enables Stable All-Solid-State Lithium Batteries.* Advanced Materials, 2023: p. e2211047.

Reference

1. B. Richter, D. Goldston, G. Crabtree, L. Glicksman, D. Goldstein, D. Greene, D. Kammen, M. Levine, M. Lubell, M. Savitz, D. Sperling, F. Schlachter, J. Scofield and J. Dawson, *How America Can Look Within To Achieve Energy Security And Reduce Global Warming.* Reviews of Modern Physics, 2008. **80**(4): p. S1-S107.
2. S. Chu and A. Majumdar, *Opportunities and challenges for a sustainable energy future.* Nature, 2012. **488**(7411): p. 294-303.
3. B. Dunn, H. Kamath and J.-M. Tarascon, *Electrical Energy Storage for the Grid: A Battery of Choices.* Science, 2011. **334**(6058): p. 928-935.
4. J.B. Goodenough and Y. Kim, *Challenges for Rechargeable Li Batteries.* Chemistry of Materials, 2010. **22**(3): p. 587-603.
5. K.M. Abraham and Z. Jiang, *A Polymer Electrolyte-Based Rechargeable Lithium/Oxygen Battery.* Journal of the Electrochemical Society, 1996. **143**(1): p. 1-5.
6. N. Nitta, F. Wu, J.T. Lee and G. Yushin, *Li-ion battery materials: present and future.* Materials Today, 2015. **18**(5): p. 252-264.
7. J.M. Tarascon and M. Armand, *Issues and challenges facing rechargeable lithium batteries.* Nature, 2001. **414**(6861): p. 359-367.
8. J. Gao, Y.-S. Zhao, S.-Q. Shi and H. Li, *Lithium-ion transport in inorganic solid state electrolyte.* Chinese Physics B, 2016. **25**(1).
9. R. Chen, W. Qu, X. Guo, L. Li and F. Wu, *The pursuit of solid-state electrolytes for lithium batteries: from comprehensive insight to emerging horizons.* Materials Horizons, 2016. **3**(6): p. 487-516.
10. Y. Meesala, A. Jena, H. Chang and R.-S. Liu, *Recent Advancements in Li-Ion Conductors for All-Solid-State Li-Ion Batteries.* ACS Energy Letters, 2017. **2**(12): p. 2734-2751.
11. A. Tomaszewska, Z.Y. Chu, X.N. Feng, S. O'Kane, X.H. Liu, J.Y. Chen, C.Z. Ji, E. Endler, R.H. Li, L.S. Liu, Y.L. Li, S.Q. Zheng, S. Vetterlein, M. Gao, J.Y. Du, M. Parkes, M.G. Ouyang, M. Marinescu, G. Offer and B. Wu, *Lithium-ion battery fast charging: A review.* Etransportation, 2019. **1**: p. 28.
12. L.-Z. Fan, H. He and C.-W. Nan, *Tailoring inorganic–polymer composites for the mass production of solid-state batteries.* Nature Reviews Materials, 2021. **6**: p. 1003–1019.
13. 许晓雄, 邱志军, 官亦标, 黄祯 and 金翼, *全固态锂电池技术的研究现状与展望.* 储能科学与技术, 2013. **2**(4): p. 331-341.
14. J. Janek and W.G. Zeier, *A solid future for battery development.* Nature Energy, 2016. **1**(9): p. 16141.
15. J. Wu, S. Liu, F. Han, X. Yao and C. Wang, *Lithium/sulfide all-solid-state batteries using sulfide electrolytes.* Advanced Materials, 2021. **33**(6): p. e2000751.
16. H.W. Kim, J. Han, Y.J. Lim, Y. Choi, E. Lee and Y. Kim, *3D Ion-Conducting, Scalable, and Mechanically Reinforced Ceramic Film for High Voltage Solid-State Batteries.* Advanced Functional Materials, 2021. **31**(2).

17. J.H. Wu, L. Shen, Z.H. Zhang, G.Z. Liu, Z.Y. Wang, D. Zhou, H.L. Wan, X.X. Xu and X.Y. Yao, *All-solid-state lithium batteries with sulfide electrolytes and oxide cathodes.* Electrochemical Energy Reviews, 2021. **4**: p. 101-135.
18. 许晓雄 and 李泓, *为全固态锂电池"正名".* 储能科学与技术, 2018(01): p. 1-7.
19. M.I. Faraday, *Experimental Researches in Electricity-Third Series.* Philosophical Transactions-Royal Society London, 1833. **123**: p. 23−54.
20. E. ZINTL and G. BRAUER, *Konstitution des Lithiumnitrids.* Zeitschrift fur Elektrochemie und Angewandte Physikalische Chemie, 1935. **41**(2): p. 102-107.
21. Y.F.Y. Yao and J.T. Kummer, *Ion exchange properties of and rates of ionic diffusion in beta-alumina* Journal of Inorganic & Nuclear Chemistry, 1967. **29**(9): p. 2453-&.
22. D.E. Fenton, J.M. Parker and P.V. Wright, *Complexes of alkali-metal ions with poly(ethylene oxide).* Polymer, 1973. **14**(11): p. 589-589.
23. Y.P. Hong, *Crystal structures and crystal chemistry in the system $Na_{1+x}Zr_2SixP_{3-x}O_{12}$* Materials Research Bulletin, 1976. **11**(2): p. 173-182.
24. J.B. Goodenough, H.Y.P. Hong and J.A. Kafalas, *Fast Na^+-ion transport in skeleton structures.* Materials Research Bulletin, 1976. **11**(2): p. 203-220.
25. H.Y.P. Hong, *CRYSTAL-STRUCTURE AND IONIC-CONDUCTIVITY OF LI14ZN(GEO4)4 AND OTHER NEW LI+ SUPERIONIC CONDUCTORS.* Materials Research Bulletin, 1978. **13**(2): p. 117-124.
26. M. Tachez, J.P. Malugani, R. Mercier and G. Robert, *Ionic-conductivity of and phase-transition in lithium thiophosphate Li_3PS_4.* Solid State Ionics, 1984. **14**(3): p. 181-185.
27. H. Aono, E. Sugimoto, Y. Sadaoka, N. Imanaka and G.Y. Adachi, *Ionic-conductivity of the lithium titanium phosphate $(Li_{1+x}Al_xTi_{2-x}(PO_4)_3$, M=Al, Sc, Y, and La) systems.* Journal of the Electrochemical Society, 1989. **136**(2): p. 590-591.
28. Y. Inaguma, L.Q. Chen, M. Itoh, T. Nakamura, T. Uchida, H. Ikuta and M. Wakihara, *HIGH IONIC-CONDUCTIVITY IN LITHIUM LANTHANUM TITANATE.* Solid State Communications, 1993. **86**(10): p. 689-693.
29. R. Kanno and M. Maruyama, *Lithium ionic conductor thio-LISICON - The Li_2S-GeS_2-P_2S_5 system.* Journal of the Electrochemical Society, 2001. **148**(7): p. A742-A746.
30. V. Thangadurai, H. Kaack and W.J.F. Weppner, *Novel fast lithium ion conduction in garnet-type $Li_5La_3M_2O_{12}$ (M = Nb, Ta).* Journal of the American Ceramic Society, 2003. **86**(3): p. 437-440.
31. K. Noriaki, H. Kenji, Y. Yuichiro, H. Masaaki, K. Ryoji, Y. Masao, K. Takashi, K. Yuki, H. Shigenori and K. Koji, *A lithium superionic conductor.* Nature Materials, 2011. **10**(9): p. 682-686.
32. Y. Kato, S. Hori, T. Saito, K. Suzuki, M. Hirayama, A. Mitsui, M. Yonemura, H. Iba and R. Kanno, *High-power all-solid-state batteries using sulfide superionic conductors.* Nature Energy, 2016. **1**.
33. Z. Zhang, Y. Shao, B. Lotsch, Y.-S. Hu, H. Li, J. Janek, L.F. Nazar, C.-W. Nan, J. Maier, M. Armand and L. Chen, *New horizons for inorganic solid state ion conductors.* Energy & Environmental Science, 2018. **11**(8): p. 1945-1976.

34. X. He, Y. Zhu and Y. Mo, *Origin of fast ion diffusion in super-ionic conductors.* Nature Communications, 2017. **8**: p. 15893.
35. S. Shi, P. Lu, Z. Liu, Y. Qi, L.G. Hector, Jr., H. Li and S.J. Harris, *Direct Calculation of Li-Ion Transport in the Solid Electrolyte Interphase.* Journal of the American Chemical Society, 2012. **134**(37): p. 15476-15487.
36. Y. Yang, Q. Wu, Y. Cui, Y. Chen, S. Shi, R.-Z. Wang and H. Yan, *Elastic Properties, Defect Thermodynamics, Electrochemical Window, Phase Stability, and Li^+ Mobility of Li_3PS_4: Insights from First-Principles Calculations.* ACS Applied Materials & Interfaces, 2016. **8**(38): p. 25229-25242.
37. Z. Zhang, Z. Zou, K. Kaup, R. Xiao, S. Shi, M. Avdeev, Y.S. Hu, D. Wang, B. He, H. Li, X. Huang, L.F. Nazar and L. Chen, *Correlated migration invokes higher Na^+-ion conductivity in NASICON-type solid electrolytes.* Advanced Energy Materials, 2019. **9**(42): p. 1902373.
38. L. Long, S. Wang, M. Xiao and Y. Meng, *Polymer electrolytes for lithium polymer batteries.* Journal of Materials Chemistry A, 2016. **4**(26): p. 10038-10069.
39. Z. Xue, D. He and X. Xie, *Poly(ethylene oxide)-based electrolytes for lithium-ion batteries.* Journal of Materials Chemistry A, 2015. **3**(38): p. 19218-19253.
40. M.B.C. Armand, J. M.; Duclot, M, *"Second International Meeting on Solid Electrolytes, St. Andrews, Scotland, September 20−22."*. Extended Abstracts, 1978.
41. Y. Jiang, X.M. Yan, Z.F. Ma, P. Mei, W. Xiao, Q.L. You and Y. Zhang, *Development of the PEO based solid polymer electrolytes for all-solid state lithium ion batteries.* Polymers, 2018. **10**(11): p. 1237.
42. F. Gebert, J. Knott, R. Gorkin, S.-L. Chou and S.-X. Dou, *Polymer electrolytes for sodium-ion batteries.* Energy Storage Materials, 2021. **36**: p. 10-30.
43. W. Jia, Z. Li, Z. Wu, L. Wang, B. Wu, Y. Wang, Y. Cao and J. Li, *Graphene oxide as a filler to improve the performance of PAN-$LiClO_4$ flexible solid polymer electrolyte.* Solid State Ionics, 2018. **315**: p. 7-13.
44. J. Mindemark, R. Mogensen, M.J. Smith, M.M. Silva and D. Brandell, *Polycarbonates as alternative electrolyte host materials for solid-state sodium batteries.* Electrochemistry Communications, 2017. **77**: p. 58-61.
45. F. Xu, S. Deng, Q. Guo, D. Zhou and X. Yao, *Quasi-Ionic Liquid Enabling Single-Phase Poly(vinylidene fluoride)-Based Polymer Electrolytes for Solid-State $LiNi_{0.6}Co_{0.2}Mn_{0.2}O_2$||Li Batteries with Rigid-Flexible Coupling Interphase.* Small Methods, 2021. **5**(7): p. 2100262.
46. M. Romero, R. Faccio and A.W. Mombru, *Novel fluorine-free 2,2 '-bis(4,5-dimethylimidazole) additive for lithium-ion poly(methyl methacrylate) solid polymer electrolytes.* RSC Advances, 2016. **6**(71): p. 67150-67156.
47. X. Cheng, J. Pan, Y. Zhao, M. Liao and H. Peng, *Gel Polymer Electrolytes for Electrochemical Energy Storage.* Advanced Energy Materials, 2018. **8**(7).
48. https://en.wikipedia.org/wiki/Bollore_Bluecar, 2011.
49. 黄祯，杨菁，陈晓添，陶益成，刘登，高超，龙鹏 and 许晓雄，

无机固体电解质材料的基础与应用研究. 储能科学与技术, 2015. **4**(01): p. 1-18.
50. Z.Z. Zhang, Y.J. Shao, B. Lotsch, Y.S. Hu, H. Li, J. Janek, L.F. Nazar, C.W. Nan, J. Maier, M. Armand and L.Q. Chen, *New horizons for inorganic solid state ion conductors.* Energy & Environmental Science, 2018. **11**(8): p. 1945-1976.
51. P. Birke, F. Salam, S. Doring and W. Weppner, *A first approach to a monolithic all solid state inorganic lithium battery.* Solid State Ionics, 1999. **118**(1-2): p. 149-157.
52. G.Y. Adachi, N. Imanaka and H. Aono, *Fast Li-circle plus conducting ceramic electrolytes.* Advanced Materials, 1996. **8**(2): p. 127.
53. S. Stramare, V. Thangadurai and W. Weppner, *Lithium lanthanum titanates: A review.* Chemistry of Materials, 2003. **15**(21): p. 3974-3990.
54. Y. Zhao and L.L. Daemen, *Superionic Conductivity in Lithium-Rich Anti-Perovskites.* Journal of the American Chemical Society, 2012. **134**(36): p. 15042-15047.
55. S. Li, J. Zhu, Y. Wang, J.W. Howard, X. Lu, Y. Li, R.S. Kumar, L. Wang, L.L. Daemen and Y. Zhao, *Reaction mechanism studies towards effective fabrication of lithium-rich anti-perovskites Li3OX (X = Cl, Br).* Solid State Ionics, 2016. **284**: p. 14-19.
56. Z.D. Hood, H. Wang, A.S. Pandian, J.K. Keum and C. Liang, *Li2OHCl Crystalline Electrolyte for Stable Metallic Lithium Anodes.* Journal of the American Chemical Society, 2016. **138**(6): p. 1768-1771.
57. A. Emly, E. Kioupakis and A. Van der Ven, *Phase Stability and Transport Mechanisms in Antiperovskite Li3OCl and Li3OBr Superionic Conductors.* Chemistry of Materials, 2013. **25**(23): p. 4663-4670.
58. W. Hou, X. Guo, X. Shen, K. Amine, H. Yu and J. Lu, *Solid electrolytes and interfaces in all-solid-state sodium batteries: Progress and perspective.* Nano Energy, 2018. **52**: p. 279-291.
59. Z. Jian, Y.-S. Hu, X. Ji and W. Chen, *NASICON-structured materials for energy storage.* Advanced Materials, 2017. **29**(20): p. 1601925.
60. D. Mazza, *Modeling ionic conductivity in Nasicon structures.* Journal of Solid State Chemistry, 2001. **156**(1): p. 154-160.
61. H. Kohler, H. Schulz and O. Melnikov, *Composition and conduction mechanism of the NASICON structure X-ray-diffraction study on 2 crystals at different temperatures.* Materials Research Bulletin, 1983. **18**(9): p. 1143-1152.
62. U.V. Alpen, M.F. Bell and W. Wichelhaus, *Phase-transition in NASICON ($Na_3Zr_2Si_2PO_{12}$).* Materials Research Bulletin, 1979. **14**(10): p. 1317-1322.
63. 杨菁, 刘高瞻, 沈麟 and 姚霞银, *NASICON 结构钠离子固体电解质及固态钠电池应用研究进展* 储能科学与技术, 2020. **9**(5): p. 1284-1299.
64. H. Aono, E. Sugimoto, Y. Sadaoka, N. Imanaka and G.Y. Adachi, *Electrical properties and sinterability for lithium germanium phosphate $Li_{1+x}M_xGe_{2-x}(PO_4)_3$, M=Al, Cr, Ga, Fe, Sc, and In systems.* Bulletin of the Chemical Society of Japan, 1992. **65**(8): p. 2200-2204.
65. R. Murugan, V. Thangadurai and W. Weppner, *Fast lithium ion conduction in garnet-type Li7La3Zr2O12.* Angewandte Chemie-International Edition, 2007. **46**(41): p. 7778-

7781.
66. J. Awaka, N. Kijima, H. Hayakawa and J. Akimoto, *Synthesis and structure analysis of tetragonal $Li_7La_3Zr_2O_{12}$ with the garnet-related type structure.* Journal of Solid State Chemistry, 2009. **182**(8): p. 2046-2052.
67. J. Awaka, A. Takashima, K. Kataoka, N. Kijima, Y. Idemoto and J. Akimoto, *Crystal Structure of Fast Lithium-ion-conducting Cubic Li7La3Zr2O12.* Chemistry Letters, 2011. **40**(1): p. 60-62.
68. C. Wang, K. Fu, S.P. Kammampata, D.W. McOwen, A.J. Samson, L. Zhang, G.T. Hitz, A.M. Nolan, E.D. Wachsman, Y. Mo, V. Thangadurai and L. Hu, *Garnet-type solid-state electrolytes: materials, interfaces, and batteries.* Chemical Reviews, 2020. **120**(10): p. 4257-4300.
69. K.H. Nie, Y.S. Hong, J.L. Qiu, Q.H. Li, X.Q. Yu, H. Li and L.Q. Chen, *Interfaces Between Cathode and Electrolyte in Solid State Lithium Batteries: Challenges and Perspectives.* Frontiers in Chemistry, 2018. **6**.
70. J.-M. Doux, Y. Yang, D.H.S. Tan, N. Han, E.A. Wu, X. Wang, A. Banerjee and Y.S. Meng, *Pressure effects on sulfide electrolytes for all solid-state batteries.* Journal of Materials Chemistry A, 2020. **8**(10): p. 5049-5055.
71. S. Chen, D. Xie, G. Liu, J.P. Mwizerwa, Q. Zhang, Y. Zhao, X. Xu and X. Yao, *Sulfide solid electrolytes for all-solid-state lithium batteries: Structure, conductivity, stability and application.* Energy Storage Materials, 2018. **14**: p. 58-74.
72. G. Liu, D. Xie, X. Wang, X. Yao, S. Chen, R. Xiao, H. Li and X. Xu, *High air-stability and superior lithium ion conduction of $Li_{3+3x}P_{1-x}Zn_xS_{4-x}O_x$ by aliovalent substitution of ZnO for all-solid-state lithium batteries.* Energy Storage Materials, 2019. **17**: p. 266-274.
73. H. Wang, Y. Chen, Z.D. Hood, G. Sahu, A.S. Pandian, J.K. Keum, K. An and C. Liang, *An air-stable Na_3SbS_4 superionic conductor prepared by a rapid and economic synthetic procedure.* Angewandte Chemie-International Edition, 2016. **55**(30): p. 8551-8555.
74. F. Croce, G.B. Appetecchi, L. Persi and B. Scrosati, *Nanocomposite polymer electrolytes for lithium batteries.* Nature, 1998. **394**(6692): p. 456-458.
75. J. Zheng and Y.Y. Hu, *New Insights into the Compositional Dependence of Li-Ion Transport in Polymer-Ceramic Composite Electrolytes.* ACS Applied Materials & Interfaces, 2018. **10**(4): p. 4113-4120.
76. L. Chen, Y.T. Li, S.P. Li, L.Z. Fan, C.W. Nan and J.B. Goodenough, *PEO/garnet composite electrolytes for solid-state lithium batteries: From "ceramic-in-polymer" to "polymer-in-ceramic".* Nano Energy, 2018. **46**: p. 176-184.
77. E.L. Littauer and K.C. Tsai, *Anodic Behavior of Lithium in Aqueous Electrolytes: IV . Influence of Temperature.* J. Electrochem. Soc.: ELECTROCHEMICAL SCIENCE AND TECHNOLOGY, 1980. **127**: p. 521-524.
78. T. Ogasawara, A. Debart, M. Holzapfel, P. Novak and P.G. Bruce, *Rechargeable Li_2O_2 electrode for lithium batteries.* JOURNAL OF THE AMERICAN CHEMICAL SOCIETY, 2006. **128**(4): p. 1390-1393.

79. H.G. Jung, J. Hassoun, J.B. Park, Y.K. Sun and B. Scrosati, *An improved high-performance lithium-air battery.* Nature Chemistry, 2012. **4**(7): p. 579-585.
80. T. Kuboki, T. Okuyama, T. Ohsaki and N. Takami, *Lithium-air batteries using hydrophobic room temperature ionic liquid electrolyte.* JOURNAL OF POWER SOURCES, 2005. **146**: p. 766-769.
81. J. Hassoun, F. Croce, M. Armand and B. Scrosati, *Investigation of the O_2 electrochemistry in a polymer electrolyte solid-state cell.* Angew Chem Int Ed Engl, 2011. **50**(13): p. 2999-3002.
82. J. Lai, Y. Xing, N. Chen, L. Li, F. Wu and R. Chen, *Electrolytes for Rechargeable Lithium-Air Batteries.* Angew Chem Int Ed Engl, 2020. **59**(8): p. 2974-2997.
83. Z.Y. Lyu, Y. Zhou, W.R. Dai, X.H. Cui, M. Lai, L. Wang, F.W. Huo, W. Huang, Z. Hu and W. Chen, *Recent advances in understanding of the mechanism and control of Li_2O_2 formation in aprotic Li-O_2 batteries* CHEMICAL SOCIETY REVIEWS, 2017. **46**(19): p. 6073-6073.
84. H.D. Lim, B. Lee, Y. Bae, H. Park, Y. Ko, H. Kim, J. Kim and K. Kang, *Reaction chemistry in rechargeable Li-O_2 batteries.* CHEMICAL SOCIETY REVIEWS, 2017. **46**(10): p. 2873-2888.
85. F.L. Qiu, X. Li, H. Deng, D. Wang, X.W. Mu, P. He and H.S. Zhou, *A Concentrated Ternary-Salts Electrolyte for High Reversible Li Metal Battery with Slight Excess Li.* Advanced Energy Materials, 2019. **9**(本文介绍了一种浓缩锂双(三氟甲烷磺酰)酰亚胺(LiTFSI)-硝酸锂(LiNO 3)-锂双(氟磺酰基)酰亚胺(LiFSI)三元盐电解质，以实现高稳定锂金属全电池，): p. 1803372.
86. B. Liu, Y.L. Sun, L. Liu, S. Xu and X.B. Yan, *Advances in Manganese-Based Oxides Cathodic Electrocatalysts for Li-Air Batteries.* Advanced Functional Materials, 2018. **28**(15): p. 34.
87. M.A. Rahman, X.J. Wang and C. Wen, *A review of high energy density lithium-air battery technology.* Journal of Applied Electrochemistry, 2014. **44**(1): p. 5-22.
88. D. Gu, Y. Wang, S. Gu, C. Zhang and D. Yang, *Research Progress and Optimization of Non-aqueous Electrolyte for Lithium Air Batteries.* ACTA CHIMICA SINICA, 2013. **71**(10): p. 1354-1364.
89. F.J. Li and J. Chen, *Mechanistic Evolution of Aprotic Lithium-Oxygen Batteries.* Advanced Energy Materials, 2017. **7**(24): p. 1602934.
90. C. Liu, W.R. Brant, R. Younesi, Y. Dong, K. Edstrom, T. Gustafsson and J. Zhu, *Towards an Understanding of Li_2O_2 Evolution in Li-O_2 Batteries: An In Operando Synchrotron X-ray Diffraction Study.* ChemSusChem, 2017. **10**(7): p. 1592-1599.
91. P. He, T. Zhang, J. Jiang and H. Zhou, *Lithium-Air Batteries with Hybrid Electrolytes.* Journal of Physical Chemistry Letters, 2016. **7**(7): p. 1267-1280.
92. P. He, Y.G. Wang and H.S. Zhou, *A Li-air fuel cell with recycle aqueous electrolyte for improved stability.* Electrochemistry Communications, 2010. **12**(12): p. 1686-1689.
93. Y.R. Wang, P. He and H.S. Zhou, *Li-Redox Flow Batteries Based on Hybrid Electrolytes: At the Cross Road between Li-ion and Redox Flow Batteries.* Advanced Energy

Materials, 2012. **2**(7): p. 770-779.
94. Y.R. Wang, Y.G. Wang and H.S. Zhou, *A Li-Liquid Cathode Battery Based on a Hybrid Electrolyte.* ChemSusChem, 2011. **4**(8): p. 1087-1090.
95. Y. Liu, P. He and H. Zhou, *Rechargeable Solid-State Li-Air and Li-S Batteries: Materials, Construction, and Challenges.* Advanced Energy Materials, 2018. **8**(4): p. 1701602.
96. B. Kumar, J. Kumar, R. Leese, J.P. Fellner, S.J. Rodrigues and K.M. Abraham, *A Solid-State, Rechargeable, Long Cycle Life Lithium-Air Battery.* Journal of the Electrochemical Society, 2010. **157**(1): p. A50-A54.
97. P. Kichambare, S. Rodrigues and J. Kumar, *Mesoporous Nitrogen-Doped Carbon-Glass Ceramic Cathodes for Solid-State Lithium-Oxygen Batteries.* ACS Applied Materials & Interfaces, 2012. **4**(1): p. 49-52.
98. X. Chi, M. Li, J. Di, P. Bai, L. Song, X. Wang, F. Li, S. Liang, J. Xu and J. Yu, *A Highly Stable and Flexible Zeolite Electrolyte Solid-State Li-Air Battery.* Nature, 2021. **592**(7855): p. 551-557.
99. Y.J. Liu, B.J. Li, H. Kitaura, X.P. Zhang, M. Han, P. He and H.S. Zhou, *Fabrication and Performance of All-Solid-State Li-Air Battery with SWCNTs/LAGP Cathode.* ACS Applied Materials & Interfaces, 2015. **7**(31): p. 17307-17310.
100. S.M. Cho, J.H. Yom and W.Y. Yoon, *Application of PEG-based solid polymer electrolyte to all-solid-state Li-O_2 batteries.* Abstracts of Papers of the American Chemical Society, 2017. **253**: p. 1-10.
101. Y. Liu, B. Li, Z. Cheng, C. Li, X. Zhang, S. Guo, P. He and H. Zhou, *Intensive investigation on all-solid-state Li-air batteries with cathode catalysts of single-walled carbon nanotube/RuO_2.* Journal of Power Source, 2018. **395**: p. 439-443.
102. C.J. Liu, W.R. Brant, R. Younesi, Y.Y. Dong, K. Edstrom, T. Gustafsson and J.F. Zhu, *Towards an Understanding of Li_2O_2 Evolution in Li-O_2 Batteries: An InOperando Synchrotron X-ray Diffraction Study.* ChemSusChem, 2017. **10**(7): p. 1592-1599.
103. T. Liu, Z.G. Liu, G.W. Kim, J.T. Frith, N. Garcia-Araez and C.P. Grey, *Understanding LiOH Chemistry in a Ruthenium-Catalyzed Li-O_2 Battery.* ANGEWANDTE CHEMIE-INTERNATIONAL EDITION, 2017. **56**(50): p. 16057-16062.
104. W. Liu, Y. Shen, Y. Yu, X. Lu, W. Zhang, Z.M. Huang, J.T. Meng, Y.H. Huang and Z.P. Guo, *Intrinsically Optimizing Charge Transfer via Tuning Charge/Discharge Mode for Lithium-Oxygen Batteries.* Small, 2019. **15**(19): p. 1900154.
105. H. Lin, Z.X. Liu, Y. Mao, X.J. Liu, Y.Q. Fang, Y. Liu, D.Y. Wang and J.Y. Xie, *Effect of nitrogen-doped carbon/Ketjenblack composite on the morphology of Li2O2 for high-energy-density Li-air batteries.* Carbon, 2016. **96**: p. 965-971.
106. F.J. Li, Y. Chen, D.M. Tang, Z.L. Jian, C. Liu, D. Golberg, A. Yamada and H.S. Zhou, *Performance-improved Li-O-2 battery with Ru nanoparticles supported on binder-free multi-walled carbon nanotube paper as cathode.* Energy & Environmental Science, 2014. **7**(5): p. 1648-1652.
107. J.J. Xu, Z.L. Wang, D. Xu, L.L. Zhang and X.B. Zhang, *Tailoring deposition and*

morphology of discharge products towards high-rate and long-life lithium-oxygen batteries. Nature Communications, 2013. **4**: p. 10.

108. Y. Shen, D. Sun, L. Yu, W. Zhang, Y.Y. Shang, H.R. Tang, J.F. Wu, A.Y. Cao and Y.H. Huang, *A high-capacity lithium-air battery with Pd modified carbon nanotube sponge cathode working in regular air.* Carbon, 2013. **62**: p. 288-295.
109. R.M. Silva, A.J.S. Fernandes, M.C. Ferro, N. Pinna and R.F. Silva, *Vertically aligned N-doped CNTs growth using Taguchi experimental design.* Applied Surface Science, 2015. **344**: p. 57-64.
110. Y.L. Li, J.J. Wang, X.F. Li, D.S. Geng, R.Y. Li and X.L. Sun, *Superior energy capacity of graphene nanosheets for a nonaqueous lithium-oxygen battery.* Chemical Communications, 2011. **47**(33): p. 9438-9440.
111. Y. Chen, F.J. Li, D.M. Tang, Z.L. Jian, C. Liu, D. Golberg, A. Yamada and H.S. Zhou, *Multi-walled carbon nanotube papers as binder-free cathodes for large capacity and reversible non-aqueous Li-O-2 batteries.* Journal of Materials Chemistry A, 2013. **1**(42): p. 13076-13081.
112. X. Xin, K. Ito and Y. Kubo, *Graphene/activated carbon composite material for oxygen electrodes in lithium–oxygen rechargeable batteries.* Carbon, 2016. **99**: p. 167-173.
113. F. Mizuno, K. Takechi, S. Higashi, T. Shiga, T. Shiotsuki, N. Takazawa, Y. Sakurabayashi, S. Okazaki, I. Nitta, T. Kodama, H. Nakamoto, H. Nishikoori, S. Nakanishi, Y. Kotani and H. Iba, *Cathode reaction mechanism of non-aqueous Li-O-2 batteries with highly oxygen radical stable electrolyte solvent.* Journal of Power Sources, 2013. **228**: p. 47-56.
114. M.M.O. Thotiyl, S.A. Freunberger, Z.Q. Peng and P.G. Bruce, *The Carbon Electrode in Nonaqueous Li-O-2 Cells.* Journal of the American Chemical Society, 2013. **135**(1): p. 494-500.
115. C.K. Lee and Y.J. Park, *Polyimide-wrapped carbon nanotube electrodes for long cycle Li-air batteries.* Chemical Communications, 2015. **51**(7): p. 1210-1213.
116. Z.Q. Peng, S.A. Freunberger, Y.H. Chen and P.G. Bruce, *A Reversible and Higher-Rate Li-O-2 Battery.* Science, 2012. **337**(6094): p. 563-566.
117. G.Y. Zhao, Y.N. Niu, L. Zhang and K.N. Sun, *Ruthenium oxide modified titanium dioxide nanotube arrays as carbon and binder free lithium air battery cathode catalyst.* Journal of Power Sources, 2014. **270**: p. 386-390.
118. G.Y. Zhao, J.X. Lv, Z.M. Xu, L. Zhang and K.N. Sun, *Carbon and binder free rechargeable Li-O-2 battery cathode with Pt/Co3O4 flake arrays as catalyst.* Journal of Power Sources, 2014. **248**: p. 1270-1274.
119. Y. Liu, L. Suo, H. Lin, W. Yang, Y. Fang, X. Liu, D. Wang, Y.S. Hu, W. Han and L. Chen, *Novel approach for a high-energy-density Li-air battery: tri-dimensional growth of Li2O2 crystals tailored by electrolyte Li+ ion concentrations.* Journal of Materials Chemistry A, 2014. **2**(24): p. 9020-9024.
120. J. Christensen, P. Albertus, R.S. Sanchez-Carrera, T. Lohmann, B. Kozinsky, R. Liedtke, J. Ahmed and A. Kojic, *A Critical Review of Li/Air Batteries.* Journal of the

Electrochemical Society, 2012. **159**(2): p. R1-R30.
121. M.D. Radin and D.J. Siegel, *Charge transport in lithium peroxide: relevance for rechargeable metal-air batteries.* Energy & Environmental Science, 2013. **6**(8): p. 2370-2379.
122. H.D. Lim, H. Song, H. Gwon, K.Y. Park, J. Kim, Y. Bae, H. Kim, S.K. Jung, T. Kim, Y.H. Kim, X. Lepro, R. Ovalle-Robles, R.H. Baughman and K. Kang, *A new catalyst-embedded hierarchical air electrode for high-performance Li-O-2 batteries.* Energy & Environmental Science, 2013. **6**(12): p. 3570-3575.
123. X. Xin, K. Ito and Y. Kubo, *Electrochemical Behavior of Ru Nanoparticles as Catalysts in Aprotic Li–O_2 Batteries.* Electrochimica Acta, 2018. **261**: p. 323-329.
124. Y.C. Lu, Z.C. Xu, H.A. Gasteiger, S. Chen, K. Hamad-Schifferli and Y. Shao-Horn, *Platinum-Gold Nanoparticles: A Highly Active Bifunctional Electrocatalyst for Rechargeable Lithium-Air Batteries.* Journal of the American Chemical Society, 2010. **132**(35): p. 12170-12171.
125. Y. Yang, W. Liu, Y.M. Wang, X.C. Wang, L. Xiao, J.T. Lu and L. Zhuang, *A PtRu catalyzed rechargeable oxygen electrode for Li-O-2 batteries: performance improvement through Li2O2 morphology control.* Physical Chemistry Chemical Physics, 2014. **16**(38): p. 20618-20623.
126. H. Cheng and K. Scott, *Carbon-supported manganese oxide nanocatalysts for rechargeable lithium-air batteries.* Journal of Power Sources, 2010. **195**(5): p. 1370-1374.
127. Y.M. Cui, Z.Y. Wen and Y. Liu, *A free-standing-type design for cathodes of rechargeable Li-O-2 batteries.* Energy & Environmental Science, 2011. **4**(11): p. 4727-4734.
128. F.J. Li, R. Ohnishi, Y. Yamada, J. Kubota, K. Domen, A. Yamada and H.S. Zhou, *Carbon supported TiN nanoparticles: an efficient bifunctional catalyst for non-aqueous Li-O-2 batteries.* Chemical Communications, 2013. **49**(12): p. 1175-1177.
129. H. Kitaura and H.S. Zhou, *Electrochemical Performance of Solid-State Lithium-Air Batteries Using Carbon Nanotube Catalyst in the Air Electrode.* Advanced Energy Materials, 2012. **2**(7): p. 889-894.
130. S.A. Wohlgemuth, F. Vilela, M.M. Titirici and M. Antonietti, *A one-pot hydrothermal synthesis of tunable dual heteroatom-doped carbon microspheres.* Green Chemistry, 2012. **14**(3): p. 741-749.
131. A.F. Holloway, G.G. Wildgoose, R.G. Compton, L.D. Shao and M.L.H. Green, *The influence of edge-plane defects and oxygen-containing surface groups on the voltammetry of acid-treated, annealed and "super-annealed" multiwalled carbon nanotubes.* Journal of Solid State Electrochemistry, 2008. **12**(10): p. 1337-1348.
132. X.M. Ren, S.S. Zhang, D.T. Tran and J. Read, *Oxygen reduction reaction catalyst on lithium/air battery discharge performance.* Journal of Materials Chemistry, 2011. **21**(27): p. 10118-10125.
133. H.D. Lim, H. Song, J. Kim, H. Gwon, Y. Bae, K.Y. Park, J. Hong, H. Kim, T. Kim, Y.H. Kim, X. Lepro, R. Ovalle-Robles, R.H. Baughman and K. Kang, *Superior*

Rechargeability and Efficiency of Lithium-Oxygen Batteries: Hierarchical Air Electrode Architecture Combined with a Soluble Catalyst. Angewandte Chemie-International Edition, 2014. **53**(15): p. 3926-3931.

134. B.J. Bergner, A. Schurmann, K. Peppler, A. Garsuch and J. Janek, *TEMPO: A Mobile Catalyst for Rechargeable Li-O-2 Batteries.* Journal of the American Chemical Society, 2014. **136**(42): p. 15054-15064.
135. Y.H. Chen, S.A. Freunberger, Z.Q. Peng, O. Fontaine and P.G. Bruce, *Charging a Li-O-2 battery using a redox mediator.* Nature Chemistry, 2013. **5**(6): p. 489-494.
136. D.S. Kim and Y.J. Park, *Effect of multi-catalysts on rechargeable Li-air batteries.* Journal of Alloys and Compounds, 2014. **591**: p. 164-169.
137. Z. Ma, X.X. Yuan, L. Li, Z.F. Ma, D.P. Wilkinson, L. Zhang and J.J. Zhang, *A review of cathode materials and structures for rechargeable lithium-air batteries.* Energy & Environmental Science, 2015. **8**(8): p. 2144-2198.
138. R. Zhang, X. Shen, X.B. Cheng and Q. Zhang, *The dendrite growth in 3D structured lithium metal anodes: Electron or ion transfer limitation?* Energy Storage Materials, 2019. **23**: p. 556-565.
139. D. Wang, W. Zhang, W.T. Zheng, X.Q. Cui, T. Rojo and Q. Zhang, *Towards High-Safe Lithium Metal Anodes: Suppressing Lithium Dendrites via Tuning Surface Energy.* Advanced Science, 2017. **4**(1): p. 11.
140. M. Asadi, B. Sayahpour, P. Abbasi, A.T. Ngo, K. Karis, J.R. Jokisaari, C. Liu, B. Narayanan, M. Gerard, P. Yasaei, X. Hu, A. Mukherjee, K.C. Lau, R.S. Assary, F. Khalili-Araghi, R.F. Klie, L.A. Curtiss and A. Salehi-Khojin, *A lithium-oxygen battery with a long cycle life in an air-like atmosphere.* Nature, 2018. **555**(7697): p. 502-+.
141. D. Gelman, B. Shvartsev and Y. Ein-Eli, *Challenges and Prospect of Non-aqueous Non-alkali (NANA) Metal-Air Batteries.* Topics in Current Chemistry, 2016. **374**(6): p. 42.
142. B.D. McCloskey, A. Speidel, R. Scheffler, D.C. Miller, V. Viswanathan, J.S. Hummelshoj, J.K. Norskov and A.C. Luntz, *Twin Problems of Interfacial Carbonate Formation in Nonaqueous Li-O-2 Batteries.* Journal of Physical Chemistry Letters, 2012. **3**(8): p. 997-1001.
143. B. Zhou, L.M. Guo, Y.T. Zhang, J.W. Wang, L.P. Ma, W.H. Zhang, Z.W. Fu and Z.Q. Peng, *A High-Performance Li-O-2 Battery with a Strongly Solvating Hexamethylphosphoramide Electrolyte and a LiPON-Protected Lithium Anode.* Advanced Materials, 2017. **29**(30): p. 6.
144. M.M.O. Thotiyl, S.A. Freunberger, Z.Q. Peng, Y.H. Chen, Z. Liu and P.G. Bruce, *A stable cathode for the aprotic Li-O-2 battery.* Nature Materials, 2013. **12**(11): p. 1049-1055.
145. Z.H. Wei, P. Tan, L. An and T.S. Zhao, *A non-carbon cathode electrode for lithium-oxygen batteries.* Applied Energy, 2014. **130**: p. 134-138.
146. T. Liu, Q.C. Liu, J.J. Xu and X.B. Zhang, *Cable-Type Water-Survivable Flexible Li-O_2 Battery.* Small, 2016. **12**(23): p. 3101-3105.
147. T. Liu, J.J. Xu, Q.C. Liu, Z.W. Chang, Y.B. Yin, X.Y. Yang and X.B. Zhang, *Ultrathin,*

Lightweight, and Wearable Li-O_2 Battery with High Robustness and Gravimetric/Volumetric Energy Density. Small, 2017. **13**(6): p. 1602952.
148. F.J. Li, D.M. Tang, T. Zhang, K.M. Liao, P. He, D. Golberg, A. Yamada and H.S. Zhou, *Superior Performance of a Li-O_2 Battery with Metallic RuO_2 Hollow Spheres as the Carbon-Free Cathode.* Advanced Energy Materials, 2015. **5**(13): p. 1500294.
149. F.J. Li, H. Kitaura and H.S. Zhou, *The Pursuit Of Rechargeable Solid-State Li-Air Batteries.* Energy & Environmental Science, 2013. **6**(8): p. 2302-2311.
150. J. Yi, S. Guo, P. He and H. Zhou, *Status and prospects of polymer electrolytes for solid-state Li–O_2 (air) batteries.* Energy & Environmental Science, 2017. **10**(4): p. 860-884.
151. S. Larfaillou, D. Guy-Bouyssou, F. le Cras and S. Franger, *Comprehensive characterization of all-solid-state thin films commercial microbatteries by Electrochemical Impedance Spectroscopy.* Journal of Power Sources, 2016. **319**: p. 139-146.
152. J. Fu, *Fast Li+ ion conduction in Li2O-Al2O3-TiO2-SiO2-P2O5 glass-ceramics.* Journal of the American Ceramic Society, 1997. **80**(7): p. 1901-1903.
153. J.K. Feng, L. Lu and M.O. Lai, *Lithium storage capability of lithium ion conductor Li1.5Al0.5Ge1.5(PO4)(3).* Journal of Alloys and Compounds, 2010. **501**(2): p. 255-258.
154. G. Girishkumar, B. McCloskey, A.C. Luntz, S. Swanson and W. Wilcke, *Lithium - Air Battery: Promise and Challenges.* Journal of Physical Chemistry Letters, 2010. **1**(14): p. 2193-2203.
155. S.A. Freunberger, Y. Chen, Z. Peng, J.M. Griffin, L.J. Hardwick, F. Barde, P. Novak and P.G. Bruce, *Reactions in the Rechargeable Lithium-O-2 Battery with Alkyl Carbonate Electrolytes.* Journal of the American Chemical Society, 2011. **133**(20): p. 8040-8047.
156. A.M. Stephan, *Review on gel polymer electrolytes for lithium batteries.* European Polymer Journal, 2006. **42**(1): p. 21-42.
157. K.S. Ngai, S. Ramesh, K. Ramesh and J.C. Juan, *A review of polymer electrolytes: fundamental, approaches and applications.* Ionics, 2016. **22**(8): p. 1259-1279.
158. R.C. Agrawal and G.P. Pandey, *Solid polymer electrolytes: materials designing and all-solid-state battery applications: an overview.* Journal Of Physics D-Applied Physics, 2008. **41**(22): p. 18.
159. J.R. Nair, M. Destro, F. Bella, G.B. Appetecchi and C. Gerbaldi, *Thermally cured semi-interpenetrating electrolyte networks (s-IPN) for safe and aging-resistant secondary lithium polymer batteries.* Journal of Power Sources, 2016. **306**: p. 258-267.
160. J.N. Feng, L. Wang, Y.J. Chen, P.Y. Wang, H.R. Zhang and X.M. He, *PEO based polymer-ceramic hybrid solid electrolytes: a review.* Nano Convergence, 2021. **8**(1): p. 12.
161. K. Tsunemi, H. Ohno and E. Tsuchida, *A MECHANISM OF IONIC-CONDUCTION OF POLY (VINYLIDENE FLUORIDE) - LITHIUM PERCHLORATE HYBRID FILMS.* Electrochimica Acta, 1983. **28**(6): p. 833-837.
162. A. Ferry, L. Edman, M. Forsyth, D.R. MacFarlane and J.Z. Sun, *NMR and Raman studies of a novel fast-ion-conducting polymer-in-salt electrolyte based on LiCF3SO3*

and PAN. Electrochimica Acta, 2000. **45**(8-9): p. 1237-1242.
163. J. Yi, S.H. Guo, P. He and H.S. Zhou, *Status and prospects of polymer electrolytes for solid-state Li-O-2 (air) batteries.* Energy & Environmental Science, 2017. **10**(4): p. 860-884.
164. B. Kumar, S.J. Rodrigues and L.G. Scanlon, *Ionic conductivity of polymer-ceramic composites.* Journal of the Electrochemical Society, 2001. **148**(10): p. A1191-A1195.
165. V. Thangadurai and W. Weppner, *Li(6)ALa(2)Ta(2)O(12) (A=Sr, Ba): Novel Garnet-Like Oxides for Fast Lithium Ion Conduction.* Advanced Functional Materials, 2005. **15**(1): p. 107-112.
166. J. Wakasugi, H. Munakata and K. Kanamura, *Effect of Gold Layer on Interface Resistance between Lithium Metal Anode and Li6.25Al0.25La3Zr2O12 Solid Electrolyte.* Journal of the Electrochemical Society, 2017. **164**(6): p. A1022-A1025.
167. L. Cheng, C.H. Wu, A. Jarry, W. Chen, Y.F. Ye, J.F. Zhu, R. Kostecki, K. Persson, J.H. Guo, M. Salmeron, G.Y. Chen and M. Doeff, *Interrelationships among Grain Size, Surface Composition, Air Stability, and Interfacial Resistance of Al-Substituted Li7La3Zr2O12 Solid Electrolytes.* ACS Applied Materials & Interfaces, 2015. **7**(32): p. 17649-17655.
168. J. Fu, *Superionic Conductivity Of Glass-Ceramics In The System Li_2O-Al_2O_3-TiO_2-P_2O_5.* Solid State Ionics, 1997. **96**(3-4): p. 195-200.
169. P. Johnson, N. Sammes, N. Imanishi, Y. Takeda and O. Yamamoto, *Effect of microstructure on the conductivity of a NASICON-type lithium ion conductor.* Solid State Ionics, 2011. **192**(1): p. 326-329.
170. X.X. Xu, Z.Y. Wen, X.W. Wu, X.L. Yang and Z.H. Gu, *Lithium ion-conducting glass-ceramics of Li1.5Al0.5Ge1.5(PO4)(3)-xLi(2)O (x=0.0-0.20) with good electrical and electrochemical properties.* Journal of the American Ceramic Society, 2007. **90**(9): p. 2802-2806.
171. Y. Zhao, W. Chen, J. Wu, Z. Hu, F. Liu, L. Wang and H. Peng, *Recent Advances In Charge Mechanism Of Noble Metal-Based Cathodes For Li-O_2 Batteries.* Chinese Chemical Letters, 2022.
172. Y. Li, X. Wang, S. Dong, X. Chen and G. Cui, *Recent Advances in Non-Aqueous Electrolyte for Rechargeable Li-O_2 Batteries.* Advanced Energy Materials, 2016. **6**(18).
173. H. Kitaura and H. Zhou, *Electrochemical Performance and Reaction Mechanism of All-Solid-State Lithium-Air Batteries Composed of Lithium, $Li_{1+x}Al_yGe_{2-y}(PO_4)_{(3)}$ Solid Electrolyte and Carbon Nanotube Air Electrode.* Energy & Environmental Science, 2012. **5**(10): p. 9077-9084.
174. B. Wu, S. Wang, J. Lochala, D. Desrochers, B. Liu, W. Zhang, J. Yang and J. Xiao, *The Role of the Solid Electrolyte Interphase Layer in Preventing Li Dendrite Growth in Solid-State Batteries.* Energy & Environmental Science, 2018. **11**(7): p. 1803-1810.
175. F. Qiu, X. Zhang, Y. Qiao, X. Zhang, H. Deng, T. Shi, P. He and H. Zhou, *An Ultra-Stable and Enhanced Reversibility Lithium Metal Anode with A Sufficient O_2 Design for Li-O_2 Battery.* Energy Storage Materials, 2018. **12**: p. 176-182.

176. K. Fu, Y. Gong, Z. Fu, H. Xie, Y. Yao, B. Liu, M. Carter, E. Wachsman and L. Hu, *Transient Behavior of the Metal Interface in Lithium Metal-Garnet Batteries.* Angewandte Chemie-International Edition, 2017. **56**(47): p. 14942-14947.
177. Q. Lu, Y.G. Gao, Q. Zhao, J. Li, X.H. Wang and F.S. Wang, *Novel Polymer Electrolyte From Poly(Carbonate-Ether) And Lithium Tetrafluoroborate For Lithium-Oxygen Battery.* Journal of Power Sources, 2013. **242**: p. 677-682.
178. Y. Zhang, L. Wang, Z.Y. Guo, Y.F. Xu, Y.G. Wang and H.S. Peng, *High-Performance Lithium-Air Battery with a Coaxial-Fiber Architecture.* Angewandte Chemie-International Edition, 2016. **55**(14): p. 4487-4491.
179. M. Balaish, E. Peled, D. Golodnitsky and Y. Ein-Eli, *Liquid-Free Lithium-Oxygen Batteries.* Angewandte Chemie-International Edition, 2015. **54**(2): p. 436-440.
180. Q. Zhong, B. Liu, B. Yang, Y. Li, J. Li and X. Yan, *Flexible Lithium Metal Capacitors Enabled By An In Situ Prepared Gel Polymer Electrolyte.* Chinese Chemical Letters, 2021. **32**(11): p. 3496-3500.
181. J. Hassoun, F. Croce, M. Armand and B. Scrosati, *Investigation of the O_2 Electrochemistry in a Polymer Electrolyte Solid-State Cell.* Angewandte Chemie-International Edition, 2011. **50**(13): p. 2999-3002.
182. Z.H. Gao, H.B. Sun, L. Fu, F.L. Ye, Y. Zhang, W. Luo and Y.H. Huang, *Promises, Challenges, and Recent Progress of Inorganic Solid-State Electrolytes for All-Solid-State Lithium Batteries.* Advanced Materials, 2018. **30**(17): p. 27.
183. C. Zhao, Q. Sun, J. Luo, J. Liang, Y. Liu, L. Zhang, J. Wang, S. Deng, X. Lin, X. Yang, H. Huang, S. Zhao, L. Zhang, S. Lu and X. Sun, *3D Porous Garnet/Gel Polymer Hybrid Electrolyte for Safe Solid-State Li–O_2 Batteries with Long Lifetimes.* Chemistry of Materials, 2020. **32**(23): p. 10113-10119.
184. H. Aono, E. Sugimoto, Y. Sadaoka, N. Imanaka and G.Y. Adachi, *Ionic-Conductivity Of The Lithium Titanium Phosphate ($Li_{1+X}Al_xTi_{2-X}(PO_4)_3$), ($Li_{1+x}Sc_xTi_{2-x}(PO_4)_3$), ($Li_{1+x}YxTi_{2-x}(PO_4)_3$), ($Li_{1+x}La_xTi_{2-}x(PO_4)_3$ Systems.* Journal of the Electrochemical Society, 1989. **136**(2): p. 590-591.
185. J. Fu, *Fast Li+ Ion Conducting Glass-Ceramics In The System Li_2O-Al_2O_3-GeO_2-P_2O_5.* Solid State Ionics, 1997. **104**(3-4): p. 191-194.
186. L. Li, R. Xu, L. Zhang, Z. Zhang, M. Yang, D. Liu, X. Yan and A. Zhou, *O-Tailored Microstructure-Engineered Interface toward Advanced Room Temperature All-Solid-State Na Batteries.* Advanced Functional Materials, 2022.
187. X.B. Zhu, T.S. Zhao, Z.H. Wei, P. Tan and L. An, *A High-Rate and Long Cycle Life Solid-State Lithium-Air Battery.* Energy & Environmental Science, 2015. **8**(12): p. 3745-3754.
188. K. Fu, Y.H. Gong, G.T. Hitz, D.W. McOwen, Y.J. Li, S.M. Xu, Y. Wen, L. Zhang, C.W. Wang, G. Pastel, J.Q. Dai, B.Y. Liu, H. Xie, Y.G. Yao, E.D. Wachsman and L.B. Hu, *Three-Dimensional Bilayer Garnet Solid Electrolyte Based High Energy Density Lithium Metal-Sulfur Batteries.* Energy & Environmental Science, 2017. **10**(7): p. 1568-1575.

189. C.P. Yang, H. Xie, W.W. Ping, K. Fu, B.Y. Liu, J.C. Rao, J.Q. Dai, C.W. Wang, G. Pastel and L.B. Hu, *An Electron/Ion Dual-Conductive Alloy Framework for High-Rate and High-Capacity Solid-State Lithium-Metal Batteries.* Advanced Materials, 2019. **31**(3): p. 7.
190. J. Wang, C. Wang, W. Wang, W. Li and J. Lou, *Carboxymethylated Nanocellulose-Based Gel Polymer Electrolyte With A High Lithium Ion Transfer Number For Flexible Lithium-Ion Batteries Application.* Chemical Engineering Journal, 2022. **428**.
191. C.-H. Tsao, H.-M. Su, H.-T. Huang, P.-L. Kuo and H. Teng, *Immobilized Cation Functional Gel Polymer Electrolytes With High Lithium Transference Number For Lithium Ion Batteries.* Journal of Membrane Science, 2019. **572**: p. 382-389.
192. H.Y.P. Hong, *Crystal-Structures And Crystal-Chemistry In System $Na_{1+x}Zr_2Si_xP_3$-xO_{12}.* Materials Research Bulletin, 1976. **11**(2): p. 173-182.
193. B.V.R. Chowdari, G.V.S. Rao and G.Y.H. Lee, *Xps And Ionic Conductivity Studies On Li_2O-Al_2O_3(TiO_2 Or GeO_2)-P_2O_5 Glass-Ceramics.* Solid State Ionics, 2000. **136**: p. 1067-1075.
194. S. Hasegawa, N. Imanishi, T. Zhang, J. Xie, A. Hirano, Y. Takeda and O. Yamamoto, *Study On Lithium/Air Secondary Batteries-Stability Of NASICON-Type Lithium Ion Conducting Glass-Ceramics With Water.* Journal of Power Sources, 2009. **189**(1): p. 371-377.
195. I. Abrahams and E. Hadzifejzovic, *Lithium Ion Conductivity And Thermal Behaviour Of Glasses And Crystallised Glasses In The System Li_2O-Al_2O_3-TiO_2-P_2O_5.* Solid State Ionics, 2000. **134**(3-4): p. 249-257.
196. Q. Yu, K. Jiang, C. Yu, X. Chen, C. Zhang, Y. Yao, B. Jiang and H. Long, *Recent Progress Of Composite Solid Polymer Electrolytes For All-Solid-State Lithium Metal Batteries.* Chinese Chemical Letters, 2021. **32**(9): p. 2659-2678.
197. J. Janek and W.G. Zeier, *A Solid Future For Battery Development.* Nature Energy, 2016. **1**.
198. A. Manthiram, X. Yu and S. Wang, *Lithium Battery Chemistries Enabled By Solid-State Electrolytes.* Nature Reviews Materials, 2017. **2**(4).
199. B. Wu, S. Wang, W.J. Evans, D.Z. Deng, J. Yang and J. Xiao, *Interfacial Behaviours Between Lithium Ion Conductors And Electrode Materials In Various Battery Systems.* Journal of Materials Chemistry A, 2016. **4**(40): p. 15266-15280.
200. C. Yu, C.T. Zhao, S.H. Liu, X.M. Fan, J. Yang, M.D. Zhang and J.S. Qiu, *Polystyrene Sphere-Mediated Ultrathin Graphene Sheet-Assembled Frameworks For High-Power Density Li-O_2 Batteries.* Chemical Communications, 2015. **51**(67): p. 13233-13236.
201. Q.C. Liu, T. Liu, D.P. Liu, Z.J. Li, X.B. Zhang and Y. Zhang, *A Flexible and Wearable Lithium-Oxygen Battery with Record Energy Density achieved by the Interlaced Architecture inspired by Bamboo Slips.* Advanced Materials, 2016. **28**(38): p. 8413-8418.
202. C.P. Yang, L. Zhang, B.Y. Liu, S.M. Xu, T. Hamann, D. McOwen, J.Q. Dai, W. Luo, Y.H. Gong, E.D. Wachsman and L.B. Hu, *Continuous Plating/Stripping Behavior Of*

Solid-State Lithium Metal Anode In A 3D Ion-Conductive Framework. Proceedings of the National Academy of Sciences of the United States of America, 2018. **115**(15): p. 3770-3775.

203. M. Tatsumisago, M. Nagao and A. Hayashi, *Recent Development Of Sulfide Solid Electrolytes And Interfacial Modification For All-Solid-State Rechargeable Lithium Batteries.* Journal of Asian Ceramic Societies, 2018. **1**(1): p. 17-25.
204. Z. Zhang, Z. Wang, L. Zhang, D. Liu, C. Yu, X. Yan, J. Xie and J. Huang, *Unraveling the Conversion Evolution on Solid-State Na-SeS_2 Battery via In Situ TEM.* Adv Sci (Weinh), 2022. **9**(14): p. e2200744.
205. P. Hartmann, T. Leichtweiss, M.R. Busche, M. Schneider, M. Reich, J. Sann, P. Adelhelm and J. Janek, *Degradation of NASICON-Type Materials in Contact with Lithium Metal: Formation of Mixed Conducting Interphases (MCI) on Solid Electrolytes.* Journal of Physical Chemistry C, 2013. **117**(41): p. 21064-21074.
206. S. Wenzel, S. Randau, T. Leichtweiss, D.A. Weber, J. Sann, W.G. Zeier and J. Janek, *Direct Observation Of The Interfacial Instability Of The Fast Ionic Conductor $Li_{10}GeP_2S_{12}$ At The Lithium Metal Anode.* Chemistry of Materials, 2016. **28**(7): p. 2400-2407.
207. M.D. Tikekar, S. Choudhury, Z.Y. Tu and L.A. Archer, *Design Principles For Electrolytes And Interfaces For Stable Lithium-Metal Batteries.* Nature Energy, 2016. **1**: p. 1-7.
208. L. Xu, S. Tang, Y. Cheng, K.Y. Wang, J.Y. Liang, C. Liu, Y.C. Cao, F. Wei and L.Q. Mai, *Interfaces in Solid-State Lithium Batteries.* Joule, 2018. **2**(10): p. 1991-2015.
209. T. Zhang, N. Imanishi, S. Hasegawa, A. Hirano, J. Xie, Y. Takeda, O. Yamamoto and N. Sammes, *Water-Stable Lithium Anode with the Three-Layer Construction for Aqueous Lithium-Air Secondary Batteries.* Electrochemical and Solid State Letters, 2009. **12**(7): p. A132-A135.
210. Y. Suzuki, K. Watanabe, S. Sakuma and N. Imanishi, *Electrochemical Performance Of An All-Solid-State Lithium-Oxygen Battery Under Humidified Oxygen.* Solid State Ionics, 2016. **289**: p. 72-76.
211. H. Kitaura and H.S. Zhou, *All-Solid-State Lithium-Oxygen Battery With High Safety In Wide Ambient Temperature Range.* Scientific Reports, 2015. **5**: p. 8.
212. D.C. Lin, W. Liu, Y.Y. Liu, H.R. Lee, P.C. Hsu, K. Liu and Y. Cui, *High Ionic Conductivity of Composite Solid Polymer Electrolyte via In Situ Synthesis of Monodispersed SiO_2 Nanospheres in Poly(ethylene oxide).* Nano Letters, 2016. **16**(1): p. 459-465.
213. M. Ge, X. Zhou, Y. Qin, Y. Liu, J. Zhou, X. Wang and B. Guo, *A Composite PEO Electrolyte With Amide-Based Polymer Matrix For Suppressing Lithium Dendrite Growth In All-Solid-State Lithium Battery.* Chinese Chemical Letters, 2021.
214. D. Zeng, J. Yao, L. Zhang, R. Xu, S. Wang, X. Yan, C. Yu and L. Wang, *Promoting Favorable Interfacial Properties In Lithium-Based Batteries Using Chlorine-Rich Sulfide Inorganic Solid-State Electrolytes.* Nat Commun, 2022. **13**(1): p. 1909.

215. Z. Wang, S. Chen, Z. Huang, Z. Wei, L. Shen, H. Gu, X. Xu and X. Yao, *High Conductivity Polymer Electrolyte with Comb-Like Structure Via a Solvent-Free UV-Cured Method for Large-Area Ambient All-Solid-Sate Lithium Batteries.* Journal of Materiomics, 2019. **5**(2): p. 195-203.
216. M. Liu, X. Li, X. Wang, R. Yu, M. Chen, Q. Lu, B. Lu, H. Shu and X. Yang, *Facile Synthesis and Electrochemical Properties of High Lithium Ionic Conductivity $Li_{1.7}Al_{0.3}Ti_{1.7}Si_{0.4}P_{2.6}O_{12}$ Ceramic Solid Electrolyte.* Journal of Alloys and Compounds, 2018. **756**: p. 103-110.
217. Z. Wang, L. Shen, S. Deng, P. Cui and X. Yao, *10 μm-Thick High-Strength Solid Polymer Electrolytes with Excellent Interface Compatibility for Flexible All-Solid-State Lithium-Metal Batteries.* Adv Mater, 2021. **33**(25): p. e2100353.
218. H. Duan, Y.X. Yin, X.X. Zeng, J.Y. Li, J.L. Shi, Y. Shi, R. Wen, Y.G. Guo and L.J. Wan, *In-situ Plasticized Polymer Electrolyte With Double-Network For Flexible Solid-State Lithium-Metal Batteries.* Energy Storage Materials, 2018. **10**: p. 85-91.
219. K. Fu, Y.H. Gong, J.Q. Dai, A. Gong, X.G. Han, Y.G. Yao, C.W. Wang, Y.B. Wang, Y.N. Chen, C.Y. Yan, Y.J. Li, E.D. Wachsman and L.B. Hu, *Flexible, Solid-State, Ion-Conducting Membrane with 3D Garnet Nanofiber Networks for Lithium Batteries.* Proceedings of the National Academy of Sciences of the United States of America, 2016. **113**(26): p. 7094-7099.
220. M.M.O. Thotiyl, S.A. Freunberger, Z.Q. Peng, Y.H. Chen, Z. Liu and P.G. Bruce, *A Stable Cathode For The Aprotic Li-O_2 Battery.* Nature Materials, 2013. **12**(11): p. 1049-1055.
221. Z. Liu, N. Feng, Z. Shen, F. Li, P. He, H. Zhang and H. Zhou, *Carbon-Free O_2 Cathode with Three-Dimensional Ultralight Nickel Foam-Supported Ruthenium Electrocatalysts for Li-O_2 Batteries.* ChemSusChem, 2017. **10**(13): p. 2714-2719.
222. Y.C. Lu and Y. Shao-Horn, *Probing the Reaction Kinetics of the Charge Reactions of Nonaqueous Li-O_2 Batteries.* Journal of Physical Chemistry Letters, 2013. **4**(1): p. 93-99.
223. F. Mizuno, S. Nakanishi, Y. Kotani, S. Yokoishi and H. Iba, *Rechargeable Li-Air Batteries with Carbonate-Based Liquid Electrolytes.* Electrochemistry, 2010. **78**(5): p. 403-405.
224. S.A. Freunberger, Y.H. Chen, Z.Q. Peng, J.M. Griffin, L.J. Hardwick, F. Barde, P. Novak and P.G. Bruce, *Reactions in the Rechargeable Lithium-O_2 Battery with Alkyl Carbonate Electrolytes.* Journal of the American Chemical Society, 2011. **133**(20): p. 8040-8047.
225. S.A. Freunberger, Y.H. Chen, N.E. Drewett, L.J. Hardwick, F. Barde and P.G. Bruce, *The Lithium-Oxygen Battery with Ether-Based Electrolytes.* Angewandte Chemie-International Edition, 2011. **50**(37): p. 8609-8613.
226. J. Yi, X.Z. Liu, S.H. Guo, K. Zhu, H.L. Xue and H.S. Zhou, *Novel Stable Gel Polymer Electrolyte: Toward a High Safety and Long Life Li-Air Battery.* ACS Applied Materials & Interfaces, 2015. **7**(42): p. 23798-23804.
227. C.S. Yang, K.N. Gao, X.P. Zhang, Z. Sun and T. Zhang, *Rechargeable Solid-State Li-*

Air Batteries: A Status Report. Rare Metals, 2018. **37**(6): p. 459-472.
228. A. Manthiram, X.W. Yu and S.F. Wang, *Lithium Battery Chemistries Enabled by Solid-State Electrolytes.* Nature Reviews Materials, 2017. **2**(4): p. 16.
229. Z. Gao, H. Sun, L. Fu, F. Ye, Y. Zhang, W. Luo and Y. Huang, *Promises, Challenges, and Recent Progress of Inorganic Solid-State Electrolytes for All-Solid-State Lithium Batteries.* Advanced Materials, 2018. **30**(17).
230. K. Fu, Y. Gong, B. Liu, Y. Zhu, S. Xu, Y. Yao, W. Luo, C. Wang, S.D. Lacey, J. Dai, Y. Chen, Y. Mo, E. Wachsman and L. Hu, *Toward Garnet Electrolyte-Based Li Metal Batteries: An Ultrathin, Highly Effective, Artificial Solid-State Electrolyte/Metallic Li Interface.* Science Advances, 2017. **3**(4).
231. J.F. Wu, E.Y. Chen, Y. Yu, L. Liu, Y. Wu, W.K. Pang, V.K. Peterson and X. Guo, *Gallium-Doped $Li_7La_3Zr_2O_{12}$ Garnet-Type Electrolytes with High Lithium-Ion Conductivity.* ACS Appl Mater Interfaces, 2017. **9**(2): p. 1542-1552.
232. V. Thangadurai, S. Narayanan and D. Pinzaru, *Garnet-Type Solid-State Fast Li Ion Conductors for Li Batteries: Critical Review.* Chemical Society Reviews, 2014. **43**(13): p. 4714-4727.
233. N. Zhao, W. Khokhar, Z. Bi, C. Shi, X. Guo, L.-Z. Fan and C.-W. Nan, *Solid Garnet Batteries.* Joule, 2019. **3**(5): p. 1190-1199.
234. C. Deviannapoorani, L.S. Shankar, S. Ramakumar and R. Murugan, *Investigation on Lithium Ion Conductivity and Structural Stability of Yttrium-Substituted $Li_7La_3Zr_2O_{12}$.* Ionics, 2016. **22**(8): p. 1281-1289.
235. I. Garbayo, M. Struzik, W.J. Bowman, R. Pfenninger, E. Stilp and J.L.M. Rupp, *Glass-Type Polyamorphism in Li-Garnet Thin Film Solid State Battery Conductors.* Advanced Energy Materials, 2018. **8**(12): p. 14.
236. Y.J. Shao, H.C. Wang, Z.L. Gong, D.W. Wang, B.Z. Zheng, J.P. Zhu, Y.X. Lu, Y.S. Hu, X.X. Guo, H. Li, X.J. Huang, Y. Yang, C.W. Nan and L.Q. Chen, *Drawing a Soft Interface: An Effective Interfacial Modification Strategy for Garnet Type Solid-State Li Batteries.* ACS Energy Letters, 2018. **3**(6): p. 1212-1218.
237. J. Meng, Y. Zhang, X. Zhou, M. Lei and C. Li, *Li_2Co_3-Affiliative Mechanism for Air-Accessible Interface Engineering of Garnet Electrolyte via Facile Liquid Metal Painting.* Nature Communications, 2020. **11**(1): p. 3716.
238. M. Cai, J. Jin, T. Xiu, Z. Song, M.E. Badding and Z. Wen, *In-Situ Constructed Lithium-Salt Lithiophilic Layer Inducing Bi-Functional Interphase for Stable LLZO/Li Interface.* Energy Storage Materials, 2022. **47**: p. 61-69.
239. W. Luo, Y.H. Gong, Y.Z. Zhu, Y.J. Li, Y.G. Yao, Y. Zhang, K. Fu, G. Pastel, C.F. Lin, Y.F. Mo, E.D. Wachsman and L.B. Hu, *Reducing Interfacial Resistance between Garnet-Structured Solid-State Electrolyte and Li-Metal Anode by a Germanium Layer.* Advanced Materials, 2017. **29**(22): p. 7.
240. Z. Gu, X. Xin, J. Yang, D. Guo, S. Yang, J. Wu, Y. Sun and X. Yao, *Bilayer NASICON/Polymer Hybrid Electrolyte for Stable Solid-State Li–O_2 Batteries.* ACS Applied Energy Materials, 2022.

241. J. Wang, G. Huang, K. Chen and X.B. Zhang, *An Adjustable-Porosity Plastic Crystal Electrolyte Enables High-Performance All-Solid-State Lithium-Oxygen Batteries.* Angew Chem Int Ed Engl, 2020. **59**(24): p. 9382-9387.
242. C. Li, Y.J. Liu, B.J. Li, F. Zhang, Z. Cheng, P. He and H.S. Zhou, *Integrated Solid Electrolyte with Porous Cathode by Facilely One-Step Sintering for An All-Solid-State Li-O_2 Battery.* Nanotechnology, 2019. **30**(36): p. 7.
243. X. Liu, X. Xin, L. Shen, Z. Gu, J. Wu and X. Yao, *Poly(methyl methacrylate)-Based Gel Polymer Electrolyte for High-Performance Solid State Li–O2 Battery with Enhanced Cycling Stability.* ACS Applied Energy Materials, 2021. **4**(4): p. 3975-3982.
244. C. Zhao, Y. Zhu, Q. Sun, C. Wang, J. Luo, X. Lin, X. Yang, Y. Zhao, R. Li, S. Zhao, H. Huang, L. Zhang, S. Lu, M. Gu and X. Sun, *Transition of the Reaction from Three-Phase to Two-Phase by Using a Hybrid Conductor for High-Energy-Density High-Rate Solid-State Li-O(2) Batteries.* Angew Chem Int Ed Engl, 2021. **60**(11): p. 5821-5826.
245. X.H. Zou, Q. Lu, Y.J. Zhong, K.M. Liao, W. Zhou and Z.P. Shao, *Flexible, Flame-Resistant, and Dendrite-Impermeable Gel-Polymer Electrolyte for Li-O-2/Air Batteries Workable Under Hurdle Conditions.* Small, 2018. **14**(34): p. 10.
246. J.Y. Sun, N. Zhao, Y.Q. Li, X.X. Guo, X.F. Feng, X.S. Liu, Z. Liu, G.L. Cui, H. Zheng, L. Gu and H. Li, *A Rechargeable Li-Air Fuel Cell Battery Based on Garnet Solid Electrolytes.* Scientific Reports, 2017. **7**: p. 8.
247. S. Wang, J. Wang, J. Liu, H. Song, Y. Liu, P. Wang, P. He, J. Xu and H. Zhou, *Ultra-Fine Surface Solid-State Electrolytes for Long Cycle Life All-Solid-State Lithium–Air Batteries.* Journal of Materials Chemistry A, 2018. **6**(43): p. 21248-21254.
248. X.B. Zhu, T.S. Zhao, Z.H. Wei, P. Tan and G. Zhao, *A Novel Solid-State Li-O_2 Battery with an Integrated Electrolyte and Cathode Structure.* Energy & Environmental Science, 2015. **8**(9): p. 2782-2790.
249. J. Hafner, *Ab-initio simulations of materials using VASP: Density-functional theory and beyond.* Journal of Computational Chemistry, 2008. **29**(13): p. 2044-2078.
250. J.P. Perdew, K. Burke and M. Ernzerhof, *Generalized Gradient Approximation Made Simple.* Phys Rev Lett, 1996. **77**(18): p. 3865-3868.
251. S. Grimme, J. Antony, S. Ehrlich and H. Krieg, *A consistent and accurate ab initio parametrization of density functional dispersion correction (DFT-D) for the 94 elements H-Pu.* Journal of Chemical Physics, 2010. **132**(15).
252. M. Balaish, E. Peled, D. Golodnitsky and Y. Ein-Eli, *Liquid-Free Lithium-Oxygen Batteries.* Angewandte Chemie, 2015. **127**(2): p. 446-450.
253. Y.J. Liu, B.J. Li, Z. Cheng, C. Li, X.Y. Zhang, S.H. Guo, P. He and H.S. Zhou, *Intensive Investigation on All-Solid-State Li-Air Batteries with Cathode Catalysts of Single-Walled Carbon Nanotube/RuO_2.* Journal of Power Sources, 2018. **395**: p. 439-443.
254. Y.J. Liu, C. Li, B.J. Li, H.C. Song, Z. Cheng, M.R. Chen, P. He and H.S. Zhou, *Germanium Thin Film Protected Lithium Aluminum Germanium Phosphate for Solid-State Li Batteries.* Advanced Energy Materials, 2018. **8**(16): p. 7.
255. W. Yu, C. Xue, B. Hu, B. Xu, L. Li and C.-W. Nan, *Oxygen- and Dendrite-Resistant*

Ultra-Dry Polymer Electrolytes for Solid-State Li–O_2 Batteries. Energy Storage Materials, 2020. **27**: p. 244-251.

256. H. Liu, L. Zhao, Y. Xing, J. Lai, L. Li, F. Wu, N. Chen and R. Chen, *Enhancing the Long Cycle Performance of Li–O_2 Batteries at High Temperatures Using Metal–Organic Framework-Based Electrolytes.* ACS Applied Energy Materials, 2022. **5**(6): p. 7185-7191.
257. Y. Long, Z. Zhang, L. Zhao, Q. Zeng, Q. Li, J. Wang, D. Li, Q. Xia, Y. Liu, X. Han, Z. Zhou, Y. Li, Y. Zhang and S. Chou, *Bucket effect on high-performance Li–O2 batteries based on P-doped 3D NiO microspheres with conformal growth of discharge products.* Journal of Materials Chemistry A, 2022.
258. H. Xia, Q.F. Xie, Y.H. Tian, Q. Chen, M. Wen, J.L. Zhang, Y. Wang, Y.P. Tang and S. Zhang, *High-Efficient CoPt/Activated Functional Carbon Catalyst for Li-O_2 batteries.* Nano Energy, 2021. **84**: p. 9.
259. Y.J. Ding, Y.C. Huang, Y.J. Li, T. Zhang and Z.S. Wu, *Regulating Surface Electron Structure of PtNi Nanoalloy Via Boron Doping For High-Current-Density Li-O_2 Batteries with Low Overpotential And Long-Life Cyclability.* Smartmat: p. 11.
260. D.Y. Zhao, P. Wang, H.X. Di, P. Zhang, X.B. Hui and L.W. Yin, *Single Semi-Metallic Selenium Atoms on Ti_3C_2 MXene Nanosheets as Excellent Cathode for Lithium-Oxygen Batteries.* Advanced Functional Materials, 2021. **31**(29): p. 11.
261. Y. Zhou, K. Yin, Q.F. Gu, L. Tao, Y.J. Li, H. Tan, J.H. Zhou, W.S. Zhang, H.B. Li and S.J. Guo, *Lewis-Acidic PtIr Multipods Enable High-Performance Li-O_2 Batteries.* Angewandte Chemie-International Edition, 2021. **60**(51): p. 26592-26598.
262. Y.J. Ji, H.L. Dong, M.Y. Yang, T.J. Hou and Y.Y. Li, *Monolayer Germanium Monochalcogenides (Ges/GesSe) as Cathode Catalysts in Nonaqueous Li-O_2 Batteries.* Physical Chemistry Chemical Physics, 2017. **19**(31): p. 20457-20462.